

New Ways to Look through Nanopores

Klughammer, N.

DOI

[10.4233/uuid:b43633d1-5722-4457-8603-8396ff34181e](https://doi.org/10.4233/uuid:b43633d1-5722-4457-8603-8396ff34181e)

Publication date

2023

Document Version

Final published version

Citation (APA)

Klughammer, N. (2023). *New Ways to Look through Nanopores*. [Dissertation (TU Delft), Delft University of Technology]. <https://doi.org/10.4233/uuid:b43633d1-5722-4457-8603-8396ff34181e>

Important note

To cite this publication, please use the final published version (if applicable).
Please check the document version above.

Copyright

Other than for strictly personal use, it is not permitted to download, forward or distribute the text or part of it, without the consent of the author(s) and/or copyright holder(s), unless the work is under an open content license such as Creative Commons.

Takedown policy

Please contact us and provide details if you believe this document breaches copyrights.
We will remove access to the work immediately and investigate your claim.

New Ways to Look through Nanopores

Klughammer, N.

DOI

[10.4233/uuid:b43633d1-5722-4457-8603-8396ff34181e](https://doi.org/10.4233/uuid:b43633d1-5722-4457-8603-8396ff34181e)

Publication date

2023

Document Version

Other version

Citation (APA)

Klughammer, N. (2023). *New Ways to Look through Nanopores*. [Dissertation (TU Delft), Delft University of Technology]. <https://doi.org/10.4233/uuid:b43633d1-5722-4457-8603-8396ff34181e>

Important note

To cite this publication, please use the final published version (if applicable).
Please check the document version above.

Copyright

Other than for strictly personal use, it is not permitted to download, forward or distribute the text or part of it, without the consent of the author(s) and/or copyright holder(s), unless the work is under an open content license such as Creative Commons.

Takedown policy

Please contact us and provide details if you believe this document breaches copyrights.
We will remove access to the work immediately and investigate your claim.

New Ways to Look through Nanopores



Nils Klughammer

NEW WAYS TO LOOK THROUGH NANOPORES

NEW WAYS TO LOOK THROUGH NANOPORES

Dissertation

for the purpose of obtaining the degree of doctor
at Delft University of Technology,
by the authority of the Rector Magnificus, Prof.dr.ir. T.H.J.J. van der Hagen,
chair of the Board for Doctorates to be defended publicly on
Friday 17th November 2023 at 15:00 o'clock

by

Nils KLUGHAMMER

Master of Science in Physics, Universität Heidelberg, Germany,
born in Kist, Germany.

This dissertation has been approved by the promotor.

Composition of the doctoral committee:

Rector Magnificus	chairperson
Prof. dr. C. Dekker	Delft University of Technology, promotor
Prof. dr. C. Joo	Delft University of Technology, promotor

Independent members:

Prof. dr. A. M. Dogterom	Delft University of Technology
Prof. dr. A. Meller	Technion - Israel Institute of Technology, Israel
Prof. dr. L. M. Veenhoff	University of Groningen
Prof. dr. F. Montel	Ecole Normale Supérieure de Lyon, France
Prof. dr. B. Rieger	Delft University of Technology, reserve member

Other member:

Prof. dr. ir. P. R. Onck	University of Groningen
--------------------------	-------------------------



Keywords: Single-molecule Biophysics; Single-molecule Fluorescence; Solid-state Nanopores; Nanofabrication; Nanotechnology; Zero-mode Waveguides; Subwavelength Apertures; Palladium Nanopores; Live-cell Imaging; Nuclear Pore Complex; Nuclear Transport; Cryo-EM; Diffusiophoresis; Free Diffusion

Printed by: Proefschriftspecialist

Front & Back: Artist's impression of a scientist looking through an 87 nm Pd Nanopore, Letters are color coded by global average temperatures from 1850-2021, Nils Klughammer

Copyright © 2023 by N. Klughammer

Casimir PhD Series, Delft-Leiden 2023-30

ISBN 978-90-8593-577-3

An electronic version of this dissertation is available at
<http://repository.tudelft.nl/>.

CONTENTS

1	General Introduction	1
1.1	Nanopores	2
1.2	Techniques used throughout this thesis	8
1.3	In this thesis	13
	References	15
2	Palladium Zero-Mode Waveguides for Optical Single-Molecule Detection with Nanopores	27
3	Diffusiophoresis-Driven DNA Translocation through Palladium Nanopores	28
3.1	Introduction	29
3.2	Materials and methods	31
3.3	Results and discussion	32
3.4	Conclusions and outlook	38
	References	39
3.5	Appendix	43
4	Diameter Dependence of Transport through Nuclear Pore Complex Mimics Studied Using Optical Nanopores	46
4.1	Introduction	47
4.2	Results	49
4.3	Discussion	63
4.4	Methods and Materials	67
4.5	Data availability	75
	References	75
4.6	Appendix	84
5	Investigating the Structure of Unstructured Nuclear Pore Complex Mimics using Cryo Electron Microscopy	117
5.1	Introduction	118
5.2	Materials and methods	121
5.3	Results and discussion	123
5.4	Conclusions and outlook	139
	References	140
5.5	Appendix	144
6	Zero-mode waveguide nanowells for single-molecule detection in living cells	145
6.1	Introduction	146
6.2	Results	147
6.3	Discussion	159

6.4	Conclusions	162
6.5	Methods and Materials	162
6.6	Data availability	167
	References	167
6.7	Appendix	174
7	Future directions	199
7.1	Pd ZMWs	200
7.2	NPCs	202
	References	203
	Summary	206
	Samenvatting	209
	Zusammenfassung	212
	Acknowledgements	216
	Curriculum Vitae	217
	List of Publications	218

1

GENERAL INTRODUCTION

In this chapter, we give a brief introduction to the relevant background that will enable to follow the various studies presented in this thesis. We start by introducing the concept of nanopores and describe the variety of settings in which nanopores are encountered. We then focus on nanopores as single-molecule sensors and the wide range of applications. We discuss different sensing modalities of nanopores and put a special focus on optical sensing in metallic nanopores. Subsequently, we introduce zero-mode waveguides that form a special class of metallic nanopores. We discuss different modes of single-molecule transport through nanopores before zooming in on the nuclear pore complex, which is a biological nanopore complex that governs the transport between a cell's cytoplasm and its nucleus. In the second part of this chapter, we introduce the relevant techniques used in this thesis, ranging from nanofabrication, optical microscopy, electron microscopy, to simulations. Finally, we conclude the chapter with an outlook on the individual chapters of the thesis.

1.1. NANOPORES

As the name suggests, nanopores are pores of nanometer size [1] in a membrane. Despite their conceptual simplicity, they have gained a lot of attention due to their application as nanopore sensors, which allow the sensing of single molecules, for instance DNA and proteins. DNA, as the bearer of genetic information, is a long polymer chain built of the four nucleobases A,C,T, and G. The information is stored in the sequence of the individual bases, which is key to cell biology. Therefore, revealing the sequence of single DNA molecules was a driving force for nanopore research over many years [2–5]. With the release of a first device based on nanopores in 2014 [6] and the commercialization by Oxford Nanopore Technologies, the academic interest in single-molecule DNA sequencing with nanopores decreased. Still, the scientific interest in nanopores has not ceased, as evidenced by recent developments towards a better understanding of biological processes such as the Nuclear Pore Complex [7–11], polymer physics [12, 13], nanoscale transport phenomena [14], and other subjects [15]. Another interesting major application of nanopores is single-molecule protein sequencing [16–19]. According to the central dogma of biology, the genetic information that is stored in the DNA gets transcribed to RNA, which in turn gets translated to proteins. Proteins are polymers consisting of a linear chain of amino acids of which the sequence is determined by the base sequence of the original DNA. Proteins are often referred as the work horses of the cell as they are performing a vast amount of functions ranging from metabolic reactions, formation of the cell's cytoskeleton, to transport [20]. The full set of proteins present in a cell, called the proteome, determines the cell's state, which explains how cells sharing the same genetic material can be so different in their functions and morphologies. The proteome is a more direct measure of the cell's state than the genome, hence showing the importance of developing tools for single-molecule protein identification [16].

Nanopore research is typically connected with single-molecule sensing. Beyond that, however, nanopores are also used to localize or deliver single molecules very precisely [21–25], for gas sensing applications [26], and for filtering applications [27]. Furthermore, biological nanopores play vital roles in many biological processes in our cells, for instance as DNA packaging motors [1], pore forming toxins, and most prominently, ion and transport channels, among which is the nuclear pore complex (NPC) [28].

When a nanopore is embedded in an electrically insulating membrane (such as silicon nitride or a lipid bilayer) the electrical conductance across the membrane - which is set by the ion current running through the nanopore - can be used as a read-out for the state of the nanopore. Whereas, as we will see later, there is a big variety in readout mechanisms, recording the electrical conductance of the nanopore is the most common probe for nanopores used as single molecule sensors. For this, silver/silver chloride electrodes are immersed in the electrolyte reservoirs and connected to an amplifier that is able to record currents in the nanoampère range which is a well-established technology. By applying a voltage between the electrodes across the nanopore, a flow of ions through the nanopore is established of which the magnitude depends on multiple factors such as pore geometry, surface charge, salt type and concentration [29]. Whereas the actual ion flux in this system can not be directly followed, its average magnitude can be measured using the electrodes. On the minus-pole electrode, chloride ions get released from the electrode by taking up an electron, while on the plus pole they form silver chloride,

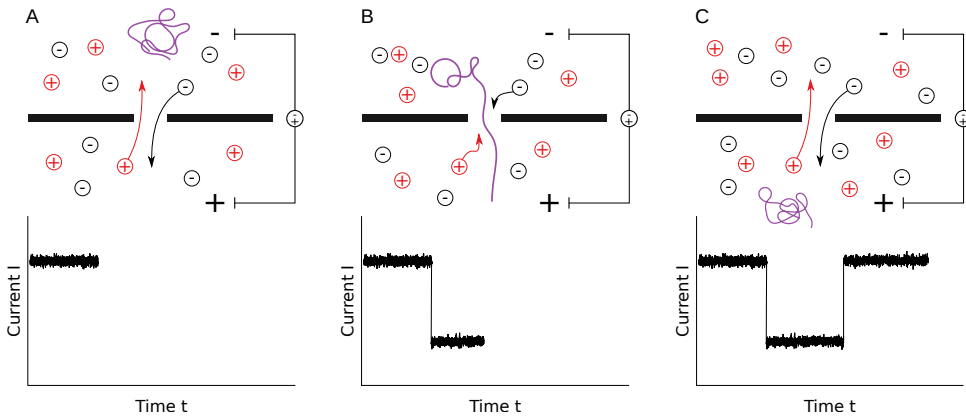


Figure 1.1: Basic principle of conductance-based nanopore sensors with the example of DNA translocations through a solid state nanopore. A: Ag/AgCl electrodes are submerged in two electrolyte baths that are separated by the insulating membrane. When a voltage is applied across the membrane, a current of ions establishes through the pore, which can be measured and recorded (bottom). B: The negatively charged DNA gets attracted to the minus pole by electrophoresis. While translocating, it sterically blocks a fraction of the pore. This blockade hinders ions from translocating which leads to a reduction of the current. The depth and duration of the current drop inform on the analyte that is translocating. C: After translocation, the current returns to the same open pore value as prior to DNA translocation.

releasing the electron to the electrode again. The resulting flow of electrons through the wires connecting the electrodes can then be measured, and is a reflection of the ion current through the nanopore.

1.1.1. DIFFERENT TYPES OF NANOPORES

Nanopores can be classified into two main classes by the material they consist of, namely organic and inorganic nanopores. For nanopores made of organic material both naturally occurring biological pores and human-designed pores have been described. Examples of naturally occurring biological pores are the nuclear pore complex, ion channels, and pore-forming toxins. The pore-forming toxins are the main nanopores used for sensing applications, with prominent examples being α -hemolysin (α -HL) [30, 31], Mycobacterium smegmatis porin A (MspA) [5, 18], and Fragaceatoxin C (FraC) [32, 33]. Depending on the application, different pores are preferred, to benefit from a certain geometry, charge distribution, stability, membrane insertion efficiency [28], or other features specific to a certain pore. One advantage of these pores is the possibility of atomic-scale modification with molecular biology techniques which has been done for instance to optimize the sensing region [34], to change internal flows [32], or to enhance specific binding inside the pore [35]. Moreover, pores were coupled to DNA structures [36] or protein machinery [37] to supplement the pores with a different functionality. One big strength of protein nanopores is the atomic similarity of different nanopores of the same type which leads to good experimental reproducibility of the observed behaviour. In addition to modifying naturally occurring pores, organic nanopores have also been fully designed by using peptides [38] or DNA origami [39, 40]. In DNA origami, a long DNA strand is folded into a specific 3D shape using short interconnecting staple strands [41].

Using easy design rules, this technique allows to build nanometric objects from scratch.

On the other hand, nanopores have been fabricated in solid-state membranes such as silicon nitride (SiN) [42], silicon oxide [43], or 2D materials such as graphene [44–46] which reduces the membrane thickness to the absolute minimum. Additionally, free-standing nanopores have been fabricated in metallic layers such as gold [47] or palladium [48]. The advantage of solid-state nanopores is that nano-fabrication techniques (as described below) can be used for production and customization of the pore geometry, which, for example, allows to make thousands of well-defined nanopores in arrays in a membrane.

1.1.2. TRANSPORT THROUGH NANOPORES

When considering single-molecule transport through nanopores, different physical effects can lead to translocations (Figure 1.2). First, there are several purely mechanical effects such as Brownian motion, fluid flow, and mechanical pulling of the analyte. In any nanopore system, particles are moving by Brownian motion which leads to diffusion. This motion can contribute to translocations through nanopores [13, 48]. In order to increase the translocation rate, the random movement can be biased, for instance by generating a fluid flow through the nanopore. Such a fluid flow does act both on charged and uncharged analytes and can have different sources such as a pressure gradient [12, 49, 50] or an electroosmotic flow [49, 51]. The latter electroosmotic flow is generated when a voltage is applied across a charged nanopore which is submersed in a salt solution. Due to electrostatic interactions, the charged nanopore surface accumulates a layer of counter ions which screen the surface charge of the nanopore and form the electric double layer. By applying a voltage across the pore, this cloud of ions is set into motion, which leads to the so-called electroosmotic fluid flow in the solvent. Regarding mechanical pulling, this was obtained by for instance optical tweezers or molecular motors [52–54]. For charged particles, nanopore translocations can also be facilitated by charged interactions, such as by electrophoresis, which was used already early on in nanopore research [30, 42, 44] and still to date is the standard way of translocating DNA through nanopore sensors. For this, typically a transmembrane voltage is applied through electrodes submersed in the bath which then drive the charged analyte towards the respective pole. Furthermore, analytes can also translocate through nanopores by diffusiophoresis [55, 56], an effect that will be discussed extensively in chapter 3 of this thesis. Diffusiophoresis is a complex interplay of different forces acting on the particle, arising from a concentration gradient of a solute interacting with the particle. This interaction can be a charged interaction but can also have a different origin.

In pursuit of direct DNA sequencing with nanopores, slowing down the translocation process was a field of active research. Several approaches to achieve this were identified, such as salt concentration, solvent viscosity, temperature, and the applied voltage [57, 58]. Additionally, DNA translocations were slowed down using molecular motors [5, 59], which finally made direct DNA sequencing with nanopores possible [6, 60]. Another possibility of slowing down DNA translocations is by opposing different forces described above so that the net force exerted on the analyte gets reduced [52, 55, 56]. In addition to that, surface interactions, an effect that is usually tried to be avoided, has been explored to slow down the translocation process [61, 62].

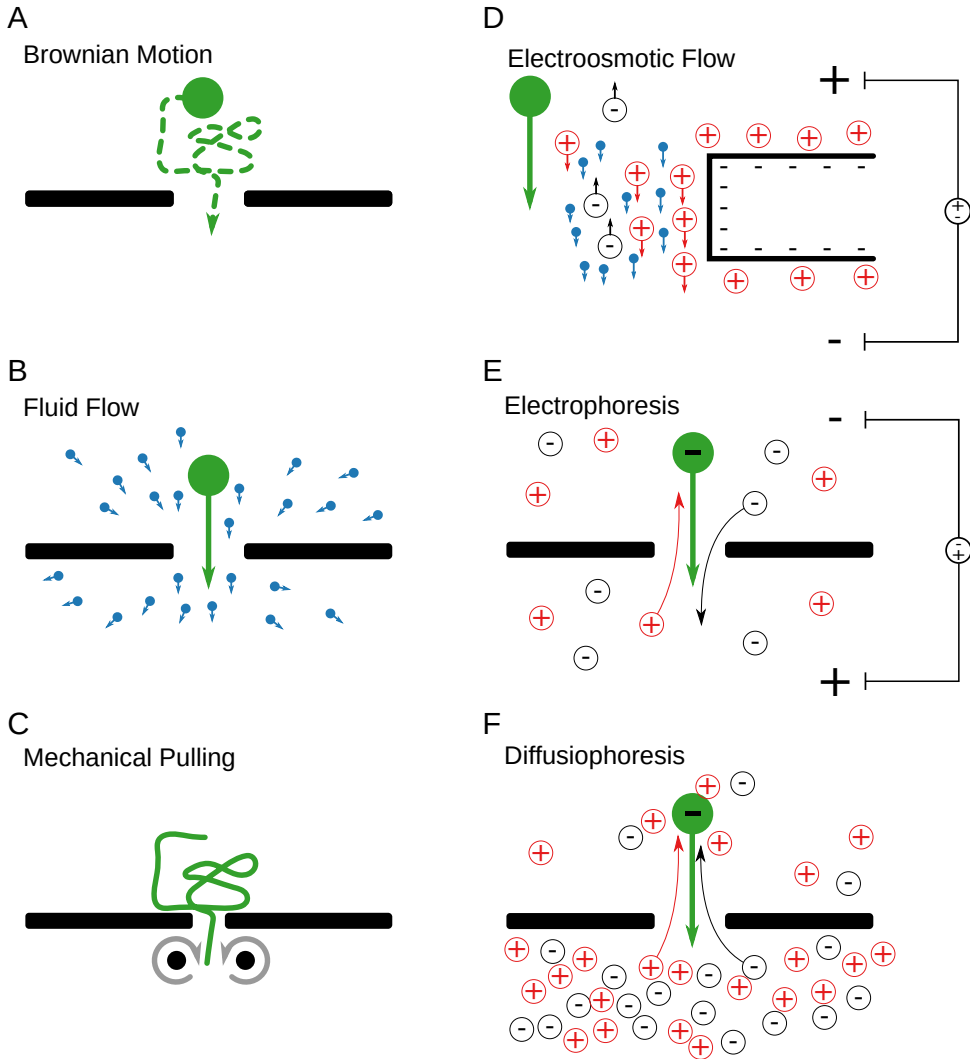


Figure 1.2: Different effects can contribute to single-molecule transport through nanopores. A: Due to Brownian motion, single analytes can find the entry of the nanopore and subsequently translocate in a stochastic manner. B: The analyte's movement can be biased by generating a fluid flow through the nanopore, for instance by applying a pressure gradient across the nanopore. The particle then simply gets dragged along in the fluid flow via friction. C: The analyte can be mechanically dragged through the nanopore, for instance by a molecular motor that exerts a force on the analyte. D: Another source of a fluid flow dragging along a particle, can be the so-called electroosmotic flow, as explained in detail in the main text. In short, a voltage across the membrane accelerates the ions in the electric double layer which leads to a hydrodynamic flow through the nanopore. E: For a charged particle, the movement of the particle can be guided through the nanopore by a voltage that leads to electrophoresis of the particle. F: A charged particle can be moved across the nanopore by diffusiophoresis of a salt concentration gradient is applied.

1.1.3. ZERO-MODE WAVEGUIDES

Nanopores formed in a metallic layer present a special class of nanopores because they can act as so called Zero-Mode Waveguides (ZMWs). The name originates from the fact that they don't allow a travelling mode of light to pass through them, an effect that occurs once the pore diameter d fulfills $d < \frac{\lambda}{1.7}$ [63], with λ being the wavelength of light in the medium filling the pore. In this case, the light field forms an evanescent wave that approximately follows an exponential intensity decay: $I(z) = I_0 \exp\left(-2z\sqrt{\frac{1}{1.7d}^2 - \frac{1}{\lambda^2}}\right)$, where z is the position into the ZMW and I_0 is the field intensity at the entry [63]. Importantly, this means that basically no light impinging on the pore travels through it if the membrane is thick enough. In the case of a freestanding ZMW, this leads to an illuminated side and a dark side, where no light penetrates. This effect can be used to follow translocations optically if an analyte is added to the dark side and only detected once it has translocated through the pore towards the bright side. Thus, complications arising from a classical current-based detection can be circumvented, such as decreasing signal-to-noise ratio with increasing pore size, with decreasing applied voltage, or with decreasing salinity. Additionally, it offers the possibility of a simultaneous detection of different colors [47], studying freely diffusing analytes [11, 48], and translocations driven by weak forces [12].

The most common application of ZMWs is not in a freestanding metal film, however, but suspended on a glass surface, such as done in several early studies of the ZMW effect [63–65]. Due to effects such as fluorescence enhancement [65–70], background suppression, and mainly volume reduction, ZMWs were used in a variety of applications, ranging from receptor-ligand binding to DNA sequencing applications [12, 47, 68, 71–81]. The main reason why ZMWs gained so much attention is their fluorescence volume reduction to the volume within the ZMW as compared to the volume of a confocal laser spot since it allows to increase the concentration of an analyte in the solution while still only observing a single particle in the ZMW at a time. In addition to in vitro studies, ZMWs have even been used in cases where live cells were protruding into the nanowells [75, 82, 83], where both the background suppression and the reduced observation volume are used to gain detailed insight on membrane bound analytes. We will present a more detailed discussion of this application in [chapter 6](#).

1.1.4. THE NUCLEAR PORE COMPLEX

One particular nanopore that gained a lot of attention due to its essential role in eukaryotic cells, is the nuclear pore complex (NPC). This very large protein complex sits within the nuclear envelope and regulates the transport between the cytoplasm and the nucleus. It features an eight-fold symmetry and is assembled from about thirty different proteins (called Nups) that appear in copy numbers ranging between 8 and 64 [84]. The transport regulation comes mainly from a tight mesh of NPC proteins bearing intrinsically-disordered domains rich in phenylalanine-glycine repeats (FG Nups). This mesh, which fills the central channel of the NPC, interacts via hydrophobic interactions and thus forms a selective barrier, allowing small molecules to translocate largely unhindered while blocking large molecules that do not interact with the FG mesh. This blockade becomes more efficient with increasing molecular mass of the inert molecule

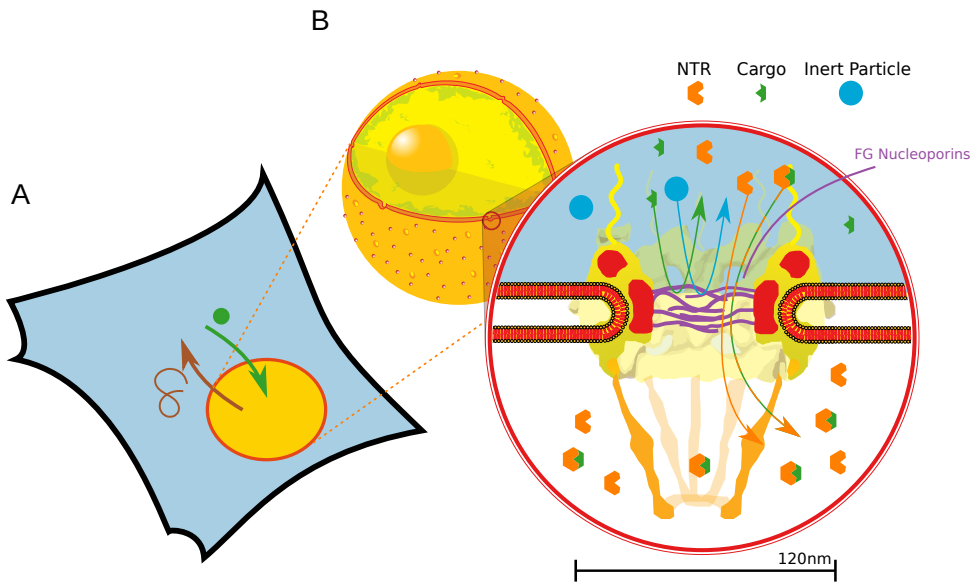


Figure 1.3: A: Between the nucleus (orange) and the cytoplasm (blue) of a eukaryotic cell, continuous transport takes place that is tightly regulated. For instance, proteins required in the nucleus need to be transported into it while mRNA needs to be transported towards the cytoplasm. On the other hand, nuclear DNA needs to be protected from potentially harming agents, such as DNA-degrading proteins. B: The nuclear pore complex (NPC) resides in the nuclear envelope and regulates the nucleo-cytoplasmic transport. The main regulation happens via a mesh of NPC proteins that occupies the central channel, which are rich in phenylalanine-glycine repeats (FG Nucleoporins). While big inert particles that do not interact with the FG mesh can not translocate, small molecules and nuclear transport receptors (NTRs) can travel through the mesh. NTRs have the capability to transport cargo through the mesh so that particles that would otherwise be hindered from translocating can travel through the NPC. This figure was adapted from Wikipedia [88] and falls under CC BY-SA 2.5.

[85]. To transport large molecules through the NPC, a specific transport system is in place, namely so-called nuclear transport receptors (NTRs), which can both bind specifically to cargo molecules that should be transported through the NPC and to the FG Nups [86]. One prominent example of nuclear transport is the system based on karyopherins (Kap95-Kap60) [87] which will be discussed in more detail in [chapter 4](#).

To explain the selective behaviour of NPCs observed *in vivo*, several models have been developed that often were based on insights gained from structural studies or *in vitro* experiments [89–95]. Whereas many models focus solely on the nature of the FG mesh, the class of *Kap-centric* models [93–95] describes the transport receptors as an integral part of the NPC. The role of NTRs in the *Kap-centric* models goes beyond its capability to transport cargoes but predictions involve modulating NPC properties such as transport rates and selectivity by residing within the FG mesh. Studying the different transport models *in vivo* is difficult for several reasons. First of all, cells can compensate the loss of specific functions by adapting so that a direct effect of a certain modification is hard to be studied. On the other hand, changes might be too drastic to maintain basic viability. For instance, most of the FG-domains of the yeast NPC can be deleted without killing the cells. If a few essential Nups were deleted, however, the cells did

not survive [96]. Furthermore, it is challenging to resolve transport through NPCs at the single-molecule level *in vivo*. Additionally, *in vivo* experiments can also be very time consuming. Therefore, a variety of minimal NPC systems have been developed, trying to reduce the full complexity of the NPC, allowing to study the behavior of individual components. Transport selectivity, as arguably the most prominent property, has been reconstituted using only single types of Nups such as Nup100, Nsp1, or even human-designed Nups [7–10, 91, 94, 97]. Here, NPC mimics based on nanopores in free-standing solid-state membranes [7–11] form a specific class that allows to study transport through a pore geometry. Technically, all of these studies were based on Nups grafted to the surface of solid-state nanopores and thus filling the pores. Together with different detection methods, this allowed to study how the transport through the pores was influenced by a certain type of Nups.

1.2. TECHNIQUES USED THROUGHOUT THIS THESIS

In this thesis, several technical methods will be employed to which we give a short introduction in this section. While different nanofabrication techniques were used to make nanometer-sized structure, we used electron microscopy to assess the fabrication success. For final data acquisition, we mainly used optical microscopy but also cryo-electron microscopy. Additionally, we introduce the basics of the simulations that we used to predict and explain the experimentally obtained results.

1.2.1. NANOFABRICATION

During the development of a nanofabrication strategy to reproducibly obtain circular palladium nanopores with diameters ranging between 20 nm to 300 nm, we used different nanofabrication strategies which we conceptually introduce in this section, taking the fabrication of freestanding palladium nanopores as the example. For solid-state nanopores in silicon nitride membranes, typically methods such as electron-beam drilling [98, 99] or dielectric breakdown [100–102] are used. In electron-beam drilling, a highly accelerated (typically 300 kV) electron beam is focused on a thin membrane which over time gets weakened until a pore opens up. A different method based on the same principle of accelerated particles impinging on the surface and thereby thinning a membrane was already used early on in solid-state nanopores where highly accelerated Argon ions were directed onto a locally thinned membrane [42] and thus removing material from the membrane until a pore would open up. By focusing the ion beam and scanning across the surface, more control about the nanopore fabrication process can be achieved [103]. The processes described so far, however, require either a scanning transmission electron microscope working at high enough acceleration voltage or a focused ion beam (FIB) scanning electron microscope and thus very specialized and expensive equipment. Therefore, also other methods were developed allowing for inexpensive and higher throughput nanopore fabrication such as dielectric breakdown [100–102] or reactive ion etching [104]. In dielectric breakdown, a voltage on the order of several volts is applied across a membrane until a pore spontaneously forms. The pore can be grown to the desired size before the voltage is switched off. This process can be accelerated by keeping the membrane in non-neutral pH [100] and has the advantage that

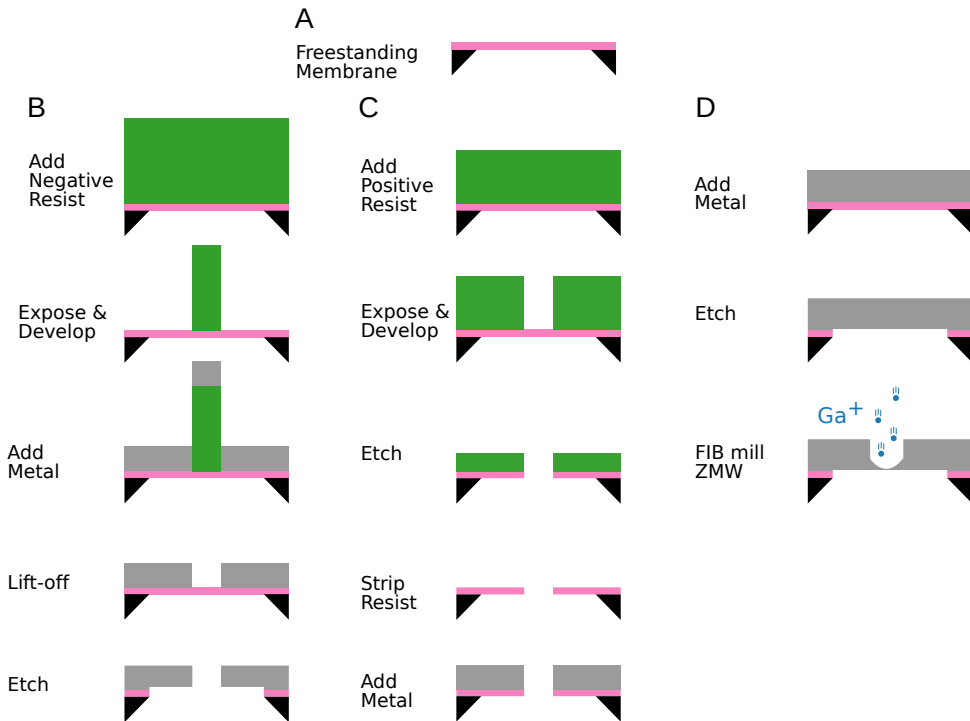


Figure 1.4: Different fabrication strategies can lead to freestanding palladium nanopores. A: Starting out with a freestanding membrane (for instance SiN allows to use different processes based on negative resist lift-off (B), reactive ion etching (C), or focused ion beam milling (FIB) (D)). B: When a negative-tone resist is used the resist is applied to the membrane and subsequently structures can be patterned using electron-beam lithography (as the feature size of optical lithography is typically too large to obtain sub-100 nm nanopores). Subsequently, the resist gets developed so that only the patterned structures stay. A metal layer is deposited to the surface which also covers the top of the resist. By removing the remaining resist together with the metal layer on top, the patterned features show up in the metal layer on the surface. To open up the pores, the supporting membrane needs to be punched by methods such as electron-beam drilling or chemical etching. C: By using a positive-tone resist, the structures get directly patterned into the resist, showing up after development. Subsequently, both the resist and the supporting membrane get etched from the resist side, so that a pore opens up. After removal of the remaining resist, a metal layer can be applied to the surface, preserving the opening in the support membrane. D: For FIB milling, first a metal layer is applied and subsequently the supporting membrane can be removed. A focused beam of highly accelerated heavy ions is focused on the location where a pore should be fabricated. The ions then mill away material until a pore is formed.

the pore is immediately submersed in liquid upon formation, making an extra wetting step obsolete. The location of pore formation, however, is stochastic. Therefore, several techniques to control the location of pore formation have been developed such as optically controlled dielectric breakdown [105], laser-assisted dielectric breakdown [106], and laser drilling [107].

Few of the typically used methods for nanopore formation such as dielectric breakdown and electron beam drilling have been used for the fabrication of ZMWs. As we did not rely on single-digit-nanometer-sized pores for our projects, we investigated the

possibilities to use standard lithographic processes such as negative resist lift-off [47, 78, 108] (Figure 1.4 B) or reactive ion etching [104] (Figure 1.4 C). In addition, we investigated the feasibility of FIB milling (Figure 1.4 D). For the lithographic processes, the surface gets covered with a thin layer of resist which is typically achieved via spin-coating. The resist then gets exposed with a pattern, either using UV light or in our case an electron beam, since we aimed to fabricate features of tens of nanometers. If the resist is a negative-tone resist, the exposed resist areas polymerize and remain in the subsequent development step in which the unpolymerized resist gets removed. For positive-tone resists, the opposite holds and the exposed features get removed during development. To obtain metallic nanopores by negative resist lift-off, a metal layer is added on top of the surface and the remaining resist. We used physical vapor deposition for this process, where a target of metal in vacuum gets heated by an electron beam and thus starts to evaporate. The metal vapor travels through the vacuum and deposits onto the sample, thus forming a metallic thin film. Once the metal is added, the remaining resist pillar can be removed, taking away the metal layer on top of it and leaving a gap in the metal surface where the resist pillar was present before. To obtain a nanopore, it can either be drilled directly in the supporting membrane using for instance electron beam drilling or the supporting surface can be fully removed which is possible either by chemical wet etching or by reactive ion etching. In reactive ion etching, a plasma of reactive ions chemically etches the material.

For a process using a positive resist and reactive ion etching, a pore gets patterned in the resist, which subsequently shows up after development. Then the whole surface gets etched from the resist side using reactive ion etching. Since the resist covers most of the supporting structure, the underlying structure gets only etched in the openings of the resist [104]. After the resist is removed a metallic layer can be added onto the surface, not closing the pore if the layer is thin enough. Whereas the lithographic processes allow for upscaling the throughput due to the potential of parallel processing, we based our fabrication process on FIB milling. We chose this strategy because FIB milling allows rapid prototyping and structures of different milling depths can be produced in the same process. Here, a focused beam of highly accelerated ions hits the surface and thus removes material from the freestanding membrane. Since the amount of samples and feature sizes were small we could still use this serial process without being limited by time constraints in our studies.

1.2.2. OPTICAL MICROSCOPY

Before discussing different optical microscopy techniques, we would like to discuss an effect often employed for contrast enhancement in modern microscopy, namely fluorescence. In fluorescence, a molecule absorbs light at a certain wavelength and gets excited to a higher energy state. From this excited state, the molecule quickly relaxes to a lower vibrational level of this state upon which it falls back to its ground state within nanoseconds, emitting a photon of longer wavelength than what it was excited with [109]. By separating the excitation light from the emission light, this wavelength shift can be used to obtain a big contrast enhancement during imaging. Additionally, the molecules of interest can be specifically labeled and thus highlighted within a background of unlabeled molecules. Another feature of fluorescence that can be used to investigate the specific

environment of a fluorophore is the fluorescence lifetime which essentially reports on how long a fluorophore needs until it falls back to its ground state. The fluorescence lifetime can be measured by exciting the molecule with a very short light pulse and then recording the time the fluorophore takes to send out a photon. It can report on the local environment of the fluorophore for instance how close a fluorophore is to a surface or on the properties of the liquid the fluorophore is submersed in [110].

In the studies presented in this thesis, several optical microscopy techniques were used. All of these techniques have the purpose to make objects visible that would otherwise not be detectable due to their small size. A very basic form of microscope is a bright-field microscope, where the whole volume of the sample in the field of view is illuminated by a light source. The sample interacts with the light by for instance absorption, fluorescence, diffraction, or refraction. The light originating from the illuminated sample is then captured by an objective lens. The captured light beam can be directed towards the detector via different optics including lenses where it forms an enlarged image of the sample [110]. In contrast to bright-field microscopy, in confocal microscopy a light beam is focused into a spot within the specimen. This spot is scanned through the sample and the light, having interacted with the sample, is then captured by the objective lens. The detection light is filtered and directed through a pinhole that removes out of focus light resulting in good optical sectioning. After the pinhole, the light is typically captured by a spot detector that reports on the intensity of light originating from the focus spot. Due to the nature of optical diffraction this focal spot can not be made infinitely small [110].

The Abbe limit gives an indication of the maximally achievable resolution of a diffraction-limited system: $\Delta x = \frac{\lambda}{2n \sin(\alpha)}$, where Δx is the minimum resolvable distance of two point sources, λ the wavelength of light, $n \sin \alpha$ the numerical aperture of the objective with n the refractive index of the medium and α the maximum opening angle under which light can still be detected [110]. For a typical setup at 480 nm this results in a resolution limit of about 160 nm assuming a numerical aperture of 1.5.

A different application for confocal microscopy is fluorescence correlation spectroscopy (FCS) where the spot is kept stationary in a liquid that is containing diffusing fluorescent analytes. The individual analyte molecules start interacting with the focused light when they enter the laser focus and stop doing so when exiting. The emitted light is recorded over time leading to a fluorescence timetrace showing intensity variations of the detected light over time from molecules that entered and got excited in the laser focus. By calculating the autocorrelation function of the signal, thus by looking how similar the signal is to itself across a certain time shift, information about the diffusion of the analyte can be gathered [110]. For example, if a molecule diffuses quickly, it will exit the focus fast after it has entered it, leading to a short peak of the emission light, so that the signal is only at this high state for a brief period of time. This means that the signal is only similar to itself for a short time, so that the correlation drops already at lower correlation times.

Fluorescence time traces can also be analyzed for emission-light bursts that can report on the presence of a single molecule in the focus. For detecting this kind of bursts, there are different algorithms [111–114]. The most simple ones are based on intensity thresholding and simply detect when the signal is intense enough to cross a certain pre-

set intensity. More sophisticated, but also in many cases more powerful, are algorithms based on variations in photon statistics. The detection of photons typically follow Poisson statistics, whereas the individual states (such as the states fluorophore present or fluorophore absent) might differ in their average photon rate. For each detected time period between two photons, a statistical test can be performed if this interphoton time belongs to the background process or rather originates from a different process. Thus, the statistical likelihood for a fluorescent burst at a specific time point can be computed.

A different commonly used technique for optical sectioning, meaning the selective illumination of the sample, is total internal reflection fluorescence (TIRF) microscopy. Here a laser beam is directed under an incident angle towards a glass surface where it undergoes total internal reflection. The reflection leads to an evanescent wave in the medium on the other side of the reflective surface, featuring an exponential intensity profile and thus reaching only several tens to hundreds of nanometers into the medium [110]. Together with fluorescence this makes it possible to only observe molecules that are close to the surface.

1.2.3. ELECTRON MICROSCOPY AND CRYO ELECTRON MICROSCOPY

As optical microscopy is fundamentally limited in its resolution by the diffraction limit, it is generally not possible to resolve nanometer-sized structures as obtained from nanofabrication. As the resolution limit scales with wavelength, however, it is possible to push the resolution below nanometers by using waves of very short wavelength as obtained from highly accelerated electrons. The basic imaging principle is comparable to optical microscopy, where now magnetic lenses replace the optical lenses in the image forming system. In this thesis, we used two different imaging modalities, first transmission electron microscopy (TEM) where the electron beam is detected after having passed through and interacted with the sample and second scattering electron microscopy (SEM) where a focused electron beam is scanned across the sample and the amount of electrons scattered is recorded. While in SEM mainly the backscattered electrons are detected, in TEM the image is formed from the transmitted electrons. Electrons can either interact inelastically, meaning that they lose energy during the scattering process, or elastically which mostly happens via deflection by electrostatic interaction with the atomic nuclei in the sample [115]. Therefore, atoms having a high atomic number such as gold can lead to very high contrast, allowing the use of nanometer-sized gold labels to highlight specific structures in electron microscopy. Since electrons would also be scattered or absorbed by remaining gas, the whole imaging system needs to be kept in high vacuum which poses a major issue for imaging biological samples that typically need to be in a liquid environment. Therefore, cryogenic electron microscopy has been developed. Here, a water-based sample is frozen very quickly to the temperature of liquid nitrogen by plunging it into a bath of liquid ethane, that the water freezes to so-called vitreous ice [116], an amorphous form of ice in which the water molecules do not exhibit any long range order. This is important because ice in a crystalline order structure would disturb the imaging process. By keeping the sample at this low temperature even during imaging, both sample evaporation in the vacuum is prevented and imaging damage is reduced.

1.2.4. SIMULATIONS

In order to gain a deeper understanding of the nanostructures' optical properties, we performed simulations to get insight into the light fields that develop within the zero-mode waveguides upon illumination. We therefore performed finite-difference time-domain (FDTD) simulations in which an electro-magnetic field is propagated in time by numerically solving Maxwell's equations in a discrete manner [117]. Maxwell's equations, as the basic equations governing the process of light propagation, are a set of partial differential equations in space and time. When discretizing, the partial derivatives present in Maxwell's equations are replaced by the differences of the fields either in space or in time. This process requires both a spatial and a temporal resolution fine enough to produce physically relevant results [117]. Additionally, it should be avoided that transient effects from starting the simulation influence the final result, which sets a lower limit on the duration of the simulation.

Another type of simulations that was used in this thesis are molecular dynamics simulations. In this type of simulations, a system of individual particles is evolved over time by solving Newton's equations of motion numerically via small time steps. The forces acting between the individual particles can be of different sort and are often calculated by using potentials or simplified by using specific force-fields [118]. Since all-atom molecular dynamics simulations often contain a number of atoms that exceeds the computing capabilities, different simplifications can be applied. One such simplification is to only implicitly model the interactions of the particles with the solvent and not simulate all solvent molecules. Another reduction of the complexity can be achieved by coarse graining where multiple particles are combined to a single effective particle. For instance, it is possible to model amino acids by combining all the atoms of a certain amino acid into a single effective amino acid particle. Since now the coarse-grained particles do not have a real physical pendant one can not use fundamental physical forces to propagate the equations of motion. Therefore, the interactions between the coarse-grained particles need to be heuristically determined to mimic the interactions that the actual atoms would have with each other [118].

1.3. IN THIS THESIS

Initially, we set out to develop a system with which translocations of single molecules traveling through 50 nm nanopores can be recorded in low salinity buffers containing less than 150 mM of salt. Additionally, we wanted to be able to clearly distinguish different analytes translocating by free diffusion avoiding perturbation by external electric fields. Therefore, we decided to use freestanding zero-mode waveguides as a platform and in [chapter 2](#) we introduce palladium (Pd) as a novel material for the fabrication of ZMWs. Typically, either aluminum or gold were used as ZMW materials, where aluminum suffers from low chemical stability [48] and gold from high photoluminescence, i.e. emission of green light when illuminated by blue light [119, 120]. We show that palladium offers advantages in chemical stability, optical background, and fabrication compared to four other metals, namely gold, aluminum, titanium, and platinum. We subsequently showcase its applicability by optically observing single-molecule transport through freestanding Pd nanopores of freely diffusing fluorophores, fluorescently labeled proteins, and double-stranded DNA at different length and under different driv-

ing forces. We conclude this chapter by giving an outlook on the concrete applicability of this system.

In the next two chapters, we use this possibility to study single-molecule transport of analytes through palladium nanopores unperturbed by an external electric field. First, we present our study on DNA translocations driven by asymmetric salt concentrations in **chapter 3**. ZMWs are specifically suitable for this task since the optical detection fully allows to avoid the use of electrodes in the system which could lead to complications in the interpretation of the data. Diffusiophoretic transport resulting from salt gradients is an effect that has not been considered in the case of nanopore transport in asymmetric salt conditions for years [121]. Therefore, we set out to highlight its importance in nanopore transport by showing that a negatively charged particle can be purely driven through a nanopore by a salt gradient. We present a measurement scheme to observe DNA translocations due to diffusiophoresis originating from varying gradients of different salts in order to compare the influence of these parameters on the translocation process. We identify three theoretically predicted trends, namely that, in the regimes we tested, DNA gets driven towards the reservoir containing the high salt concentration, that a higher gradient leads to more translocations, and that KCl leads to fewer translocations than NaCl. Due to high experiment-to-experiment variability, a thorough quantification of these trends still remains to be performed.

In the next chapter, **chapter 4**, we use the possibility to follow freely diffusing proteins through Pd ZMWs to examine the transport selectivity in NPC mimics. More specifically, we were interested what influence the pore size would have on the transport selectivity of Nsp1 pores since it was recently discovered that the actual size of the NPC exhibits a non-negligible size variability [122, 123]. The NPC mimics were made by attaching the nucleoporin Nsp1 with its C-terminus to the surface of Pd ZMWs thus filling the pores with a mesh of the Nup Nsp1. To study transport selectivity, we compared the translocation rate of the nucleocytoplasmic transporter Kap95 with an inert control protein, namely bovine serum albumin (BSA). Whereas both followed the expected trend of translocation rates for open pores that served as a control, we found that BSA did barely translocate through the Nup mesh of small Nsp1-coated pores. Kap95, however, translocated at almost the same rate, which showed that small Nsp1 pores based on Pd ZMWs indeed act as NPC mimics, exhibiting transport selectivity. With increasing pore diameter, this selectivity was gradually lost, an observation that could be perfectly explained by coarse-grained molecular-dynamics simulations. These showed that with increasing pore diameter transient openings in the Nup mesh became more abundant until the mesh fully opened up to form a central channel. BSA leakage would occur through these openings and therefore approach the open pore value for very big pores. In a second step, we present the influence of the transporter Kap95 on the Nsp1 mesh indirectly via the BSA leakage through the pores. Specifically, the Kap-centric models, treating Kap95 as an essential part of the NPC, predict that the presence of Kap95 in the Nup mesh should influence the properties, such as the selectivity, of the Nup mesh. Until now, it was not possible to put this prediction to test in single-molecule experiments. Whereas 1 μM of Kap95 did not modulate the BSA leakage in small Nsp1 pores, we found that the BSA translocation rate even increased for large Nsp1 pores, which suggested a collapse of the Nsp1 brush.

After indirectly studying the Nup mesh via the BSA translocations, we propose a new technique to directly study the structure of the intrinsically disordered Nup mesh in NPC mimics made from solid-state nanopores grafted with nucleoporins. The technique is based on cryo-EM which allows to study proteins in their instantaneous conformation. In cryo-EM, both unstructured proteins and small proteins, however, give too little contrast to be directly visible. Therefore, we attached gold particles, providing enough contrast during imaging, at specific locations of both Nsp1 and Kap95 to record their positions in NPC mimics. By imaging thousands of similar pores and recording the locations of the contained gold particles, it is thus possible to make statements about the distributions of both the Nups and Kap95 within NPC mimics. In [chapter 5](#), we show the potential of this technique for both the distribution of Nsp1 and Kap95 selectivity. We found that Nsp1-coated pores above 60 nm exhibited a ring-like structure of the Nup termini. Additionally, we found good indication for selectivity of these NPC mimics for Kap95 versus BSA, even though a thorough quantification of this still needs to be performed. Thus, we are confident that by using cryo-EM imaging together with gold labelling, we can study the structure of solid-state nanopore based NPC mimics.

In [chapter 6](#) we move away from pure in vitro systems to an application of Pd ZMWs for imaging fluorescently labelled proteins bound to the inner membrane of living cells. When the same type of fluorophores are both present on the cell membrane and in high concentration within the cytoplasm, it poses a big challenge to follow single membrane-bound fluorophores with standard microscopy techniques, such as TIRF. For this case, we developed overmilled Pd ZMWs on a glass coverslip and cultivated living cells on them. We could show that for optimized ZMW parameters, the cells would penetrate into the nanowells and thus the signal emerging from the cytoplasmic fluorophores could be suppressed while the signal from the membrane-bound ones did not decrease significantly in intensity. In addition, we thoroughly characterized the ZMWs by their photophysical properties such as fluorescence signal enhancement and a decrease in fluorescence lifetime. By performing field simulations of the system, we could fully explain these experimentally observed features. Furthermore, we optimized the amount of populated pores by finetuning the milling depth and ZMW diameter. All in all, we introduced over-milled ZMWs together with non-perpendicular illumination as a new tool to study single membrane-bound fluorescent markers in live cells despite a high cytosolic background fluorescence.

In [chapter 7](#) we provide an outlook on interesting directions that could be followed building on the work presented in this thesis. We discuss both new applications for the methods we developed in this thesis and questions leading towards improving these methods. Additionally, we present interesting open questions to study NPC transport.

REFERENCES

- [1] S. Iqbal and R. Bashir, *Nanopores : sensing and fundamental biological interactions*, (Springer, 2011) doi:[10.1007/978-1-4419-8252-0](https://doi.org/10.1007/978-1-4419-8252-0).
- [2] C. Dekker, *Solid-state nanopores*, [Nature nanotechnology](#) **2**, 209 (2007), doi:[10.1142/9789814287005_0007](https://doi.org/10.1142/9789814287005_0007).
- [3] D. Branton, D. W. Deamer, A. Marziali, H. Bayley, S. A. Benner, T. But-

- ler, M. Di Ventra, S. Garaj, A. Hibbs, X. Huang, *et al.*, *The potential and challenges of nanopore sequencing*, *Nature biotechnology* **26**, 1146 (2008), doi:[10.1142/9789814287005_0027](https://doi.org/10.1142/9789814287005_0027).
- [4] M. Wanunu, *Nanopores: A journey towards dna sequencing*, *Physics of Life Reviews* **9**, 125 (2012), doi:[10.1016/j.plrev.2012.05.010](https://doi.org/10.1016/j.plrev.2012.05.010).
- [5] E. A. Manrao, I. M. Derrington, A. H. Laszlo, K. W. Langford, M. K. Hopper, N. Gillgren, M. Pavlenok, M. Niederweis, and J. H. Gundlach, *Reading DNA at single-nucleotide resolution with a mutant MspA nanopore and phi29 DNA polymerase*, *Nature Biotechnology* **30**, 349 (2012), doi:[10.1038/nbt.2171](https://doi.org/10.1038/nbt.2171).
- [6] D. Deamer, M. Akeson, and D. Branton, *Three decades of nanopore sequencing*, *Nature Biotechnology* **34**, 518 (2016), doi:[10.1038/nbt.3423](https://doi.org/10.1038/nbt.3423).
- [7] T. Jovanovic-Taliman, J. Tetenbaum-Novatt, A. S. McKenney, A. Zilman, R. Peters, M. P. Rout, and B. T. Chait, *Artificial nanopores that mimic the transport selectivity of the nuclear pore complex*, *Nature* **457**, 1023 (2009), doi:[10.1038/nature07600](https://doi.org/10.1038/nature07600).
- [8] S. W. Kowalczyk, L. Kapinos, T. R. Blosser, T. Magalhães, P. van Nies, R. Y. H. Lim, and C. Dekker, *Single-molecule transport across an individual biomimetic nuclear pore complex*, *Nature Nanotechnology* **6**, 433 (2011).
- [9] A. N. Ananth, A. Mishra, S. Frey, A. Dwarkasing, R. Versloot, E. van der Giessen, D. Görlich, P. Onck, and C. Dekker, *Spatial structure of disordered proteins dictates conductance and selectivity in nuclear pore complex mimics*, *eLife* **7**, e31510 (2018), doi:[10.7554/eLife.31510](https://doi.org/10.7554/eLife.31510).
- [10] A. Fragasso, H. W. de Vries, J. Andersson, E. O. van der Sluis, E. van der Giessen, A. Dahlin, P. R. Onck, and C. Dekker, *A designer fg-nup that reconstitutes the selective transport barrier of the nuclear pore complex*, *Nature Communications* **12**, 2010 (2021), doi:[10.1038/s41467-021-22293-y](https://doi.org/10.1038/s41467-021-22293-y).
- [11] N. Klughammer, A. Barth, M. Dekker, A. Fragasso, P. Onck, and C. Dekker, *Diameter dependence of transport through nuclear pore complex mimics studied using optical nanopores*, *eLife* **12** (2023), [10.7554/eLife.87174](https://doi.org/10.7554/eLife.87174), doi:[10.7554/eLife.87174](https://doi.org/10.7554/eLife.87174).
- [12] T. Auger, J. Mathé, V. Viasnoff, G. Charron, J.-M. Di Meglio, L. Auvray, and F. Montel, *Zero-mode waveguide detection of flow-driven dna translocation through nanopores*, *Phys. Rev. Lett.* **113**, 028302 (2014), doi:[10.1103/PhysRevLett.113.028302](https://doi.org/10.1103/PhysRevLett.113.028302).
- [13] K. Chen, I. Jou, N. Ermann, M. Muthukumar, U. F. Keyser, and N. A. W. Bell, *Dynamics of driven polymer transport through a nanopore*, *Nature Physics* **17**, 1043 (2021), doi:[10.1038/s41567-021-01268-2](https://doi.org/10.1038/s41567-021-01268-2).
- [14] A. Keerthi, A. Geim, A. Janardanan, A. Rooney, A. Esfandiar, S. Hu, S. Dar, I. Grigorieva, S. Haigh, F. Wang, *et al.*, *Ballistic molecular transport through two-dimensional channels*, *Nature* (2018), [10.1038/s41586-018-0203-2](https://doi.org/10.1038/s41586-018-0203-2), doi:[10.1038/s41586-018-0203-2](https://doi.org/10.1038/s41586-018-0203-2).

- [15] Y.-L. Ying, Z.-L. Hu, S. Zhang, Y. Qing, A. Fragasso, G. Maglia, A. Meller, H. Bayley, C. Dekker, and Y.-T. Long, *Nanopore-based technologies beyond DNA sequencing*, *Nature Nanotechnology* **17**, 1136 (2022), doi:[10.1038/s41565-022-01193-2](https://doi.org/10.1038/s41565-022-01193-2).
- [16] L. Restrepo-Pérez, C. Joo, and C. Dekker, *Paving the way to single-molecule protein sequencing*, *Nature Nanotechnology* **13**, 786 (2018), doi:[10.1038/s41565-018-0236-6](https://doi.org/10.1038/s41565-018-0236-6).
- [17] J. A. Alfaro, P. Bohländer, M. Dai, M. Filius, C. J. Howard, X. F. van Kooten, S. Ohayon, A. Pomorski, S. Schmid, A. Aksimentiev, E. V. Anslyn, G. Bedran, C. Cao, M. Chinappi, E. Coyaud, C. Dekker, G. Dittmar, N. Drachman, R. Eelkema, D. Goodlett, S. Hentz, U. Kalathiya, N. L. Kelleher, R. T. Kelly, Z. Kelman, S. H. Kim, B. Kuster, D. Rodriguez-Larrea, S. Lindsay, G. Maglia, E. M. Marcotte, J. P. Marino, C. Masselon, M. Mayer, P. Samaras, K. Sarthak, L. Sepiashvili, D. Stein, M. Wanunu, M. Wilhelm, P. Yin, A. Meller, and C. Joo, *The emerging landscape of single-molecule protein sequencing technologies*, *Nature Methods* **18**, 604 (2021), doi:[10.1038/s41592-021-01143-1](https://doi.org/10.1038/s41592-021-01143-1).
- [18] H. Brinkerhoff, A. S. W. Kang, J. Liu, A. Aksimentiev, and C. Dekker, *Multiple rereads of single proteins at single amino acid resolution using nanopores*, *Science* **374**, 1509 (2021), doi:[10.1126/science.abl4381](https://doi.org/10.1126/science.abl4381).
- [19] B. D. Reed, M. J. Meyer, V. Abramzon, O. Ad, P. Adcock, F. R. Ahmad, G. Alpay, J. A. Ball, J. Beach, D. Belhachemi, A. Bellofiore, M. Bellos, J. F. Beltrán, A. Betts, M. W. Bhuiya, K. Blacklock, R. Boer, D. Boisvert, N. D. Brault, A. Buxbaum, S. Caprio, C. Choi, T. D. Christian, R. Clancy, J. Clark, T. Connolly, K. F. Croce, R. Cullen, M. Davey, J. Davidson, M. M. Elshenawy, M. Ferrigno, D. Frier, S. Gudipati, S. Hamill, Z. He, S. Hosali, H. Huang, L. Huang, A. Kabiri, G. Kriger, B. Lathrop, A. Li, P. Lim, S. Liu, F. Luo, C. Lv, X. Ma, E. McCormack, M. Millham, R. Nani, M. Pandey, J. Parillo, G. Patel, D. H. Pike, K. Preston, A. Pichard-Kostuch, K. Rearick, T. Rearick, M. Ribezzi-Crivellari, G. Schmid, J. Schultz, X. Shi, B. Singh, N. Srivastava, S. F. Stewman, T. Thurston, T. R. Thurston, P. Trioli, J. Tullman, X. Wang, Y.-C. Wang, E. A. G. Webster, Z. Zhang, J. Zuniga, S. S. Patel, A. D. Griffiths, A. M. van Oijen, M. McKenna, M. D. Dyer, and J. M. Rothberg, *Real-time dynamic single-molecule protein sequencing on an integrated semiconductor device*, *Science* **378**, 186 (2022), doi:[10.1126/science.abo7651](https://doi.org/10.1126/science.abo7651).
- [20] V. Schünemann, *Biophysik: Eine Einführung*, SpringerLink : Bücher (Springer Berlin Heidelberg, 2005) doi:[10.1007/b137686](https://doi.org/10.1007/b137686).
- [21] X. Shi, D. Verschueren, S. Pud, and C. Dekker, *Integrating sub-3 nm plasmonic gaps into solid-state nanopores*, *Small* **14**, 1703307 (2017), doi:[10.1002/smll.201703307](https://doi.org/10.1002/smll.201703307).
- [22] X. Shi, D. V. Verschueren, and C. Dekker, *Active delivery of single dna molecules into a plasmonic nanopore for label-free optical sensing*, *Nano Letters* **18**, 8003 (2018), doi:[10.1021/acs.nanolett.8b04146](https://doi.org/10.1021/acs.nanolett.8b04146).

- [23] D. V. Verschuieren, S. Pud, X. Shi, L. De Angelis, L. Kuipers, and C. Dekker, *Label-free optical detection of dna translocations through plasmonic nanopores*, *ACS Nano* **13**, 61 (2019), doi:10.1021/acsnano.8b06758.
- [24] N. Drachman, M. LePoitevin, H. Szapary, B. Wiener, W. Maulbetsch, and D. Stein, *Nanopore ion sources deliver single amino acid and peptide ions directly into high vacuum*, *bioRxiv* (2022), 10.1101/2021.08.15.456243, doi:10.1101/2021.08.15.456243.
- [25] J. Zhou, Q. Lan, W. Li, L.-N. Ji, K. Wang, and X.-H. Xia, *Single Molecule Protein Segments Sequencing by a Plasmonic Nanopore*, *Nano Letters* (2023), 10.1021/acs.nanolett.3c00086, doi:10.1021/acs.nanolett.3c00086.
- [26] G. M. Lu and X. S. Zhao, *Nanoporous materials: science and engineering*, Vol. 4 (World Scientific, 2004).
- [27] C. C. Striemer, T. R. Gaborski, J. L. McGrath, and P. M. Fauchet, *Charge- and size-based separation of macromolecules using ultrathin silicon membranes*, *Nature* **445**, 749 (2007), doi:10.1038/nature05532.
- [28] M. Zhang, C. Chen, Y. Zhang, and J. Geng, *Biological nanopores for sensing applications*, *Proteins: Structure, Function, and Bioinformatics* **90**, 1786 (2022), doi:10.1002/prot.26308.
- [29] R. M. M. Smeets, U. F. Keyser, D. Krapf, M.-Y. Wu, N. H. Dekker, and C. Dekker, *Salt Dependence of Ion Transport and DNA Translocation through Solid-State Nanopores*, *Nano Letters* **6**, 89 (2006), doi:10.1021/nl052107w.
- [30] J. J. Kasianowicz, E. Brandin, D. Branton, and D. W. Deamer, *Characterization of individual polynucleotide molecules using a membrane channel*, *Proceedings of the National Academy of Sciences* **93**, 13770 (1996), doi:10.1073/pnas.93.24.13770.
- [31] D. Rodriguez-Larrea and H. Bayley, *Multistep protein unfolding during nanopore translocation*, *Nature Nanotechnology* **8**, 288 (2013), doi:10.1038/nnano.2013.22.
- [32] G. Huang, K. Willems, M. Soskine, C. Wloka, and G. Maglia, *Electro-osmotic capture and ionic discrimination of peptide and protein biomarkers with frac nanopores*, *Nature Communications* **8**, 935 (2017), doi:10.1038/s41467-017-01006-4.
- [33] L. Restrepo-Pérez, G. Huang, P. R. Bohländer, N. Worp, R. Eelkema, G. Maglia, C. Joo, and C. Dekker, *Resolving chemical modifications to a single amino acid within a peptide using a biological nanopore*, *ACS Nano* **13**, 13668 (2019), doi:10.1021/acsnano.9b05156.
- [34] T. Z. Butler, M. Pavlenok, I. M. Derrington, M. Niederweis, and J. H. Gundlach, *Single-molecule DNA detection with an engineered MspA protein nanopore*, *Proceedings of the National Academy of Sciences* **105**, 20647 (2008), doi:10.1073/pnas.0807514106.

- [35] Y. Qing, M. D. Liu, D. Hartmann, L. Zhou, W. J. Ramsay, and H. Bayley, *Single-Molecule Observation of Intermediates in Bioorthogonal 2-Cyanobenzothiazole Chemistry*, *Angewandte Chemie International Edition* **59**, 15711 (2020), doi:[10.1002/anie.202005729](https://doi.org/10.1002/anie.202005729).
- [36] Q. Shen, Q. Xiong, K. Zhou, Q. Feng, L. Liu, T. Tian, C. Wu, Y. Xiong, T. J. Melia, C. P. Lusk, and C. Lin, *Functionalized dna-origami-protein nanopores generate large transmembrane channels with programmable size-selectivity*, *Journal of the American Chemical Society* **145**, 1292 (2023), doi:[10.1021/jacs.2c11226](https://doi.org/10.1021/jacs.2c11226).
- [37] S. Zhang, G. Huang, R. C. A. Versloot, B. M. H. Bruininks, P. C. T. de Souza, S.-J. Marrink, and G. Maglia, *Bottom-up fabrication of a proteasome–nanopore that unravels and processes single proteins*, *Nature Chemistry* (2021), [10.1038/s41557-021-00824-w](https://doi.org/10.1038/s41557-021-00824-w), doi:[10.1038/s41557-021-00824-w](https://doi.org/10.1038/s41557-021-00824-w).
- [38] A. J. Scott, A. Niitsu, H. T. Kratochvil, E. J. M. Lang, J. T. Sengel, W. M. Dawson, K. R. Mahendran, M. Mravic, A. R. Thomson, R. L. Brady, L. Liu, A. J. Mulholland, H. Bayley, W. F. DeGrado, M. I. Wallace, and D. N. Woolfson, *Constructing ion channels from water-soluble α -helical barrels*, *Nature Chemistry* **13**, 643 (2021), doi:[10.1038/s41557-021-00688-0](https://doi.org/10.1038/s41557-021-00688-0).
- [39] M. Langecker, V. Arnaut, T. G. Martin, J. List, S. Renner, M. Mayer, H. Dietz, and F. C. Simmel, *Synthetic Lipid Membrane Channels Formed by Designed DNA Nanostructures*, *Science* **338**, 932 (2012), doi:[10.1126/science.1225624](https://doi.org/10.1126/science.1225624).
- [40] N. A. W. Bell, C. R. Engst, M. Ablay, G. Divitini, C. Ducati, T. Liedl, and U. F. Keyser, *DNA Origami Nanopores*, *Nano Letters* **12**, 512 (2012), doi:[10.1021/nl204098n](https://doi.org/10.1021/nl204098n).
- [41] P. W. K. Rothemund, *Folding DNA to create nanoscale shapes and patterns*, *Nature* **440**, 297 (2006), doi:[10.1038/nature04586](https://doi.org/10.1038/nature04586).
- [42] J. Li, D. Stein, C. McMullan, D. Branton, M. J. Aziz, and J. A. Golovchenko, *Ion-beam sculpting at nanometre length scales*, *Nature* **412**, 166 (2001), doi:[10.1038/35084037](https://doi.org/10.1038/35084037).
- [43] A. J. Storm, J. H. Chen, H. W. Zandbergen, and C. Dekker, *Translocation of double-strand dna through a silicon oxide nanopore*, *Phys. Rev. E* **71**, 051903 (2005), doi:[10.1103/PhysRevE.71.051903](https://doi.org/10.1103/PhysRevE.71.051903).
- [44] S. Garaj, W. Hubbard, A. Reina, J. Kong, D. Branton, and J. A. Golovchenko, *Graphene as a subnanometre trans-electrode membrane*, *Nature* **467**, 190 (2010), doi:[10.1038/nature09379](https://doi.org/10.1038/nature09379).
- [45] G. F. Schneider, S. W. Kowalczyk, V. E. Calado, G. Pandraud, H. W. Zandbergen, L. M. K. Vandersypen, and C. Dekker, *DNA Translocation through Graphene Nanopores*, *Nano Letters* **10**, 3163 (2010), doi:[10.1021/nl102069z](https://doi.org/10.1021/nl102069z).
- [46] C. A. Merchant, K. Healy, M. Wanunu, V. Ray, N. Peterman, J. Bartel, M. D. Fischbein, K. Venta, Z. Luo, A. T. C. Johnson, and M. Drndić, *DNA*

- Translocation through Graphene Nanopores*, *Nano Letters* **10**, 2915 (2010), doi:[10.1021/nl101046t](https://doi.org/10.1021/nl101046t).
- [47] O. N. Assad, T. Gilboa, J. Spitzberg, M. Juhasz, E. Weinhold, and A. Meller, *Light-enhancing plasmonic-nanopore biosensor for superior single-molecule detection*, *Advanced Materials* **29**, 1605442 (2016), doi:[10.1002/adma.201605442](https://doi.org/10.1002/adma.201605442).
- [48] N. Klughammer and C. Dekker, *Palladium zero-mode waveguides for optical single-molecule detection with nanopores*, *Nanotechnology* **32**, 18LT01 (2021), doi:[10.1088/1361-6528/abd976](https://doi.org/10.1088/1361-6528/abd976).
- [49] M. Firnkes, D. Pedone, J. Knezevic, M. Döblinger, and U. Rant, *Electrically facilitated translocations of proteins through silicon nitride nanopores: Conjoint and competitive action of diffusion, electrophoresis, and electroosmosis*, *Nano Letters* **10**, 2162 (2010), doi:[10.1021/nl100861c](https://doi.org/10.1021/nl100861c).
- [50] A. Zrehen, D. Huttner, and A. Meller, *On-chip stretching, sorting, and electro-optical nanopore sensing of ultralong human genomic dna*, *ACS Nano* **13**, 14388 (2019), doi:[10.1021/acsnano.9b07873](https://doi.org/10.1021/acsnano.9b07873).
- [51] D. V. Melnikov, Z. K. Hulings, and M. E. Gracheva, *Electro-osmotic flow through nanopores in thin and ultrathin membranes*, *Phys. Rev. E* **95**, 063105 (2017), doi:[10.1103/PhysRevE.95.063105](https://doi.org/10.1103/PhysRevE.95.063105).
- [52] U. F. Keyser, B. N. Koeleman, S. van Dorp, D. Krapf, R. M. M. Smeets, S. G. Lemay, N. H. Dekker, and C. Dekker, *Direct force measurements on DNA in a solid-state nanopore*, *Nature Physics* **2**, 473 (2006), doi:[10.1038/nphys344](https://doi.org/10.1038/nphys344).
- [53] J. Nivala, D. B. Marks, and M. Akeson, *Unfoldase-mediated protein translocation through an α -hemolysin nanopore*, *Nature Biotechnology* **31**, 247 EP (2013), doi:[10.1038/nbt.2503](https://doi.org/10.1038/nbt.2503).
- [54] J. Nivala, L. Mulrone, G. Li, J. Schreiber, and M. Akeson, *Discrimination among protein variants using an unfoldase-coupled nanopore*, *ACS Nano* **8**, 12365 (2014), doi:[10.1021/nm5049987](https://doi.org/10.1021/nm5049987).
- [55] A. McMullen, G. Araujo, M. Winter, and D. Stein, *Osmotically driven and detected dna translocations*, *Scientific Reports* **9**, 15065 (2019), doi:[10.1038/s41598-019-51049-4](https://doi.org/10.1038/s41598-019-51049-4).
- [56] M. Charron, L. Philipp, L. He, and V. Tabard-Cossa, *Elucidating the dynamics of polymer transport through nanopores using asymmetric salt concentrations*, *Nano Research* **15**, 9943 (2022), doi:[10.1007/s12274-022-4886-3](https://doi.org/10.1007/s12274-022-4886-3).
- [57] D. Fologea, J. Uplinger, B. Thomas, D. S. McNabb, and J. Li, *Slowing DNA Translocation in a Solid-State Nanopore*, *Nano Letters* **5**, 1734 (2005), doi:[10.1021/nl051063o](https://doi.org/10.1021/nl051063o).

- [58] S. W. Kowalczyk, D. B. Wells, A. Aksimentiev, and C. Dekker, *Slowing down DNA Translocation through a Nanopore in Lithium Chloride*, *Nano Letters* **12**, 1038 (2012), doi:[10.1021/nl204273h](https://doi.org/10.1021/nl204273h).
- [59] G. M. Cherf, K. R. Lieberman, H. Rashid, C. E. Lam, K. Karplus, and M. Akeson, *Automated forward and reverse ratcheting of DNA in a nanopore at 5-Å precision*, *Nature Biotechnology* **30**, 344 (2012), doi:[10.1038/nbt.2147](https://doi.org/10.1038/nbt.2147).
- [60] M. Jain, H. E. Olsen, B. Paten, and M. Akeson, *The Oxford Nanopore MinION: delivery of nanopore sequencing to the genomics community*, *Genome Biology* **17**, 239 (2016), doi:[10.1186/s13059-016-1103-0](https://doi.org/10.1186/s13059-016-1103-0).
- [61] J. Larkin, R. Henley, D. C. Bell, T. Cohen-Karni, J. K. Rosenstein, and M. Wanunu, *Slow dna transport through nanopores in hafnium oxide membranes*, *ACS Nano* **7**, 10121 (2013), doi:[10.1021/nm404326f](https://doi.org/10.1021/nm404326f).
- [62] E. C. Yusko, J. M. Johnson, S. Majd, P. Prangkio, R. C. Rollings, J. Li, J. Yang, and M. Mayer, *Controlling protein translocation through nanopores with bio-inspired fluid walls*, *Nature Nanotechnology* **6**, 253 (2011), doi:[10.1038/nnano.2011.12](https://doi.org/10.1038/nnano.2011.12).
- [63] M. J. Levene, J. Korlach, S. W. Turner, M. Foquet, H. G. Craighead, and W. W. Webb, *Zero-mode waveguides for single-molecule analysis at high concentrations*, *science* **299**, 682 (2003), doi:[10.1126/science.1079700](https://doi.org/10.1126/science.1079700).
- [64] K. T. Samiee, M. Foquet, L. Guo, E. C. Cox, and H. G. Craighead, *λ -repressor oligomerization kinetics at high concentrations using fluorescence correlation spectroscopy in zero-mode waveguides*, *Biophysical Journal* **88**, 2145 (2005), doi:[10.1529/biophysj.104.052795](https://doi.org/10.1529/biophysj.104.052795).
- [65] H. Rigneault, J. Capoulade, J. Dintinger, J. Wenger, N. Bonod, E. Popov, T. W. Ebbesen, and P-F. Lenne, *Enhancement of single-molecule fluorescence detection in subwavelength apertures*, *Phys. Rev. Lett.* **95**, 117401 (2005), doi:[10.1103/PhysRevLett.95.117401](https://doi.org/10.1103/PhysRevLett.95.117401).
- [66] D. Gérard, J. Wenger, N. Bonod, E. Popov, H. Rigneault, F. Mahdavi, S. Blair, J. Dintinger, and T. W. Ebbesen, *Nanoaperture-enhanced fluorescence: Towards higher detection rates with plasmonic metals*, *Physical Review B* **77**, 045413 (2008), doi:[10.1103/PhysRevB.77.045413](https://doi.org/10.1103/PhysRevB.77.045413).
- [67] P-F. Lenne, H. Rigneault, D. Marguet, and J. Wenger, *Fluorescence fluctuations analysis in nanoapertures: physical concepts and biological applications*, *Histochemistry and Cell Biology* **130**, 795 (2008), doi:[10.1007/s00418-008-0507-7](https://doi.org/10.1007/s00418-008-0507-7).
- [68] H. Aouani, J. Wenger, D. Gérard, H. Rigneault, E. Devaux, T. W. Ebbesen, F. Mahdavi, T. Xu, and S. Blair, *Crucial role of the adhesion layer on the plasmonic fluorescence enhancement*, *ACS Nano* **3**, 2043 (2009), doi:[10.1021/nn900460t](https://doi.org/10.1021/nn900460t).
- [69] M. Wu, W. Liu, J. Hu, Z. Zhong, T. Rujiralai, L. Zhou, X. Cai, and J. Ma, *Fluorescence enhancement in an over-etched gold zero-mode waveguide*. *Optics express* **27** **13**, 19002 (2019), doi:<https://doi.org/10.1364/OE.27.019002>.

- [70] A. Al Masud, W. E. Martin, F. H. Moonschi, S. M. Park, B. R. Srijanto, K. R. Graham, C. P. Collier, and C. I. Richards, *Mixed metal zero-mode guides (zmgws) for tunable fluorescence enhancement*, *Nanoscale Adv.* **2**, 1894 (2020), doi:[10.1039/C9NA00641A](https://doi.org/10.1039/C9NA00641A).
- [71] K. Samiee, J. Moran-Mirabal, Y. Cheung, and H. Craighead, *Zero Mode Waveguides for Single-Molecule Spectroscopy on Lipid Membranes*, *Biophysical Journal* **90**, 3288 (2006), doi:[10.1529/biophysj.105.072819](https://doi.org/10.1529/biophysj.105.072819).
- [72] T. Miyake, T. Tanii, H. Sonobe, R. Akahori, N. Shimamoto, T. Ueno, T. Funatsu, and I. Ohdomari, *Real-time imaging of single-molecule fluorescence with a zero-mode waveguide for the analysis of protein-protein interaction*, *Analytical Chemistry* **80**, 6018 (2008), doi:[10.1021/ac800726g](https://doi.org/10.1021/ac800726g).
- [73] J. M. Moran-Mirabal and H. G. Craighead, *Zero-mode waveguides: Sub-wavelength nanostructures for single molecule studies at high concentrations*, *Methods* **46**, 11 (2008), doi:<https://doi.org/10.1016/j.ymeth.2008.05.010>.
- [74] P. Zhu and H. G. Craighead, *Zero-mode waveguides for single-molecule analysis*, *Annual Review of Biophysics* **41**, 269 (2012), doi:[10.1146/annurev-biophys-050511-102338](https://doi.org/10.1146/annurev-biophys-050511-102338).
- [75] C. I. Richards, K. Luong, R. Srinivasan, S. W. Turner, D. A. Dougherty, J. Korlach, and H. A. Lester, *Live-cell imaging of single receptor composition using zero-mode waveguide nanostructures*, *Nano Letters* **12**, 3690 (2012), doi:[10.1021/nl301480h](https://doi.org/10.1021/nl301480h).
- [76] A. Rhoads and K. F. Au, *PacBio Sequencing and Its Applications*, *Genomics, Proteomics & Bioinformatics SI: Metagenomics of Marine Environments*, **13**, 278 (2015), doi:[10.1016/j.gpb.2015.08.002](https://doi.org/10.1016/j.gpb.2015.08.002).
- [77] W. E. Martin, B. R. Srijanto, C. P. Collier, T. Vosch, and C. I. Richards, *A comparison of single-molecule emission in aluminum and gold zero-mode waveguides*, *The Journal of Physical Chemistry A* **120**, 6719 (2016), doi:[10.1021/acs.jpca.6b03309](https://doi.org/10.1021/acs.jpca.6b03309).
- [78] J. Larkin, R. Y. Henley, V. Jadhav, J. Korlach, and M. Wanunu, *Length-independent dna packing into nanopore zero-mode waveguides for low-input dna sequencing*, *Nature nanotechnology* **12**, 1169 (2017), doi:[10.1038/nnano.2017.176](https://doi.org/10.1038/nnano.2017.176).
- [79] M. Baibakov, S. Patra, J.-B. Claude, A. Moreau, J. Lumeau, and J. Wenger, *Extending single molecule förster resonance energy transfer (fret) range beyond 10 nanometers in zero-mode waveguides*, *ACS Nano* **13**, 8469–8480 (2019), doi:[10.1021/acsnano.9b04378](https://doi.org/10.1021/acsnano.9b04378).
- [80] S. Patra, M. Baibakov, J.-B. Claude, and J. Wenger, *Surface passivation of zero-mode waveguide nanostructures: benchmarking protocols and fluorescent labels*, *Scientific Reports* **10**, 5235 (2020), doi:[10.1038/s41598-020-61856-9](https://doi.org/10.1038/s41598-020-61856-9).
- [81] S. Patra, J.-B. Claude, and J. Wenger, *Fluorescence Brightness, Photostability, and Energy Transfer Enhancement of Immobilized Single Molecules*

- in Zero-Mode Waveguide Nanoapertures*, *ACS Photonics* **9**, 2109 (2022), doi:[10.1021/acsp Photonics.2c00349](https://doi.org/10.1021/acsp Photonics.2c00349).
- [82] J. M. Moran-Mirabal, A. J. Torres, K. T. Samiee, B. A. Baird, and H. G. Craighead, *Cell investigation of nanostructures: zero-mode waveguides for plasma membrane studies with single molecule resolution*, *Nanotechnology* **18**, 195101 (2007), doi:[10.1088/0957-4484/18/19/195101](https://doi.org/10.1088/0957-4484/18/19/195101).
- [83] S. Yang, N. Klughammer, A. Barth, M. E. Tanenbaum, and C. Dekker, *Zero-mode waveguide nanowells for single-molecule detection in living cells*, *ACSNano* (2023), [10.1021/acsnano.3c05959](https://doi.org/10.1021/acsnano.3c05959), doi:[10.1021/acsnano.3c05959](https://doi.org/10.1021/acsnano.3c05959).
- [84] S. J. Kim, J. Fernandez-Martinez, I. Nudelman, Y. Shi, W. Zhang, B. Raveh, T. Herricks, B. D. Slaughter, J. A. Hogan, P. Upla, I. E. Chemmama, R. Pellarin, I. Echeverria, M. Shivaraju, A. S. Chaudhury, J. Wang, R. Williams, J. R. Unruh, C. H. Greenberg, E. Y. Jacobs, Z. Yu, M. J. de la Cruz, R. Mironska, D. L. Stokes, J. D. Aitchison, M. F. Jarrold, J. L. Gerton, S. J. Ludtke, C. W. Akey, B. T. Chait, A. Sali, and M. P. Rout, *Integrative structure and functional anatomy of a nuclear pore complex*, *Nature* **555**, 475 (2018), doi:[10.1038/nature26003](https://doi.org/10.1038/nature26003).
- [85] D. Cowburn and M. Rout, *Improving the Hole Picture: Towards a Consensus on the Mechanism of Nuclear Transport*, *ArXiv* (2023).
- [86] M. Beck and E. Hurt, *The nuclear pore complex: understanding its function through structural insight*, *Nature Reviews Molecular Cell Biology* **18**, 73 (2017), doi:[10.1038/nrm.2016.147](https://doi.org/10.1038/nrm.2016.147).
- [87] D. Görlich and U. Kutay, *Transport between the cell nucleus and the cytoplasm*, *Annual Review of Cell and Developmental Biology* **15**, 607 (1999), doi:[10.1146/annurev.cellbio.15.1.607](https://doi.org/10.1146/annurev.cellbio.15.1.607).
- [88] M. Jones, *Side-view diagram of a nuclear pore*. (2006), license: Creative Commons Attribution-Share Alike 2.5 Generic, <https://creativecommons.org/licenses/by-sa/2.5/>, Visited: 2023-04-03, <https://en.wikipedia.org/wiki/File:NuclearPore.svg>.
- [89] M. P. Rout, J. D. Aitchison, M. O. Magnasco, and B. T. Chait, *Virtual gating and nuclear transport: the hole picture*, *Trends in Cell Biology* **13**, 622 (2003), doi:<https://doi.org/10.1016/j.tcb.2003.10.007>.
- [90] S. Frey, R. P. Richter, and D. Görlich, *Fg-rich repeats of nuclear pore proteins form a three-dimensional meshwork with hydrogel-like properties*, *Science* **314**, 815 (2006), doi:[10.1126/science.1132516](https://doi.org/10.1126/science.1132516).
- [91] S. Frey and D. Görlich, *A saturated fg-repeat hydrogel can reproduce the permeability properties of nuclear pore complexes*, *Cell* **130**, 512 (2007), doi:<https://doi.org/10.1016/j.cell.2007.06.024>.

- [92] J. Yamada, J. L. Phillips, S. Patel, G. Goldfien, A. Calestagne-Morelli, H. Huang, R. Reza, J. Acheson, V. V. Krishnan, S. Newsam, A. Gopinathan, E. Y. Lau, M. E. Colvin, V. N. Uversky, and M. F. Rexach, *A bimodal distribution of two distinct categories of intrinsically disordered structures with separate functions in fg nucleoporins*, *Molecular & Cellular Proteomics* **9**, 2205 (2010), doi:[10.1074/mcp.M000035-MCP201](https://doi.org/10.1074/mcp.M000035-MCP201).
- [93] K. D. Schleicher, S. L. Dettmer, L. E. Kapinos, S. Pagliara, U. F. Keyser, S. Jeney, and R. Y. H. Lim, *Selective transport control on molecular velcro made from intrinsically disordered proteins*, *Nature Nanotechnology* **9**, 525 (2014), doi:[10.1038/nnano.2014.103](https://doi.org/10.1038/nnano.2014.103).
- [94] L. Kapinos, R. Schoch, R. Wagner, K. Schleicher, and R. Lim, *Karyopherin-centric control of nuclear pores based on molecular occupancy and kinetic analysis of multivalent binding with fg nucleoporins*, *Biophysical Journal* **106**, 1751 (2014), doi:<https://doi.org/10.1016/j.bpj.2014.02.021>.
- [95] L. E. Kapinos, B. Huang, C. Rencurel, and R. Y. Lim, *Karyopherins regulate nuclear pore complex barrier and transport function*, *Journal of Cell Biology* **216**, 3609 (2017), doi:[10.1083/jcb.201702092](https://doi.org/10.1083/jcb.201702092).
- [96] L. A. Strawn, T. Shen, N. Shulga, D. S. Goldfarb, and S. R. Wentz, *Minimal nuclear pore complexes define fg repeat domains essential for transport*, *Nature Cell Biology* **6**, 197 (2004), doi:[10.1038/ncb1097](https://doi.org/10.1038/ncb1097).
- [97] S. C. Ng, T. Güttler, and D. Görlich, *Recapitulation of selective nuclear import and export with a perfectly repeated 12mer glfg peptide*, *Nature Communications* **12**, 4047 (2021), doi:[10.1038/s41467-021-24292-5](https://doi.org/10.1038/s41467-021-24292-5).
- [98] A. J. Storm, J. H. Chen, X. S. Ling, H. W. Zandbergen, and C. Dekker, *Fabrication of solid-state nanopores with single-nanometre precision*, *Nature Materials* **2**, 537 (2003), doi:[10.1038/nmat941](https://doi.org/10.1038/nmat941).
- [99] M. J. Kim, M. Wanunu, D. C. Bell, and A. Meller, *Rapid Fabrication of Uniformly Sized Nanopores and Nanopore Arrays for Parallel DNA Analysis*, *Advanced Materials* **18**, 3149 (2006), doi:[10.1002/adma.200601191](https://doi.org/10.1002/adma.200601191).
- [100] H. Kwok, K. Briggs, and V. Tabard-Cossa, *Nanopore Fabrication by Controlled Dielectric Breakdown*, *PLoS ONE* **9**, e92880 (2014), doi:[10.1371/journal.pone.0092880](https://doi.org/10.1371/journal.pone.0092880).
- [101] K. Briggs, H. Kwok, and V. Tabard-Cossa, *Automated Fabrication of 2-nm Solid-State Nanopores for Nucleic Acid Analysis*, *Small* **10**, 2077 (2014), doi:[10.1002/smll.201303602](https://doi.org/10.1002/smll.201303602).
- [102] K. Briggs, M. Charron, H. Kwok, T. Le, S. Chahal, J. Bustamante, M. Waugh, and V. Tabard-Cossa, *Kinetics of nanopore fabrication during controlled breakdown of dielectric membranes in solution*, *Nanotechnology* **26**, 084004 (2015), doi:[10.1088/0957-4484/26/8/084004](https://doi.org/10.1088/0957-4484/26/8/084004).

- [103] Y. H. Lanyon, G. De Marzi, Y. E. Watson, A. J. Quinn, J. P. Gleeson, G. Redmond, and D. W. M. Arrigan, *Fabrication of Nanopore Array Electrodes by Focused Ion Beam Milling*, *Analytical Chemistry* **79**, 3048 (2007), doi:10.1021/ac061878x.
- [104] D. V. Verschueren, W. Yang, and C. Dekker, *Lithography-based fabrication of nanopore arrays in freestanding Si and graphene membranes*, *Nanotechnology* **29**, 145302 (2018), doi:10.1088/1361-6528/aaabce.
- [105] S. Pud, D. Verschueren, N. Vukovic, C. Plesa, M. P. Jonsson, and C. Dekker, *Self-aligned plasmonic nanopores by optically controlled dielectric breakdown*, *Nano letters* **15**, 7112 (2015), doi:10.1021/acs.nanolett.5b03239.
- [106] C. Ying, J. Houghtaling, O. M. Eggenberger, A. Guha, P. Nirmalraj, S. Awasthi, J. Tian, and M. Mayer, *Formation of single nanopores with diameters of 20–50 nm in silicon nitride membranes using laser-assisted controlled breakdown*, *ACS Nano* **12**, 11458 (2018), doi:10.1021/acsnano.8b06489.
- [107] E. Zvuloni, A. Zreben, T. Gilboa, and A. Meller, *Fast and deterministic fabrication of sub-5 nanometer solid-state pores by feedback-controlled laser processing*, *ACS Nano* **15**, 12189 (2021), doi:10.1021/acsnano.1c03773.
- [108] J. Larkin, M. Foquet, S. W. Turner, J. Korlach, and M. Wanunu, *Reversible positioning of single molecules inside zero-mode waveguides*, *Nano Letters* **14**, 6023 (2014), doi:10.1021/nl503134x.
- [109] J. R. Lakowicz, *Principles of Fluorescence Spectroscopy*, 3rd ed., edited by J. R. Lakowicz (Springer US, 2006) doi:10.1007/978-0-387-46312-4.
- [110] U. Kubitschek, *Fluorescence Microscopy: From Principles to Biological Applications.*, 2nd ed. (John Wiley & Sons, Incorporated, 2017).
- [111] J. R. Fries, L. Brand, C. Eggeling, M. Köllner, and C. A. M. Seidel, *Quantitative Identification of Different Single Molecules by Selective Time-Resolved Confocal Fluorescence Spectroscopy*, *The Journal of Physical Chemistry A* **102**, 6601 (1998), doi:10.1021/jp980965t.
- [112] K. Zhang and H. Yang, *Photon-by-photon determination of emission bursts from diffusing single chromophores*, *The Journal of Physical Chemistry B* **109**, 21930 (2005), doi:10.1021/jp0546047.
- [113] E. Nir, X. Michalet, K. M. Hamadani, T. A. Laurence, D. Neuhauser, Y. Kovchegov, and S. Weiss, *Shot-Noise Limited Single-Molecule FRET Histograms: Comparison between Theory and Experiments*, *The Journal of Physical Chemistry B* **110**, 22103 (2006), doi:10.1021/jp063483n.
- [114] L. P. Watkins and H. Yang, *Detection of intensity change points in time-resolved single-molecule measurements*, *The Journal of Physical Chemistry B* **109**, 617 (2005), doi:10.1021/jp0467548.

- [115] M. Mhadhbi, ed., *Electron Microscopy* (IntechOpen, 2022), doi:[10.5772/intechopen.97922](https://doi.org/10.5772/intechopen.97922).
- [116] J. Ayache, *Sample preparation handbook for transmission electron microscopy: techniques* (Springer, 2010).
- [117] D. M. Sullivan, *Electromagnetic Simulation Using the FDTD Method*. (Wiley, 2013).
- [118] K. C. Zhou and B. Liu, *Molecular dynamics simulation: fundamentals and applications* (Academic Press, 2022).
- [119] A. Mooradian, *Photoluminescence of Metals*, *Physical Review Letters* **22**, 185 (1969), doi:[10.1103/PhysRevLett.22.185](https://doi.org/10.1103/PhysRevLett.22.185).
- [120] G. T. Boyd, Z. H. Yu, and Y. R. Shen, *Photoinduced luminescence from the noble metals and its enhancement on roughened surfaces*, *Phys. Rev. B* **33**, 7923 (1986), doi:[10.1103/PhysRevB.33.7923](https://doi.org/10.1103/PhysRevB.33.7923).
- [121] M. Wanunu, W. Morrison, Y. Rabin, A. Y. Grosberg, and A. Meller, *Electrostatic focusing of unlabelled dna into nanoscale pores using a salt gradient*, *Nature Nanotechnology* **5**, 160 (2009), doi:[10.1038/nnano.2009.379](https://doi.org/10.1038/nnano.2009.379).
- [122] C. E. Zimmerli, M. Allegretti, V. Rantos, S. K. Goetz, A. Obarska-Kosinska, I. Zagoriy, A. Halavatyi, G. Hummer, J. Mahamid, J. Kosinski, and M. Beck, *Nuclear pores dilate and constrict in cellulose*, *Science* **374**, eabd9776 (2021), doi:[10.1126/science.abd9776](https://doi.org/10.1126/science.abd9776).
- [123] C. W. Akey, D. Singh, C. Ouch, I. Echeverria, I. Nudelman, J. M. Varberg, Z. Yu, F. Fang, Y. Shi, J. Wang, D. Salzberg, K. Song, C. Xu, J. C. Gumbart, S. Suslov, J. Unruh, S. L. Jaspersen, B. T. Chait, A. Sali, J. Fernandez-Martinez, S. J. Ludtke, E. Villa, and M. P. Rout, *Comprehensive structure and functional adaptations of the yeast nuclear pore complex*, *Cell* **185**, 361 (2022), doi:<https://doi.org/10.1016/j.cell.2021.12.015>.

2

PALLADIUM ZERO-MODE WAVEGUIDES FOR OPTICAL SINGLE-MOLECULE DETECTION WITH NANOPORES

Holes in metal films do not allow the propagation of light if the wavelength is much larger than the hole diameter, establishing such nanopores as so-called Zero Mode Waveguides (ZMWs). Molecules on the other hand, can still passage through these holes. We use this to detect individual fluorophore-labelled molecules as they travel through a ZMW and thereby traverse from the dark region to the illuminated side, upon which they emit fluorescent light. This is beneficial both for background suppression and to prevent premature bleaching. We use palladium as a novel metal-film material for ZMWs, which is advantageous compared to conventionally used metals. We demonstrate that it is possible to simultaneously detect translocations of individual free fluorophores of different colors. Labeled DNA and protein biomolecules can be detected as well at the single-molecule level with a high signal-to-noise ratio and at high bandwidth, which opens the door to a variety of single-molecule biophysics studies.

Due to copyright reasons this chapter is not included in the digital version. Please visit the links in the footnote for the full text of the chapter or contact Nils Klughammer.

This chapter has been published as Nils Klughammer and Cees Dekker, Palladium zero-mode waveguides for optical single molecule detection with nanopores. *Nanotechnology*, 32(18):18LT01, feb 2021. <https://doi.org/10.1088/1361-6528/abd976>. The "Just Accepted" version can be found at: <http://resolver.tudelft.nl/uuid:5513ea77-f0d8-4458-918e-f31493083ec9>

3

DIFFUSIOPHORESIS-DRIVEN DNA TRANSLOCATION THROUGH PALLADIUM NANOPORES

A salt concentration gradient across a nanopore can drive biomolecules such as DNA through the pore due to so-called diffusiophoresis. This was recently demonstrated using ion-conductance nanopore experiments with asymmetric salt conditions. The application of a voltage and the use of electrodes in these experiments can lead to electrophoresis and electrochemistry that potentially influence the translocation process. In this chapter, we study the influence of salt concentration gradients on DNA translocation rates through palladium nanopores using an optical approach, which avoids these potential caveats. We observed three trends: Diffusiophoresis can indeed drive DNA through a nanopore towards the high salt concentration. Translocations get more frequent with larger concentration differences between the cis and trans reservoirs. By varying different salt types, we found that the event rates for NaCl were higher than for both KCl and RbCl. Whereas our findings agree with existing literature and computational predictions, we encountered large quantitative variations between different experiments, of which the origin needs further investigation.

This chapter has not been published. Contributions to the work were made by Nils Klughammer, Ali Sentissi, Chenyu Wen, Xin Shi, and Cees Dekker

3.1. INTRODUCTION

Nanopore sensors have proven to be useful not only for DNA sequencing but for a variety of applications where single-molecule resolution is needed [1]. They can be both made from biological material such as proteins or DNA origami [2–5] but also as openings in solid-state membranes, fabricated in materials such as SiN [6], graphene [7–10], and metal films like gold [11] or palladium [12]. In typical nanopore-sensing applications, the measured signal is a conductance blockade due to the presence of an analyte in the pore sensing region, and thus a voltage needs to be applied across the nanopore and the conductance needs to be monitored continuously.

An alternative readout approach is provided by metallic nanopore that act as so-called Zero-Mode Waveguides (ZMW) that strongly suppress light from travelling through them if their pore diameter is below a certain cutoff. This light-blocking behaviour was first calculated by Bethe [13] for a perfectly conducting sheet with a hole. For these idealized subwavelength apertures, a cutoff wavelength, which is the maximum wavelength that is still transmitted through a pore of diameter d , can be calculated as $\lambda_c = 1.7d$. If the light's wavelength in the medium $\lambda > \lambda_c$, an evanescent field inside the pore is formed that follows an exponential intensity profile: $I(z) = I_0 \exp\left(-2z\sqrt{\frac{1}{\lambda_c^2} - \frac{1}{\lambda^2}}\right)$. Here, z is the depth in the ZMW and I_0 is the intensity at the surface [14]. This idealized formula is only an approximation for real metals, which can be better described using explicit field simulations [14–16]. Zero-mode waveguides have been used in various fields of research including fluorescence correlation spectroscopy, DNA sequencing, and cell imaging [11, 14, 17–24]. Typically, they are fabricated on glass surfaces, where the fluorescence volume reduction inside the ZMW is exploited. When translocations should be monitored through ZMWs, they are fabricated in a freestanding membrane, as was previously done in various studies [11, 12, 16, 23]. In this case, impinging light still gets blocked at the nanopore, but molecules can freely translocate through the opening. The optical detection with these ZMW variants, which are also called optical nanopores, has the advantage that it avoids the application of a voltage which can disturb or drive the translocation process. This is especially relevant when studying translocation processes that are driven by weak effects such as free diffusion [12, 16], hydrodynamic pressure [23] or asymmetric salt conditions, where a different salt concentration is applied in both reservoirs that connect to the nanopore [25, 26].

The movement of particles driven by salt gradients has been studied already for decades [27–30], also due to its interest in industrial applications such as membrane technologies and metal coating [30]. Additionally, the effect of asymmetric salt concentrations on DNA translocations through nanopores has been discussed for many years [31], but only recently, it became apparent that diffusiophoresis due to the resulting salt gradient can not be neglected in this case [25, 26, 30, 32].

The term diffusiophoresis specifies the movement of a particle immersed in a fluid up or down the concentration gradient of a solute that is interacting with the particle [30]. This interaction can be of any sort but in the case of salt gradients typically originates from the electrostatic interaction of the salt ions with charged particles. Consider, for example, the special case where a charged particle (such as a protein or DNA molecule) is immersed in a salt gradient. In this case, diffusiophoresis can be split up

in two contributions that originate from two effects, chemiphoresis and electrophoresis [30]. Regarding the latter, the charged particle attracts counter-ions into its electric double layer (EDL). Due to the imposed salt gradient, the EDL will be thinner on the high concentration side and thicker on the low concentration side, leading to a double-layer polarization and subsequently to a dipole moment which in turn generates an electric field. The same happens for the co-ions, which leads to an electric field opposing the one that is emerging from the counter-ions. When the salt ions have different diffusivities (such as is the case for NaCl) a global electric field is established that decelerates the fast ions and accelerates the ions with low diffusivity. This electric field can drive the motion of the charged particle. The resulting movement from these three electric fields (counter-ions, co-ions, diffusivities) is referred to as electrophoresis. Chemiphoresis, however, does not require electrostatic interactions but emerges from any interaction between a particle and a surrounding solute that is non-uniformly distributed. Due to the interactions, the solute's concentration in the vicinity of the particle is modulated, which leads to an osmotic pressure gradient within the interfacial layer along the surface [33]. This pressure gradient lets the particle move up the concentration gradient in the case of electrostatic interaction, irrespective of the charge of the particle [32]. A different view on this effect is that it is energetically favorable for the particle to be in the high concentration region of the solute that is attractively interacting with. Whereas chemiphoresis in a salt solution drives the particle up the concentration gradient, the resulting movement due to electrophoresis, in the absence of external applied fields, depends on the charge of the particle and the diffusivities of the ions, so that both movement directions, up or down the gradient, can be found in systems driven by diffusiophoresis. While diffusiophoresis describes the motion of a particle in a solute concentration gradient, diffusiostosis (or capillary osmosis) describes the opposite effect, namely that a solvent flow is generated due to a concentration gradient of a solute interacting with a fixed wall [30].

It was reported that diffusiophoresis can force DNA to translocate through a nanopore in asymmetric salt conditions, which was shown theoretically by calculating the velocity of a charged DNA-like particle inside a nanopore depending on the salt gradient [32] as well as experimentally by following DNA translocations in a salt gradient of KCl [25] and LiCl [26] in conductance-based nanopore experiments. These experimental studies were restricted to the investigation of a single salt each. Furthermore, the use of electrodes in the reservoirs of differential salt concentration resulted in electrical currents due to electrochemistry that needed to be taken into account. Additionally, due to current-based detection, both studies relied on the use of electrodes and partially applied an external voltage to the pore, which obviously can bias the transport phenomena.

Here, we establish a system to study diffusiophoresis driven DNA translocations through nanopores without electrical detection. We used palladium nanopores that act as ZMWs where analytes can be detected optically after translocation. We measured the event rates of short double-stranded DNA oligomers labelled with fluorophores. We studied the dependence of the event rate both on the salt concentration gradient and on the type of salt. We were able to identify three qualitative trends: (i) Diffusiophoresis can lead to DNA translocations through nanopores in asymmetric salt conditions. (ii) Diffusiophoresis results in higher translocation rates for larger salt gradients. (iii) NaCl drives

DNA at a higher rate through nanopores than KCl and RbCl, which led to very comparable event rates. Finally, we discuss limitations of this approach, as we encountered inconsistencies between different experimental realizations, which prohibited the full quantification of the three trends.

3.2. MATERIALS AND METHODS

Nanopore chips were fabricated as described in [12, 16]. Chips were treated by 2 min oxygen plasma at 50 W at a pressure below 60 mTorr before mounting in a flowcell. The chips were submersed in Ethanol-Water within minutes after the oxygen plasma. The Ethanol-water was directly exchanged with PBS solution for ion conductance measurements in order to verify wetting of the pores. Measurement of DNA translocations were performed on the same setup as described in [12, 16]. Doubly labeled DNA was added to the cis side, while the trans detection side was filled with salt solution not containing any DNA. The liquid was kept stationary in the flow cell in order to minimize disturbance of the DNA translocation process. Excitation of translocated analytes was performed using alternating excitation with picosecond pulsed lasers of 485 nm and 640 nm at 10 μ W focus power on a confocal Picoquant Microtime TCSPC microscope using a long working distance water dipping objective with 60x magnification. Salts (LiCl, KCl, NaCl, RbCl) and 100x Tris-EDTA (TE) pH 8.0 were purchased from Sigma.

During the translocation experiments, we typically kept the dark cis side at 150 mM salt concentration, buffered by 1xTE to pH 8.0 and added either 10 nM or 20 nM of DNA to this side. The salt concentration on the laser illuminated trans side was changed up to 1500 mM of the respective salt also containing 1xTE (pH 8.0). Between different salts, the flowcell and the reservoir were washed with deionized water. Before recording a time trace, the reservoirs were prewashed with the respective solutions.

We used two different versions of DNA: DNA oligomer 1 was a 90 bp (30.6 nm) long dsDNA with Cy5 (fluorescent in the 640 nm channel) on the 5' end of one strand and FAM Fluorescein (fluorescent in the 485 nm channel) on the 5' end of the other strand. Its sequence was optimized to avoid any secondary structure and was purchased from IDT. For the DNA oligomer 2, we used DNA as described in [34]. It was a 38 bp (13 nm) long double stranded oligomer that had Alexa 488 (fluorescent in the 485 nm channel) and Alexa 647 (fluorescent in the 640 nm channel) fluorophores placed at a mutual distance of 8.2 nm on the two strands. The DNA oligomers 1 and 2 were applied at concentrations of 10 nM and 20 nM to the dark cis side respectively. The diffusion coefficient used for prediction of the translocation rates of the DNA was measured using fluorescence correlation spectroscopy (FCS). The sequences are given in the Appendix 3.5.

Time traces were analyzed as described in [12] using the change-point algorithm [35] which provides the locations of change points in the photon statistics from which fluorescent burst events in a single detection channel can be identified. 'Double events' were defined as two events in the 640 nm and the 485 nm channel overlapping. For this type of events, we could be sure that they originated from the double-stranded DNA. Event rates were computed by dividing the number of events N recorded in a time trace by the time trace duration. A purely statistical uncertainty on the event rate can be estimated assuming that translocations underlie a Poisson process and thus the standard deviation could be estimated as $\sigma = \sqrt{N}$. This measure, however, highly underestimates the

variability found experimentally, as will be discussed later.

3.3. RESULTS AND DISCUSSION

In this section, we show that diffusiophoresis can drive DNA translocations through nanopores in the case of asymmetric salt conditions. First, we show that DNA translocation rates increase with increasing salt gradient and that the rates are different for NaCl, KCl, and LiCl. By refining the experiment, we could remove background events resulting from DNA accumulation on the detection side. We identified that event rates became unreliable after measuring translocations in LiCl. Therefore in subsequent experiments, we tested the effects of KCl, NaCl, and RbCl on DNA translocations, avoiding LiCl. When comparing different experiments, we could conclude that DNA translocation rates emanating from diffusiophoresis are higher for higher salt gradients and for NaCl compared to both KCl and RbCl. Since the observed variation between these experiments was too high, it was not possible to draw conclusive quantitative results, however.

3.3.1. EXPERIMENTAL SETUP TO OBSERVE DNA TRANSLOCATIONS DUE TO DIFFUSIOPHORESIS THROUGH NANOPORES

As a first step, we wanted to reproduce previous results [25, 26] to establish that DNA can be translocated through nanopores driven by diffusiophoresis, so that as a next step we could study the effect of different salt concentration gradients and different salts. From our earlier study [12], we had seen that DNA translocations can be directly observed at high signal-to-noise ratio using optical detection and Pd nanopores. We chose to use the same system, since this allows us to circumvent the use of electrodes and an applied voltage which may potentially influence the translocation behaviour of the DNA in asymmetric salt conditions. Our optical detection thus should provide a cleaner readout of the translocation rate compared to a conductance-based readout. The optical approach sacrifices information about the translocation speed, however, but this is not of our main interest in this diffusiophoresis study. We chose to work on Pd nanopores of sizes between 50 nm to 70 nm, since these provided good wetting capabilities as well as good light-blocking properties [16]. We chose to use short dsDNA below the persistence length of 50 nm [36] so that the DNA could be modeled as a stiff rod. Notably, the DNA should preferably be as long as possible, since the movement by diffusiophoresis scales with the length and the charge of the analyte [32]. We placed two different fluorophores (one for the blue and one for the red excitation channel), one on each of the strands of the DNA, at a large enough mutual distance such that any FRET would be highly suppressed between the fluorophores. This ensured that when we observed an event that showed up simultaneously in both fluorescence channels, it could unambiguously be identified as arising from a dsDNA oligomer and not from contamination or a piece of ssDNA. We called this kind of events 'double events' (Figure 3.1).

First, we chose to work on samples containing multiple nanopores in a single membrane in order to get a higher statistical coverage within one experiment. We studied two different effects emerging from varying the salt gradient and from different types of salt such as KCl, LiCl and NaCl. We developed an experimental scheme, where we kept the salt and DNA concentration on the cis-side of the nanopore constant while we varied

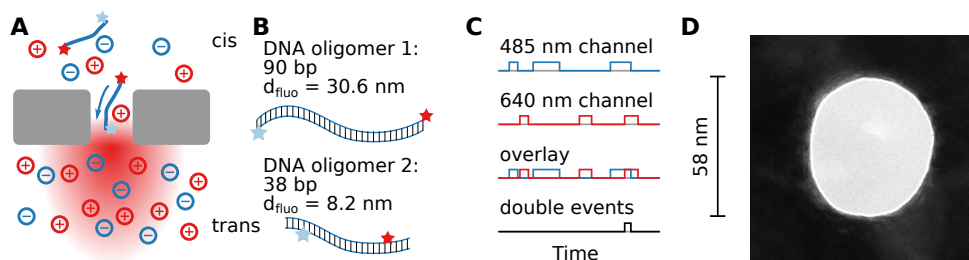


Figure 3.1: Setup of the experiment. A: On the cis side of a Pd nanopore, doubly labeled short dsDNA was applied within a low salt concentration solution. The analyte was transported to the trans side by diffusio-phoresis, where it was detected via its fluorescence. Due to the small diameter of the pore, the light field could not penetrate through the pore and excited only molecules on the trans side. B: We used two different short DNAs, both labeled with one fluorophore on each strand. Detection of both fluorophores ensured that the event resulted from the translocation of a dsDNA. C: Fluorescent bursts were recorded as events in both the 485 nm channel and 640 nm excitation channel separately. Double events were defined as events overlapping between both channels. D: TEM image of an example nanopore used in this study.

only the salt concentration on the trans side. For testing different salt types, the type of salt of both the cis-side and trans-side were changed. For both a negative gradient (from 150 mM on cis to 0 mM trans) and for an absence of a gradient (i.e., 150 mM on cis and 150 mM trans), barely any translocations could be observed on any of the eight pores (<0.3 Hz), as can be seen for the double event rate in Figure 3.2. When the gradient was increased to higher salt concentrations in trans, such as 500, 1000, or 1500 mM, significantly higher event rates were observed (0.4 Hz to 1.5 Hz for 1500 mM KCl, 6 Hz to 19 Hz for 1000 mM LiCl, and 3 Hz to 11 Hz for 1000 mM NaCl). This showed that indeed a salt gradient from low to high concentration does drive the DNA through the nanopores, as predicted theoretically [32] and reported earlier in ion-conduction experiments [25, 26].

After observing the expected translocation behaviour, we identified several shortcomings in the setup which prevented an adequate quantification of the event rates. First, the pore to pore variability was found to be approximately a factor of 3 which could not be explained by pore size variations, as the pore area changed by less than 30%. Next, when measuring directly on the membrane (location x in Figure 3.2 B) we still observed a sizeable event rate, which was on the order of the lowest event rates measured on one of the pores, even though there was no pore present in the Pd film. When moving further away from the array of pores, this event rate decreased. Therefore, we concluded that these events resulted from DNA molecules that had translocated and subsequently accumulated in the detection volume. This could happen, since the liquid was kept stationary in order not to disturb the DNA translocations, and thus DNA molecules that had translocated would not be washed out from the detection side. Therefore, DNA could accumulate on the detection side over the time of the measurement. In order to solve this issue, we reduced the number of pores to one in subsequent experiments, so that any observed event came from a DNA that had translocated through this nanopore. An additional issue we encountered in several experiments, was that individual pores would frequently show no translocations even though neighboring pores would do so under

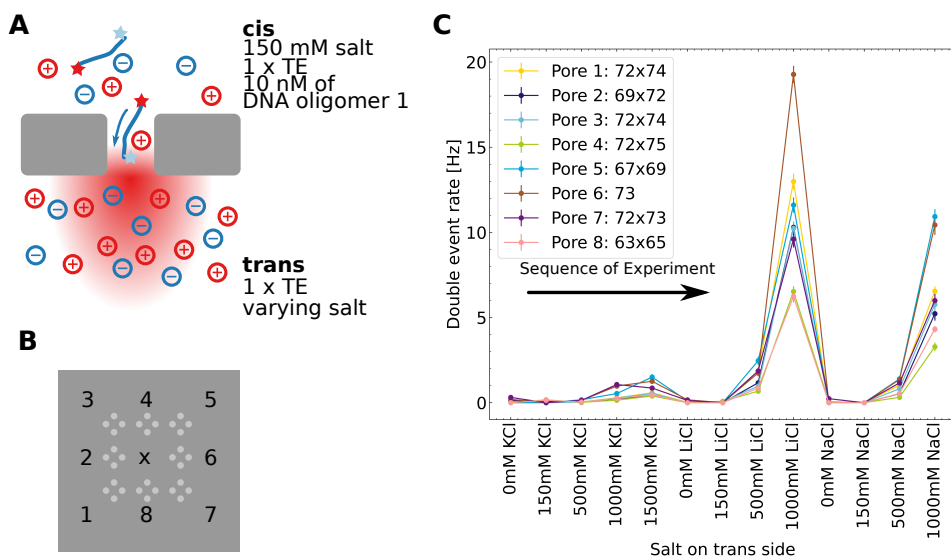


Figure 3.2: DNA translocations due to diffusiophoresis A: Experiments were performed with DNA oligomer 1 testing KCl, LiCl, and NaCl, for increasing salt concentrations on the trans side. B: Eight individual pores with markers were placed on one membrane spaced by $10\ \mu\text{m}$. The fluorescence in the centre of the 8 pores, where no pore was located, (marked by x) was recorded as well as a control. C: Double event rates for different salt concentrations on the trans side and the different salts for the eight pores. Error bars are SD estimated from Poisson statistics. The experiment started on the left and proceeded to the right. We find sizeable variations in the event rates from pore to pore.

the same conditions, which we interpreted as pores being blocked. On some pores, we also encountered extraordinarily long DNA events as quantified by fluorescence correlation spectroscopy (data not shown). Therefore, we tested to work with a shorter DNA, hosting different fluorophores than those of the DNA oligomer 1 (Figure 3.1). In subsequent experiments with this shorter DNA, we encountered fewer blocked pores and fewer extraordinarily long events, so we decided to continue to work with DNA oligomer 2. Next to high pore-to-pore variation, we also found a large variation between experiments, especially when the sequence of salts was changed. Not only did the absolute values for the event rates change then, but occasionally even the observation which salt would drive the DNA the strongest (data not shown). In order to get more reproducible results, we decided to systematically investigate the influence of different salts on the translocation rates.

Thus, we performed diffusiophoresis experiments on a single pore. We alternated the different types of salt KCl, NaCl and LiCl, always probing the same gradient from 150 mM on cis to 1000 mM on trans. In Figure 3.3 we show the results of one example experiment performed on a 57 nm pore. We started by observing a double event rate of 0.9 Hz to 1.2 Hz for KCl, 3.3 Hz to 4 Hz for NaCl in the beginning of the experiment. This did not hold for LiCl, which already produced two rather different event rates of 4.8 ± 0.3 Hz and 3.3 ± 0.2 Hz. After exposure of the pore to LiCl, the NaCl rate dropped by a factor of 2 to 1.9 ± 0.2 Hz. We also observed in several other experiments that the event rates dropped

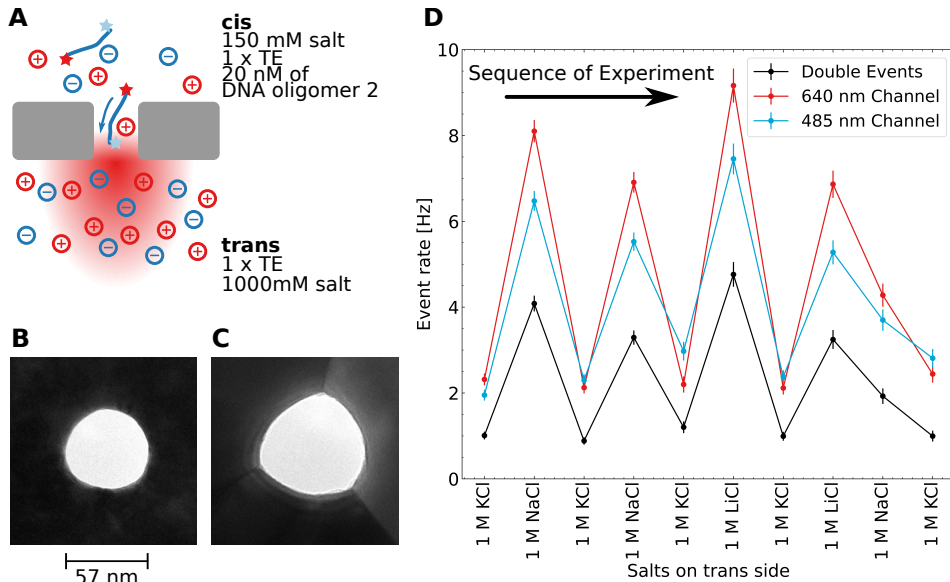


Figure 3.3: Testing the influence of the order of salt type A: To assess if specific salts pose a problem to the reproducibility of the event rates, we performed diffusiophoresis experiments for a fixed gradient from 150 mM to 1000 mM, but varying the salt type between KCl, NaCl, and LiCl. B,C: TEM image of the nanopore before (B) and (C) after the experiment. The experiment (including an oxygen plasma step) did change the structure of the Pd slightly and let the pore deform. In TEM, the pore did look fully open after the experiment. D: Double event rates for different types of salt, measured for the same concentration gradient. The experiment started on the left and proceeded to the right. In the beginning, only KCl and NaCl were alternated and the event rates were reproducible. After LiCl was added, however, the event rates dropped to lower values than in the beginning of the experiment (e.g. for NaCl)

partially or fully to around 0 Hz after pore exposure to LiCl. Hence, we decided to remove LiCl from the set of salts and replace it with RbCl in further experiments, which indeed reduced the issue of pores where no translocations could be observed. The cause of the issues upon LiCl exposure remains to be studied.

3.3.2. DIFFUSIOPHORESIS DRIVEN DNA TRANSLOCATION RATES FOLLOW THE PREDICTED TRENDS

We performed six experiments on different days and with different pores of diameters from 50 nm to 58 nm, systematically testing KCl, NaCl, and RbCl. We performed both ramps as in Figure 3.2 and salt alternating tests as in Figure 3.3. The results are displayed in Figure 3.4. When comparing the event rates for a gradient from 150 mM to 1000 mM within a single experiment, we found factors up to 10 between the measured rates among different measurements ((Figure 3.4 A, KCl 1208, open symbols). To facilitate the comparison between different experiments, we computed averages. For the case where 150 mM of salt was added to the trans reservoir (horizontal bars in Figure 3.4) - where only free diffusion should contribute to translocations - we found lower translocation rates than when a salt gradient from 150 mM (cis) to 1000 mM (trans) was applied.

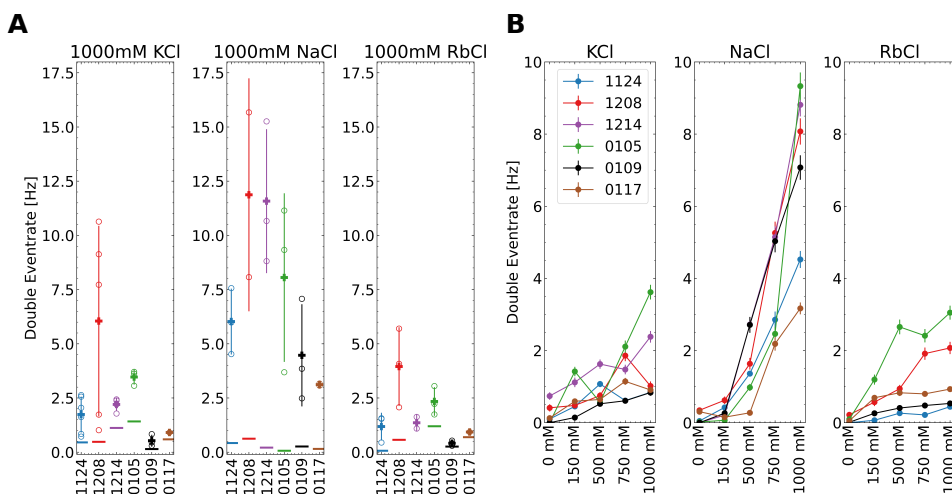


Figure 3.4: High experiment-to-experiment variability of diffusiophoresis rates A: Double event rates testing KCl, NaCl, and RbCl for a gradient from 150 mM to 1000 mM in six experiments labeled by a 4 digit code (x-axis). Data are shown as open symbols together with the averages (plus) and standard deviation (error bars). Corresponding free diffusion event rate from 150 mM salt on trans is shown as a horizontal bar. All event rates are significantly higher than the rates for free diffusion. Average event rates varied by a factor of 4 between different experiments. B: The same variation from experiment to experiment was found when the trans salt concentration was increased from 0 mM to 1000 mM (Error bars show the statistical SD). Two trends can be identified: (i) for higher concentration gradients, the event rates increased; and (ii) NaCl drives DNA stronger through the nanopores than KCl and RbCl, where the later two showed comparable event rates.

This was observed in all experiments and for all salt types. We observed that the event rates for NaCl were consistently higher compared to KCl and RbCl. The latter two salts produced double event rates at the same magnitude. When comparing the averages for measured rates in individual experiments, we observed a large variation, of up to a factor of 4 (e.g., Figure 3.4 A, NaCl 1208 vs. 0117). We hypothesized that this variation might be a consequence of systematic differences from pore to pore. Therefore, we also computed the double event rate normalized to the highest event rate encountered on a single pore (Supplementary Figure 3.1). Such a normalization did however not significantly reduce the pore to pore variations, and therefore we concluded that the event rate variations were not explained by some pores showing a structurally higher event rate than others.

When having a closer look at the concentration ramps displayed in Figure 3.4 B, we observed a trend, in all salts, that a higher gradient produced higher event rates, although variation within the experiment led to individual datapoints not following this trend beyond their statistical uncertainty (compare 1000 mM KCl for 1208). The experiment-to-experiment variability was found to be high (e.g. in RbCl at 1000 mM we found a factor of 6 between the lowest and the highest event rates). Furthermore, we observed that there was considerable spread among data for an inverse gradient (i.e. experiments for the gradient from 150 mM KCl in cis to 0 mM in trans) and for the absence of a concentration gradient (i.e. 150 mM RbCl and KCl, where event rates ranged from 0.1 Hz to 1.4 Hz).

For the latter case of same concentrations at cis and trans sides, the event rate ex-

pected from pure diffusion can be estimated based on Fick's law of diffusion. Specifically, this expresses the translocation rate J through a pore of radius r , length l , of the DNA with a diffusion coefficient of $D = 72 \mu\text{m}^2/\text{s}$, as measured by FCS, and the concentration difference of the DNA between cis and trans $\Delta c = 20 \text{ nM}$ as

$$J = \pi r^2 D \frac{\Delta c}{L}. \quad (3.1)$$

This yields an event rate of 17 Hz. The estimate was obtained from the diffusion coefficient measured in open space and does not take into account any steric hindrance inside the pore due to the linear extension of the DNA. The lower bound of the translocation rate due to steric hindrance can be estimated by assuming a spherical particle the size of the length of the DNA, thus heavily overestimating the dimensions of the DNA. For this lower bound of the translocation rate we obtain a reduction to 4.4 Hz [37]. In total, this means that the translocation rate due to free diffusion should lie between 4.4 Hz and 17 Hz in our system.

For comparison of this number with our experiments, we need to estimate the detection efficiency of our system which relates the translocation rate to the experimentally measured 'double event' rate. From Figure 3.3 we found that the 'double event' rate was roughly half of the event rates measured in the individual channels. When making the simplifying assumption that the detection in both channels was independent of each other, we found that only a quarter of the actual translocation events were detected as double events in that experiment. This number only forms an upper bound for the detection efficiency, however, since in previous studies we had seen that multiple detections of the same molecule after translocation significantly contributed to the event rate [12].

Experimentally, the actually measured 'double event' rate was found to be lower than 1.5 Hz for cases without a gradient (i.e. 150 mM salt) as presented in Figure 3.4. In Supplementary Figure 3.2 we compare the measured event rates with the theoretical prediction corrected by the detection efficiency. We found that only 3 out of 15 data points fall above the predicted lower limit expected from Fick's law of diffusion. We can envision two reasons that could lead to this discrepancy between the experimentally measured rates and the theoretical prediction: First, there could be nonspecific interaction of the DNA or the fluorophores with the pore surface. Additionally, there could have been loss of DNA in the reservoir, which we tried to avoid by preflushing. Both could also explain the high variability between different experiments, especially when also (partial) blocking of the pore by DNA is considered.

After having discussed the limitations, it is interesting to compare the three translocation trends that we identified with theoretical predictions. Joo *et al.* [32] simulated a very comparable system and computed the translocation velocity of a uniformly charged rod-shape particle resulting from diffusiophoresis due to a difference in salt concentrations between two reservoirs connected by the nanopore. Since the translocation rate that we measured is not only dependent on the translocation speed but also on the capture rate at the entrance of the pore, the computational predictions of translocation velocity can not be mapped directly to the results presented earlier in this study. Still, we believe that trends such as translocation direction and relative magnitude of the translocation rate can be deduced from the computational predictions. Joo *et al.* [32] quanti-

fied the salt gradient by the ratio of salt concentrations in the reservoirs (e.g. from 10 mM to 100 mM would give a ratio of 10). The same ratio can be achieved at different overall salt concentrations (e.g. from 1 mM to 10 mM also gives a ratio of 10). The two gradients don't produce the same translocation speeds, however, since the size of the electric double layer (EDL) is influenced by salt concentration. Joo *et al.* [32] discussed different ranges of salt concentrations, but the salt concentrations that we used experimentally were about a factor of 500 higher than the highest concentrations Joo *et al.* [32] considered. Additionally, Joo *et al.* [32] only considered pores up to a diameter of 20 nm. They showed that the interaction of the pore with the EDL (as found in the small-pore-large-EDL limit) does heavily influence the translocation dynamics, while for large-pores, this interaction can be neglected. Since in our experimental setup the pores were even larger and the EDLs much smaller than as discussed in [32], we believe that the results presented earlier in this study can be compared to the case presented in [32] for small EDLs and large pores.

When looking at the translocation direction, Joo *et al.* [32] found three regimes: In the first regime with a thick EDL they found that DNA travels down the salt gradient towards the low concentration for both NaCl and KCl. For an intermediate EDL thickness, DNA can travel up the gradient for NaCl but down the gradient for KCl. And for low EDL thicknesses, they found that DNA moves up the gradient for both NaCl and KCl. In our experiments, we used high salt concentrations leading to very thin EDLs, and we found that DNA travels up the gradient for all four salts LiCl, NaCl, RbCl, and KCl, in line with previous experimental studies [25, 26]. Regarding the theoretically predicted translocation velocity, Joo *et al.* [32] found a monotonous increase for increasing salt gradients for both NaCl and KCl, a trend that we also found in our experiments, again in line with previous experimental findings [25, 26]. When quantitatively comparing the event rates for NaCl and KCl, Joo *et al.* [32] predicted the translocation velocity for NaCl to be higher than for KCl, due to different diffusivities of Na and K ions. We identified a similar trend of a higher translocation rate for NaCl than for KCl, see [Figure 3.4 A](#). Given the chemical similarity of potassium and rubidium, for instance in their hydration shell and diffusivity [32, 38, 39] (which is different for sodium), it is not surprising that the potassium and rubidium salts behaved very comparably in our translocation experiments.

3.4. CONCLUSIONS AND OUTLOOK

In this chapter, we have shown that a salt gradient can lead to DNA translocations through nanopores due to diffusiophoresis. We achieved an experimental verification of this using palladium nanopores that allowed for optical detection of the translocated DNA without the need to apply a voltage across the membrane. This made it possible to observe undisturbed translocations that were only driven by diffusion and diffusiophoresis. We did, however, encounter several experimental problems with the quantitative reproducibility of translocation rates between different experiments. One potential cause of this may be non-specific interactions between the DNA and the palladium surface. This could for instance originate from an electrostatic interaction due to counter charges accumulating in the metal when the charged DNA comes close to the surface. For further studies, the surface properties of Pd should be investigated more carefully, especially when in contact with different salt solutions. In our studies we excluded the use of LiCl

without further investigation about the cause of the inconsistencies that we observed experimentally. Understanding of the interaction of LiCl and other salts with Pd would be useful for future work using Pd nanopores. Additionally, Joo *et al.* [32] showed that surface charges in the pore can promote translocations towards the high salt concentration and the surface charge should therefore be tightly controlled. A potential solution for the surface charges and the non-specific interaction would be to coat the surface with a self-assembled monolayer with a neutral head group, which could both serve as passivation layer but also allow to control the surface charge. Another way to tackle this problem might be to coat the Pd surface with a thin layer of SiO₂ together with subsequent pH adjustment of the salt solutions to cancel potential surface charges. Since exact knowledge of the surface charge is difficult, we would propose control experiments using an uncharged molecule of the same dimensions as the DNA labeled with a fluorophore. A candidate for such a molecule would be polyethylene glycol even though its stiffness is very different. Such an uncharged molecule should barely be driven by diffusiophoresis and would only react to potential surface flows present in the pores.

In our work, we could identify three effects that had been predicted theoretically before, see e.g. Joo *et al.* [32]. First, in our experimental regime, diffusiophoresis drove DNA up the gradient towards the higher salt concentration. Second, a higher concentration gradient led to higher translocation rates. And third, NaCl drove DNA stronger through nanopores than KCl and RbCl. Some of these trends had been already experimentally studied using conductance-based readout, see McMullen *et al.* [25] and [26]. Due to the need for electrodes, however, such conductance-based readouts are conceptually more complex than the method proposed here. Also, McMullen *et al.* [25] used long λ -DNA for efficient detection, which was much longer than the DNA's persistence length and therefore could not be treated as a stiff rod during translocations. Furthermore, immersing the electrodes in salt reservoirs of different molarity led to a conductance that needed to be corrected for as a consequence of electrochemistry [25]. Due to the conceptual simplicity of our system, we think the use of optical nanopores offers a good platform to study DNA translocations driven by diffusiophoresis, despite several technical challenges that still need to be overcome.

REFERENCES

- [1] Y.-L. Ying, Z.-L. Hu, S. Zhang, Y. Qing, A. Fragasso, G. Maglia, A. Meller, H. Bayley, C. Dekker, and Y.-T. Long, *Nanopore-based technologies beyond DNA sequencing*, *Nature Nanotechnology* **17**, 1136 (2022), doi:[10.1038/s41565-022-01193-2](https://doi.org/10.1038/s41565-022-01193-2).
- [2] S. Iqbal and R. Bashir, *Nanopores: sensing and fundamental biological interactions*, (Springer, 2011) doi:[10.1007/978-1-4419-8252-0](https://doi.org/10.1007/978-1-4419-8252-0).
- [3] N. A. W. Bell, C. R. Engst, M. Ablay, G. Divitini, C. Ducati, T. Liedl, and U. F. Keyser, *DNA Origami Nanopores*, *Nano Letters* **12**, 512 (2012), doi:[10.1021/nl204098n](https://doi.org/10.1021/nl204098n).
- [4] A. Fragasso, N. De Franceschi, P. Stömmmer, E. O. van der Sluis, H. Dietz, and C. Dekker, *Reconstitution of Ultrawide DNA Origami Pores in Liposomes for Transmembrane Transport of Macromolecules*, *ACS Nano* **15**, 12768 (2021), doi:[10.1021/acsnano.1c01669](https://doi.org/10.1021/acsnano.1c01669).

- [5] Q. Shen, Q. Xiong, K. Zhou, Q. Feng, L. Liu, T. Tian, C. Wu, Y. Xiong, T. J. Melia, C. P. Lusk, and C. Lin, *Functionalized dna-origami-protein nanopores generate large transmembrane channels with programmable size-selectivity*, *Journal of the American Chemical Society* **145**, 1292 (2023), doi:10.1021/jacs.2c11226.
- [6] J. Li, D. Stein, C. McMullan, D. Branton, M. J. Aziz, and J. A. Golovchenko, *Ion-beam sculpting at nanometre length scales*, *Nature* **412**, 166 (2001), doi:10.1038/35084037.
- [7] S. Garaj, W. Hubbard, A. Reina, J. Kong, D. Branton, and J. A. Golovchenko, *Graphene as a subnanometre trans-electrode membrane*, *Nature* **467**, 190 (2010), doi:10.1038/nature09379.
- [8] G. F. Schneider, S. W. Kowalczyk, V. E. Calado, G. Pandraud, H. W. Zandbergen, L. M. K. Vandersypen, and C. Dekker, *DNA Translocation through Graphene Nanopores*, *Nano Letters* **10**, 3163 (2010), doi:10.1021/nl102069z.
- [9] C. A. Merchant, K. Healy, M. Wanunu, V. Ray, N. Peterman, J. Bartel, M. D. Fischbein, K. Venta, Z. Luo, A. T. C. Johnson, and M. Drndić, *DNA Translocation through Graphene Nanopores*, *Nano Letters* **10**, 2915 (2010), doi:10.1021/nl101046t.
- [10] D. V. Verschueren, W. Yang, and C. Dekker, *Lithography-based fabrication of nanopore arrays in freestanding sin and graphene membranes*, *Nanotechnology* **29**, 145302 (2018), doi:10.1088/1361-6528/aaabce.
- [11] O. N. Assad, T. Gilboa, J. Spitzberg, M. Juhasz, E. Weinhold, and A. Meller, *Light-enhancing plasmonic-nanopore biosensor for superior single-molecule detection*, *Advanced Materials* **29**, 1605442 (2016), doi:10.1002/adma.201605442.
- [12] N. Klughammer and C. Dekker, *Palladium zero-mode waveguides for optical single-molecule detection with nanopores*, *Nanotechnology* **32**, 18LT01 (2021), doi:10.1088/1361-6528/abd976.
- [13] H. A. Bethe, *Theory of diffraction by small holes*, *Physical Reviews* **66**, 163 (1944), doi:10.1103/PhysRev.66.163.
- [14] M. J. Levene, J. Korlach, S. W. Turner, M. Foquet, H. G. Craighead, and W. W. Webb, *Zero-mode waveguides for single-molecule analysis at high concentrations*, *science* **299**, 682 (2003), doi:10.1126/science.1079700.
- [15] P. Zhu and H. G. Craighead, *Zero-mode waveguides for single-molecule analysis*, *Annual Review of Biophysics* **41**, 269 (2012), doi:10.1146/annurev-biophys-050511-102338.
- [16] N. Klughammer, A. Barth, M. Dekker, A. Fragasso, P. Onck, and C. Dekker, *Diameter dependence of transport through nuclear pore complex mimics studied using optical nanopores*, *eLife* **12** (2023), 10.7554/eLife.87174, doi:10.7554/eLife.87174.
- [17] K. T. Samiee, M. Foquet, L. Guo, E. C. Cox, and H. G. Craighead, *λ -repressor oligomerization kinetics at high concentrations using fluorescence correlation spectroscopy in zero-mode waveguides*, *Biophysical Journal* **88**, 2145 (2005), doi:10.1529/biophysj.104.052795.

- [18] H. Rigneault, J. Capoulade, J. Dintinger, J. Wenger, N. Bonod, E. Popov, T. W. Ebbesen, and P.-E. Lenne, *Enhancement of single-molecule fluorescence detection in subwavelength apertures*, *Phys. Rev. Lett.* **95**, 117401 (2005), doi:10.1103/PhysRevLett.95.117401.
- [19] D. Gérard, J. Wenger, N. Bonod, E. Popov, H. Rigneault, F. Mahdavi, S. Blair, J. Dintinger, and T. W. Ebbesen, *Nanoaperture-enhanced fluorescence: Towards higher detection rates with plasmonic metals*, *Physical Review B* **77**, 045413 (2008), doi:10.1103/PhysRevB.77.045413.
- [20] J. M. Moran-Mirabal, A. J. Torres, K. T. Samiee, B. A. Baird, and H. G. Craighead, *Cell investigation of nanostructures: zero-mode waveguides for plasma membrane studies with single molecule resolution*, *Nanotechnology* **18**, 195101 (2007), doi:10.1088/0957-4484/18/19/195101.
- [21] H. Aouani, J. Wenger, D. Gérard, H. Rigneault, E. Devaux, T. W. Ebbesen, F. Mahdavi, T. Xu, and S. Blair, *Crucial role of the adhesion layer on the plasmonic fluorescence enhancement*, *ACS Nano* **3**, 2043 (2009), doi:10.1021/nn900460t.
- [22] C. I. Richards, K. Luong, R. Srinivasan, S. W. Turner, D. A. Dougherty, J. Korch, and H. A. Lester, *Live-cell imaging of single receptor composition using zero-mode waveguide nanostructures*, *Nano Letters* **12**, 3690 (2012), doi:10.1021/nl301480h.
- [23] T. Auger, J. Mathé, V. Viasnoff, G. Charron, J.-M. Di Meglio, L. Auvray, and F. Montel, *Zero-mode waveguide detection of flow-driven dna translocation through nanopores*, *Phys. Rev. Lett.* **113**, 028302 (2014), doi:10.1103/PhysRevLett.113.028302.
- [24] J. Larkin, R. Y. Henley, V. Jadhav, J. Korch, and M. Wanunu, *Length-independent dna packing into nanopore zero-mode waveguides for low-input dna sequencing*, *Nature nanotechnology* **12**, 1169 (2017), doi:10.1038/nnano.2017.176.
- [25] A. McMullen, G. Araujo, M. Winter, and D. Stein, *Osmotically driven and detected dna translocations*, *Scientific Reports* **9**, 15065 (2019), doi:10.1038/s41598-019-51049-4.
- [26] M. Charron, L. Philipp, L. He, and V. Tabard-Cossa, *Elucidating the dynamics of polymer transport through nanopores using asymmetric salt concentrations*, *Nano Research* **15**, 9943 (2022), doi:10.1007/s12274-022-4886-3.
- [27] D. C. Prieve and R. Roman, *Diffusiophoresis of a rigid sphere through a viscous electrolyte solution*, *J. Chem. Soc., Faraday Trans. 2* **83**, 1287 (1987), doi:10.1039/F29878301287.
- [28] J. L. Anderson, *Colloid transport by interfacial forces*, *Annual Review of Fluid Mechanics* **21**, 61 (1989), doi:10.1146/annurev.fl.21.010189.000425.
- [29] H. J. Keh and L. Y. Hsu, *Diffusioosmotic flow of electrolyte solutions in fibrous porous media at arbitrary zeta potential and double-layer thickness*, *Microfluidics and Nanofluidics* **7**, 773 (2009), doi:10.1007/s10404-009-0435-4.

- [30] H. J. Keh, *Diffusiophoresis of charged particles and diffusioosmosis of electrolyte solutions*, *Current Opinion in Colloid & Interface Science* **24**, 13 (2016), doi:<https://doi.org/10.1016/j.cocis.2016.05.008>.
- [31] M. Wanunu, W. Morrison, Y. Rabin, A. Y. Grosberg, and A. Meller, *Electrostatic focusing of unlabelled dna into nanoscale pores using a salt gradient*, *Nature Nanotechnology* **5**, 160 (2009), doi:[10.1038/nnano.2009.379](https://doi.org/10.1038/nnano.2009.379).
- [32] S. W. Joo, S. Y. Lee, J. Liu, and S. Qian, *Diffusiophoresis of an elongated cylindrical nanoparticle along the axis of a nanopore*, *ChemPhysChem* **11**, 3281 (2010), doi:<https://doi.org/10.1002/cphc.201000433>.
- [33] A. Ajdari and L. Bocquet, *Giant amplification of interfacially driven transport by hydrodynamic slip: Diffusio-osmosis and beyond*, *Phys. Rev. Lett.* **96**, 186102 (2006), doi:[10.1103/PhysRevLett.96.186102](https://doi.org/10.1103/PhysRevLett.96.186102).
- [34] B. Hellenkamp, S. Schmid, O. Doroshenko, O. Opanasyuk, R. Kühnemuth, S. Rezaei Adariani, B. Ambrose, M. Aznauryan, A. Barth, V. Birkedal, M. E. Bowen, H. Chen, T. Cordes, T. Eilert, C. Fijen, C. Gebhardt, M. Götz, G. Gouridis, E. Gratton, T. Ha, P. Hao, C. A. Hanke, A. Hartmann, J. Hendrix, L. L. Hildebrandt, V. Hirschfeld, J. Hohlbein, B. Hua, C. G. Hübner, E. Kallis, A. N. Kapanidis, J.-Y. Kim, G. Krainer, D. C. Lamb, N. K. Lee, E. A. Lemke, B. Levesque, M. Levitus, J. J. McCann, N. Naredi-Rainer, D. Nettels, T. Ngo, R. Qiu, N. C. Robb, C. Röcker, H. Sanabria, M. Schlierf, T. Schröder, B. Schuler, H. Seidel, L. Streit, J. Thurn, P. Tinnefeld, S. Tyagi, N. Vandenberk, A. M. Vera, K. R. Weninger, B. Wünsch, I. S. Yanez-Orozco, J. Michaelis, C. A. M. Seidel, T. D. Craggs, and T. Hugel, *Precision and accuracy of single-molecule FRET measurements—a multi-laboratory benchmark study*, *Nature Methods* **15**, 669 (2018-09), doi:[10.1038/s41592-018-0085-0](https://doi.org/10.1038/s41592-018-0085-0).
- [35] L. P. Watkins and H. Yang, *Detection of intensity change points in time-resolved single-molecule measurements*, *The Journal of Physical Chemistry B* **109**, 617 (2005), doi:[10.1021/jp0467548](https://doi.org/10.1021/jp0467548).
- [36] D. R. Tree, A. Muralidhar, P. S. Doyle, and K. D. Dorfman, *Is dna a good model polymer?* *Macromolecules* **46**, 8369 (2013), doi:[10.1021/ma401507f](https://doi.org/10.1021/ma401507f).
- [37] P. Dechadilok and W. M. Deen, *Hindrance factors for diffusion and convection in pores*, *Industrial & Engineering Chemistry Research* **45**, 6953 (2006), doi:[10.1021/ie051387n](https://doi.org/10.1021/ie051387n).
- [38] R. Mills and J. W. Kennedy, *The Self-diffusion Coefficients of Iodide, Potassium and Rubidium Ions in Aqueous Solutions*¹, *Journal of the American Chemical Society* **75**, 5696 (1953), doi:[10.1021/ja01118a063](https://doi.org/10.1021/ja01118a063).
- [39] Y. Marcus, *Thermodynamics of solvation of ions. Part 5.—Gibbs free energy of hydration at 298.15 K*, *J. Chem. Soc., Faraday Trans.* **87**, 2995 (1991), doi:[10.1039/FT9918702995](https://doi.org/10.1039/FT9918702995).

3.5. APPENDIX

3.5.1. SEQUENCES OF THE DNAs USED

The sequence of the DNA oligomers 1 used here was:

5'-**C**CTCACGGATCAGCTTATCATTCTCGTCGTA**C**TTTCGTGTTTCATGCGGCTATCCAGAA
TTTGCGCAACATGCTTGGTAATCTGACGGGTCT-3' and
3'-GGAGTGCTAGTCGAATAGTAAGAGCAGCATGAAGCACAAAGTACGCCGATAGGTCT
TAAACGCGTTGTACGAACCATTAGACTGCC**C**AGA-5'

The red labeled base was linked to a Cy5 fluorophore and the blue highlighted base was linked to a 6-FAM (fluorescein) fluorophore.

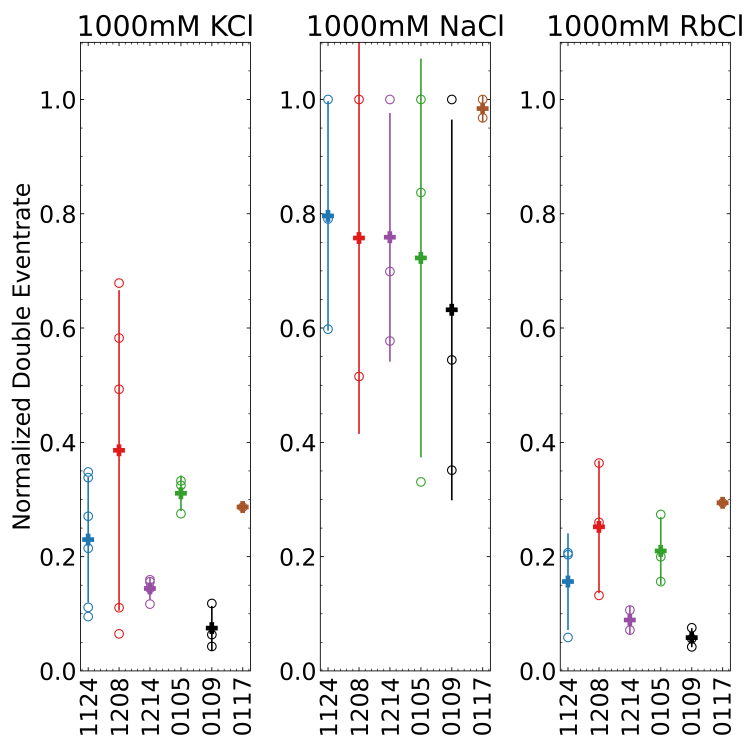
And the sequence of DNA oligomer 2 used here was:

5'-GAGCTGAAAGTGT**C**GAGTTTGT**T**TGAGTGT**T**TGTCTGG-3' and
3'-CTCGACT**T**TCACAGCTCAAACAACTC**C**AAACAGACC-5'-biotin

The red labeled base was linked to an Alexa647 fluorophore and the blue highlighted base was linked to a Alexa488 fluorophore.

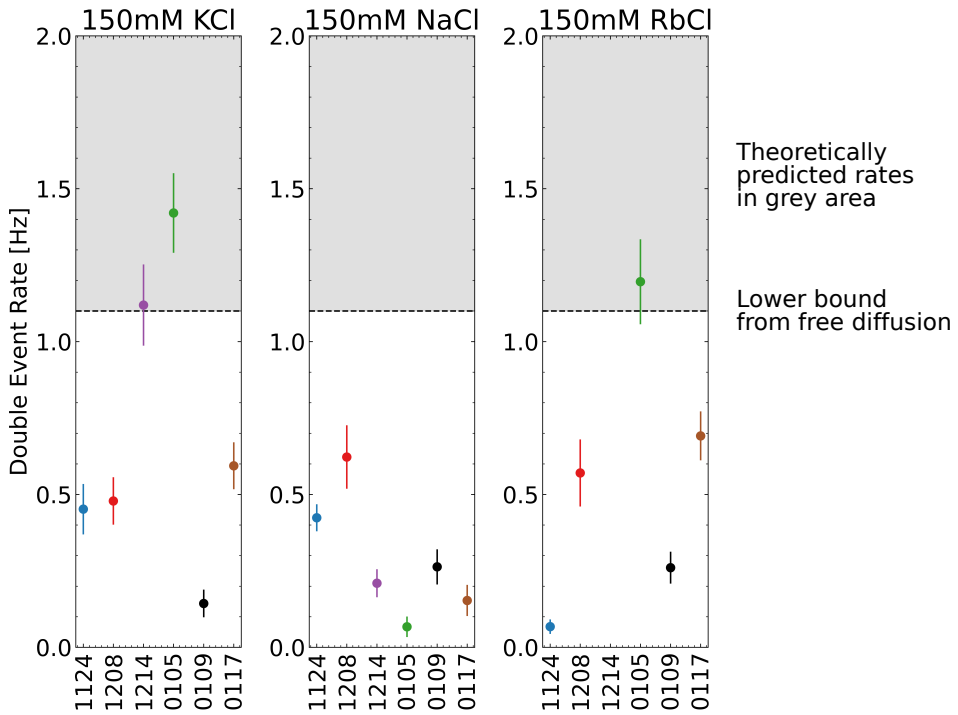
3.5.2. NORMALIZED DOUBLE EVENT RATES

3



Supplementary Figure 3.1: Six diffusiophoresis experiments for a gradient from 150 mM to 1000 mM with KCl, NaCl and RbCl, labeled by a 4 digit code (x-axis). Normalized double event rates are shown as open symbols together with the averages (plus) and standard deviation (errorbars). Normalization of the event rate of all salts (KCl, RbCl, and NaCl) was done with respect to the highest individual event rate measured in NaCl. Even after normalization, the average event rates still varied by a factor of 4 among different experiments.

3.5.3. EVENT RATES FROM FREE DIFFUSION



Supplementary Figure 3.2: Double event rates (y-axis) together with their statistical uncertainties (SD, error bars) measured in different experiments (x-axis) in the absence of a salt concentration gradient (150 mM of the salt indicated on top on cis and trans). An estimate for the double event rate is indicated by the shaded area with a lower boundary given by the dashed line. Except for three data points, all measured double event rates fall below the lower threshold.

4

DIAMETER DEPENDENCE OF TRANSPORT THROUGH NUCLEAR PORE COMPLEX MIMICS STUDIED USING OPTICAL NANOPORES

The nuclear pore complex (NPC) regulates the selective transport of large biomolecules through the nuclear envelope. As a model system for nuclear transport, we construct NPC mimics by functionalizing the pore walls of freestanding palladium zero-mode waveguides with the FG-nucleoporin Nsp1. This approach enables the measurement of single-molecule translocations through individual pores using optical detection. We probe the selectivity of Nsp1-coated pores by quantitatively comparing the translocation rates of the nuclear transport receptor Kap95 to the inert probe BSA over a wide range of pore sizes from 35 nm to 160 nm. Pores below 55 ± 5 nm show significant selectivity that gradually decreases for larger pores. This finding is corroborated by coarse-grained molecular-dynamics simulations of the Nsp1 mesh within the pore, which suggest that leakage of BSA occurs by diffusion through transient openings within the dynamic mesh. Furthermore, we experimentally observe a modulation of the BSA permeation when varying the concentration of Kap95. The results demonstrate the potential of single-molecule fluorescence measurements on biomimetic NPCs to elucidate the principles of nuclear transport.

This chapter has been published at *eLife* as Nils Klughammer*, Anders Barth*, Maurice Dekker, Alessio Fraggasso, Patrick R. Onck and Cees Dekker, Diameter Dependence of Transport through Nuclear Pore Complex Mimics Studied Using Optical Nanopores. *eLife*, 2023, 12. <https://doi.org/10.7554/eLife.87174>

4.1. INTRODUCTION

The nuclear pore complex (NPC) forms the sole connection across the nuclear envelope that regulates all transport between the cytoplasm and nucleus. The central channel of this large protein complex (52 MDa in yeast to about 120 MDa in humans, [1, 2]) is lined with intrinsically disordered proteins that are rich in phenylalanine–glycine (FG) repeats, termed FG-Nups. The central transporter mesh constituted by these FG-Nups forms a selective barrier that facilitates the transport of dedicated nuclear transport receptors while blocking other proteins [2]. Recently, it has been discovered that the inner diameter of the central transporter is variable and can dilate from 40 nm to 70 nm under different stress conditions [3, 4]. How NPC dilation affects the efficiency and selectivity of nuclear transport remains an open question.

Despite extensive structural knowledge of the NPC scaffold, the mechanism of the selective barrier formed by the disordered FG-Nups remain highly debated [5–7]. Remarkably, the NPC poses this selective barrier while enabling very high transport rates of ~1000 molecules per second that traverse the pore, referred to as the ‘transport paradox’ [8]. Whereas small molecules pass through the NPC channel without much obstruction, translocation of larger biomolecules is increasingly hindered in a continuous manner above a diameter of ~5 nm or a mass of ~30 kDa to ~40 kDa which leads to an effective blockade for large molecules unless they specifically interact with the FG-Nups mesh [6, 9–12]. The efficient transport of large cargoes that carry a nuclear localization signal is facilitated by nuclear transport receptors (NTRs) which engage in multivalent interactions with the FG-repeats in the central transporter [13]. One of the most studied systems is the Kap95–Kap60 system in yeast (*Imp β –Imp α* in humans), responsible for the import of proteins into the nucleus [14].

Over the years, many models have been proposed to explain the selective properties of the central transporter, often originating from *in vitro* studies of isolated FG Nups [15–23]. Following early models that explained the selectivity solely based on the properties of the FG Nups, more recent ‘Kap-centric’ models suggested a central role of NTRs as an active component of the selective barrier [19–21, 23, 24], supported by the presence of a large amount of strongly interacting transport receptors within the central transporter that engage in multivalent interactions with the FG repeats [2]. This ‘slow phase’ shows reduced mobility due to the high affinity of NTRs to the FG-Nup mesh. As the FG-mesh is saturated with NTRs, a mobile phase of NTRs emerges [19] that is thought to diffuse along dedicated channels. So far, however, the dependence of transport rates and selectivity on the concentration of NTRs has hardly been studied directly.

Much research on the transport mechanism is carried out using *in vitro* experiments, since direct studies on the native NPC in its full complexity remain challenging. Using minimal biomimetic systems, it has been shown that a selective barrier with similar properties as the native NPC can be reconstituted using even a single native FG-Nup [17, 25–30] or artificial mimics thereof [31, 32]. Probing translocations through the FG-Nup mesh using solid-state nanopores grafted with FG-Nups was pioneered by [25] using optical detection of fluorescently tagged molecules. However, this approach was limited to bulk measurements of transport through porous membranes that contained many such pores in parallel, thus lacking single-pore and single-molecule resolution. This limitation was subsequently addressed by measuring the electric current through

individual functionalized SiN_x nanopores [26, 27, 31]. While this approach offers single-molecule sensitivity, the current-based readout remains unspecific (i.e. cannot distinguish different proteins), requires the application of a bias voltage which may influence the transport rate and speed of the translocations, and offers limited signal-to-noise ratio. It remains therefore restricted to pore sizes around 30 nm to 50 nm where the translocation of single molecules leads to a detectable current drop. For larger pores, the relative current blockage caused by a translocating molecule is too small compared to the noise, while the conductance of smaller coated pores is too low to detect translocation events.

Here, we implement a fluorescence-based assay for the simultaneous detection of single-molecule translocations of different molecular species through solid-state metal nanopores made of palladium, based on our previous work [33]. The translocation of individual molecules that were fluorescently labeled is monitored by a focused laser beam at a single nanopore which selectively excites molecules that exit from the pore (Figure 4.1 A). By labeling different molecular species with different fluorophores, the species can be distinguished in their signal. The <200 nm nanopores act as zero-mode waveguides (ZMW, [34]) that block the propagation of the 485 nm to 640 nm wavelength excitation light through the metal membrane. Such ZMWs have been used on top of glass surfaces [34–36] but also in a freestanding manner [33, 37, 38] which we chose in this study as well. Notably, our method does not require a bias voltage as it relies solely on the free diffusion of the fluorescent molecules, nor does the detection efficiency depend on the pore diameter. We developed robust protocols for efficient passivation of open pores and functionalization of the palladium surface with the FG-Nup Nsp1 to build a functional NPC mimic. After establishing a baseline for the translocation of fluorescently labeled proteins through open pores, we probe the selectivity of the biomimetic NPCs over a range of pore diameters from 35 nm to 160 nm by comparing the event rates of the transporter Kap95 to that of the inert probe BSA. We find that the selectivity of Nsp1-coated pores decreases with pore diameter, with the main loss of selectivity happening at about a diameter of 55 nm. We observe that smaller pores were selective, because Kap95 proteins can efficiently cross the pore while BSA transport is hindered. For larger pores, transport selectivity is gradually lost as both Kap95 and BSA were observed to cross the pore. Coarse-grained molecular dynamics simulations reproduce these experimental findings and show that the loss of selectivity is due to the formation of voids within the Nsp1 mesh that fit BSA molecules. For small pores these voids are transient, whereas for large pores they become persistent and a central channel forms. Upon increasing the concentration of the transporter Kap95 in the experiment, we observe a moderate increase of the transport selectivity for pores with a diameter below 50 nm. Intriguingly, we find that the event rate of BSA translocations for large pores *increases* with Kap95 concentration, suggesting that filling the FG-Nup mesh with NTRs reduces the selective volume. These results highlight the potential of our approach to unravel the physical principles underlying nuclear transport.

4.2. RESULTS

4.2.1. FABRICATION, SURFACE GRAFTING, AND MEASUREMENT SETUP

Our experimental approach is based on a free-standing palladium membrane into which nanopores were drilled using focused ion beam (FIB) milling (Figure 4.1 B). Fabrication of the metal membranes was achieved by evaporating a layer of Pd onto a SiN_x membrane (20 nm thickness) that was subsequently removed by reactive ion etching (in a process that was slightly adapted from [33], see section [Fabrication of freestanding Pd ZMWs](#) for details). After processing, the Pd membrane had a thickness of ≈ 90 nm. To functionalize the metal surface we applied standard thiol chemistry which is well established for metals such as gold or palladium [39, 40]. After the FIB-milling step, a cleaning step was required to remove impurities from the Pd surface prior to thiol binding to ensure efficient surface grafting. Since previous protocols relied on freshly prepared surfaces, we developed a gentle cleaning protocol that used either hydrogen peroxide or boiling ethanol, inspired by Majid *et al.* [41] (see Methods and Appendix 4.6.1). The cleaning step ensured that the Pd surface was competent for thiol binding, as validated by quartz crystal microbalance with dissipation monitoring (QCM-D) experiments (see Appendix 4.6.2 — Figures 4.1–4.3) and surface plasmon resonance measurements [42]. We additionally confirmed that the cleaning procedure does not alter the pore shape or closes the pores by transmission electron microscopy (TEM), cf. images shown at [43]).

To prevent unspecific sticking of proteins to the metal surface, the control open pores were passivated using 1-mercaptoundec-11-yl)hexa(ethylene glycol) (MUHEG), which forms a self-assembled monolayer by thiol-Pd binding enhanced with a dense packing due to the hydrophobic interactions between the alkane groups while providing a hydrophilic surface through the terminal hexaethylene glycol groups [44] (Figure 4.1 A, top). Coating of the biomimetic pores was performed with Nsp1 containing a C-terminal cysteine at a concentration of 1 μ M. We expect a lower limit for the grafting distance in the pore of 6.5 nm as measured previously by surface plasmon resonance experiments on flat gold surfaces [24]. Additional passivation of the remaining free area between Nsp1 molecules was achieved using short thiolated 350 Da PEG molecules [25, 45] (Figure 4.1 A, bottom).

After functionalization, the palladium membrane was mounted in a flow cell made of polydimethylsiloxan (PDMS) which provides a reservoir on the upper side for the addition of analyte, as well as a flow channel on the lower detection side to which a constant flow was applied to avoid accumulation of fluorescently labeled molecules (Figure 4.2 A). By diffusion, single proteins travelled through the pore upon which their attached fluorophore got excited by the laser. The fluorescence signal of molecules exiting the pore on the lower side was measured using a two-color confocal fluorescence microscope. A high-numerical aperture objective lens with a long working distance was used to focus the picosecond pulsed lasers in a diffraction-limited spot on the pore exit. The fluorescence signal was detected on single-photon avalanche photodiodes after passing through a pinhole and bandpass filter. For accurate and unbiased detection of the signal spikes originating from single-molecule translocation, we adapted a change point detection algorithm [46] that takes full advantage of the single photon information, as described previously in [33]. To avoid biases in the event detection, we ensured that experimental parameters such as the event duration and the photons per molecule did not

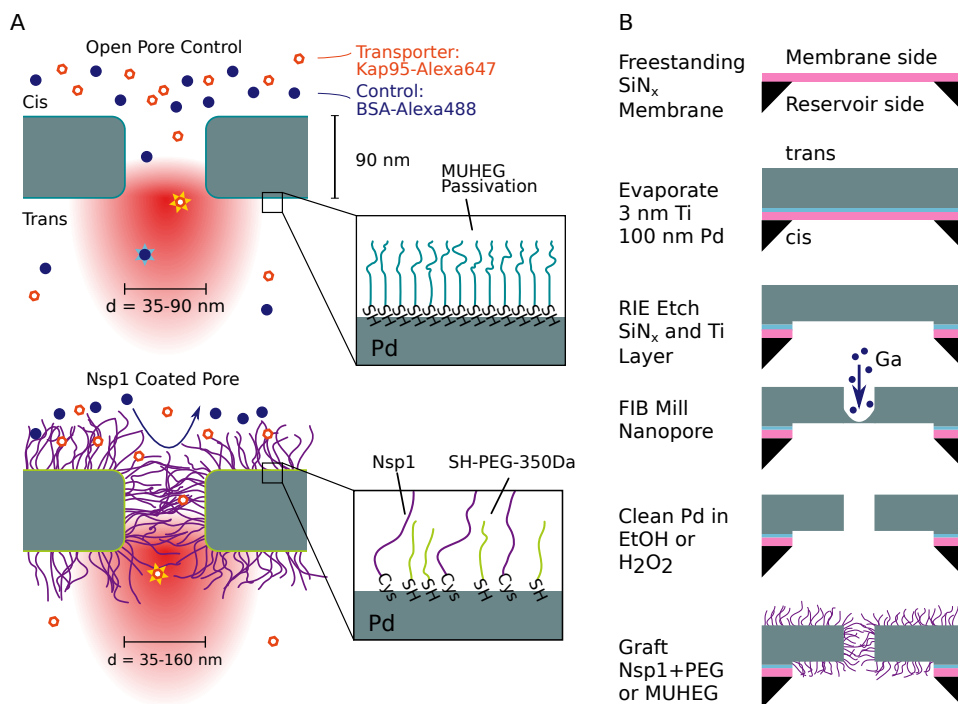


Figure 4.1: Experimental principle and nanofabrication. (A) Sketch of the experimental principle. Nanopores in a metal membrane block light from traversing if the pore diameter is small compared to the wavelength of light. The selectivity of Nsp1-coated metal nanopores is probed by measuring the translocation rate of fluorescently labeled proteins from the top reservoir (cis) to the detection (trans) side, where they rapidly diffuse out of the laser focus. Measurements on open pores (top) serve as a control where both the NTR Kap95 and the inert protein probe BSA pass unhindered. Nsp1-coated pores are expected to block the translocation of BSA while still allowing Kap95 to translocate. Zooms at bottom right illustrate the passivation of open pores with MUHEG (top) and functionalization of the palladium surface with the FG-nucleoporin Nsp1 and 350 Da SH-PEG (bottom), achieved via thiol-palladium chemistry. (B) Fabrication of nanopores in a free-standing palladium membrane was performed by physical vapor deposition of palladium onto silicon nitride (SiN_x), reactive ion etching (RIE), and focused-ion-beam (FIB) milling of the nanopores. The palladium surface was then cleaned either with H_2O_2 or ethanol to remove contaminants before the functionalization step.

vary between experiments, e.g. due to variations of the laser intensity or setup alignment (see [Data analysis](#) for more details). Note that the applied pressure induces a hydrodynamic flow that acts against the concentration gradient and results in an approximate reduction of the measured event rates by 5% ([subsection 4.6.4](#) — [Figure 4.10](#)).

The metal membrane was thick enough to prevent the incident laser light from reaching the other side, which served to suppress the background fluorescence coming from the reservoir side. Additionally, the nanopore acted as a zero-mode waveguide (ZMW), resulting in an evanescent wave within the pore that exponentially decays on a length scale of 10 nm to 20 nm, depending on the pore size [34]. To obtain more detailed insights into the optical properties in the proximity of the freestanding ZMW, we performed finite-difference time-domain simulations of the excitation electric field intensity

and fluorescence emission (Figure 4.2 C,D and Appendix 4.6.3 — Supplementary Figure 4.4).

As expected, the propagation of the excitation light is effectively blocked by the nanoperture and the electric field intensity $|E|^2$ decays exponentially within the nanopore. Interestingly, the presence of the reflecting metal surface also affects the intensity distribution further away from the nanopore, leading to the formation of a standing wave pattern. This effect is most visible for plane wave excitation (see Appendix 4.6.3 — Supplementary Figure 4.6), but is also present for focused excitation (Figure 4.2 C and Appendix 4.6.3 — Supplementary Figure 4.5). Molecules exiting the pore were hence mostly detected in the first lobe of the excitation profile and will likely diffuse away laterally before reaching intensity maxima further away from the membrane. To fully model the detected fluorescence signal $S(z)$, it is necessary to account for the modulation of the fluorescence quantum yield due to enhancement of the radiative and non-radiative rates by the metal nanostructure, as well as for the fraction of the signal that is emitted towards the upper side and thus cannot be detected (see Methods and Appendix 4.6.3 — Supplementary Figure 4.7). This further improves the blocking capability of the ZMW such that background signal from the reservoir is effectively suppressed even for large pores of 150 nm diameter (Figure 4.2 D and [47] for a more detailed discussion). The detected fluorescence signal thus originates predominantly from molecules that exit from the pore and diffuse into the surrounding solution, which were excited by the truncated excitation volume below the pore.

Since the nanopores block the propagation of the excitation light across the membrane, they were not visible in a bright-field optical image. To facilitate the precise localization of the nanopores, we hence added a grid of *partially* milled markers centered around each pore that were easily visible on the microscope (Figure 4.2 B). To improve the throughput of the measurements, a linear array of eight pores of varying size was milled into the palladium membrane, and these pores were probed consecutively during the experiments. Crosstalk between pores was minimized by applying a flow orthogonal to the pore array, resulting in a false detection rate of less than 2% (Appendix 4.6.4).

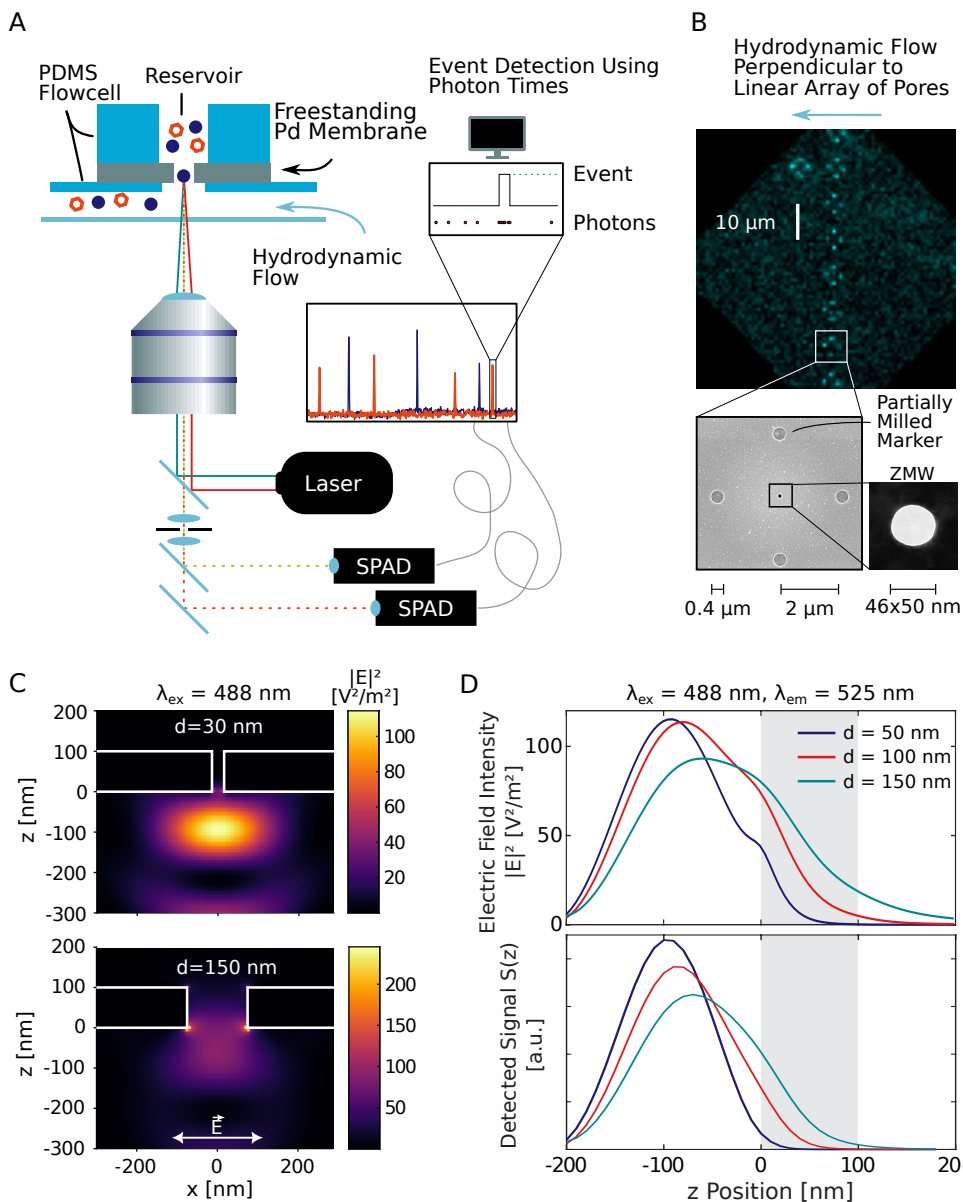


Figure 4.2: Experimental setup. (A) A free-standing Pd membrane containing the nanopores was mounted on a confocal microscope using a PDMS flow cell with a reservoir of $\approx 3 \mu\text{L}$ on the dark (cis) side and a flow channel on the detection (trans) side that faced the objective lens. A constant flow in the channel avoided the accumulation of analytes on the detection side. The lasers were focused onto the nanopore by a high NA objective lens and the fluorescence signal was detected on single-photon avalanche photodiodes. From the recorded photon arrival times, fluorescence bursts were detected using a change point detection algorithm. (B) A total of eight pores were milled into the Pd membrane, each surrounded by partially milled markers that facilitate the localization of the nanopores in a bright-field image (top). An additional marker was added such that the individual pores in the array could be identified. A scanning electron microscope image of a single pore with markers is shown below. The size and shape of each ZMW pore used in this study was determined using transmission electron microscopy (bottom right). (C) Simulated electric field intensity distributions in the xz plane near a freestanding ZMW for pore diameters of 30 (top) and 150 nm (bottom). A Gaussian laser beam was focused on the pore at a wavelength of 488 nm, polarized in the x -direction. See Appendix 4.6.3 — Supplementary Figure 4.4 for different pore sizes and excitation at 640 nm. (D) Electric field intensity $|E^2|$ (top) and total detected signal $S(z)$ (bottom) as a function of the z -position along the center of the pore for an excitation wavelength of 488 nm and an emission wavelength of 525 nm, corresponding to the blue detection channel, for pores of 50, 100, and 150 nm diameter. The palladium membrane is indicated by the gray shaded area. See Appendix 4.6.3 — Supplementary Figure 4.7 for the corresponding plots for the red channel.

4.2.2. NPC MIMICS SHOW TRANSPORT SELECTIVITY

To illustrate the workflow for estimating the transport selectivity of Nsp1-coated pores, we first describe our experiments on a pore with a diameter of 50 nm for which selectivity has previously been reported with Nsp1 in conductance measurements [27] as shown in Figure 4.3 A,B. The recorded time traces of Kap95 labeled with the Alexa Fluor 647 dye (Alexa647, orange) at a concentration of 100 nM and BSA labeled with the Alexa Fluor 488 dye (Alexa488, blue) at a concentration of 250 nM show efficient translocations for both proteins through the open pore (Figure 4.3 C). While Kap95 still translocated through the Nsp1-coated pore at a high rate, BSA was clearly hindered as is evident from the reduction of the number of signal spikes in the time trace (Figure 4.3 D).

For each pore, we probed a total of three different concentrations of BSA (0 nM, 250 nM, 500 nM) and Kap95 (0 nM, 100 nM, 1000 nM), and all combinations thereof. This resulted in nine different conditions that were tested consecutively (see Figure 4.3 E–F, bottom), which allowed us to assess the linearity of the measured event rates with respect to the analyte concentration. Since Kap95 interacts strongly with the Nsp1 mesh, we performed a step-wise increase of the Kap95 concentration throughout the measurement while probing the BSA response at every step (see Appendix 4.6.8). Importantly, this scheme enables us to test the influence of the Kap95 concentration on the event rates of BSA, as will be discussed below.

The measured event rates for Kap95 and BSA at the probed concentrations are shown in Figure 4.3 E–F, confirming the reduction of the BSA translocation for the Nsp1-coated pore. To quantify the selectivity, we computed the concentration-normalized event rate k_{Kap95} or k_{BSA} in units of Hz/nM as the average over all probed conditions and corrected for the degree of the fluorescent labeling (1 for BSA and 0.7 for Kap95, Figure 4.3 G). Finally, we define the selectivity of the pore as the ratio of the average normalized event rates for Kap95 and BSA, $\frac{k_{\text{Kap95}}}{k_{\text{BSA}}}$, which should be independent of the pore diameter for open pores. High selectivity values indicate that Kap95 translocates at a higher rate compared to BSA. For the open pore, we find an selectivity of 0.73 ± 0.05 . A selectivity value

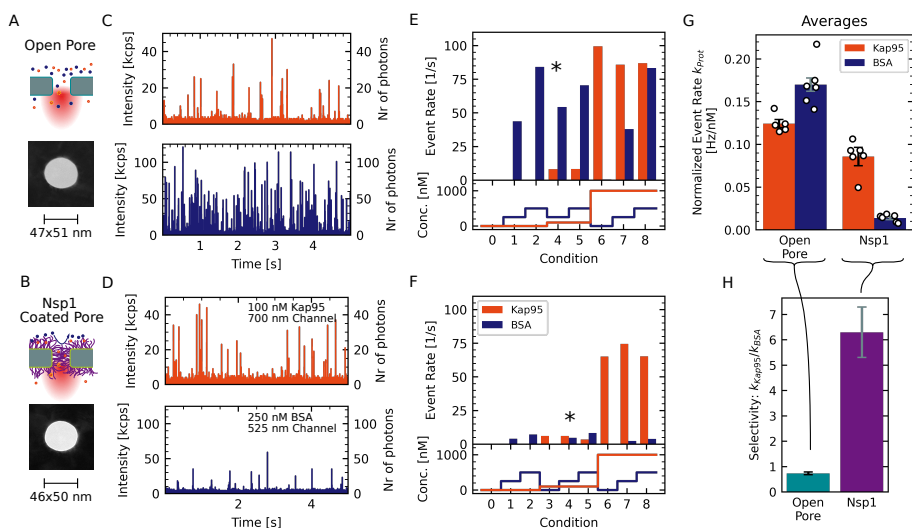


Figure 4.3: Experimental workflow for measuring the selectivity of Nsp1-coated nanopores. (A, B) Two pores of approximately 48 nm diameter were coated with MUHEG (A) or functionalized with Nsp1 (B). Pore dimensions were measured from TEM micrographs. (C, D) Fluorescence time traces recorded for the open and Nsp1-coated pores that are shown in A and B for Kap95–Alexa647 at 100 nM (red) and BSA–Alexa488 at 250 nM (blue). Both proteins were present at the same time. Whereas the Kap95 signal is comparable between the open and Nsp1-coated pores, a clear decrease of the BSA event rate is evident for the Nsp1-coated pore. (E, F) Measured event rates (top panel) resulting from the analyte concentrations for the different conditions probed sequentially during the experiment (bottom panel; see Appendix 4.6.8 for details). The concentrations used in the time traces shown in C and D are indicated with an asterisk. (G) In order to compare the different conditions, the obtained event rates are normalized to the respective protein concentration and corrected for the labeling degree (white dots in G). Bars indicate the average normalized event rates k_{Kap95} or k_{BSA} of the pore. Error bars represent the standard error of the mean. (H) The selectivity was calculated as the ratio of the average normalized event rates $\frac{k_{\text{Kap95}}}{k_{\text{BSA}}}$. Errors are propagated from the data shown in G. The data show a clear selectivity of the Nsp1-coated pore compared to the open pore.

between 0.7 and 0.8 is expected due to the smaller size and thus faster diffusivity of BSA, leading to a higher translocation rate compared to Kap95 (see Appendix 4.6.9 — [Supplementary Figure 4.12 E](#)). By contrast, the Nsp1-coated pore shows a significantly higher value of 6.3 ± 1.0 , indicating a clear selectivity induced by the Nsp1 coating.

4.2.3. SELECTIVITY IS LOST AT LARGE PORE DIAMETERS

Given recent reports on the dilation of the NPC central channel under stress conditions [3], we set out to investigate the dependence of the transport selectivity on the pore diameter. Importantly, our approach allows us to measure pore sizes well above 60 nm that were previously inaccessible in conductance-based experiments [26, 27, 31]. We measured the normalized event rates and apparent selectivity of a total of 46 pores with diameters ranging from 35 nm to 160 nm, which were either open or coated with Nsp1 (Figure 4.4). Note that for pores above 80 nm diameter, it was necessary to reduce the fraction of labeled proteins five-fold in order to avoid too high event rates that

would lead to non-linearity in the event detection due to overlapping events. This dilution is accounted for in the reported normalized event rates. We made sure that all data sets showed the same average molecular brightness (i.e., fluorescence signal per molecule). Data sets with lower average molecular brightness, which could occur due to sub-optimal alignment or trapping of air bubbles in the flow cell, were removed from further analysis (see [Data analysis](#) for details).

We measured protein translocation rates versus pore diameter for transport of both Kap95 and BSA through both open pores and Nsp1-coated pores, see [Figure 4.4](#). According to Fick's law of diffusion, the absolute translocation rate κ_{Prot} is expected to scale linearly with the concentration difference Δc between the cis and the trans side, and with the diffusivity of the probe, D . Additionally it scales linearly with the cross-sectional area of the pore, given by $A = \pi r^2$ and thus it scales quadratically with the pore radius r . Further on, it scales inversely with the length of the pore, L . This results in a protein dependent translocation rate,

$$\kappa_{\text{Prot}} = AD \frac{\Delta c}{L} = \pi r^2 D \frac{\Delta c}{L}. \quad (4.1)$$

As a guide to the eye and for numerical comparison, we fitted the normalized event rates versus pore radius with such a quadratic function,

$$k_{\text{Prot}} = \alpha (r - r_{\text{Prot}})^2, \quad (4.2)$$

where k_{Prot} is the concentration-normalized event rate, r is the pore radius, and r_{Prot} is the radius of the protein (Kap95 in this case). Note that this equation accounts for a reduction of the effective cross-sectional pore area due to the fact that a protein has a finite volume and hence its center can not fully reach the rim of the pore. The only free parameter in the model is the multiplicative scaling factor α which combines the effects of the pore length, concentration gradient, and protein diffusivity, as well as any experimental factors arising from event detection and protein-pore interaction (see [Appendix 4.6.10](#) for further details). Note that this simple model does not include the pore diameter-dependent reduction of the diffusivity due to confinement [\[48\]](#) which is discussed in [Appendix 4.6.9](#).

For Kap95, the translocation rate through Nsp1-coated pores was reduced by only about 10 percent compared to open pores, see [Figure 4.4](#) and [Appendix 4.6.10 — Supplementary Figure 4.14 E](#). In other words, we observed *no* significant reduction of the normalized event rate for Nsp1-coated pores compared to open pores ([Figure 4.4 A,C](#)). While this is remarkable, since one might a priori expect a reduction of the rate as an Nsp1-filled pore might obstruct protein transport, this finding signals the optimized properties of the Kap95 that interacts in a highly dynamic way with the FG repeats in Nsp1, which facilitate efficient transport. Our finding is in agreement with previous results on pores smaller than 30 nm [\[25\]](#). Interestingly, we also observed no reduced diffusivity of Kap95 molecules on the pore exit side, as quantified by fluorescence correlation spectroscopy (FCS) ([Appendix 4.6.11 — Figure 4.15 A,B](#)). However, we observed a shortening of the fluorescence lifetime of Kap95–Alexa647 for Nsp1-coated pores compared to open pores, which was not observed for BSA–Alexa488 ([Appendix 4.6.11 — Figure 4.15 C,D](#)). As the fluorescence lifetime is shortened in the proximity of the metal nanostructure

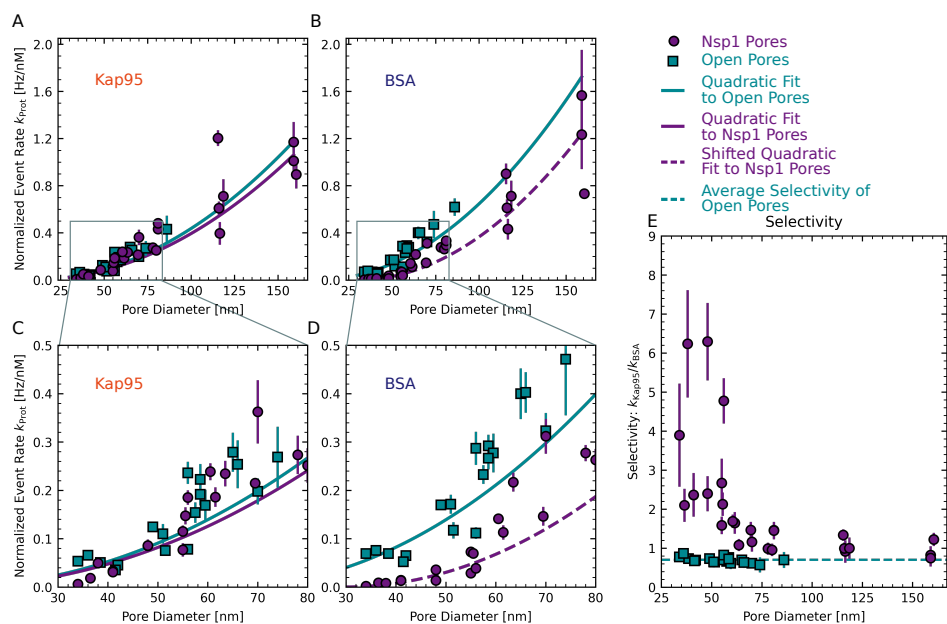


Figure 4.4: Dependence of translocation rates and selectivity on pore diameter (A–D) Concentration-normalized event rate of Kap95 (A) and BSA (B) as a function of pore diameter for open pores (cyan squares) and Nsp1-coated pores (purple circles). While the normalized event rate for Kap95 did not change significantly between open and Nsp1-coated pores, a clear reduction was observed for BSA, which was most pronounced at small pore sizes. Solid lines are fits to a quadratic function given in Equation 4.2. To model the size dependence of BSA translocations through Nsp1 pores, an offset was introduced that shifts the onset of the quadratic curve to higher diameters (dashed line, Equation 4.3). (C, D) Zoom-ins of the indicated regions in A,B. In A–D, the error bars represent the standard error of the mean of the normalized event rates obtained at different protein concentrations. (E) Apparent selectivity versus pore diameter. The data show that selectivity was lost for Nsp1-coated pores with increasing diameter. The average selectivity for open pores of 0.70 ± 0.01 is shown by the dashed cyan line. Error bars indicate the propagated error from the normalized event rates shown in A–D.

(see Appendix 4.6.3 — Supplementary Figure 4.7), this indicates that, on the exit side, Kap95 diffuses closer to the pore walls compared to BSA due to interactions with the Nsp1 mesh.

For BSA, the normalized event rates for Nsp1-coated pores were, by contrast, significantly reduced, especially at small pore diameters (Figure 4.4 B,D). More specifically, we observed an approximate 10-fold reduction of the event rate for Nsp1-coated pores with a diameter of 35 nm, whereas only a two-fold reduction was observed for pores with a diameter of 100 nm, which further decreases for larger pores (Appendix 4.6.10 — Supplementary Figure 4.14 E). Normalized event rates for open pores were well described by the quadratic function Equation 4.2. However, the BSA data for Nsp1-coated pores could not be described using the quadratic dependence with a single scaling factor over the whole range of pore diameters due to the steep increase of the event rate for larger pores (Appendix 4.6.10 — Supplementary Figure 4.14 B,D). We hence introduced an ad-

ditional fit parameter b , which shifts the onset of the curve to higher pore diameters:

$$k_{\text{Prot}} = \alpha (r - r_{\text{Prot}} - b)^2. \quad (4.3)$$

The parameter b reduces the effective pore diameter accessible to BSA and can be seen as an estimate of the amount of Nsp1 inside the pore. From the fit, we obtained $b = 11.5 \pm 0.4$ nm (error is SD estimated from the fit), which indeed is comparable to the height of Nsp1 brushes on flat surfaces [49].

Next, we calculated the selectivity ratio $\frac{k_{\text{Kap95}}}{k_{\text{BSA}}}$ to facilitate a direct comparison of pores with different diameters (Figure 4.4 E). For open pores, we find a selectivity ratio of 0.70 ± 0.02 , independent of the pore diameter. This agrees well with predicted selectivity values of 0.7 to 0.8 for open pores, based on Fick's law for the different pore diameters (see Appendix 4.6.9 — Supplementary Figure 4.12). Note that the value of 0.70 deviates from 1 due to the different size of the two proteins which leads to different diffusion coefficients. For Nsp1-coated pores below 50 nm, selectivity ratios of individual pores ranged between 2.1 ± 0.4 and 6.3 ± 1.0 , which is three to nine times higher than for open pores. This observed selectivity for smaller pores originates predominantly from a blockage of BSA translocations by the Nsp1 mesh, while the Kap translocation rates remain largely unaffected. For pores larger than 60 nm, we see a gradual decrease of the selectivity ratio with increasing pore diameter from 1.7 ± 0.2 to a value of 0.7 ± 0.2 for the largest pores, that approaches the selectivity ratio of open pores. The finite selectivity for large pores suggests that the Nsp1 coating on the pore walls still hindered the translocation of BSA, even after most of the selectivity was lost. The remaining selectivity decreased gradually with the pore diameter because the relative amount of Nsp1 molecules per pore cross-sectional area is reduced, as will be discussed in more detail below.

While the event rates were adequately described by the quadratic function, we observed a large variability between pores of similar size, even for open pores (Figure 4.4 A–D). As the variation of the event rate of Kap95 and BSA showed a high degree of correlation (see Appendix 4.6.12 — Supplementary Figure 4.16), the spread of the selectivity ratio was markedly reduced for open pore experiments. However, the spread remained high for Nsp1-coated pores (Figure 4.4 E), which we estimate to be due to pore-to-pore variations of the grafting density. We note that the variability was not due to chip-to-chip variation as a similar spread is also seen within pores that were measured together on one chip in the same experiment (see Appendix 4.6.12 — Supplementary Figure 4.17).

4.2.4. COARSE-GRAINED MODELING REVEALS TRANSITION OF THE NSP1 MESH

To gain a microscopic understanding of the structure and dynamics of the Nsp1 meshwork, we performed coarse-grained molecular dynamics (CGMD) simulations of Nsp1-coated nanopores over a range of diameters and grafting densities. We used an earlier-developed residue-scale model [50–52] that has been used to study Nsp1-functionalized nanopores [24, 27, 53] and liquid-liquid phase separation of FG-Nups [52]. Within the microsecond time scale of our CGMD simulations, we found that passive diffusion of BSA through the nanopore channel was a rare event, especially at the smaller-size pores. To obtain statistically meaningful estimates of the translocation rates, we applied a void analysis method developed by [54]. Rather than explicitly simulating translocation events of BSA molecules through the Nsp1 mesh, we used this theoretical approach to predict

translocation rates based on the equilibrium fluctuations of the Nsp1 mesh in the absence of Kap95 or BSA. Because this method uses the entire simulation volume to characterize the energy barrier that a translocating protein such as BSA would need to overcome, the resulting event rates have much better statistical sampling than can be obtained from brute-force passive diffusion simulations. In brief, we estimated the energy barrier for the translocation of inert probes with the size of BSA from simulations of the Nsp1 mesh alone by quantifying the occurrence of openings ('voids') within the mesh that can accommodate the inert probe without steric clashes. The resulting probability distribution of the occupancy along the pore axis can then be converted into a potential of mean force (PMF) using Boltzmann inversion, which represents the energy barrier for translocation. From this, protein translocation rates were computed by relating the energy barrier to $k_B T$ using the Arrhenius relation.

We performed simulations of nanopores with a length of 90 nm and diameters in the range of 40 nm to 160 nm. Nsp1 proteins were anchored at their C-terminus to the interior wall of the nanopore scaffold in a close-packed triangular distribution (Figure 4.5 A). From the equilibrium trajectories, we computed the PMF and use that to estimate the energy barrier, ΔE , that BSA proteins need to overcome during translocation as the average value of the PMF at the center of the pore (Appendix 4.6.13 — Supplementary Figure 4.19). Translocation rates were then obtained using the Arrhenius relation:

$$k_{\text{BSA}} = k_{0,\text{BSA}} \exp(-\Delta E/k_B T), \quad (4.4)$$

where $k_{0,\text{BSA}}$ is a proportionality constant to match the experimental event rates for open pores (see Appendix 4.6.13 — Supplementary Figure 4.18). While $k_{0,\text{BSA}}$ is the same for open and Nsp1-coated pores of any diameter, ΔE is calculated for each individual pore using the void analysis method.

As the precise grafting density of Nsp1 proteins within the pore in the experiment is not known accurately, we treated it as the only tunable parameter in the simulations to match the experimental BSA translocation rates. Using a previously estimated grafting density of 1 Nsp1 per 28 nm² for 20 nm thick solid state nanopores [27], the calculated BSA translocation rates significantly underestimated the experimental values (not shown here), which prompted us to probe much lower grafting densities between 1 Nsp1 per 200–400 nm². The best match between the experimental and calculated BSA event rates over the whole range of probed diameters was obtained at a grafting density of 1 Nsp1 per 300 nm² (Figure 4.5 D and Appendix 4.6.13 — Supplementary Figure 4.20 A,B). Note that the estimated grafting density is approximately one order of magnitude lower compared to 20 nm-thick NPC mimics [27]. Yet, we still obtain comparable protein densities of 50–150 mg/mL because the relatively long channel of the ZMW pores prevents the Nsp1 molecules from spilling out of the pore as in the case for 20 nm thick SiN_x nanopores. Indeed, these FG-Nup densities are comparable to densities of 30–300 mg/ml found in simulations of full NPCs [51, 54].

The calculated BSA translocation rates continuously increased with increasing diameter and reproduced the trend of the experimental data well (Figure 4.5 C). Similar to the experimental data, we observed a delayed onset of the BSA translocation rate for Nsp1-coated pores with an offset of 9.9 ± 0.1 nm, which compares quite well to the experimental value of 11.5 ± 0.4 nm. To compute the selectivity ratio from the BSA translo-

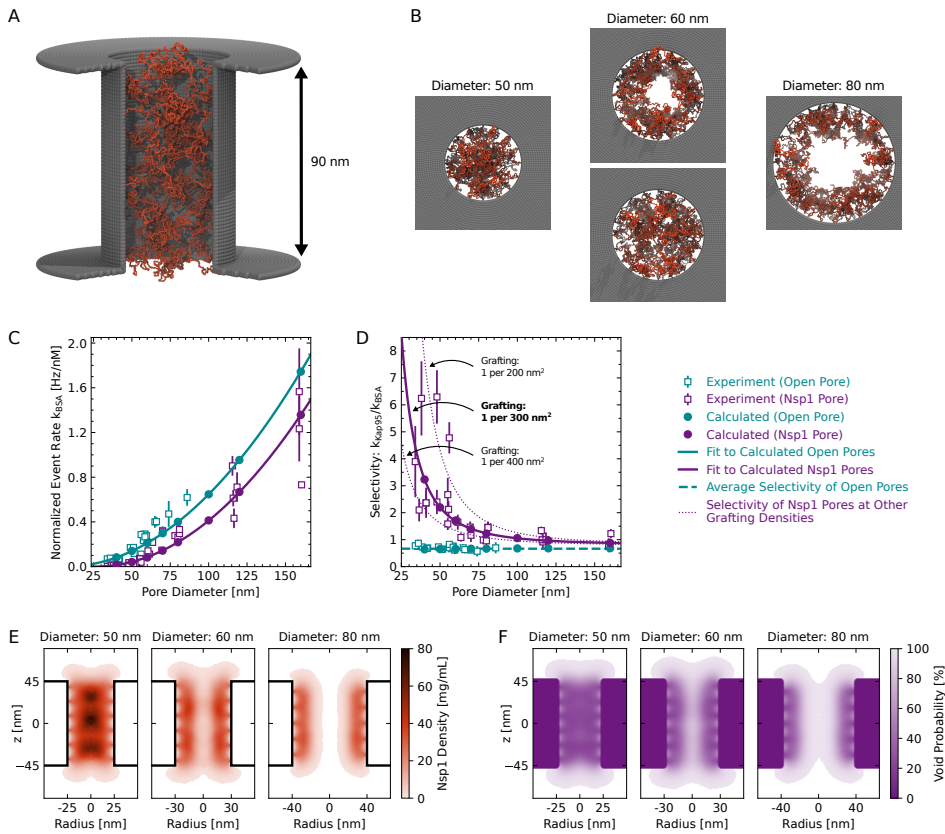


Figure 4.5: Coarse-grained modeling of Nsp1-coated pores. (A) One-bead-per-residue representation of an Nsp1-coated nanopore. (B) Top views of the Nsp1 meshwork in pores of 50 nm, 60 nm and 80 nm diameter (for a grafting density of 1 Nsp1 per 300 nm²). For pores with a diameter below 60 nm the Nsp1 meshwork was closed throughout the entire simulation, while for pores with diameters ≈ 60 nm transient openings were observed in the center of the pore, that were persistent for diameters ≥ 80 nm. Video online. (C) Calculated event rate of BSA as a function of pore diameter for open pores (cyan filled dots) and Nsp1-coated pores (purple dots) for a grafting density of 1 Nsp1 per 300 nm². The calculated event rates are in good agreement with the experimental event rates (open squares). Solid lines are fits to the calculated event rates using the quadratic function given in (4.2) for open pores and (4.3) for Nsp1-coated pores. (D) Calculated selectivity versus pore diameter, showing that the selectivity is lost for Nsp1-coated pores with increasing diameter. The average selectivity for open pores is shown as a green dashed line. The effect of grafting density on the apparent selectivity is indicated by the purple dotted lines that depict the results for grafting densities of 1 Nsp1 per 200 nm² and 1 Nsp1 per 400 nm² (see Appendix 4.6.13 — Supplementary Figure 4.20). (E) Axi-radial and time-averaged protein density distributions inside Nsp1-coated pores of 50 nm, 60 nm and 80 nm diameter at a grafting density of 1 Nsp1 per 300 nm². For pore diameters below 60 nm, we observed the highest protein density along the pore axis, while for diameters ≥ 60 nm, the highest density was found near the pore walls. This observation was valid for each of the probed Nsp1 grafting densities (see Appendix 4.6.13 — Supplementary Figure 4.21). (F) Axi-radial and time-averaged void distributions inside Nsp1-coated pores of 50 nm, 60 nm and 80 nm diameter at a grafting density of 1 Nsp1 per 300 nm². The void distributions suggest that for pores of 50 nm diameter there is no preferred pathway for the BSA proteins, while for larger pores the translocations happen mostly along the central axis.

cation rates, we assumed that the Kap95 translocation rate through Nsp1-coated pores is equal to that for open pores, as we did not observe any significant hindrance of Kap95 translocation by the Nsp1 mesh in the experiment (Figure 4.4 A,C). The computed selectivity ratios for a grafting density of 1 Nsp1 per 300 nm² are in good agreement with the experimental values (Figure 4.5 D), especially given that we basically only employ a single fitting parameter.

Similar to the experiments, we observed a strong decrease of the selectivity with pore diameter that gradually approached the open pore base line. Additionally, we found that the selectivity ratio is highly sensitive to variations of the grafting density, suggesting that the considerable variation in the experimental data might originate from variations of the grafting density between 1 Nsp1 per 200 nm² to 1 Nsp1 per 400 nm² (Figure 4.5 D).

The simulations provide a microscopic view of the structure of the Nsp1 mesh within the pore (Figure 4.5 A,B,E). At pore diameters below 60 nm, the Nsp1 mesh remained closed over the entire duration of the simulation and the highest protein density was found along the central axis. This is facilitated by the high cohesiveness of the N-terminal domains of Nsp1 which contain a large amount of hydrophobic amino acids [52]. For pore diameters above 60 nm, however, the highest protein density was found at the pore walls (Figure 4.5 E) and we observed the transient formation of a central channel that became persistent at pore diameters above 80 nm (Figure 4.5 B,E). Despite the transient appearance of a central channel at pore diameters of 60 nm and the shift of the highest protein density away from the center, the predicted translocation rates increased continuously and followed the quadratic model over the whole range of probed diameters (Figure 4.5 C). This finding is in contrast to an instantaneous onset of translocations as one might expect from a static opening of a central channel. As the pore diameter increased, the selectivity ratio became less dependent on the grafting density (Figure 4.5 D) because BSA translocated mainly through the wide central channel (Figure 4.5 B,C).

To estimate the pathways through which proteins can permeate the Nsp1 mesh, we determined the spatial distribution of the voids that can accommodate BSA, which represents the potential occupancy of BSA in the pore (Figure 4.5 F). For diameters below 60 nm, the distribution of the voids was homogeneous across the Nsp1 mesh, suggesting the absence of a preferred pathway. Surprisingly, the potential occupancy of BSA was not markedly reduced along the pore axis compared to the periphery, despite the high protein density in this region. For diameters above 60 nm, the distribution of voids closely followed the time-averaged protein density inside the pores, confirming that most BSA translocations occur through the central channel of the Nsp1 mesh. Although this central channel was not continuously present in the 60 nm pores, the void distribution confirms that most translocations still occurred through the center at this diameter.

4.2.5. KAP95 MODULATES THE PERMEABILITY FOR BSA

In the context of Kap-centric models of nuclear transport, it has recently been shown that depletion of Kaps from the FG-Nup mesh reduces the selectivity of the NPC in cells [55]. To test if a similar effect was present in our data, we averaged the concentration-normalized event rates for the two BSA concentrations (of 250 nM and 500 nM) measured at Kap95 concentrations of either 0 nM, 100 nM, or 1000 nM, and denoted them as $k_{\text{BSA},0}$, $k_{\text{BSA},100}$, and $k_{\text{BSA},1000}$ (Figure 4.6 A). To minimize the dependence of the rates on

the pore diameter, we assessed the relative rates with respect to the event rate in the absence of Kap95, $\frac{k_{\text{BSA},100}}{k_{\text{BSA},0}}$ and $\frac{k_{\text{BSA},1000}}{k_{\text{BSA},0}}$, which serve as a measure for Kap-induced changes of the permeability of the pore for BSA (Figure 4.6 B,C). In other words, a factor of 1 for this ratio would indicate that BSA transport does not depend on the Kap95 concentration.

We found no significant change of the BSA event rate at 100 nM Kap95 compared to the absence of Kap95 ($\frac{k_{\text{BSA},100}}{k_{\text{BSA},0}} = 1.2 \pm 0.1$) (Figure 4.6 B), which is similar to the value measured for open pores ($\frac{k_{\text{BSA},100}}{k_{\text{BSA},0}} = 1.3 \pm 0.1$). However, at a Kap95 concentration of 1000 nM, we observed a clear increase of the BSA leakage for pores larger than 60 nm ($\frac{k_{\text{BSA},1000}}{k_{\text{BSA},0}} = 1.6 \pm 0.2$), and a small reduction of the BSA translocation rates for smaller Nsp1-coated pores ($\frac{k_{\text{BSA},1000}}{k_{\text{BSA},0}} = 0.8 \pm 0.1$) similar to open pores ($\frac{k_{\text{BSA},1000}}{k_{\text{BSA},0}} = 0.9 \pm 0.1$), see Figure 4.6 C. The increase of the BSA translocation rate at a high concentration of Kap95 seems counter-intuitive given that the accumulation of Kap95 in the Nsp1 mesh is expected to obstruct BSA translocations by steric hindrance [23]. However, we thus observed the opposite effect, where a high concentration of Kap95 appeared to increase the event rates of BSA. Since this effect was not observed for open pores, it must have been induced by a rearrangement of the Nsp1 mesh.

Next, we computed the selectivity ratio based on the normalized event rates of BSA measured at the different Kap95 concentrations (Figure 4.6 D). Note that for the calculation of the selectivity ratio, we assumed that the normalized event rate of Kap95 is independent of the Kap95 concentration by using the average normalized event rate over all concentrations, k_{Kap95} , which is an approximation for the more complex behavior discussed in (Appendix 4.6.18 — Supplementary Figure 4.22). For small pores (<50 nm), we observed a moderate increase of the selectivity ratio at 1000 nM Kap95 compared to lower concentrations of Kap95 (Figure 4.6 E). Interestingly, we found an almost two-fold increase of the Kap95 translocation rate for small pores at 1000 nM compared to 100 nM, which was absent for large pores (see Appendix 4.6.18 — Supplementary Figure 4.22). Combined, the reduction of the translocation rate for BSA and the increase for Kap95 resulted in an increase of the apparent selectivity for small pores to 7.1 ± 1.6 at a Kap95 concentration of 1000 nM. No effect of the BSA concentration on the translocation rates of Kap95 was observed (Appendix 4.6.18 — Supplementary Figure 4.22). This suggests that the binding of Kap95 to the FG-Nup mesh increased the selectivity of Nsp1-coated pores, leading to a reduction of the BSA translocation rate, whereas no such effect was seen for open pores. In contrast, larger pores above 60 nm showed a lower selectivity at all Kap95 concentration compared to small Nsp1 pores (Figure 4.6 D). While this difference was small for Kap95 concentrations of 0 nM and 100 nM, a considerable reduction to almost the bare pore selectivity was observed for 1000 nM Kap95. After this initial step, we found a gradual decrease of the selectivity with the pore diameter, which is expected because the amount of Nsp1 deposited on the pore wall scales only linearly with the pore diameter while the pores cross-sectional area scales quadratically.

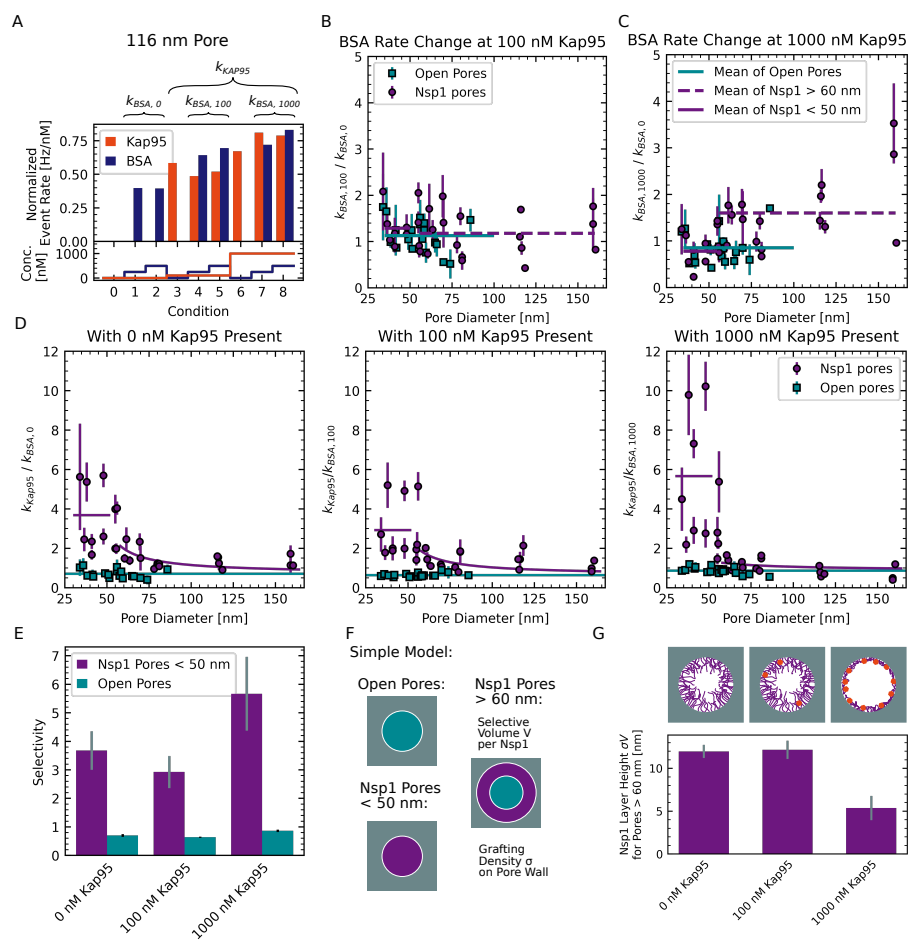


Figure 4.6: BSA permeation depends on Kap95 concentration. (A) BSA event rates measured at the different Kap95 concentrations of 0 nM, 100 nM, and 1000 nM were averaged to obtain the Kap95-concentration dependent event rates $k_{BSA,0}$, $k_{BSA,100}$ and $k_{BSA,1000}$. Data shown were obtained using an Nsp1-coated pore with a diameter of 116 nm. (B,C) Plots of the relative change of the BSA event rate measured at 100 nM and 1000 nM Kap95 compared to no Kap95, i.e. $\frac{k_{BSA,100}}{k_{BSA,0}}$ and $\frac{k_{BSA,1000}}{k_{BSA,0}}$, versus pore diameter. A considerable increase of the BSA event rate is observed for large pores in the presence of 1000 nM Kap95. (D) Plots of the selectivity ratio, defined as the ratio of the normalized BSA event rate measured at a given Kap95 concentration to the average normalized Kap95 event rate of the pore, i.e. $\frac{k_{BSA,i}}{k_{Kap95}}$ for $i = 0, 100$ and 1000 , against the pore diameter. The average selectivity ratio of open pores (cyan) and Nsp1-coated pore smaller than 50 nm (purple) are shown as a horizontal line. Data of large Nsp1-coated pores above 60 nm diameter were fitted to the selective area model function (purple lines, see Equation 4.5). (E) Average selectivity defined as $\frac{k_{BSA,i}}{k_{Kap95}}$ for open pores and Nsp1-coated pores below 50 nm. Error bars represent standard deviations estimated from fitting horizontal lines. A moderate increase of the selectivity of Nsp1-coated pores is observed at 1000 nM Kap95. (F) Simple model for the selectivity of Nsp1-coated pores. We assume large Nsp1-coated pores ≥ 60 nm to separate into unselective and selective areas with selectivities equivalent to that of open pores or small Nsp1-coated pores, respectively. (G) The parameter σV quantifies the thickness of the Nsp1 layer, which decreases in the presence of 1000 nM Kap95. Error bars represent standard deviations estimated from the fits.

As suggested by the MD simulations, the loss of selectivity for pores above 60 nm may be explained by the opening of a central channel that allows BSA to pass unhindered. To obtain an estimate for the size of such a channel, we devised a simple model to estimate the fraction of the cross-sectional pore area that is occupied by the selective FG-Nup phase (Figure 4.6 F). The selective area fraction was obtained from the measured selectivity ratio under the assumption that large Nsp1-coated pores are divided into selective and non-selective areas, where the selective area was assumed to have a selectivity equivalent to the value measured for small pores.

We related the selective area fraction to the structural change of the Nsp1 brush by assuming that each Nsp1 molecule renders a certain volume V selective. At a given grafting density σ on the pore wall of diameter r , the selective area fraction $\frac{A_{\text{Nsp1}}}{A}$ is then given by:

$$\frac{A_{\text{Nsp1}}}{A} = \frac{2}{r} \sigma V, \quad (4.5)$$

where the factor σV was the only fit parameter. The unit of the product σV is a length which can be related to the apparent Nsp1 layer thickness at the pore wall (see Appendix 4.6.19 for the details of the model). From the selective area fraction, we computed the apparent selectivity of a pore and estimated the factor σV by fitting it to the experimentally obtained selectivities (Figure 4.6 D and G). The estimated thickness in the absence of Kap95 of ~ 12 nm agrees well with measurements on flat surfaces [49]. While no significant change was detected at 100 nM Kap95, we observed a drastic decrease of the estimated layer thickness by a factor of ≈ 2 at 1000 nM Kap95 compared to the absence of Kap95 (Figure 4.6 G), suggesting that the Nsp1 layer collapsed as it was occupied by Kap95.

4.3. DISCUSSION

In this study, we present an assay to measure the selectivity of nanopore-based NPC mimics at single molecule resolution using optical detection. Our assay is based on nanopores drilled into freestanding palladium membranes that act as zero-mode waveguides to block the propagation of the excitation light. This allows the localized and selective detection of fluorescently labeled molecules that exit from the pore. We build on our previous work which established palladium nanopores as a viable tool for single-molecule studies [33] by functionalizing the nanopores with the FG-Nup Nsp1 to build a minimal biomimetic system of the NPC. To this end, we developed a gentle cleaning protocol that leaves the pore shape unaltered while rendering the metal surface susceptible for efficient thiol binding.

Our approach offers several advantages compared to conductance-based nanopore measurements [24, 26, 27, 31], namely a superior signal-to-noise ratio (see Appendix 4.6.4), an excellent specificity for the labeled analyte that enables simultaneous detection of different components, increased throughput by measuring multiple pores in a single experiment, no limitations on pore size, and the potential to add unlabeled components while still investigating their effects. Importantly, our approach also allows us to measure translocations by free diffusion in the absence of an external electric field which may potentially bias the experiment. Compared to previous optical approaches

[25], our assay offers the capability to follow single molecules through individual pores. On the technological side, one could increase the throughput of our approach by moving towards a camera-based readout which would enable the simultaneous reading of hundreds of pores. Despite the many benefits of our approach, some differences remain when comparing our biomimetic ZMW pores to the NPC, as e.g. the 90 nm long channel used here is approximately three times longer [2], and FG-Nups are grafted to the entire metal surface rather than being limited to the pore walls. In spite of these differences, the *in vitro* biomimetic approaches remain useful to study key elements of nuclear transport.

To evaluate the performance and sensitivity of our approach, it is relevant to compare the absolute event rates through open pores to theoretical expectations. Compared to Fick's law of diffusion, the absolute event rates for BSA and Kap95 through open pores were underestimated by approximately a factor of 3, as estimated from the scaling factors (Appendix 4.6.9 — [Supplementary Figure 4.12](#)). Additionally, we had previously found that repeated detection of the same molecule leads to an overestimation of the event rate compared to the actual translocation rate by approximately a factor of 2 [33]. Combined, this resulted in a ≈ 6 -times lower translocation rate compared to what is predicted from Fick's law, potentially due to the hydrodynamic pressure applied in our experiments [37], protein-pore interactions, and missing of low-signal events by the detection algorithm.

Compared to the study of Jovanovic-Talisman *et al.* [25], who report rate values of 0.003 Hz/nM obtained from bulk studies on 30 nm pores, we find an order of magnitude higher event rates of approximately 0.04 Hz/nM for pores of similar size. This discrepancy can be explained by the fact that the functionalized pores used by Jovanovic-Talisman *et al.* [25] were placed at the ends of 6 μm long channels which is expected to considerably reduce the translocation rates. When comparing with conductance-based nanopore measurements in 20 nm thick silicon nitride membranes, previous studies have reported rates of 0.0003 Hz/nM for 30 nm pores [31] and 0.00005 Hz/nM for 42 nm to 46 nm pores [26]. Both these values are many orders of magnitude lower compared to what is predicted by Fick's law, indicating that a large fraction of potential translocation events was previously not detected, cf. [56]. On the other hand, Ananth *et al.* [27] measured event rates of Kap95 through open 48 nm pores of 0.017 Hz/nM, which is much closer to our measurements of 0.08 Hz/nM compared to other conductance-based studies. The system in conductance-based experiments is more complex, however, with an interplay of diffusion and electro-osmotic and electro-phoretic forces. This illustrates that our optical approach offers a higher detection efficiency of translocation events and provides a better mimic of the diffusion driven transport through the real NPC, compared to conductance-based nanopore experiments.

We implemented an experimental scheme to assess the selectivity of single Nsp1-coated pores by measuring the concentration-dependent translocation rates of the inert probe BSA and the NTR Kap95. To elucidate the size dependence of the selectivity, we scanned a wide range of pore diameters from 35 nm to 160 nm, which was previously not possible in conductance-based approaches. We found a steep decrease of the selectivity with the pore diameter, where the BSA event rate approaches its open pore value for large pore diameters. For small diameters, the BSA event rate was decreased 10-fold compared to open pores, similar to a 5-fold decrease reported for pores smaller than

30 nm by Jovanovic-Talisman *et al.* [25]. For large pores, BSA translocation was only hindered by a factor of 1.4 (Appendix 4.6.10 — Supplementary Figure 4.14 E). On the other hand, translocation rates for Kap95 were unaffected by the Nsp1 coating (reduction factor of 1.1), in agreement with previous reports [25–27, 31]. Notably, our data reveals a gradual decrease of the selectivity rather than a threshold-like behavior, in line with the results of Jovanovic-Talisman *et al.* [25] who found a gradual decrease of the selectivity for three distinct pore sizes of 30 nm, 50 nm, and 100 nm.

Coarse-grained molecular dynamics simulations allowed us to reproduce the experimental selectivities for a grafting density of $1/(300 \text{ nm}^2)$. While this value is lower compared to previous reports on silicon nitride nanopores [31], we still achieve similar protein densities at the center of the 90 nm-long channel. Similar to the experimental data, the steepest decrease of the selectivity occurred at small diameters. In addition, simulations at varying grafting density revealed that stochastic variation of the surface grafting efficiency is a likely cause for the pore-to-pore variation of the event rates observed in the experiment. The simulations reveal the opening of a central channel in the Nsp1 mesh for pore diameters above 60 nm. However, the event rates predicted by the void analysis showed a continuous decrease of the selectivity with pore diameter even before a central channel was observed in the Nsp1 mesh. This suggests that the formation of a stable transport conduit is not required for the permeation of BSA through the Nsp1 mesh, but may also occur efficiently through transient openings. The absence of a discrete step in the experimental selectivity at a specific pore diameter is thus at odds with a static picture of either an extended or collapsed Nsp1-mesh but rather supports a dynamic transition between both states for intermediate pore diameters. For larger pore diameters, a central channel opened and only a peripheral ring was occupied by Nsp1. This occurred due to the following factors. First, the increased entropic cost of extension for the Nsp1 molecules to interact across the pore. Second, the amount of Nsp1 molecules per pore volume decreases with pore diameter, as the volume increases quadratically while the number of molecules increases linearly. Last, while increasing the diameter, also the curvature decreases which reduces the lateral constraint of neighbouring Nsp1.

We found experimentally that the main loss of selectivity falls in a size range between 40 nm to 60 nm. Intriguingly, it has recently been reported that the inner ring diameter of the NPC can be significantly larger in situ at 60 nm compared to 40 nm for isolated NPCs [4]. Furthermore, NPC dilation is modulated in cellulose in response to stress conditions such as energy depletion or osmotic shock [3]. This suggests that the dilation of the NPC might be a way for the cell to tune the permeability of the NPC under stress to increase the selectivity at the cost of lower transport rate.

In light of Kap-centric models of nuclear transport [5], we also tested the influence of the Kap95 concentration on the selectivity and permeability of Nsp1-coated pores. Small pores below 50 nm showed a moderate increase in selectivity at a Kap95 concentration of $1 \mu\text{M}$ compared to the absence of Kap95, caused by a slight reduction of the permeability of the pores for BSA. A comparable effect was described by Jovanovic-Talisman *et al.* [25], who found that the BSA flux through 30 nm pores halved when $2 \mu\text{M}$ of the nuclear transport factor NTF2 was present due to increased competition for the unoccupied space within the pore in the presence of transporters [23]. In contrast, we observed an almost 2-fold increase of the BSA translocation rate for large pores above 60 nm by in-

creasing the Kap95 concentration from 0 μM to 1 μM . This result seems counterintuitive considering that Kap95 occupancy within the pore should pose an additional hindrance for the translocation of BSA. Quantification of this effect, however, showed that the selective area fraction within the pore was significantly reduced at 1 μM Kap95, which we attribute to a compaction of the Nsp1 layer. From our data, we found a 2-fold reduction of the cross-sectional area of the Nsp1 layer inside the pore. A much smaller Kap-induced compaction of 16 nm high Nsp1 brushes on flat surfaces of <10% was observed in SPR measurements at a Kap95 concentration of 100 nM by Wagner *et al.* [49], where however only a fragment of the extended domain of Nsp1 was used. The stark change of the Nsp1 layer thickness seen in our experiments could be a consequence of the pore geometry, which resembles the actual NPC much better than flat surfaces. Here, our measurements on large pores above 100 nm diameter provide an effective bridge between nanopore studies and surface techniques such as QCM-D and SPR. Note that the reported height change of the Nsp1 brushes serves as an approximate quantification due to the high pore-to-pore variability in the dataset. Additionally, we acknowledge that 1 μM of Kap95 is still considerably below physiological Kap95 concentrations of around 4 μM [55], so it is hard to relate the effect we observed to the physiological NPC.

We have limited this study to a case study with single combination of FG-Nup (Nsp1) and NTR (Kap95), but our approach could easily be expanded to other FG-Nups, transporters, or control proteins. The NPC contains two main classes of FG-Nups that differ in their cohesiveness, amino acid composition and localization within the central channel. For instance, FxFG-type FG-Nups, such as Nsp1, contain mainly FxFG repeats and have a high content of charged amino acids in its extended domain. Consequently, they are more extended and do not phase separate [18, 52] but instead form percolating hydrogels at high concentration [16]. These FxFG-Nups are predominantly anchored on the nuclear and cytosolic side of the NPC, with Nsp1 being an exception that is also located in the center [2]. On the other hand, GLFG-type FG-Nups contain a low amount of charged amino acids and, as a result, are more cohesive and prone to phase separation [52, 57]. They are localized mainly at the central channel of the NPC, where they might be necessary to form the selective barrier [58, 59]. While we observed moderate selectivity ratios of 2 to 6 for Nsp1, we expect that more cohesive GLFG-type FG-Nups, such as Nup100 in yeast or Nup98 in humans, would form a tighter, more selective barrier with lower permeability for BSA. While we did not observe a significant obstruction of the diffusion of Kap95 through the Nsp1 mesh, the dense FG-Nup phase formed by GLFG-type FG-Nups could pose a tighter barrier for Kap95 diffusion. Recent efforts have also focused on designing FG-Nups with desired properties from the bottom up, where our assay could provide important information on the relation between protein properties and transport selectivity and kinetics [31, 32, 60].

Finally, our approach could be used to study the full systems for protein import or export with all required cofactors, including, for example, the Ran system that provides directionality to molecular transport across the nuclear envelope [14]. In particular, by using specific labeling coupled with multicolor detection it will be possible to simultaneously follow different components of the transport machinery, providing direct mechanistic insights into important steps of the transport cycle, such as cargo release or transport factor recycling. An open question in the field also regards how large cargoes such

as mRNA [61] or even viral particles [62–64] can pass through the NPC, which could be readily tested with our assay. We envision that NPC mimics based on metal nanopores will continue to provide important answers to key questions on the mechanism of nucleocytoplasmic transport.

4.4. METHODS AND MATERIALS

4.4.1. FABRICATION OF FREESTANDING Pd ZMWs

Fabrication of nanopores in freestanding palladium membranes was performed as shown in Figure 4.1 based on the procedures described in [33] with minor modifications. Freestanding 20 nm SiN_x membranes were manufactured as described in [65] and cleaned using oxygen plasma for 2 min at 100 W at an oxygen flow rate of 200 ml/min using a PVA Tepla 300 plasma cleaner. As an adhesion layer, 3 nm titanium was deposited onto the SiN_x membrane at 0.05 nm/sec under a base pressure of 3×10^{-6} torr in a Temescal FC2000 e-gun evaporator, immediately followed by a 100 nm layer of Pd at 0.1 nm/sec to 0.2 nm/sec with a base pressure below 2×10^{-6} torr without venting the chamber in between.

The SiN_x and Ti layers were removed by dry etching using CHF₃ at a flow of 50 SCCM and O₂ at a flow of 2.5 SCCM for 10 min at 52 W power in a Sentech Etchlab 200 plasma etcher, resulting in an effective chamber pressure of 1.2 Pa. To ensure that the SiN_x and Ti layers are completely removed, the etch time was chosen to partly etch into the Pd layer, resulting in a palladium membrane thickness of 90 nm after etching, estimated by cutting a slit into the palladium membrane using FIB milling and measuring the resulting wall thickness using an SEM on a FEI Helios G4 CX microscope. On the same FIB/SEM we developed a protocol to reproducibly mill circular nanopores into Pd membranes: After adjusting the eucentric height, the ion column for a 1.1 pA Ga beam at 30 kV acceleration voltage was automatically aligned on a reference sample of gold sputtered on carbon.

A test pore was then milled and inspected for circularity at high magnification using the immersion mode of the SEM. If the test pore was not circular due to astigmatism of the Ga beam, the ion column alignment was repeated. Linear pore arrays with surrounding markers were then milled on the membrane using an automatic script written in Nanobuilder. Individual pores were made at a distance of at least 9 μm, in order to avoid later cross talk between the individual pores during the experiment. An additional marker pattern without pore was added for the identification of individual pores on the membrane. Subsequently, each membrane was examined on a JEOL JEM-1400 transmission electron microscope (TEM) for integrity and the minimum and maximum diameter was determined for each pore from the TEM images. The two diameters typically differed by less than 10%. Pore sizes stated in this study are the arithmetic means of these two values.

4.4.2. CHEMICALS, PROTEIN PURIFICATION AND PROTEIN LABELING

MUHEG ((11-Mercapoundecyl)hexa(ethylene glycol)) with 90% purity (Sigma-Aldrich) was dissolved at a concentration of 200 mM in degassed ethanol. Aliquots were prepared under nitrogen atmosphere and stored at -20 °C until use. 350 Da thiol-PEG (Polyethy-

lene glycol) with more than 95% purity (Nanocs Inc., New York) was aliquoted under nitrogen atmosphere and stored at -20°C until use. Nsp1 protein (Appendix 4.6.20) was kindly provided by the Görlich lab (Göttingen, Germany) in lyophilized form and resuspended in denaturing buffer at $10\ \mu\text{M}$. For long term storage, samples were snap frozen in liquid nitrogen and stored at -80°C . Alexa488 labeled BSA was purchased from Invitrogen, Thermo Fisher. On average one BSA molecule was labeled with 6 Alexa488 molecules. It was diluted in PBS to a final concentration of $72.6\ \mu\text{M}$. The diluted sample was dialysed on ice using 10K Slide-A-Lyzer Dialysis Cassettes for 3 mL for 24 h, exchanging the 250 mL PBS dialysis buffer four times until no free fluorophores were detectable in the dialysis buffer in an FCS experiment. The protein solution was snap frozen in aliquots and stored at -20°C until use in the experiment. Unlabeled BSA was purchased from Thermo Fisher (Ultra Pure BSA (50 mg/ml), Invitrogen), diluted to 5 mg/ml split into aliquots, snap frozen and stored at -20°C until use in the experiment. Kap95 (Appendix 4.6.20) was purified as described previously [31] and C-terminally labeled with AZDye647, which is structurally identical to AlexaFluor647, using sortase-mediated ligation. Sortase labeling was performed following published protocols at 50-fold excess of the dye-triglycine conjugate (Click Chemistry Tools, USA) for 1 h at room temperature in Tris buffer (50 mM Tris, 150 mM NaCl, pH 7.4) [66]. Unreacted dyes were removed by size exclusion chromatography on a Superdex S200 column pre-equilibrated with PBS buffer. To fully remove free fluorophores, labeled Kap95 was further dialyzed as described above. We used two separate preparations of the labeled Kap95 with 70% and 62.5% degree of labeling and $16.8\ \mu\text{M}$ and $5.9\ \mu\text{M}$ stock concentrations. The stock solutions were split into aliquots and stored at -80°C after snap-freezing. The purity of Nsp1 and Kap95 samples was assessed using sodium dodecyl sulfate-polyacrylamide gel electrophoresis (SDS-PAGE).

4.4.3. CLEANING AND SURFACE GRAFTING OF PD

GRAFTING OF THIOLS TO PD SURFACE

In order to make Pd accessible for thiol binding, a cleaning procedure was performed. Two different cleaning methods were used depending on the grafting solution. For ethanol based grafting solutions we performed cleaning in hydrogen peroxide and for PBS based grafting solutions we performed cleaning in boiling ethanol.

For MUHEG grafting, chips were mounted in a custom built teflon holder, rinsed with DI water and submersed in $>99\%$ isopropylalcohol to remove bubbles. 30% hydrogen peroxide was brought to 45°C in a water bath. The chip was rinsed in DI water and then submersed in the hot H_2O_2 for 15 min. MUHEG solution was prepared by diluting stock solutions in absolute ethanol to a final concentration of $250\ \mu\text{M}$. The solution was sonicated for 5 min to 15 min at 20°C . The chip was taken out of the teflon holder, washed in DI water and submersed fully in the MUHEG solution for grafting. During the grafting, the chips were gently shaken over night at 450 rpm for 11 h to 22 h at 20°C . Before mounting, the chip was washed in ethanol for 15 min, dried under a stream of nitrogen and mounted within minutes after drying.

For Nsp1 grafting, chips were mounted in a teflon holder and rinsed with DI water. Pure Ethanol was heated in a water bath until boiling to 78° . The chip was submersed in boiling ethanol for 15 min and rinsed with DI water. Boiling ethanol was proposed

to efficiently remove organic residues from silver surfaces [41]. Nsp1 aliquots were diluted to 1 μM in PBS buffer. Tris-(2-Carboxyethyl)phosphine, Hydrochloride (TCEP, Supelco, Sigma-Aldrich) was added until a final concentration of 1 mM to reduce potential disulfide bonds. The solution was briefly vortexed and then incubated for 15 min at 20 °C. Chips were incubated in the Nsp1 solution for 1 h while shaking at 450 rpm. The chips were then transferred to a solution containing 2 mM 350-Da PEG in PBS buffer with 5 mM TCEP for 1 h. Before mounting, the chip was washed in PBS for 15 min by shaking at 450 rpm, subsequently rinsed with DI water and dried under a flow of nitrogen. The chip was reimmersed in buffer within minutes after drying.

QCM-D EXPERIMENTS

QSense Analyzer gold-coated quartz QCM-D chips were purchased from Biolin Scientific, Västra Frölunda, Sweden. Similar to the freestanding Pd membranes, a 3 nm titanium layer was deposited onto the Au surface at 0.05 nm/sec and a 100 nm layer of Pd was evaporated at 0.1 nm/sec with a base pressure below 2×10^{-6} torr in a Temescal FC2000 e-gun evaporator. The cleaned chips were mounted in the flow cell in dried state. The flow cell was filled with buffer or ethanol until a stable base line was detected, before the respective grafting solution was applied. The experiments were conducted at 21 °C. See Appendix 4.6.2 for details.

4.4.4. EXPERIMENTAL SETUP AND MEASUREMENT

Freestanding Pd membranes were mounted in a modified flow cell as described in [67] and are very comparable to what was used in [33]. The reservoir was made from a polydimethylsiloxane (PDMS) ring that was pressed onto the membrane chip. The reservoir volume was approximately 3 μL . To avoid cross-contamination, the reservoir ring was discarded after each experiment, while the flow channel on the detection side was reused several times.

After drying, the chips were immediately mounted within minutes such that the Pd membrane faced towards the flow channel and the microscope objective. Nsp1-coated chips were immediately immersed in PBS buffer and contact with ethanol was avoided. MUHEG coated chips were flushed with 1:1 ethanol:water mixtures to remove air bubbles. The conductance of the chip was measured using Ag/AgCl electrodes and an Axopatch 200B amplifier (Molecular Devices) to check that they were properly wetted. The flow cell was subsequently mounted onto the stage of the confocal microscope. We applied a flow to the channel on the detection side using a Fluigent Microfluidic Flow Control System to prevent the accumulation of fluorophores. We applied 50 hPa of pressure to a vessel directly connected via 1 m of tubing (Masterflex Microbore Transfer Tubing, Tygon ND-100-80) to the flow cell. The outlet of the flow cell was connected to another tubing of the same length. Due to symmetry, this results in an estimated pressure of 25 hPa at the location of the membrane. The flow of buffer was measured to be 0.7 mL h^{-1} . The applied pressure induces a hydrodynamic back flow through the pores against the concentration gradient, which results in an approximate reduction of the detected event rates of 5 % compared to the when no pressure is applied (Appendix 4.6.4 — Figure 4.10). We ensured that the flow was constant between different experiments such that the relative event rates remain unchanged. Experiments were performed at 21 ± 1 °C

in a temperature and vibration controlled room.

After positioning the membrane in the field of view, markers were localized using transmitted light and the laser focus was centered on the nanopore between the markers. Data was acquired on a Picoquant Microtime 200 microscope using the Symphotime software. We used a 60x Olympus LUMFLN60XW water immersion objective (NA 1.1) which provides a working distance of 1.5 mm to enable imaging of the mounted chip. Excitation lasers at wavelengths of 640 nm and 485 nm were operated in pulsed interleaved excitation at a repetition frequency of 40 MHz and 10 μ W power as measured at the imaging plane. Before each experiment, the collar ring of the objective was aligned by optimizing the molecular brightness of a solution of Alexa488 fluorophores. The emission light was passed through a 50 μ m pinhole, split by a dichroic mirror, and filtered by either a 600/75 or 525/50 optical band pass filters (Chroma, USA) before being focused on single-photon avalanche-diode detector (PD5CTC and PD1CTC, Micro Photon Devices, Italy).

For each experiment the same measurement scheme was followed as shown in [Figure 4.3](#) and described in detail in [Appendix 4.6.8](#). In this scheme, we continuously increased the Kap95 concentration during the experiment to avoid accumulation of Kap95 in the Nsp1 brushes. Before decreasing the BSA concentration, a wash with 5 % Hexane-1-6-diol was performed. For experiments involving pores of diameter larger than 70 nm, the labeled protein was mixed with unlabeled protein at a ratio of 1:4 to avoid that the event rate exceeded the detection limit. During the translocation experiment, the respective dilutions of proteins were prepared with PBS and kept on ice before pipetting them into the reservoir. After the experiment, translocations of free Alexa647 and Alexa488 were measured to exclude that pores were clogged (see [Appendix 4.6.4 — Supplementary Figure 4.9](#)).

4.4.5. DATA ANALYSIS

Event rate detection was performed using a custom written python script based on several packages [68–72]. The analysis pipeline was based on previously published work [33, 73] and is deposited in an open repository [74]. In brief, photon bursts were detected using a change point detection algorithm [46] that detects discrete changes of the photon statistics from the single-photon arrival times. Background events were discarded based on an empirical criterion. In previous work, we had interpreted subsequent events on the millisecond timescale as reentry events of the same molecule [33]. To avoid potential biases, no combination of closely spaced events was performed here. However, we could not exclude that molecules may re-enter the laser focus after translocation. Normalized event rates were calculated by dividing the measured event rate by the degree of labeling and the concentration of the respective protein. A purely statistical uncertainty of the event rate was estimated from the assumption that translocation events follow Poisson statistics.

Over the course of the study, several data sets had to be discarded based on the following criteria. First, we discarded a data set for which a lower excitation power was used (8 pores). Next, we discarded the data of 4 pores that showed negligible protein translocations due to clogging. For three full data sets totalling 24 pores, we found a significant reduction in the amount of photons detected per molecule which biased the event de-

tection (see Appendix 4.6.21 — Figures 4.23,4.24 for details). Further, in cases where the normalized Kap95 event rate differed significantly for one out of the three measurements for the same concentration, the condition was removed (17 conditions). When there was doubt about perfect focusing of the lasers for certain pores, these were discarded from further analysis (2 pores). Finally, if there was any indication of sticking of proteins to the pore surface, as visible from the FCS curve, these pores were removed (2 pores). In total, 46 pores (27 with Nsp1 coating, 19 open pores) with 400 time traces (248 for Nsp1-coated pore, 152 for open pores) from seven individual measurement days and chips were used for the final analysis.

Normalized event rates in Figure 4.4 and Figure 4.5 were fitted using Equation 4.2 and Equation 4.3 by optimizing the functions to the individual translocation datasets, taking into account their statistical errors using the least squares method (see Appendix 4.6.10 — Figure 4.13).

Fluorescence Correlation Spectroscopy (FCS) and lifetime analyses were performed using the PAM software package [75]. For fitting of the FCS curves, the size of the confocal volume was determined from measurements of the free dyes Alexa647 and Alexa488 by fitting a single-component diffusion model with triplet state. The diffusion coefficients at 21 °C were set to $297 \mu\text{m}^2/\text{s}$ for Alexa647 and $372 \mu\text{m}^2/\text{s}$ for Alexa488, based on the values provided in [76]. The axial and lateral sizes of the confocal volume, ω_z and ω_r , were fixed for further analysis. FCS amplitudes and diffusion coefficients were subsequently fitted for each dataset separately. For Kap95–Alexa647 containing samples, the triplet state was fitted individually for each FCS curve. Fluorescence lifetimes were determined by a single-exponential tail fit of the fluorescence decays, ignoring the first 1160 ps of the decay in order to reduce variations introduced by the instrument response function.

4.4.6. COARSE-GRAINED MOLECULAR DYNAMICS SIMULATIONS

Coarse-grained molecular dynamics simulations were performed with the implicit-solvent 1BPA-1.1 model for intrinsically disordered proteins [50–52, 77, 78]. This residue-scale model discriminates between all 20 amino acids through residue-specific hydrophobic, charge and cation–pi interactions, and accounts for the sequence-specific backbone stiffness (see [52] for a detailed description of the 1BPA-1.1 model). Simulations were performed with the GROMACS [79] molecular dynamics software (version 2019.4) using a time step of 0.02 ps and inverse friction coefficient $\gamma^{-1} = 50 \text{ ps}$ for the Langevin dynamics integrator. All nanopores were simulated at 294 K and a salt concentration of 150 mM KCl by setting the Debye screening constant $\kappa = 1.27 \text{ nm}^{-1}$. Nanopore scaffolds were generated from partly-overlapping sterically inert beads with a diameter of 3.0 nm with their centres placed 1.5 nm apart. Nsp1 proteins were then grafted to the scaffold wall at their C-terminal Cys-residue, with the N-terminus of the Nsp1 proteins pointing out of the nanopore occlusion. Nanopore systems were equilibrated for 1.0×10^8 steps (2 μs), followed by a production run of 2.5×10^8 steps (5 μs) to generate the equilibrium trajectories.

Axi-radial density maps were obtained from the equilibrium trajectories using the *gmx densmap* utility of GROMACS, where a sample was taken every 5000 steps (100 ps). The 2D number-density maps created by GROMACS (in nm^{-3}) were converted to mass

densities (in mg/mL) using the average mass of an Nsp1 residue (~ 100 Da). We note that the obtained densities are slightly lower than observed previously for 20 nm-pores [27], as there a simplified average residue mass of 120 Da was used.

VOID ANALYSIS METHOD AND CALCULATION OF TRANSLOCATION RATES

Protein translocations both for BSA and Kap95 were not explicitly simulated. BSA and Kap95 translocation rates were calculated as described in the following paragraph. As experimentally only a negligible hindrance of Kap95 by Nsp1 was observed, the same calculated translocation rates of Kap95 through open pores were assumed both for Nsp1 coated pores as well.

Potential of mean force (PMF) curves for protein translocation across the Nsp1 pores obtained using the void analysis method of Winogradoff *et al.* [54]. The simulation volume was converted into a 3D grid where each voxel has a side length of 6 Å. For each instantaneous configuration of the Nsp1 mesh, we probed for each voxel whether a spherical probe with the size of the translocating protein (BSA or Kap95, see Appendix 4.6.13) could be placed at its center without sterically overlapping with an Nsp1 bead or the pore scaffold. The resulting 3D void map was then converted into a 1D potential occupancy map by calculating the percentage of available voxels for each slice along the pore axis. The potential occupancy function was calculated for every 5×10^4 steps (1 ns) of the equilibrium trajectory. The trajectory average of the potential occupancy function was converted into an effective PMF curve through Boltzmann inversion, as shown in Appendix 4.6.13 — Figures 4.18 and 4.19 (see [54] for a more detailed description of the procedure). The analysis was performed with the codes provided by the paper, where a custom constraint was used for each nanopore to exclude the Pd layer volume from the void analysis. Protein translocation rates were obtained from the PMF barriers, calculated by averaging the PMF over a specified range (Appendix 4.6.13 — Figures 4.18 and 4.19), using an Arrhenius relation:

$$k = k_0 \exp(-\Delta E / k_B T), \quad (4.6)$$

in which ΔE is the energy barrier that the translocating protein has to overcome and k_0 is a proportionality constant that is obtained by fitting the calculated rates to the experimental event rates for open pores (see Appendix 4.6.13). This resulted in two independent scaling factors, $k_{0,BSA}$ and $k_{0,Kap95}$, for BSA and Kap95, respectively. We note that the use of protein-specific scaling factors follows from the observation that the void analysis method does not take into account any diffusion properties of the translocating protein. Nevertheless, the same scaling factor was used for both open and Nsp1-coated pores.

To assess the path that BSA proteins take through the Nsp1 mesh, we determined the time-averaged distribution of the ‘voids’ in the Nsp1 mesh. This was done by computing the 3D void map for each instantaneous configuration of the Nsp1 meshwork, and calculating the simulation average. This time-averaged void map represents the probability for each voxel to accommodate a BSA protein. The 3D void map was then circumferentially averaged around the pore’s axis to obtain the 2D (r, z) void map shown in Figure 4.5 F.

4.4.7. FINITE-DIFFERENCE TIME-DOMAIN (FDTD) SIMULATIONS

Three-dimensional FDTD simulations were performed using Lumerical FDTD (ANSYS, Inc., USA). The surrounding medium was modeled as water with a refractive index of 1.33. The refractive index of the 100 nm thick palladium membrane was modelled according to Alterovitz *et al.* [80]. For the simulation of the excitation field, the ZMW was illuminated by a pulse from a total-field scattered-field source polarized in the x-direction, set as a plane wave source for widefield excitation and a Gaussian source with a numerical aperture of 1.1 for focused excitation. The simulation box size was $1 \times 1 \times 0.8 \mu\text{m}^3$ for widefield excitation. A larger box of $4 \times 4 \times 0.8 \mu\text{m}^3$ was required for the Gaussian source to correctly model the focused beam. The electromagnetic field intensity distribution was monitored in the xz and yz planes passing through the center of the pore and in the xy plane at the pore entry with a grid resolution of 5 nm (Appendix 4.6.3). To model the dipole emission in the proximity of the ZMW, a dipole emitter was placed at varying z-positions at the center of the pore. For the estimation of the quantum yield, the radiated power was integrated over all sides of the box (see below). For the estimation of the detection efficiency, the emitted power was integrated only on the detection side of the ZMW. To isolate the effect of the ZMW on the distribution of the signal on the two sides of the metal membrane, we did not account for the numerical aperture of the objective lens in the computation of the detection efficiency, which represents an additional loss factor in the experimental system. To model isotropic emission, all reported quantities were averaged over horizontal and vertical orientations of the dipole. The power was only weakly affected by the lateral position of the emitter with respect to the center of the pore (data not shown) [34]. The simulated electric field intensities $|E|^2$ are shown in Appendix 4.6.3 — Figures 4.4–4.6.

ESTIMATION OF DETECTED SIGNAL AND FLUORESCENCE LIFETIMES

In the absence of the ZMW, the decay rate of the excited molecule is given by $\gamma^0 = \gamma_r^0 + \gamma_{nr}^0$, where γ_r^0 and γ_{nr}^0 are the radiative and non-radiative decay rates. Note that γ_{nr}^0 accounts only for internal processes that lead to non-radiative relaxation to the ground state and was assumed to be unchanged in the presence of the ZMW. The intrinsic quantum yield is defined as $\Phi_0 = \gamma_r^0 / (\gamma_r^0 + \gamma_{nr}^0)$ and was estimated from the measured fluorescence lifetimes τ_0 for BSA–Alexa488 and Kap95–Alexa647 of 2.30 ns and 1.37 ns, respectively, as:

$$\Phi_0 = \frac{\tau_0}{\tau_{\text{lit}}} \Phi_{\text{lit}}, \quad (4.7)$$

where τ_{lit} and Φ_{lit} are reference values for the free dyes ($\tau_{\text{lit}} = 4.0$ ns and $\Phi_{\text{lit}} = 0.80$ for Alexa488, $\tau_{\text{lit}} = 1.37$ ns and $\Phi_{\text{lit}} = 0.33$ for Alexa647) [81, 82]. This led to quantum yields of $\Phi_0 = 0.46$ and 0.39 for BSA–Alexa488 and Kap95–Alexa647, respectively. Note that the quantum yield of Alexa647 increased slightly due to steric restriction when attached to the protein, an effect known as protein-induced fluorescence enhancement [83]. The lower quantum yield for BSA–Alexa488 compared to the literature value is most likely a consequence of dye-dye interactions due to the high degree of labeling of ≈ 6 dye molecules per protein, as specified by the manufacturer.

In the presence of the nanostructure, the radiative decay rate γ_r is modified and an additional non-radiative rate γ_{loss} is introduced because part of the power emitted by

the dipole is absorbed by the metal nanostructure. The quantum yield Φ in the presence of the ZMW was given by Bharadwaj and Novotny [84]:

$$\Phi = \frac{\gamma_r / \gamma_r^0}{\gamma_r / \gamma_r^0 + \gamma_{\text{loss}} / \gamma_r^0 + (1 - \Phi_0) / \Phi_0}, \quad (4.8)$$

where γ_r^0 and γ_r are the radiative rates in the absence and the presence of the ZMW respectively. The absolute decay rates γ_r , γ_{loss} , and γ_r^0 cannot be obtained from FDTD simulations. However, relative rates with respect to the radiative rate in the absence of the ZMW, γ_r^0 , can be estimated from the power P radiated by the dipole as [85]:

$$\frac{\gamma_r}{\gamma_r^0} = \frac{P_{\text{ff}}}{P_r^0} \text{ and } \frac{\gamma_{\text{loss}}}{\gamma_r^0} = \frac{P_r}{P_r^0} - \frac{P_{\text{ff}}}{P_r^0}, \quad (4.9)$$

where P_r and P_r^0 are the powers radiated by the dipole in the presence and absence of the ZMW, and P_{ff} is the power that is radiated into the far-field in the presence of the ZMW. The fluorescence lifetime τ is given by the inverse of the sum of all de-excitation rates and can be obtained from eq. 4.8 using the relation $\tau = \Phi / \gamma_r$ as:

$$\tau = \frac{1}{\gamma_r + \gamma_{\text{loss}} + \gamma_{nr}^0} = \frac{1 / \gamma_r^0}{\gamma_r / \gamma_r^0 + \gamma_{\text{loss}} / \gamma_r^0 + (1 - \Phi_0) / \Phi_0}. \quad (4.10)$$

Here, the intrinsic radiative rate γ_r^0 in the numerator was estimated as $\gamma_r^0 = \Phi_{\text{lit}} / \tau_{\text{lit}}$. The detection efficiency η was estimated from the ratio of the power radiated towards the lower (detection) side of the ZMW, P_{ff}^{z-} , to the total radiated power:

$$\eta = \frac{P_{\text{ff}}^{z-}}{P_{\text{ff}}}. \quad (4.11)$$

Finally, the total detected signal as a function of the z -position of the emitter with respect to the ZMW was computed as the product of the excitation intensity $I_{\text{ex}}(z)$, detection efficiency $\eta(z)$, and quantum yield $\Phi(z)$ as:

$$S(z) \propto I_{\text{ex}}(z) \eta(z) \Phi(z) \quad (4.12)$$

and normalized to unity. The radiative and loss rates obtained from the FDTD simulations (γ_r / γ_r^0 and $\gamma_{\text{loss}} / \gamma_r^0$), which are used to compute the quantities Φ , τ and η , are given in [subsection 4.6.3—Supplementary Figure 4.8](#) as a function of the z -position within the ZMW. Z -profiles of the computed detection efficiency η , quantum yield Φ , detected signal $S(z)$, and lifetime τ are shown in [Appendix 4.6.3 — Supplementary Figure 4.7](#).

Using the signal profile $S(z)$, we compute the signal-averaged fluorescence lifetime $\langle \tau \rangle_S$ as:

$$\langle \tau \rangle_S = \frac{\int S(z) \tau(z) dz}{\int S(z) dz}, \quad (4.13)$$

which agrees well with the experimental fluorescence lifetimes measured in the translocation experiments ([subsection 4.6.3 — Supplementary Figure 4.7](#)).

4.5. DATA AVAILABILITY

All single photon counting data is deposited in the open Photon-HDF5 file format [86] together with the unprocessed TEM images of nanopores are in a repository at [43]).

REFERENCES

- [1] R. Reichelt, A. Holzenburg, J. Buhle, E. L. M. Jarnik, A. Engel, and U. Aebi, *Correlation between structure and mass distribution of the nuclear pore complex and of distinct pore complex components*. *Journal of Cell Biology* **110**, 883 (1990), doi:[10.1083/jcb.110.4.883](https://doi.org/10.1083/jcb.110.4.883).
- [2] S. J. Kim, J. Fernandez-Martinez, I. Nudelman, Y. Shi, W. Zhang, B. Raveh, T. Herricks, B. D. Slaughter, J. A. Hogan, P. Upla, I. E. Chemmama, R. Pellarin, I. Echeverria, M. Shivaraju, A. S. Chaudhury, J. Wang, R. Williams, J. R. Unruh, C. H. Greenberg, E. Y. Jacobs, Z. Yu, M. J. de la Cruz, R. Mironska, D. L. Stokes, J. D. Aitchison, M. F. Jarrold, J. L. Gerton, S. J. Ludtke, C. W. Akey, B. T. Chait, A. Sali, and M. P. Rout, *Integrative structure and functional anatomy of a nuclear pore complex*, *Nature* **555**, 475 (2018), doi:[10.1038/nature26003](https://doi.org/10.1038/nature26003).
- [3] C. E. Zimmerli, M. Allegretti, V. Rantos, S. K. Goetz, A. Obarska-Kosinska, I. Zagoriy, A. Halavatyi, G. Hummer, J. Mahamid, J. Kosinski, and M. Beck, *Nuclear pores dilate and constrict in cellulo*, *Science* **374**, eabd9776 (2021), doi:[10.1126/science.abd9776](https://doi.org/10.1126/science.abd9776).
- [4] C. W. Akey, D. Singh, C. Ouch, I. Echeverria, I. Nudelman, J. M. Varberg, Z. Yu, F. Fang, Y. Shi, J. Wang, D. Salzberg, K. Song, C. Xu, J. C. Gumbart, S. Suslov, J. Unruh, S. L. Jaspersen, B. T. Chait, A. Sali, J. Fernandez-Martinez, S. J. Ludtke, E. Villa, and M. P. Rout, *Comprehensive structure and functional adaptations of the yeast nuclear pore complex*, *Cell* **185**, 361 (2022), doi:<https://doi.org/10.1016/j.cell.2021.12.015>.
- [5] R. Y. H. Lim, B. Huang, and L. E. Kapinos, *How to operate a nuclear pore complex by kap-centric control*, *Nucleus* **6**, 366 (2015), doi:[10.1080/19491034.2015.1090061](https://doi.org/10.1080/19491034.2015.1090061).
- [6] H. B. Schmidt and D. Görlich, *Transport selectivity of nuclear pores, phase separation, and membraneless organelles*, *Trends in Biochemical Sciences* **41**, 46 (2016), doi:<https://doi.org/10.1016/j.tibs.2015.11.001>.
- [7] T. Jovanovic-Talisman and A. Zilman, *Protein transport by the nuclear pore complex: Simple biophysics of a complex biomachine*. *Biophys J* **113**, 6–14 (2017).
- [8] M. Beck and E. Hurt, *The nuclear pore complex: understanding its function through structural insight*, *Nature Reviews Molecular Cell Biology* **18**, 73 (2017), doi:[10.1038/nrm.2016.147](https://doi.org/10.1038/nrm.2016.147).
- [9] O. Keminer and R. Peters, *Permeability of single nuclear pores*. *Biophys J* **77**, 217–228 (1999).
- [10] D. Mohr, S. Frey, T. Fischer, T. Güttler, and D. Görlich, *Characterisation of the passive permeability barrier of nuclear pore complexes*, *The EMBO Journal* **28**, 2541 (2009), doi:<https://doi.org/10.1038/emboj.2009.200>.

- [11] P. Popken, A. Ghavami, P. R. Onck, B. Poolman, and L. M. Veenhoff, *Size-dependent leak of soluble and membrane proteins through the yeast nuclear pore complex*, *Molecular Biology of the Cell* **26**, 1386 (2015), doi:[10.1091/mbc.E14-07-1175](https://doi.org/10.1091/mbc.E14-07-1175).
- [12] B. L. Timney, B. Raveh, R. Mironska, J. M. Trivedi, S. J. Kim, D. Russel, S. R. Wentz, A. Sali, and M. P. Rout, *Simple rules for passive diffusion through the nuclear pore complex*, *Journal of Cell Biology* **215**, 57 (2016), doi:[10.1083/jcb.201601004](https://doi.org/10.1083/jcb.201601004).
- [13] I. V. Aramburu and E. A. Lemke, *Floppy but not sloppy: Interaction mechanism of fg-nucleoporins and nuclear transport receptors*, *Seminars in Cell & Developmental Biology* **68**, 34 (2017), doi:<https://doi.org/10.1016/j.semcdb.2017.06.026>.
- [14] D. Görlich and U. Kutay, *Transport between the cell nucleus and the cytoplasm*, *Annual Review of Cell and Developmental Biology* **15**, 607 (1999), doi:[10.1146/annurev.cellbio.15.1.607](https://doi.org/10.1146/annurev.cellbio.15.1.607).
- [15] M. P. Rout, J. D. Aitchison, M. O. Magnasco, and B. T. Chait, *Virtual gating and nuclear transport: the hole picture*, *Trends in Cell Biology* **13**, 622 (2003), doi:<https://doi.org/10.1016/j.tcb.2003.10.007>.
- [16] S. Frey, R. P. Richter, and D. Görlich, *Fg-rich repeats of nuclear pore proteins form a three-dimensional meshwork with hydrogel-like properties*, *Science* **314**, 815 (2006), doi:[10.1126/science.1132516](https://doi.org/10.1126/science.1132516).
- [17] S. Frey and D. Görlich, *A saturated fg-repeat hydrogel can reproduce the permeability properties of nuclear pore complexes*, *Cell* **130**, 512 (2007), doi:<https://doi.org/10.1016/j.cell.2007.06.024>.
- [18] J. Yamada, J. L. Phillips, S. Patel, G. Goldfien, A. Calestagne-Morelli, H. Huang, R. Reza, J. Acheson, V. V. Krishnan, S. Newsam, A. Gopinathan, E. Y. Lau, M. E. Colvin, V. N. Uversky, and M. F. Rexach, *A bimodal distribution of two distinct categories of intrinsically disordered structures with separate functions in fg nucleoporins*, *Molecular & Cellular Proteomics* **9**, 2205 (2010), doi:[10.1074/mcp.M000035-MCP201](https://doi.org/10.1074/mcp.M000035-MCP201).
- [19] K. D. Schleicher, S. L. Dettmer, L. E. Kapinos, S. Pagliara, U. F. Keyser, S. Jeney, and R. Y. H. Lim, *Selective transport control on molecular velcro made from intrinsically disordered proteins*, *Nature Nanotechnology* **9**, 525 (2014), doi:[10.1038/nnano.2014.103](https://doi.org/10.1038/nnano.2014.103).
- [20] L. Kapinos, R. Schoch, R. Wagner, K. Schleicher, and R. Lim, *Karyopherin-centric control of nuclear pores based on molecular occupancy and kinetic analysis of multivalent binding with fg nucleoporins*, *Biophysical Journal* **106**, 1751 (2014), doi:<https://doi.org/10.1016/j.bpj.2014.02.021>.
- [21] L. E. Kapinos, B. Huang, C. Rencurel, and R. Y. Lim, *Karyopherins regulate nuclear pore complex barrier and transport function*, *Journal of Cell Biology* **216**, 3609 (2017), doi:[10.1083/jcb.201702092](https://doi.org/10.1083/jcb.201702092).

- [22] A. Zilman, S. D. Talia, B. T. Chait, M. P. Rout, and M. O. Magnasco, *Efficiency, Selectivity, and Robustness of Nucleocytoplasmic Transport*, *PLOS Computational Biology* **3**, e125 (2007), doi:10.1371/journal.pcbi.0030125.
- [23] A. Zilman, S. D. Talia, T. Jovanovic-Talisman, B. T. Chait, M. P. Rout, and M. O. Magnasco, *Enhancement of Transport Selectivity through Nano-Channels by Non-Specific Competition*, *PLOS Computational Biology* **6**, e1000804 (2010-06), doi:10.1371/journal.pcbi.1000804.
- [24] A. Fragasso, H. W. de Vries, J. Andersson, E. O. van der Sluis, E. van der Giessen, P. R. Onck, and C. Dekker, *Transport receptor occupancy in nuclear pore complex mimics*, *Nano Research* (2022), 10.1007/s12274-022-4647-1, doi:10.1007/s12274-022-4647-1.
- [25] T. Jovanovic-Talisman, J. Tetenbaum-Novatt, A. S. McKenney, A. Zilman, R. Peters, M. P. Rout, and B. T. Chait, *Artificial nanopores that mimic the transport selectivity of the nuclear pore complex*, *Nature* **457**, 1023 (2009), doi:10.1038/nature07600.
- [26] S. W. Kowalczyk, L. Kapinos, T. R. Blosser, T. Magalhães, P. van Nies, R. Y. H. Lim, and C. Dekker, *Single-molecule transport across an individual biomimetic nuclear pore complex*, *Nature Nanotechnology* **6**, 433 (2011).
- [27] A. N. Ananth, A. Mishra, S. Frey, A. Dwarkasing, R. Versloot, E. van der Giessen, D. Görlich, P. Onck, and C. Dekker, *Spatial structure of disordered proteins dictates conductance and selectivity in nuclear pore complex mimics*, *eLife* **7**, e31510 (2018), doi:10.7554/eLife.31510.
- [28] G. Celetti, G. Paci, J. Caria, V. VanDelinder, G. Bachand, and E. A. Lemke, *The liquid state of FG-nucleoporins mimics permeability barrier properties of nuclear pore complexes*, *Journal of Cell Biology* **219** (2019), 10.1083/jcb.201907157, doi:10.1083/jcb.201907157.
- [29] Q. Shen, T. Tian, Q. Xiong, P. Ellis Fisher, Y. Xiong, T. Melia, C. Lusk, and C. Lin, *Dna-origami nanotrap for studying the selective barriers formed by phenylalanine-glycine-rich nucleoporins*. *J Am Chem Soc* **143**, 12294–12303 (2021).
- [30] Q. Shen, Q. Xiong, K. Zhou, Q. Feng, L. Liu, T. Tian, C. Wu, Y. Xiong, T. J. Melia, C. P. Lusk, and C. Lin, *Functionalized dna-origami-protein nanopores generate large transmembrane channels with programmable size-selectivity*, *Journal of the American Chemical Society* **145**, 1292 (2023), doi:10.1021/jacs.2c11226.
- [31] A. Fragasso, H. W. de Vries, J. Andersson, E. O. van der Sluis, E. van der Giessen, A. Dahlin, P. R. Onck, and C. Dekker, *A designer fg-nup that reconstitutes the selective transport barrier of the nuclear pore complex*, *Nature Communications* **12**, 2010 (2021), doi:10.1038/s41467-021-22293-y.
- [32] S. C. Ng, T. Güttler, and D. Görlich, *Recapitulation of selective nuclear import and export with a perfectly repeated 12mer glfg peptide*, *Nature Communications* **12**, 4047 (2021), doi:10.1038/s41467-021-24292-5.

- [33] N. Klughammer and C. Dekker, *Palladium zero-mode waveguides for optical single-molecule detection with nanopores*, *Nanotechnology* **32**, 18LT01 (2021), doi:[10.1088/1361-6528/abd976](https://doi.org/10.1088/1361-6528/abd976).
- [34] M. J. Levene, J. Korlach, S. W. Turner, M. Foquet, H. G. Craighead, and W. W. Webb, *Zero-mode waveguides for single-molecule analysis at high concentrations*, *science* **299**, 682 (2003), doi:[10.1126/science.1079700](https://doi.org/10.1126/science.1079700).
- [35] K. T. Samiee, M. Foquet, L. Guo, E. C. Cox, and H. G. Craighead, *λ -repressor oligomerization kinetics at high concentrations using fluorescence correlation spectroscopy in zero-mode waveguides*, *Biophysical Journal* **88**, 2145 (2005), doi:[10.1529/biophysj.104.052795](https://doi.org/10.1529/biophysj.104.052795).
- [36] H. Rigneault, J. Capoulade, J. Dintinger, J. Wenger, N. Bonod, E. Popov, T. W. Ebbesen, and P.-F. Lenne, *Enhancement of single-molecule fluorescence detection in subwavelength apertures*, *Phys. Rev. Lett.* **95**, 117401 (2005), doi:[10.1103/PhysRevLett.95.117401](https://doi.org/10.1103/PhysRevLett.95.117401).
- [37] T. Auger, J. Mathé, V. Viasnoff, G. Charron, J.-M. Di Meglio, L. Auvray, and F. Montel, *Zero-mode waveguide detection of flow-driven dna translocation through nanopores*, *Phys. Rev. Lett.* **113**, 028302 (2014), doi:[10.1103/PhysRevLett.113.028302](https://doi.org/10.1103/PhysRevLett.113.028302).
- [38] O. N. Assad, T. Gilboa, J. Spitzberg, M. Juhasz, E. Weinhold, and A. Meller, *Light-enhancing plasmonic-nanopore biosensor for superior single-molecule detection*, *Advanced Materials* **29**, 1605442 (2016), doi:[10.1002/adma.201605442](https://doi.org/10.1002/adma.201605442).
- [39] J. C. Love, D. B. Wolfe, R. Haasch, M. L. Chabinyc, K. E. Paul, G. M. Whitesides, and R. G. Nuzzo, *Formation and structure of self-assembled monolayers of alkanethiols on palladium*, *Journal of the American Chemical Society* **125**, 2597 (2003), doi:[10.1021/ja028692+](https://doi.org/10.1021/ja028692+).
- [40] X. Jiang, D. A. Bruzewicz, M. M. Thant, and G. M. Whitesides, *Palladium as a substrate for self-assembled monolayers used in biotechnology*, *Analytical Chemistry* **76**, 6116 (2004), doi:[10.1021/ac049152t](https://doi.org/10.1021/ac049152t).
- [41] A. Majid, F. Bensebaa, P. L. Ecuyer, G. Pleizier, and Y. Deslandes, *Modification of the metallic surface of silver by the formation of alkanethiol self-assembled monolayers with subsequent reaction with chlorosilanes*, *Rev. Adv. Mater. Sci* **4**, 25 (2003).
- [42] J. Andersson, J. Svirelis, G. Ferrand-Drake del Castillo, T. Sannomiya, and A. Dahlin, *Surface plasmon resonance sensing with thin films of palladium and platinum – quantitative and real-time analysis*, *Phys. Chem. Chem. Phys.* **24**, 4588 (2022), doi:[10.1039/D1CP05381G](https://doi.org/10.1039/D1CP05381G).
- [43] N. Klughammer, A. Barth, and M. Dekker, *Data from paper diameter dependence of transport through nuclear pore complex mimics studied using optical nanopores*, Online (4TU.ResearchData, 2023) doi:[10.4121/22059227](https://doi.org/10.4121/22059227).

- [44] K. L. Prime and G. M. Whitesides, *Adsorption of proteins onto surfaces containing end-attached oligo(ethylene oxide): a model system using self-assembled monolayers*, *Journal of the American Chemical Society* **115**, 10714 (1993), doi:[10.1021/ja00076a032](https://doi.org/10.1021/ja00076a032).
- [45] T. Jovanovic-Talisman, B. T. Chait, and M. P. Rout, *Npc mimics: probing the mechanism of nucleocytoplasmic transport*, in *Methods in cell biology*, Vol. 122 (Elsevier, 2014) pp. 379–393, doi:[10.1016/B978-0-12-417160-2.00017-5](https://doi.org/10.1016/B978-0-12-417160-2.00017-5).
- [46] L. P. Watkins and H. Yang, *Detection of intensity change points in time-resolved single-molecule measurements*, *The Journal of Physical Chemistry B* **109**, 617 (2005), doi:[10.1021/jp0467548](https://doi.org/10.1021/jp0467548).
- [47] S. Yang, N. Klughammer, A. Barth, M. E. Tanenbaum, and C. Dekker, *Zero-mode waveguide nanowells for single-molecule detection in living cells*, *ACS Nano* (2023), [10.1021/acsnano.3c05959](https://doi.org/10.1021/acsnano.3c05959), doi:[10.1021/acsnano.3c05959](https://doi.org/10.1021/acsnano.3c05959).
- [48] P. Dechadilok and W. M. Deen, *Hindrance factors for diffusion and convection in pores*, *Industrial & Engineering Chemistry Research* **45**, 6953 (2006), doi:[10.1021/ie051387n](https://doi.org/10.1021/ie051387n).
- [49] R. Wagner, L. Kapinos, N. Marshall, M. Stewart, and R. Lim, *Promiscuous binding of karyopherin β 1 modulates fg nucleoporin barrier function and expedites ntf2 transport kinetics*, *Biophysical Journal* **108**, 918 (2015), doi:<https://doi.org/10.1016/j.bpj.2014.12.041>.
- [50] A. Ghavami, E. van der Giessen, and P. R. Onck, *Coarse-grained potentials for local interactions in unfolded proteins*, *Journal of Chemical Theory and Computation* **9**, 432 (2013), doi:[10.1021/ct300684j](https://doi.org/10.1021/ct300684j).
- [51] A. Ghavami, L. Veenhoff, E. van der Giessen, and P. Onck, *Probing the disordered domain of the nuclear pore complex through coarse-grained molecular dynamics simulations*, *Biophysical Journal* **107**, 1393 (2014), doi:[10.1016/j.bpj.2014.07.060](https://doi.org/10.1016/j.bpj.2014.07.060).
- [52] M. Dekker, E. Van der Giessen, and P. R. Onck, *Phase separation of intrinsically disordered fg-nups is driven by highly dynamic fg motifs*, *Proceedings of the National Academy of Sciences* **120**, e2221804120 (2023), doi:[10.1073/pnas.2221804120](https://doi.org/10.1073/pnas.2221804120).
- [53] P. Ketterer, A. N. Ananth, D. S. L. Trip, A. Mishra, E. Bertosin, M. Ganji, J. van der Torre, P. Onck, H. Dietz, and C. Dekker, *Dna origami scaffold for studying intrinsically disordered proteins of the nuclear pore complex*, *Nature Communications* **9**, 902 (2018), doi:[10.1038/s41467-018-03313-w](https://doi.org/10.1038/s41467-018-03313-w).
- [54] D. Winogradoff, H.-Y. Chou, C. Maffeo, and A. Aksimentiev, *Percolation transition prescribes protein size-specific barrier to passive transport through the nuclear pore complex*, *Nature Communications* **13**, 5138 (2022), doi:[10.1038/s41467-022-32857-1](https://doi.org/10.1038/s41467-022-32857-1).

- [55] J. Kalita, L. E. Kapinos, T. Zheng, C. Rencurel, A. Zilman, and R. Y. Lim, *Karyopherin enrichment and compensation fortifies the nuclear pore complex against nucleocytoplasmic leakage*, *Journal of Cell Biology* **221** (2022), [10.1083/jcb.202108107](https://doi.org/10.1083/jcb.202108107), doi:[10.1083/jcb.202108107](https://doi.org/10.1083/jcb.202108107).
- [56] C. Plesa, S. W. Kowalczyk, R. Zinsmeister, A. Y. Grosberg, Y. Rabin, and C. Dekker, *Fast translocation of proteins through solid state nanopores*, *Nano Letters* **13**, 658 (2013), doi:[10.1021/nl3042678](https://doi.org/10.1021/nl3042678).
- [57] H. B. Schmidt and D. Görlich, *Nup98 fg domains from diverse species spontaneously phase-separate into particles with nuclear pore-like permselectivity*, *eLife* **4**, e04251 (2015), doi:[10.7554/eLife.04251](https://doi.org/10.7554/eLife.04251).
- [58] L. A. Strawn, T. Shen, N. Shulga, D. S. Goldfarb, and S. R. Wentz, *Minimal nuclear pore complexes define fg repeat domains essential for transport*, *Nature Cell Biology* **6**, 197 (2004), doi:[10.1038/ncb1097](https://doi.org/10.1038/ncb1097).
- [59] R. L. Adams, L. J. Terry, and S. R. Wentz, *A Novel Saccharomyces cerevisiae FG Nucleoporin Mutant Collection for Use in Nuclear Pore Complex Functional Experiments*, *G3 Genes|Genomes|Genetics* **6**, 51 (2016), doi:[10.1534/g3.115.023002](https://doi.org/10.1534/g3.115.023002).
- [60] S. C. Ng, A. Biswas, T. Huyton, J. Schünemann, S. Reber, and D. Görlich, *Barrier properties of nup98 fg phases ruled by fg motif identity and inter-fg spacer length*, *bioRxiv* (2022).
- [61] P. De Magistris, *The great escape: mrna export through the nuclear pore complex*, *International Journal of Molecular Sciences* **22** (2021), [10.3390/ijms222111767](https://doi.org/10.3390/ijms222111767), doi:[10.3390/ijms222111767](https://doi.org/10.3390/ijms222111767).
- [62] R. C. Burdick, C. Li, M. Munshi, J. M. O. Rawson, K. Nagashima, W.-S. Hu, and V. K. Pathak, *Hiv-1 uncoats in the nucleus near sites of integration*, *Proceedings of the National Academy of Sciences* **117**, 5486 (2020), doi:[10.1073/pnas.1920631117](https://doi.org/10.1073/pnas.1920631117).
- [63] V. Zila, E. Margiotta, B. Turoňová, T. G. Müller, C. E. Zimmerli, S. Mattei, M. Allegretti, K. Börner, J. Rada, B. Müller, M. Lusic, H.-G. Kräusslich, and M. Beck, *Cone-shaped hiv-1 capsids are transported through intact nuclear pores*, *Cell* **184**, 1032 (2021), doi:<https://doi.org/10.1016/j.cell.2021.01.025>.
- [64] Q. Shen, Q. Feng, C. Wu, Q. Xiong, T. Tian, S. Yuan, J. Shi, G. J. Bedwell, R. Yang, C. Aiken, A. N. Engelman, C. P. Lusk, C. Lin, and Y. Xiong, *Modeling HIV-1 nuclear entry with nucleoporin-gated DNA-origami channels*, *Nature Structural & Molecular Biology* **30**, 425 (2023), doi:[10.1038/s41594-023-00925-9](https://doi.org/10.1038/s41594-023-00925-9).
- [65] X. J. A. Janssen, M. P. Jonsson, C. Plesa, G. V. Soni, C. Dekker, and N. H. Dekker, *Rapid manufacturing of low-noise membranes for nanopore sensors by trans-chip illumination lithography*, *Nanotechnology* **23**, 475302 (2012), doi:[10.1088/0957-4484/23/47/475302](https://doi.org/10.1088/0957-4484/23/47/475302).

- [66] C. P. Guimaraes, M. D. Witte, C. S. Theile, G. Bozkurt, L. Kundrat, A. E. M. Blom, and H. L. Ploegh, *Site-specific c-terminal and internal loop labeling of proteins using sortase-mediated reactions*, *Nature Protocols* **8**, 1787 (2013), doi:[10.1038/nprot.2013.101](https://doi.org/10.1038/nprot.2013.101).
- [67] U. F. Keyser, J. van der Does, C. Dekker, and N. H. Dekker, *Optical tweezers for force measurements on dna in nanopores*, *Review of Scientific Instruments* **77**, 105105 (2006), doi:[10.1063/1.2358705](https://doi.org/10.1063/1.2358705).
- [68] J. D. Hunter, *Matplotlib: A 2d graphics environment*, *Computing in Science & Engineering* **9**, 90 (2007), doi:[10.1109/MCSE.2007.55](https://doi.org/10.1109/MCSE.2007.55).
- [69] P. Virtanen, R. Gommers, T. E. Oliphant, M. Haberland, T. Reddy, D. Cournapeau, E. Burovski, P. Peterson, W. Weckesser, J. Bright, S. J. van der Walt, M. Brett, J. Wilson, K. Jarrod Millman, N. Mayorov, A. R. J. Nelson, E. Jones, R. Kern, E. Larson, C. Carey, Í. Polat, Y. Feng, E. W. Moore, J. VanderPlas, D. Laxalde, J. Perktold, R. Cimrman, I. Henriksen, E. A. Quintero, C. R. Harris, A. M. Archibald, A. H. Ribeiro, F. Pedregosa, P. van Mulbregt, and S. . . Contributors, *SciPy 1.0: Fundamental Algorithms for Scientific Computing in Python*, *Nature Methods* **17**, 261 (2020), doi:[10.1038/s41592-019-0686-2](https://doi.org/10.1038/s41592-019-0686-2).
- [70] Wes McKinney, *Data Structures for Statistical Computing in Python*, in *Proceedings of the 9th Python in Science Conference*, edited by Stéfan van der Walt and Jarrod Millman (2010) pp. 56 – 61, doi:[10.25080/Majora-92bf1922-00a](https://doi.org/10.25080/Majora-92bf1922-00a).
- [71] S. van der Walt, S. C. Colbert, and G. Varoquaux, *The numpy array: A structure for efficient numerical computation*, *Computing in Science Engineering* **13**, 22 (2011).
- [72] F. Perez and B. E. Granger, *Ipython: A system for interactive scientific computing*, *Computing in Science Engineering* **9**, 21 (2007).
- [73] N. Klughammer, *Code from Paper Palladium Zero-Mode Waveguides for Optical Single Molecule Detection with Nanopores*, Online (2020) doi:[10.4121/12888551.v1](https://doi.org/10.4121/12888551.v1).
- [74] N. Klughammer, A. Barth, and M. Dekker, *Code for paper diameter dependence of transport through nuclear pore complex mimics studied using optical nanopores*, Online (4TU.ResearchData, 2023) doi:[10.4121/21027850](https://doi.org/10.4121/21027850).
- [75] W. Schrimpf, A. Barth, J. Hendrix, and D. C. Lamb, *Pam: A framework for integrated analysis of imaging, single-molecule, and ensemble fluorescence data*, *Biophysical Journal* **114**, 1518 (2018), doi:<https://doi.org/10.1016/j.bpj.2018.02.035>.
- [76] P. Kapusta, *Absolute Diffusion Coefficients: Compilation of Reference Data for FC-SCalibration*, Tech. Rep. (PicoQuant GmbH, 2020).
- [77] H. Jafarinia, E. Van der Giessen, and P. R. Onck, *Phase separation of toxic dipeptide repeat proteins related to c9orf72 als/ftd*, *Biophysical Journal* **119**, 843 (2020), doi:[10.1016/j.bpj.2020.07.005](https://doi.org/10.1016/j.bpj.2020.07.005).

- [78] H. Jafarinia, E. Van der Giessen, and P. R. Onck, *Molecular basis of c9orf72 poly-pr interference with the β -karyopherin family of nuclear transport receptors*, *Scientific Reports* **12**, 21324 (2022), doi:[10.1038/s41598-022-25732-y](https://doi.org/10.1038/s41598-022-25732-y).
- [79] D. van der Spoel, E. Lindahl, B. Hess, G. Groenhof, A. E. Mark, and H. J. C. Berendsen, *GROMACS: Fast, flexible, and free*, *J. Comput. Chem.* **26**, 1701 (2005), doi:[10.1002/jcc.20291](https://doi.org/10.1002/jcc.20291).
- [80] S. A. Alterovitz, P. M. Amirtharaj, P. Apell, E. T. Arakawa, J. Ashok, J. Barth, D. F. Bezuidenhout, J. R. Birch, H.-G. Birken, C. Blessing, I. Bloomer, A. Borghesi, T. A. Callcott, M. Cardona, Y.-c. Chang, T. M. Cotter, D. F. Edwards, J. E. Eldridge, J. Fink, A. R. Forouhi, F. Gervais, O. J. Glembocki, G. Guizzetti, R. T. Holm, D. R. Huffman, J. Humlíček, O. Hunderi, W. R. Hunter, T. Inagaki, B. Jensen, R. Johnson, C. Kunz, F. Lukeš, D. W. Lynch, K. Navrátil, L. Ohlídal, E. D. Palik, E. Pelletier, J. Pflüger, A. Pignaggi, H. Piller, M. R. Querry, C. G. Ribbing, D. M. Roessler, A. Roos, N. Savvides, E. Schmidt, M. L. Scott, D. J. Segelstein, F. W. Smith, G. J. Sprokel, J. D. Swalen, K. Takarabe, R. Tatchyn, Y. Y. Teng, M. E. Thomas, W. J. Tropf, P. L. H. Varaprasad, L. Ward, R. H. White, D. M. Wieliczka, J. A. Woollam, and C. Wong, *Handbook of Optical Constants of Solids*, edited by E. D. Palik, Vol. 3 (Academic Press, Boston, 1998) p. 1096, doi:[10.1016/B978-0-08-055630-7.50003-1](https://doi.org/10.1016/B978-0-08-055630-7.50003-1).
- [81] H. Sanabria, D. Rodnin, K. Hemmen, T. Peulen, S. Felekyan, M. Fleissner, M. Dimura, F. Koberling, R. Kühnemuth, W. Hubbell, H. Gohlke, and C. Seidel, *Resolving dynamics and function of transient states in single enzyme molecules*. *Nat Commun* **11**, 1231 (2020), doi:[10.1038/s41467-020-14886-w](https://doi.org/10.1038/s41467-020-14886-w).
- [82] B. Hellenkamp, S. Schmid, O. Doroshenko, O. Opanasyuk, R. Kühnemuth, S. Rezaei Adariani, B. Ambrose, M. Aznauryan, A. Barth, V. Birkedal, M. E. Bowen, H. Chen, T. Cordes, T. Eilert, C. Fijen, C. Gebhardt, M. Götz, G. Gouridis, E. Gratton, T. Ha, P. Hao, C. A. Hanke, A. Hartmann, J. Hendrix, L. L. Hildebrandt, V. Hirschfeld, J. Hohlbein, B. Hua, C. G. Hübner, E. Kallis, A. N. Kapanidis, J.-Y. Kim, G. Krainer, D. C. Lamb, N. K. Lee, E. A. Lemke, B. Levesque, M. Levitus, J. J. McCann, N. Naredi-Rainer, D. Nettels, T. Ngo, R. Qiu, N. C. Robb, C. Röcker, H. Sanabria, M. Schlierf, T. Schröder, B. Schuler, H. Seidel, L. Streit, J. Thurn, P. Tinnefeld, S. Tyagi, N. Vandenberk, A. M. Vera, K. R. Weninger, B. Wünsch, I. S. Yanez-Orozco, J. Michaelis, C. A. M. Seidel, T. D. Craggs, and T. Hugel, *Precision and accuracy of single-molecule FRET measurements—a multi-laboratory benchmark study*, *Nature Methods* **15**, 669 (2018-09), doi:[10.1038/s41592-018-0085-0](https://doi.org/10.1038/s41592-018-0085-0).
- [83] E. Stennett, M. Ciuba, S. Lin, and M. Levitus, *Demystifying pife: The photophysics behind the protein-induced fluorescence enhancement phenomenon in cy3*. *J Phys Chem Lett* **6**, 1819–1823 (2015).
- [84] P. Bharadwaj and L. Novotny, *Spectral dependence of single molecule fluorescence enhancement*, *Optics Express* **15**, 14266–14274 (2007), doi:[10.1364/oe.15.014266](https://doi.org/10.1364/oe.15.014266).
- [85] F. Kaminski, V. Sandoghdar, and M. Agio, *Finite-difference time-domain modeling of decay rates in the near field of metal nanostructures*, *Journal of Computational and Theoretical Nanoscience* **4**, 635–643 (2007).

- [86] A. Ingargiola, T. Laurence, R. Boutelle, S. Weiss, and X. Michalet, *Photon-hdf5: An open file format for timestamp-based single-molecule fluorescence experiments*, *Bio-physical Journal* **110**, 26 (2016), doi:<https://doi.org/10.1016/j.bpj.2015.11.013>.
- [87] I. Gregor, A. Chizhik, N. Karedla, and J. Enderlein, *Metal-induced energy transfer*, *Nanophotonics* **8**, 1689 (2019), doi:[10.1515/nanoph-2019-0201](https://doi.org/10.1515/nanoph-2019-0201).
- [88] R. Chowdhury, A. Sau, and S. M. Musser, *Super-resolved 3d tracking of cargo transport through nuclear pore complexes*, *Nature Cell Biology* **24**, 112 (2022), doi:[10.1038/s41556-021-00815-6](https://doi.org/10.1038/s41556-021-00815-6).

4.6. APPENDIX

4.6.1. DIFFERENT CLEANING METHODS TESTED

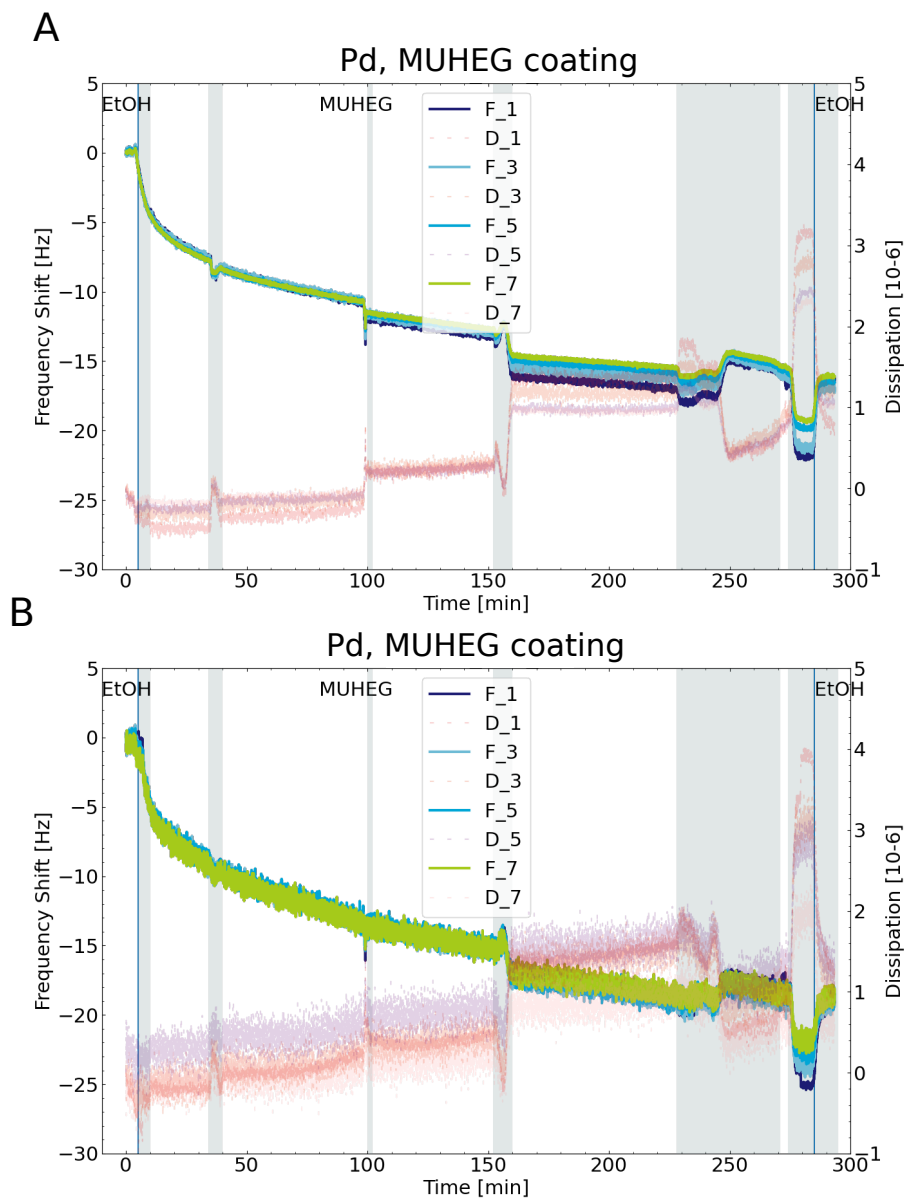
We encountered that after fabrication, the Pd surface inside the pores needed thorough cleaning to be accessible for thiol binding. During the study we tested cleaning with 100 W Oxygen plasma, 25 % and 5 % nitric acid, 1 h and 15 min RCA1, 15 min sulfuric acid piranha solution, 1 M potassium hydroxide solution, 10 min fuming sulfuric acid, 1 min 1 M sulfuric acid, 15 min hydrogen peroxide solution at 45 °C and 20 °C, 3 % and 37 % hydrochloric acid, 1 min gold etch (KI and I₂), 1:20 and 1:40 diluted commercial copper etch (Sigma Aldrich, comparable composition as commercial Pd etch), 30 % Ammonia, 2 min 1 M sodium hydroxide solution and boiling ethanol. Cleaning methods were evaluated based on two criteria. First, nanopores should remain intact, i.e. neither closed nor grew, and surfaces needed to be competent for thiol binding as monitored by QCM-D. Only hydrogen peroxide and ethanol boiling fulfilled both these conditions.

4.6.2. QCM-D EXPERIMENTS

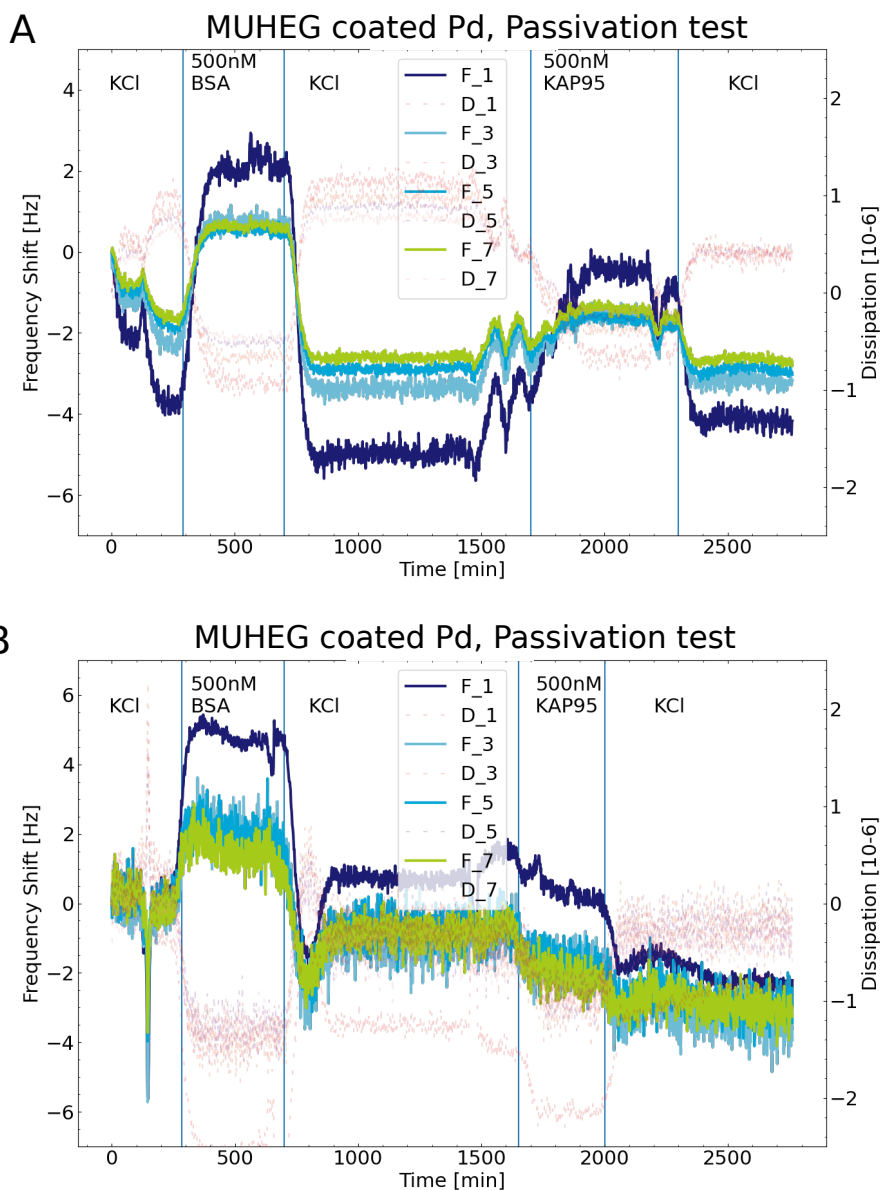
In order to test how well MUHEG passivates a hydrogenperoxide-cleaned Pd surface, we coated two QCM-D chips with MUHEG and monitored their frequency and dissipation shifts. We found a resulting frequency shift of about 15 Hz when switching back to ethanol after incubating the chip with 250 μM of MUHEG in ethanol, indicating that mass had attached to the QCM-D chip and that the cleaning procedure thus allowed the thiols to bind to the surface (Appendix 4.6.2 — Figure 4.1).

Next, we switched the buffers to 150 mM of KCl in 1xTE and flushed 500 nM of BSA followed by TE buffer and 500 nM of Kap95. After switching back to TE buffer, we found a frequency shift of less than 5 Hz, which was much less than expected for untreated surfaces (Appendix 4.6.2 — Figure 4.2). This result indicates that the surface had been passivated against proteins adhering to the surface. While this was a promising result, we knew from previous experiments that even if a surface is passivated well enough on QCM-D, we might still see considerable effects of protein sticking in translocation experiments. Thus we determined a real proof of good passivation to be a linear relationship of concentration versus event rate in open pore experiments.

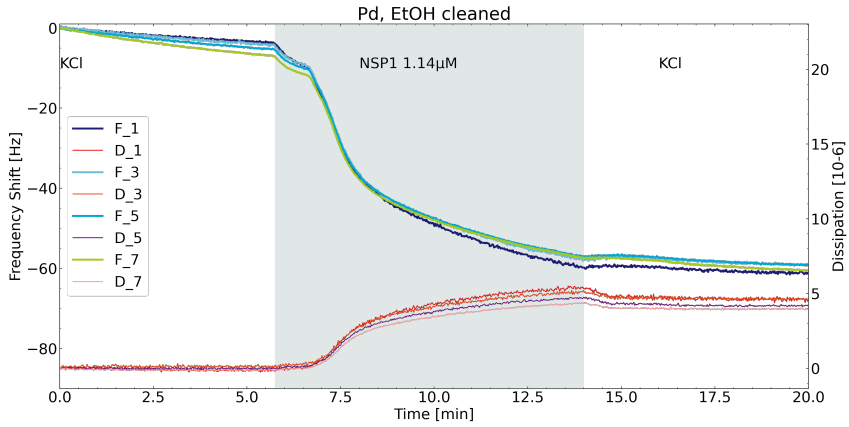
During our study, we noted that Pd nanopores could close upon incubation in PBS after peroxide cleaning. This effect was not observed for MUHEG coated pores that were incubated for extended time in ethanol after the peroxide cleaning. Thus we developed another cleaning strategy for Pd surfaces based on ethanol boiling, inspired by [41]. In order to test the capability to bind Nsp1 after this treatment, we performed a QCM-D experiment. The cleaned chip was flushed with 150 mM KCl + 1xTE buffer, then 1.14 μM of Nsp1 and then TE buffer again. The resulting frequency shift due to Nsp1 attachment was determined to be approximately 60 Hz (Appendix 4.6.2 — Supplementary Figure 4.3). This was comparable to previous experiments on piranha cleaned gold QCM-D chips. Since deducing a grafting density from QCM-D experiments was difficult, this serves more as a qualitative result and the actual test of sufficient grafting needed to be made in the nanopore.



Supplementary Figure 4.1: MUHEG grafting established on QCM-D. (A,B) The frequency (F1-F7) and dissipation (D1-D7) response of the different harmonics (numbers) for two QCM-D sensors versus time upon grafting of 250 μM MUHEG in ethanol (see [Cleaning and surface grafting of Pd](#)). The blue vertical lines show when the solution was switched in the flow cell. The grey shaded regions show the time when the solution was flowed through the flow cell. Upon MUHEG binding a decreasing frequency can be observed, which shows that mass attaches to the sensor's surfaces.

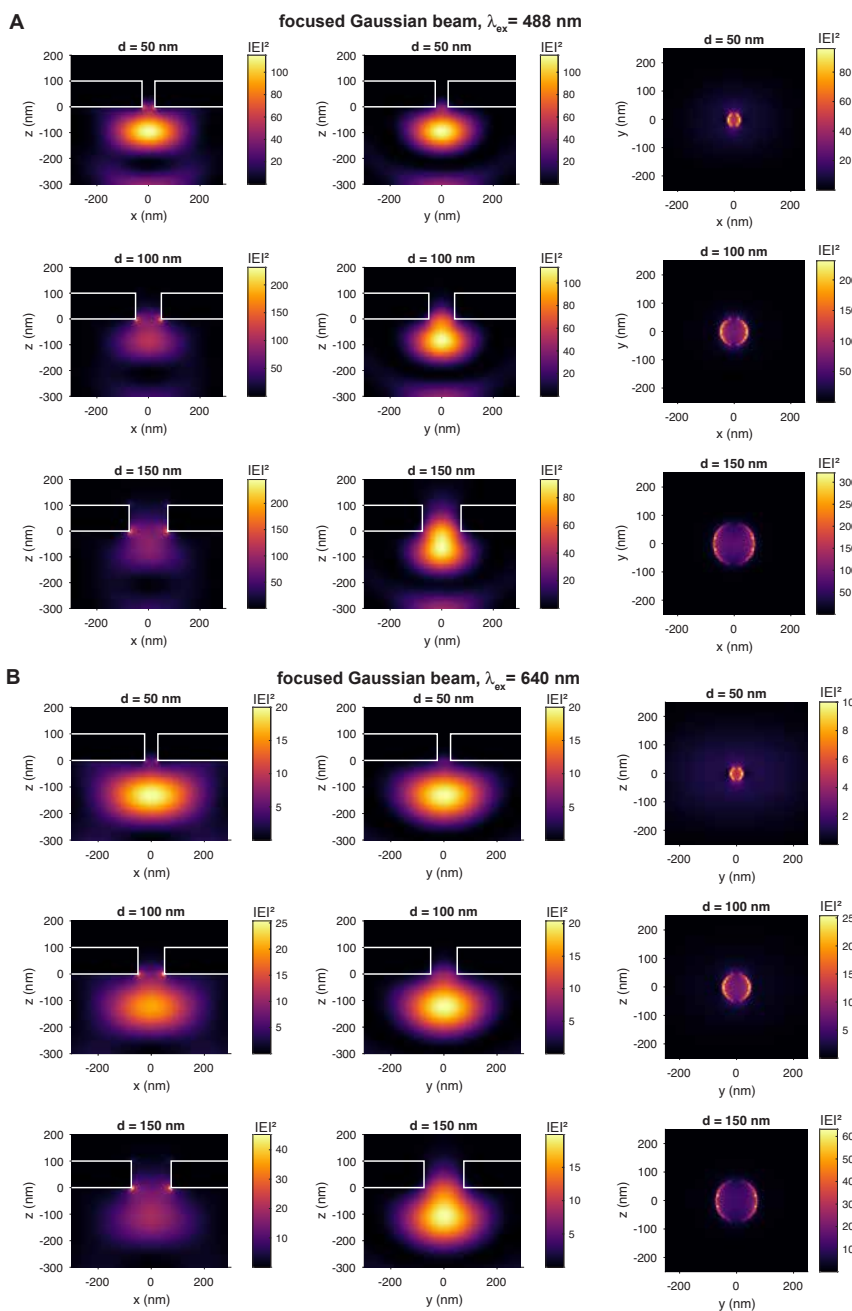


Supplementary Figure 4.2: MUHEG passivation established on QCM-D. (A,B) Same chips and setup as in Appendix 4.6.2 — Figure 4.1 The frequency response of flushing 500 nM of BSA and 500 nM of Kap95 over the MUHEG passivated surface of the QCM-D chips only shows a minor frequency shift of less than 5 Hz (KCl level before and after flushing the proteins). This suggests that the Pd surface can be effectively passivated against adhering proteins by a MUHEG coating.

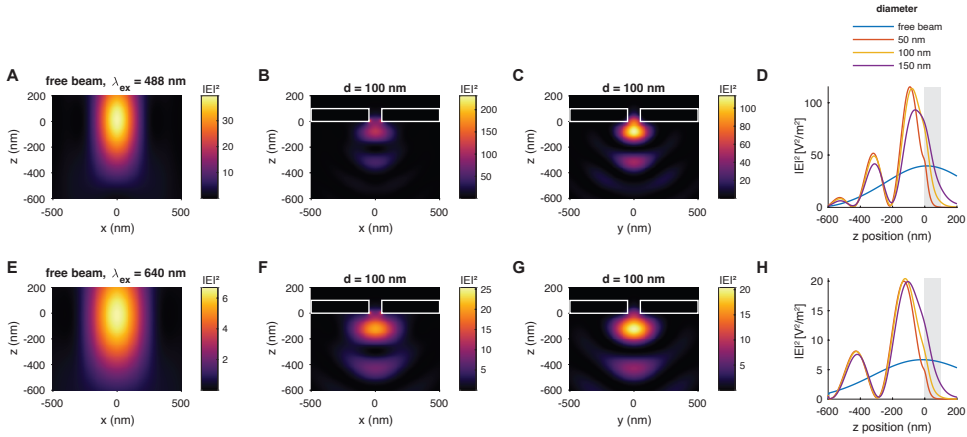


Supplementary Figure 4.3: Nsp1 binding on QCM-D The frequency (F1-F7) and dissipation (D1-D7) response of the different harmonics (numbers) for a Pd coated QCM-D sensors versus time upon grafting of 1.14 μM Nsp1 in PBS. The QCM-D chip was cleaned by boiling ethanol (see [Cleaning and surface grafting of Pd](#)). The frequency shift from before the Nsp1 coating to after was approximately 60 Hz which shows an acceptable coating efficiency. Nsp1 was flushed in the grey shaded area.

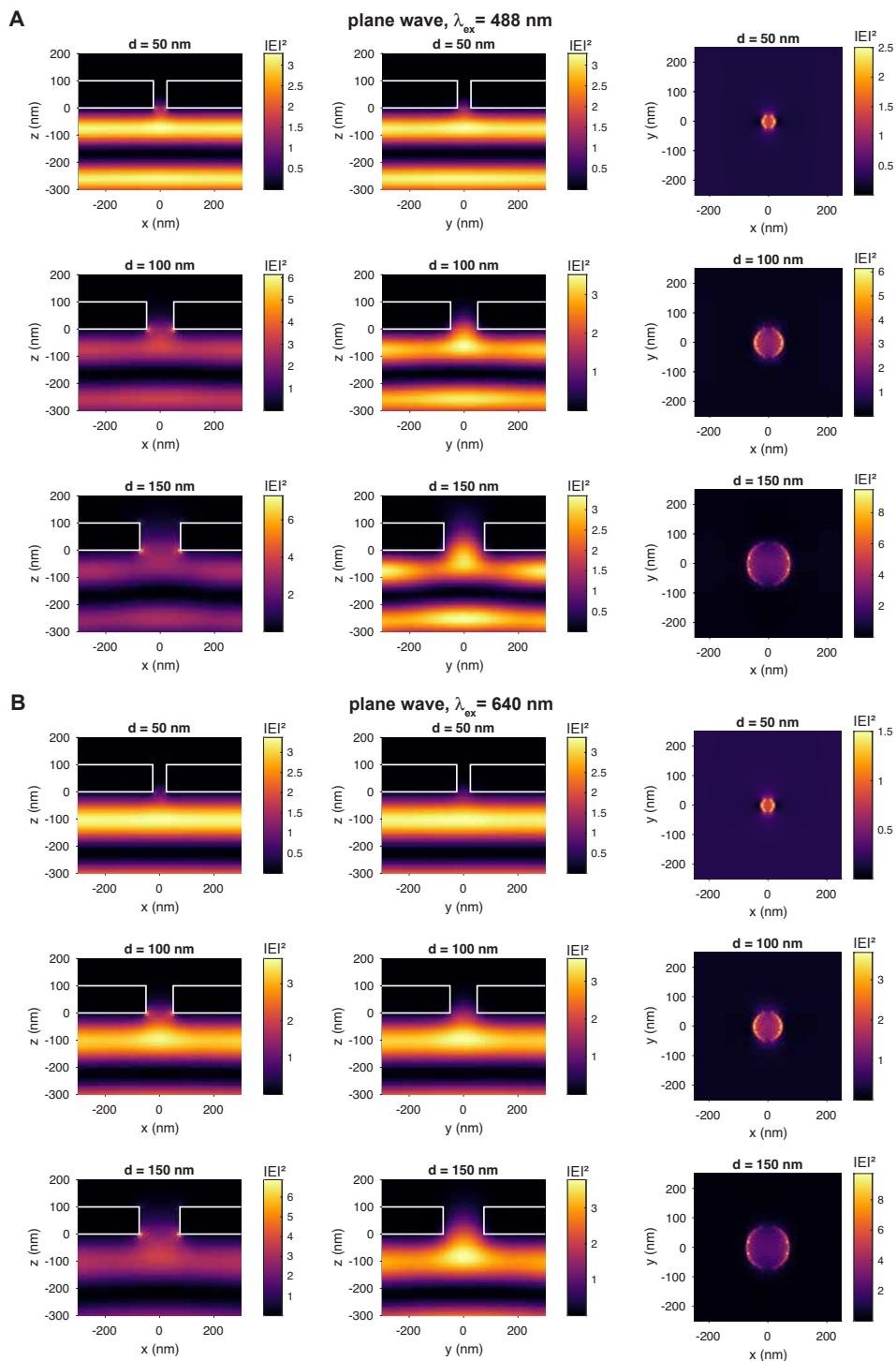
4.6.3. FINITE-DIFFERENCE TIME DOMAIN (FDTD) SIMULATIONS



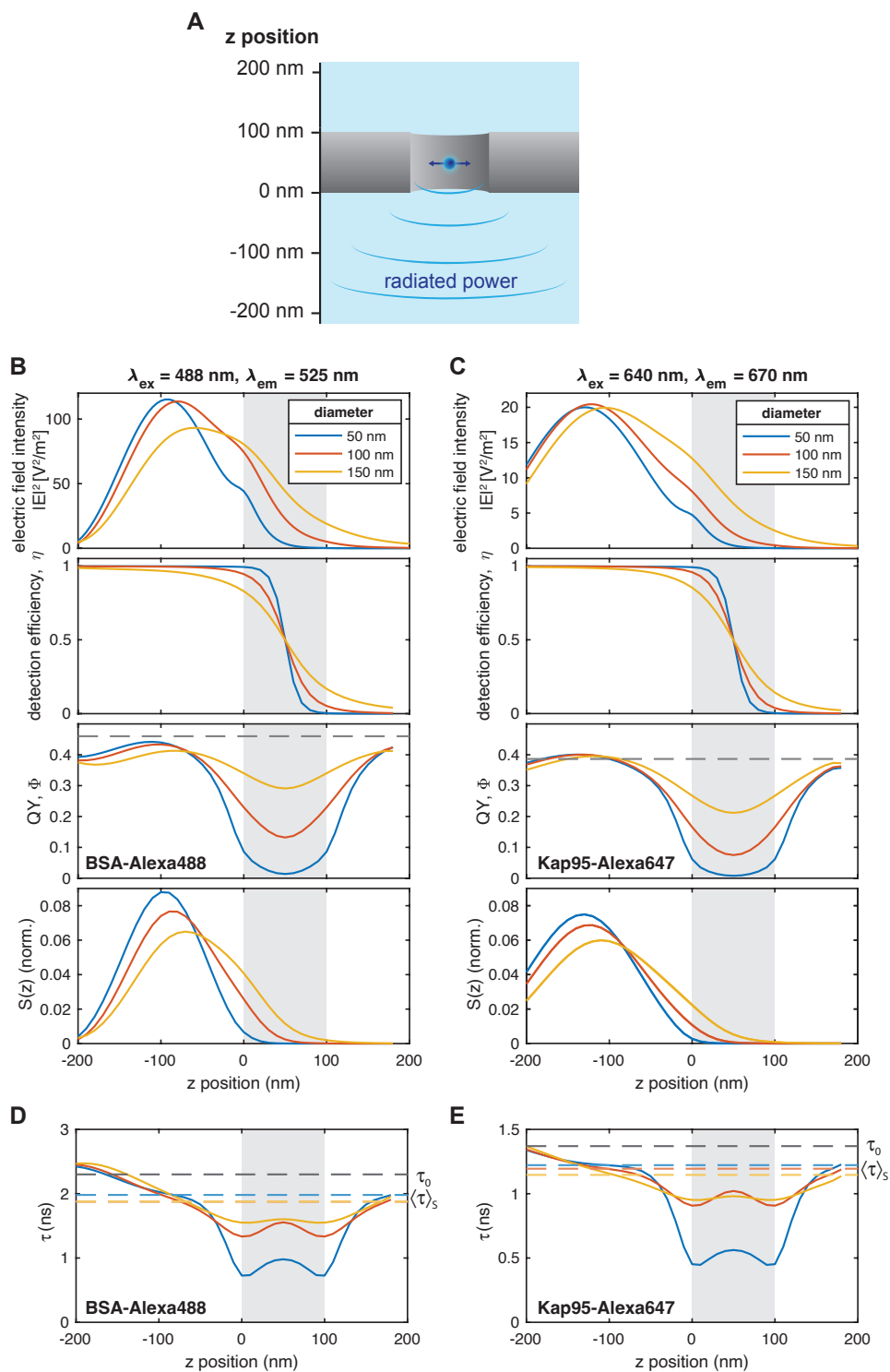
Supplementary Figure 4.4: Threedimensional finite-difference time-domain simulations of the electric field intensity distribution $|E|^2$ in units of V^2/m^2 in the proximity of the ZMW for excitation by a diffraction-limited focused Gaussian beam with wavelengths of 488 nm (A) and 640 nm (B). The lower side of the 100 nm thick palladium membrane is placed at $z = 0$ nm. The source is located at the bottom and the electric field is polarized in the x-direction. The electric field intensity distributions are shown for pores with a diameter of 50, 100, and 200 nm (from top to bottom) in the xz (left) and yz (middle) planes passing through the center of the pore, and the xy (right) plane at the entrance to the pore at $z = 0$ nm. See Appendix 4.6.3 — Supplementary Figure 4.5 for a zoomed out representation of the intensity distribution.



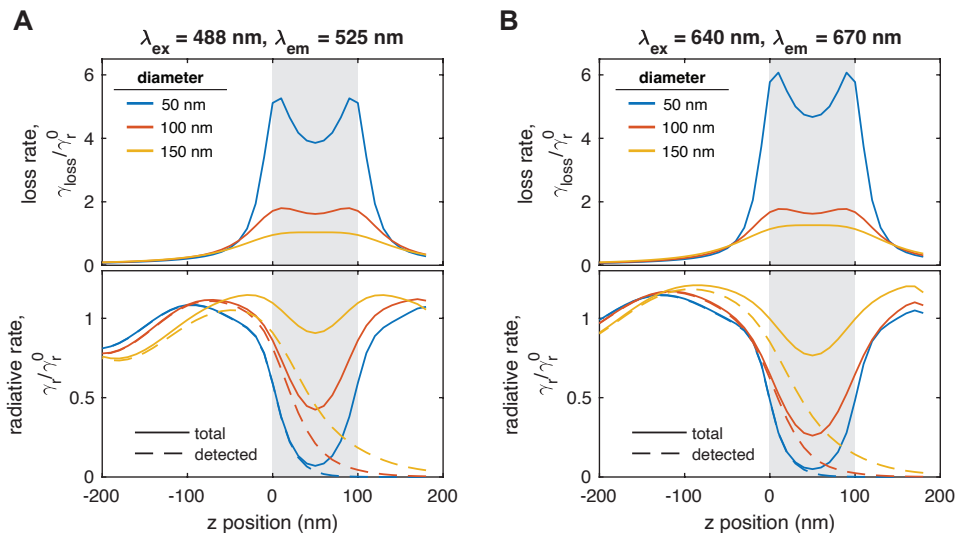
Supplementary Figure 4.5: Threedimensional finite-difference time-domain simulations of the electric field intensity distribution of the excitation spot in the presence of a freestanding ZMW (compare Appendix 4.6.3 — Supplementary Figure 4.4), at excitation wavelengths of 488 nm (A-D) and 640 nm (E-H). Shown are the intensity distributions of the focused Gaussian beam in the absence (A,E) and presence (B-C,F-G) of the freestanding palladium ZMW. (D,H) The z-profiles of the intensity distribution along the center of the pore. The position of the palladium membrane is indicated as a gray shaded area.



Supplementary Figure 4.6: Threedimensional finite-difference time-domain simulations of the electric field intensity distribution $|E|^2$ in units of V^2/m^2 in the proximity of the ZMW for excitation by a plane wave with wavelengths of 488 nm (A) and 640 nm (B). The lower side of the 100 nm thick palladium membrane is placed at $z = 0$ nm. The source is located at the bottom and the electric field is polarized in the x-direction. The electric field intensity distributions are shown for pores with a diameter of 50, 100, and 200 nm (from top to bottom) in the xz (left) and yz (middle) planes passing through the center of the pore, and the xy (right) plane at the entrance to the pore at $z = 0$ nm.



Supplementary Figure 4.7: Finite-difference time-domain simulations of the dipole emission in the proximity of the freestanding ZMW. (A) A scheme of the simulation setup. The dipole is placed in the center of the pore in the xy plane at varying z-positions. The detected signal is monitored on the detection (i.e., lower) side. (B-C) From top to bottom: The z-profiles of the excitation probability, the detection efficiency η , the emitter quantum yield Φ , and the total detected signal, along the center of the nanopore are shown for the blue (B, $\lambda_{ex} = 488$ nm, $\lambda_{em} = 525$ nm) and red (C, $\lambda_{ex} = 640$ nm, $\lambda_{em} = 670$ nm) channels. The total detected signal $S(z)$ is defined as the product of the excitation intensity, detection efficiency, and quantum yield. (D-E) Predicted fluorescence lifetimes τ of BSA–Alexa488 and Kap95–Alexa647. The position of the palladium membrane is indicated as a gray shaded area. The weighted averages of the fluorescence lifetime based on the detected signal $S(z)$, $\langle \tau \rangle_S$, are shown as colored horizontal dashed lines. The gray dashed line indicates the measured fluorescence lifetime τ_0 in the absence of the ZMW. The predicted signal-averaged lifetimes $\langle \tau \rangle_S$ are 1.98, 1.88, and 1.88 ns for BSA–Alexa488, and 1.22, 1.95, and 1.15 ns for Kap95–Alexa647, for pore diameters of 50, 100, and 150 nm, respectively (see eq. 4.13). The quantum yields and fluorescence lifetimes were estimated based on a literature values of $\Phi_{\text{fit}} = 0.8$ and $\tau_{\text{fit}} = 4.0$ ns for Alexa488 [81], and $\Phi_{\text{fit}} = 0.33$ and $\tau_{\text{fit}} = 1.17$ ns for Alexa647 [82], and measured lifetimes in the absence of the ZMW of $\tau_0 = 2.3$ ns for BSA–Alexa488 and $\tau_0 = 1.37$ ns for Kap95–Alexa647 (compare Appendix 4.6.11 — Figure 4.15).

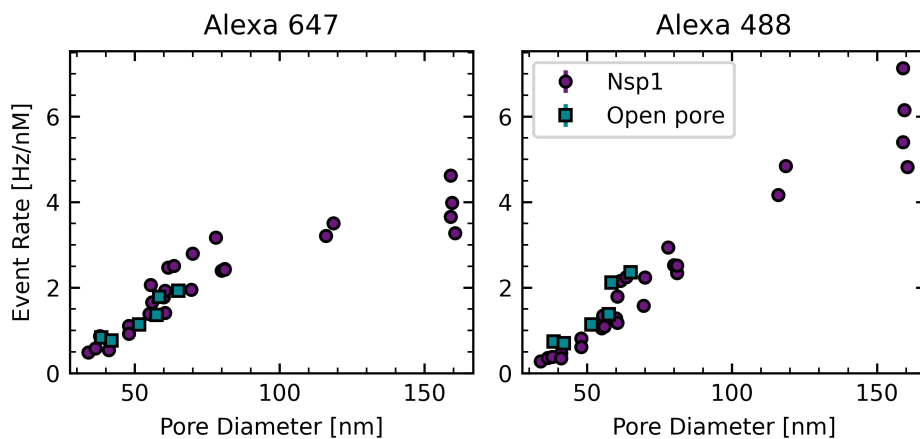


Supplementary Figure 4.8: Z-profiles of the radiative (emission) and non-radiative (loss) rates in the proximity of the freestanding ZMW obtained from FDTD simulations for the blue (A, $\lambda_{ex} = 488$ nm, $\lambda_{em} = 525$ nm) and red (B, $\lambda_{ex} = 640$ nm, $\lambda_{em} = 670$ nm) channels. The position of the palladium membrane is indicated as a gray shaded area. The z-axis is defined as in subsection 4.6.3–Supplementary Figure 4.7 A. For the radiative rate (bottom), the rate of emission directed towards the objective lens is displayed in addition as a dashed line. The normalized loss rate $\gamma_{\text{loss}}/\gamma_r^0$ and radiative emission rate γ_r/γ_r^0 are obtained by measuring the total power emitted by the dipole and comparing it to the power that is emitted into the far field, i.e., not absorbed by the metal. From these rates, the quantum yield Φ and fluorescence lifetime τ are computed according to eqs. 4.8 and 4.10. The ratio of the total emission rate and the rate of the detected emission (solid and dashes lines) is used to compute the detection efficiency η as given in eq. 4.11. See methods for details.

4.6.4. FREE ALEXA FLUOROPHORE TRANSLOCATION

At the end of a full experiment with BSA and KAP95, mixtures of 50 nM or 100 nM Alexa 647 and Alexa 488 were flushed into the reservoir to detect clogged pores from the absence of events for the small fluorophores. As expected, small fluorophores were barely hindered in their diffusion from the Nsp1 molecules in the pore. Notably, this contrasts

the findings of Ananth *et al.* [27], who reported only a residual conductance of (charged) ions through Nsp1-coated pores smaller than 40 nm, whereas we still found unhindered diffusion of free fluorescent dyes.



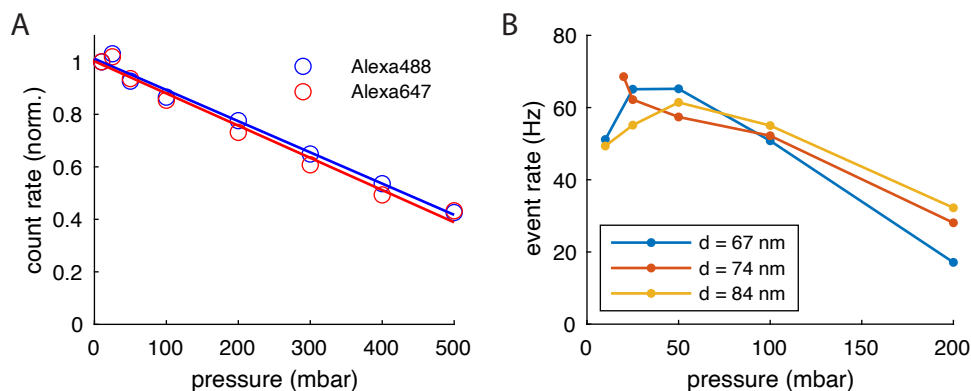
Supplementary Figure 4.9: Free fluorophore translocations (A) Event rate versus pore diameter for Alexa 647. (B) Event rate versus pore diameter for Alexa 488. The event rate of both fluorophores does barely change between Nsp1-coated pores and open pores.

4.6.5. INFLUENCE OF NEIGHBORING PORES

In order to estimate an upper limit on the event rate that is found at a pore location due to analytes that diffused into the detection region from adjacent pores, we looked for an experiment where a closed pore was neighbored by two unblocked pores. In an open pore experiment, we encountered such a setting, where the closed pore was identified by its very low event rate. Specifically, in this case, pore 6 had a diameter of 56 nm, pore 7 was closed and pore 8 had a diameter of 70 nm. The respective BSA translocation rates at 250 nM were: 36 Hz, 0.8 Hz, 93 Hz. Assuming that all events found on pore 7 were due to diffusion from their neighboring pores, this gives that on any pore less than $2\% \approx \frac{0.8 \text{ Hz}}{36 \text{ Hz}}$ of the events are not due to translocations through the pore itself but are due to diffusion from neighboring pores.

4.6.6. EFFECT OF PRESSURE-INDUCED HYDRODYNAMIC FLOW

In the experiments, we applied a constant flow to the microfluidic channel below the nanopore to continuously remove translocated analytes from solution by applying a pressure of 50 mbar. As a side effect, this will also induce a back flow through the pore from the detection side to the reservoir side, with a theoretical pressure difference over the membrane of 25 mbar. Because all experiments were performed under identical pressure, this effect should result in a constant reduction of the event rate and not affect the conclusions. To test the magnitude of the pressure-induced reduction of translocation rates, we performed control experiments on an open pore with a diameter of 76 nm using free fluorophores (Alexa488, Alexa647) at concentrations of 100 nM. At these con-



Supplementary Figure 4.10: Pressure-dependent reduction of translocation rates. **A)** A solution of the free fluorophores Alexa488 and Alexa647 at a concentration of 100 nM was placed in the reservoir. The signal count rate was monitored at the exit of a pore with a diameter of 74 nm as a function of the applied pressure to the flow channel. Count rates were normalized to the values obtained in the absence of a pressure difference. Due to the pressure-induced hydrodynamic flow against the concentration gradient, the translocation rates decrease linearly with the applied pressure. **B)** Event rates for Kap95 at a concentration of 1 μ M acquired for three different open pores with diameters in the range of 67–84 nm. The event rates decrease markedly at a high pressure of 200 mbar, but remain approximately constant in the range below 100 mbar.

centrations, it was not possible to detect single events owing to the high event rates, hence we quantified the total count rate detected at varying pressures. The normalized signal count rates as function of the applied pressure are shown in Appendix 4.6.4 — Figure 4.10A, showing the expected linear dependence as predicted by the Hagen-Poiseuille equation. At the applied pressure of 50 mbar, we observe an approximate 5% reduction of the detected count rate, suggesting only a minor effect of the pressure gradient on the observed translocation rates. This is confirmed by direct measurements of the Kap95 event rates for open pores as a function of the applied pressure (Appendix 4.6.4 — Figure 4.10B), which show only a minor effect of the pressure in the range below 100 mbar. However, at 200 mbar, event rates are approximately reduced by half, which exceeds the count rate reduction observed for the dye solution in panel A, most likely due to increased viscous drag acting on the larger protein compared to the small organic dyes. Note that the absolute event rates obtained for these experiments are not directly comparable to the results presented in the main text as the experiments have been performed on gold pores using a different cleaning protocol using acidic piranha etching.

4.6.7. SIGNAL-TO-BACKGROUND RATIO

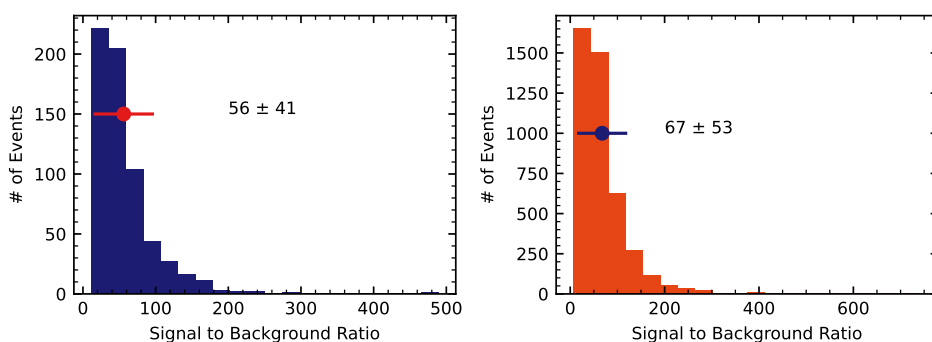
The single-molecule signal obtained in this study offers a significantly higher signal-to-background ratio compared to previous approaches. To illustrate this point, we compare the signal-to-background ratio in our experiments to the average signal-to-noise ratio for a comparable conductance based system [24].

By quantifying the event-wise signal-to-background ratios for the measurement shown in Figure 4.3, we estimate an average signal-to-background ratio of 56 ± 41 for BSA and 67 ± 53 for Kap95 (Supplementary Figure 4.11). Using a representative segment of a

1 min-long current trace of a Nsp1- coated pore with a diameter of 55 nm acquired under experimental similar conditions (TE buffer, pH=7.4, 150 mM KCl, 21 °C, 100 mV bias voltage), we estimate a current noise of 0.014 nA with a mean current of 3.139 nA (compare Fig. 1d in [24]). The average current blockade of single Kap95 translocations was reported to be to 0.08 nA at the applied voltage, which results in a signal-to-noise ratio of approximately 5.6 for conductance based experiments. Compared to a value of 67 reported here, the ZMW approach thus offers a more than 10-times better separation of spikes originating from single translocations events.

In [24], individual Kap95 translocations could only be resolved at low concentrations of 119 nM, above which single events were not visible due to an insufficient signal-to-noise ratio, as stated by the authors. Such a limitation does not exist for the ZMW approach, where we could detect single protein translocations also at high occupancy of Kap95 in Nsp1 coated pores. Moreover, as pointed out in the discussion section, the discrepancy between theoretically predicted translocation rates and experimentally measured translocation rates is orders of magnitude better for the ZMW approach compared to the conductance based readout. We hence conclude that the capability to resolve single translocations is markedly improved for the ZMW-based fluorescence readout compared to the conductance based approach.

4



Supplementary Figure 4.11: Signal-to-background ratios of single molecule events Distributions of the signal-to-background ratio for BSA (left) and Kap95, defined as the ratio of the event signal to the average background signal. The background level was estimated as the average photon rate in the absence of fluorescently-labeled analytes. The dot represents the mean and the bar the standard deviation of the distribution.

4.6.8. MEASUREMENT SCHEME

The measurement scheme was the following:

- No Kap95
 - Measure PBS as a background reference
 - pre-incubate with 500 nM of BSA, wash it out with 250 nM of BSA
 - measure 250 nM of BSA
 - measure 500 nM of BSA
- Wash

- wash with PBS
- wash with 5 % Hexane-1-6-diol
- wash with PBS
- 100 nM Kap95
 - measure 100 nM of Kap95
 - measure 100 nM of Kap95 and 250 nM of BSA
 - measure 100 nM of Kap95 and 500 nM of BSA
- Wash
 - wash with PBS
 - wash with 5 % Hexane-1-6-diol
 - wash with PBS
- For some experiments an additional 200 nM of Kap95 measurement was performed at this point.
- 1000 nM Kap95
 - measure 1000 nM of Kap95
 - measure 1000 nM of Kap95 and 250 nM of BSA
 - measure 1000 nM of Kap95 and 500 nM of BSA
- Wash with PBS
- Measure 50 nM of Alexa 488 and 50 nM of Alexa 647 in PBS.

Changing the analyte in the reservoir was done by replacing the volume at least three times. After changing the contents of the reservoir, a new transmission light scan of all pores was performed to obtain the accurate locations. Subsequently each pore was measured one after another.

Hexane-1-6-diol (Sigma-Aldrich) was diluted to 5 % in 150 mM KCl with 1xTE buffer.

4.6.9. DETAILED DIFFUSION MODEL

We explored how well the translocation rates can be accurately described by a diffusion model. In theory, the event rates should follow a diffusion model based on Fick's law. For reference, such a model was fit to the individual data points underlying the averages shown in [Figure 4.4 A-D](#) based on Fick's law of diffusion:

$$k_{\text{Prot}} = \alpha \pi r^2 D_p(r) \frac{\Delta c}{L}, \quad (4.14)$$

where k_{Prot} is the translocation rate, r the pore radius, Δc the concentration difference between cis and trans, and L the length of the pore. The scaling factor α accounts for deviation from the ideal behavior due to protein pore interactions and events missed by the detection algorithm. $D_p(r)$ is the reduced diffusion coefficient due to confinement

in the pore and is calculated as given by Dechadilok and Deen [48]:

$$\begin{aligned} \frac{D_p(r)}{D} = & 1 + \frac{9}{8} \left(\frac{R_g}{r} \right) \ln \left(\frac{R_g}{r} \right) - 1.56034 \left(\frac{R_g}{r} \right) + 0.528155 \left(\frac{R_g}{r} \right)^2 + 1.91521 \left(\frac{R_g}{r} \right)^3 \\ & - 2.81903 \left(\frac{R_g}{r} \right)^4 + 0.270788 \left(\frac{R_g}{r} \right)^5 + 1.10115 \left(\frac{R_g}{r} \right)^6 - 0.435933 \left(\frac{R_g}{r} \right)^7, \end{aligned} \quad (4.15)$$

where R_g the radius of gyration of the protein ($R_g = 3.15$ nm for Kap95 and $R_g = 2.68$ nm for BSA as determined from their crystal structures) and D is the diffusion coefficient which was obtained from FCS measurements as $D = 46 \mu\text{m}^2/\text{s}$ for Kap95 and $D = 54 \mu\text{m}^2/\text{s}$ for BSA at 21 °C. As an alternative analysis, this model was fitted using the least-squares method to the individual data points underlying the averages from Figure 4.4 in the main text, as shown in Appendix 4.6.10 — Supplementary Figure 4.12. The open pore data as well as the Nsp1-pore data for Kap95 can be well fitted by the diffusion model. The BSA-rates through Nsp1 pores, however, can not be described with a single diffusion model. Inspired by the opening of the Nsp1 mesh seen in the CGMD simulations, we introduced a threshold, where the translocation rates would follow a different diffusion regime. We note however, that in this transition region between 48 nm and 55 nm the data is better described by the shifted quadratic function.

4.6.10. FITTING OF TRANSLOCATION RATES

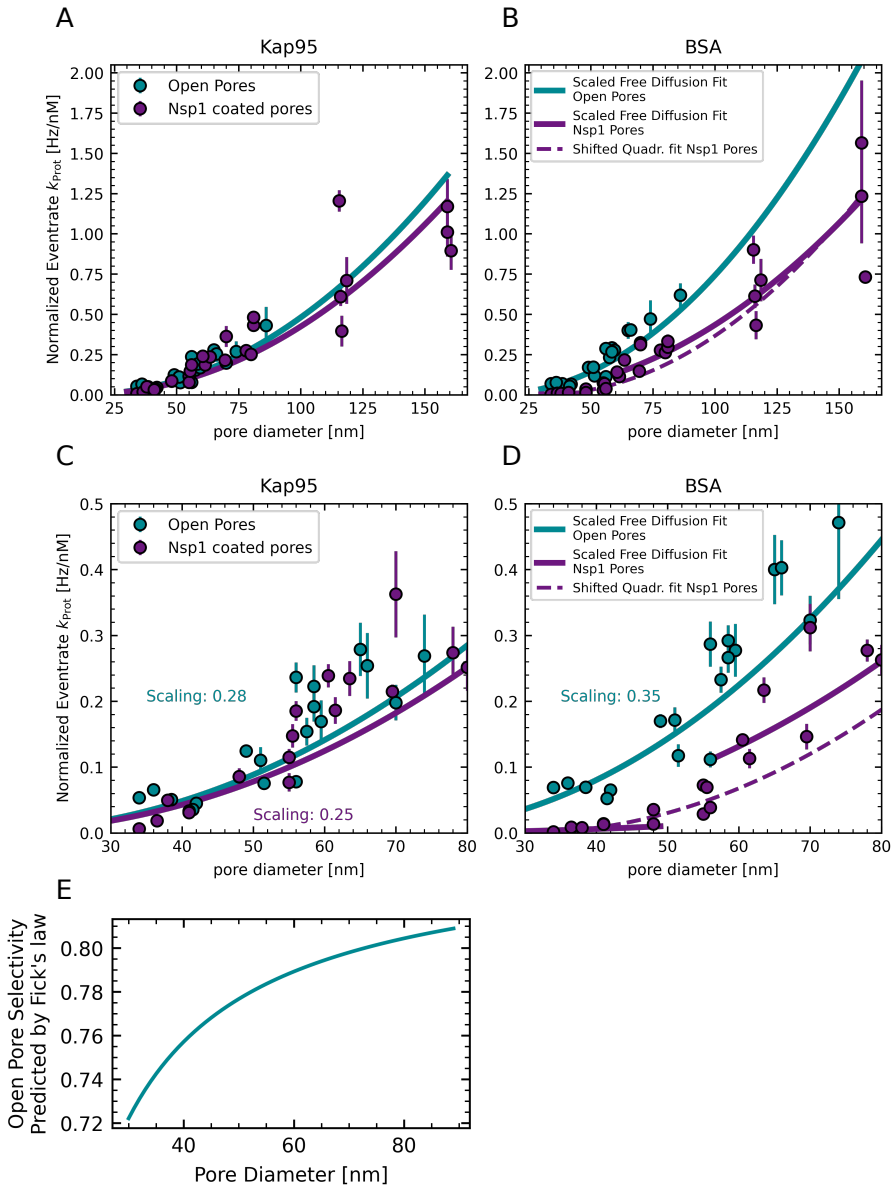
For congruence with the computational data, we fit a simplified diffusion model to the individual data points underlying the averages presented in Figure 4.4 using a quadratic function:

$$k_{\text{Prot}} = \alpha (r - r_{\text{Prot}})^2, \quad (4.16)$$

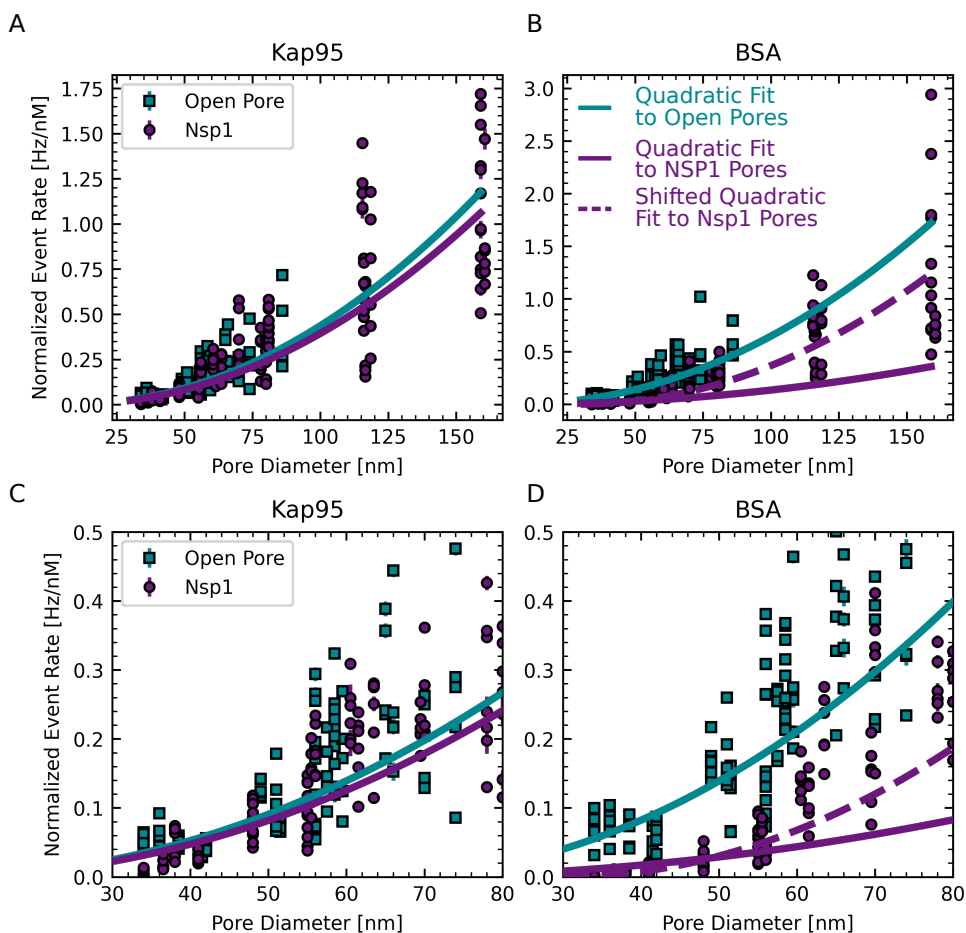
where k_{Prot} is the concentration-normalized translocation rate, r is the pore radius, r_{Prot} the protein's equivalent radius as proposed by Winogradoff *et al.* [54] (see Appendix 4.6.13 for details), and α a multiplicative scaling factor incorporating all factors such as concentration gradient, pore length, etc. All fits were performed using a least squares fitting, taking a statistical error on the individual event rates into account. This error was estimated from Poisson statistics, where the number N of events within a timetrace leads to $\Delta N = \sqrt{N}$. α was fitted individually on the event rates of Kap95 through open and Nsp1-coated pores. Additionally, the BSA event rates through open pores were fitted separately. The parameter α resulting from the BSA translocations for open pores, was used as a fixed parameter when fitting the BSA event rates through Nsp1-coated pores with a shifted and reduced quadratic function:

$$k_{\text{Prot}} = \alpha (r - r_{\text{Prot}} - b)^2, \quad (4.17)$$

where b is a shift parameter introduced to take into account a further reduction of the BSA event rate at small pore diameters.



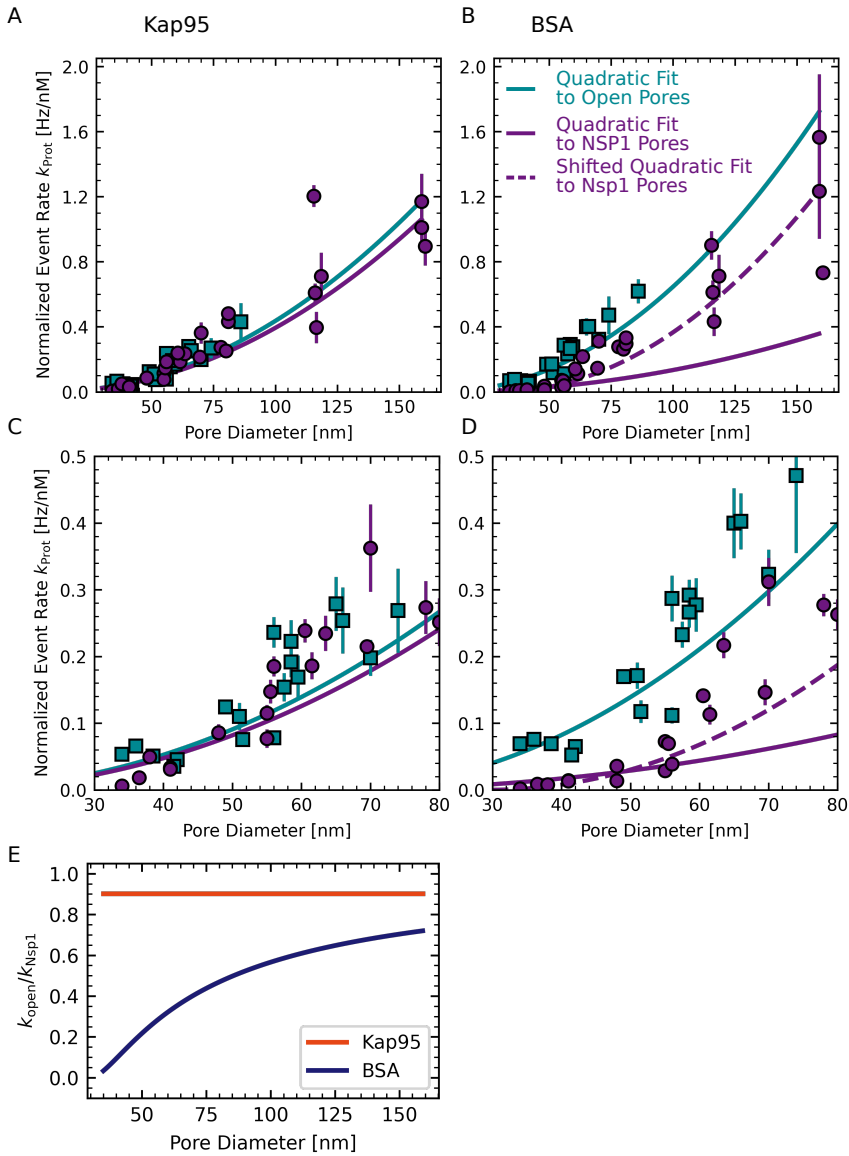
Supplementary Figure 4.12: (A,B) Normalized and averaged event rate vs. pore diameter as in [Figure 4.4](#). Solid lines are fits of a diffusion model as described in this section. A single fit for BSA through Nsp1 would deviate both for small and large pore diameters. Therefore the dataset was split into two regimes: Below 50 nm and above 60 nm in order to fit the data. This threshold was inspired by the results of the CGMD simulations. The dashed line shows a fit of the shifted quadratic function to the BSA data through Nsp1 pores as described in the main text. (C,D) Zoom ins of (A,B). E: Selectivity of open pores, predicted by the diffusion model. The value is pore size dependent because of the different sizes of Kap95 and BSA.



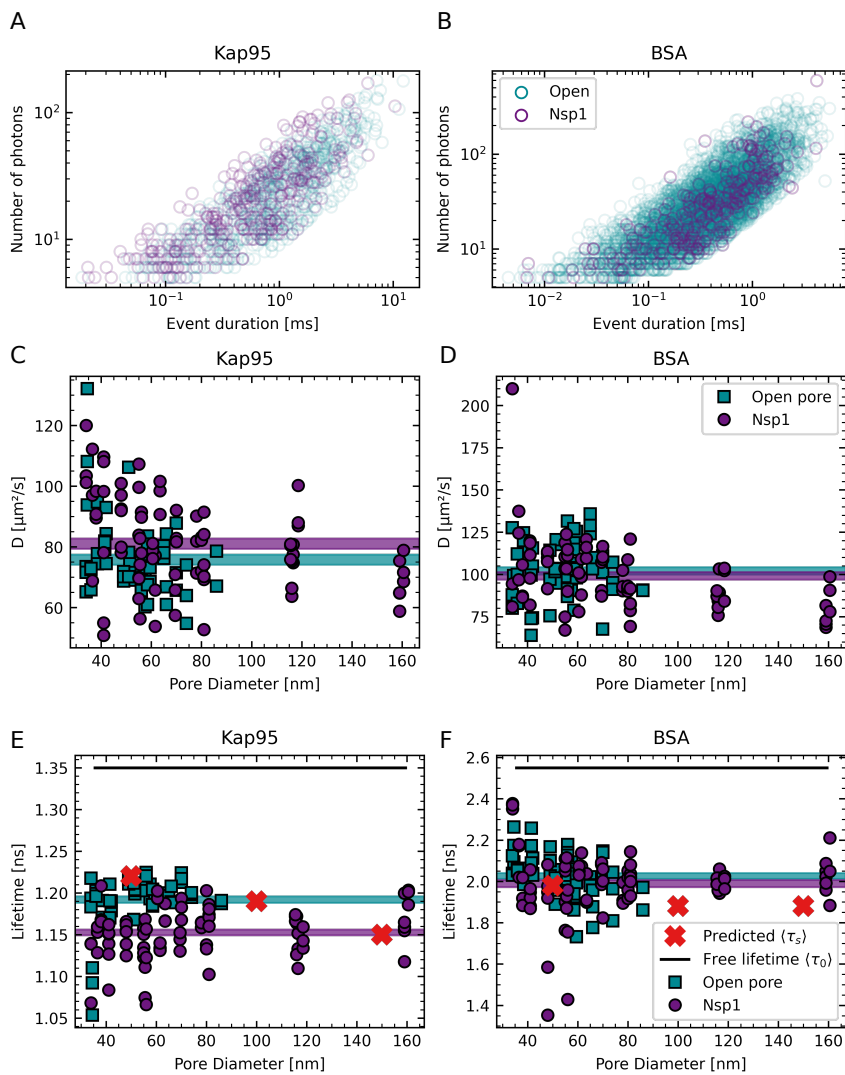
Supplementary Figure 4.13: (A,B) Normalized event rate vs. pore diameter of the individual conditions underlying the points shown in Figure 4.4. Solid lines are fits of a quadratic function as given in Equation 4.16. The BSA event rates through Nsp1-coated pores were not well described by the quadratic function. Therefore, a shift parameter was introduced as given in eq. Equation 4.17 (dashed line). (C,D) Zoom ins of (A,B).

4.6.11. DIFFUSION COEFFICIENTS AND FLUORESCENCE LIFETIMES

Our measurements provide additional information on the diffusivity of the proteins and the fluorescence lifetime of the fluorophores (Appendix 4.6.11 — Figure 4.15). From this, we can gain additional insight on the interaction of the proteins with the Nsp1 mesh within the pore. Interestingly, we do not observe a significant hindrance of the diffusivity for either BSA or Kap95, despite the known interaction of Kap95 with the FG repeats of the Nsp1 mesh. This indicates that the dynamic and multivalent interactions do not markedly slow down the diffusion of Kap95. Alternatively, it is possible that the fluorescence signal of the interacting species is quenched due to the close proximity to the metal surface due to metal-induced electron transfer [87]. This would render it impossi-



Supplementary Figure 4.14: (A,B) Normalized and averaged event rate vs. pore diameter as in Figure 4.4. Solid lines are fits of a quadratic function as given in Equation 4.16. The fit for BSA through Nsp1 deviates both for small and large pore diameters. Therefore a shift parameter was introduced as given in Equation 4.17 to fit the data (dashed line). (C,D) Zoom ins of (A,B). (E) Open pore event rates obtained from the quadratic fit divided by Nsp1 pore event rates obtained from the quadratic fit vs. pore diameter. While there is barely any decrease of the event rate for Kap95 when Nsp1 is present, BSA experiences an approximately 10-fold decrease for small pores of 35 nm diameter. This ratio increases with pore diameter and approaches a value of 1 in the limit to very large pores.



Supplementary Figure 4.15: (A,B) Scatter plots of the events detected for Kap95 (A) and BSA (B) indicating the distributions of event duration and the amount of photons within an event for the data shown in Figure 4.3 C,D. Both distributions overlap, showing that the spike detection works equally for coated and open pores. (C,D) Plots of the diffusion coefficient vs. pore diameter for Kap95 and BSA, respectively. The diffusion coefficient is estimated by FCS analysis of the time traces obtained in the nanopore experiments at the highest protein concentration. The horizontal lines indicates the average diffusion coefficient and the width corresponds to twice the standard error of the mean. The average diffusion coefficient of both Kap95 and BSA shows no significant difference between open pores and Nsp1-coated pores. This indicates that interactions of the proteins with the Nsp1 mesh do not obstruct the diffusion. Alternatively, it is possible that the bound fraction is not detected in our experiments if it is close to the metal surface due to metal-induced quenching of the fluorescence signal. (E,F) Plots of the fluorescence lifetime vs. pore diameter for Kap95 and BSA, respectively. The fluorescence lifetime is calculated based on the individual time traces of the highest protein concentration. The mean (horizontal lines) with twice the standard error of the mean (width of the lines) gives an estimate of the spread. For both Kap95 and BSA, the average fluorescence lifetime is significantly lower than what is measured in open solution (black lines). This can be attributed to the influence of the nearby metal nanostructure on the radiative and non-radiative rates. The predicted lifetimes based on FDTD simulations are shown as red crosses (compare Appendix 4.6.3 — Supplementary Figure 4.7). Whereas for BSA the lifetime in Nsp1-coated pores and open pores does not differ significantly, there is a significant decrease of the fluorescence lifetime of Kap95 in Nsp1-coated pores compared to open pores. This suggests that Kap95 remains within the proximity of the pore for a longer time when Nsp1 is present.

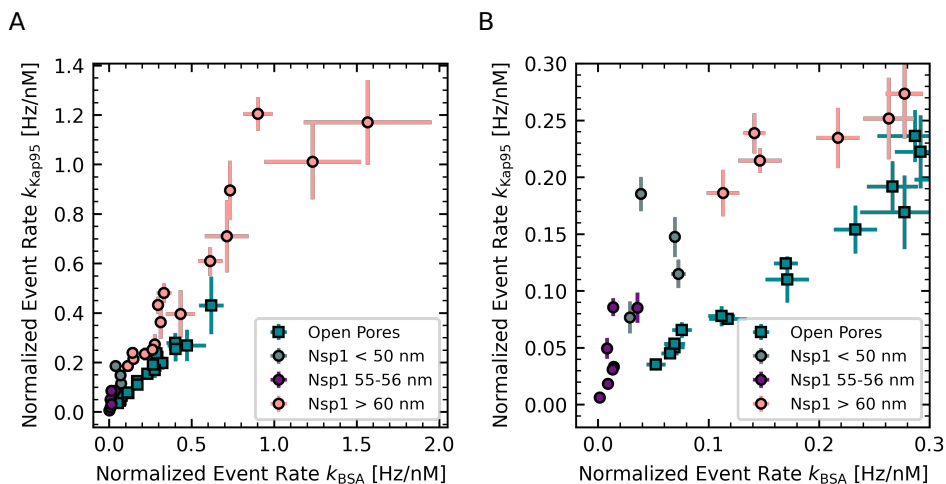
ble to detect the interactions because the detected signal would originate predominantly from freely diffusing molecules that have left the Nsp1 mesh.

Additional information on the photophysics is obtained from the fluorescence lifetime. We find a significant decrease of the fluorescence lifetime in the presence of the metal nanostructure (compared to open focus measurements) both for the dyes Alexa488 on BSA and Alexa647 on Kap95. Note that this lifetime reduction can originate both from metal-induced quenching [87] or a radiative rate enhancement within the zero-mode waveguide [34]. FDTD simulations of the dipole emission confirm that the fluorescence lifetime is shortened in the proximity of the metal nanostructure (Appendix 4.6.3 — Supplementary Figure 4.7 D-E) and provide good qualitative agreement with the measured fluorescence lifetimes of translocating molecules (see red crosses in Appendix 4.6.11 — Figure 4.15 E,F).

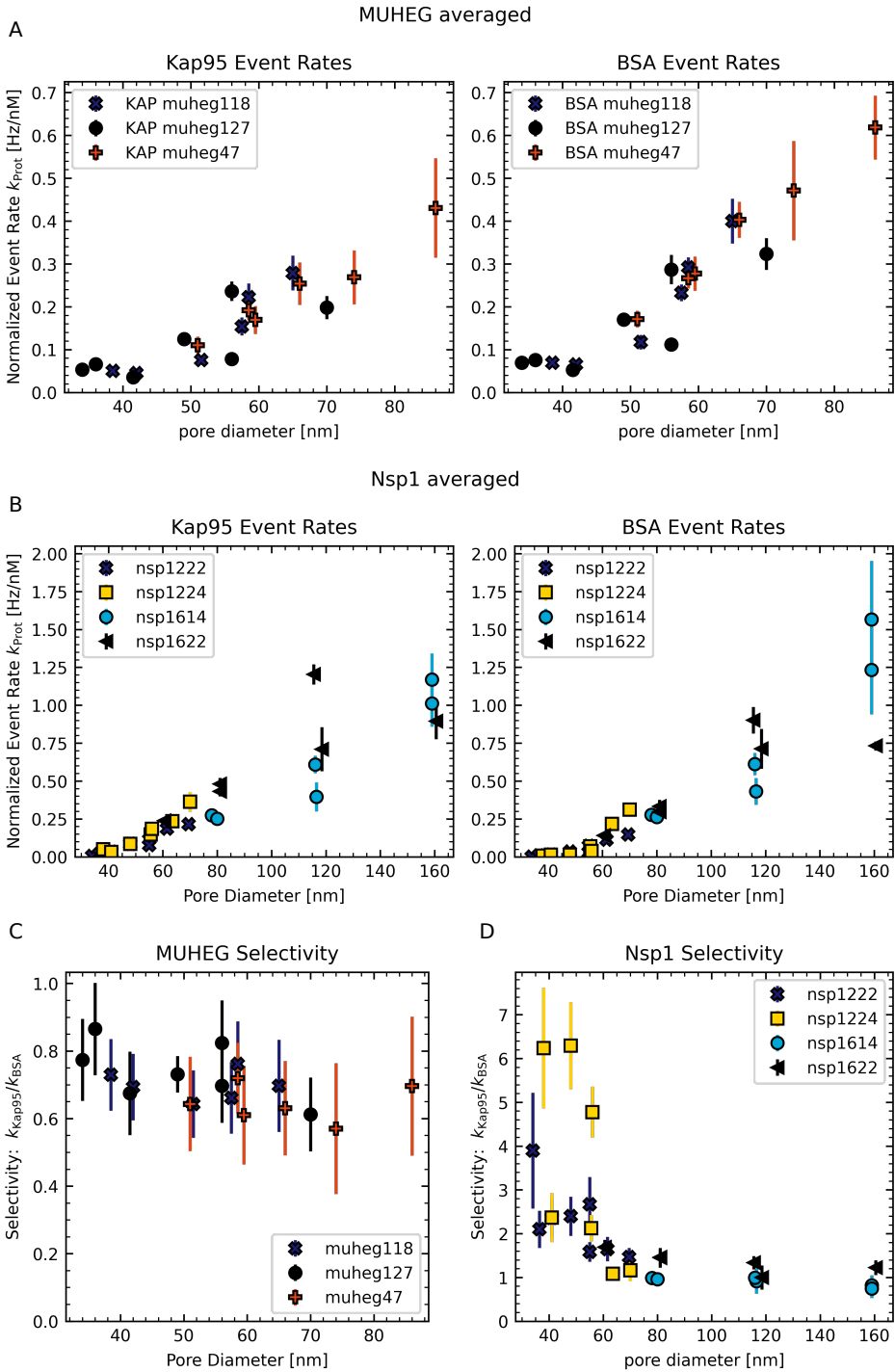
Whereas for BSA there was no difference between the fluorescence lifetimes obtained for Nsp1-coated pores and open pores, we found a small but significant reduction of the fluorescence lifetime for Kap95 for Nsp1-coated pores. This indicates that, in the presence of Nsp1, Kap95 molecules diffuse closer to or spend more time in proximity of the metal nanoaperture on the exit side. Intriguingly, it has recently been reported that Kap95 predominantly translocates along the periphery of the NPC [88], which falls in line with our observation of a stronger coupling to the metal nanoaperture.

4.6.12. DETAILED INSPECTION ON EVENT RATES

4



Supplementary Figure 4.16: Correlation between event rates for Kap95 and BSA. (A) Normalized event rates of Kap95 vs. BSA for small (purple) and large (pink) Nsp1-coated pores and open pores (cyan). The event rates show a high degree of correlation with correlation coefficients of 0.72, 0.93, and 0.98 respectively. Additionally pores with diameters of 55 nm to 56 nm are shown in grey. (B) zoom in of (A).



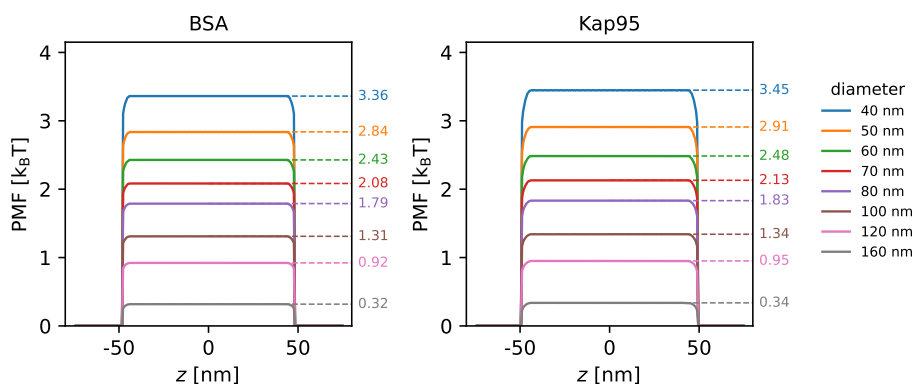
Supplementary Figure 4.17: (A, B) Normalized event rates for different open pore and Nsp1 pore experiments, respectively. The different data sets were highlighted according to their experimental day. A label for each experimental realisation is given in the legend. We don't observe any striking day-to-day variation. (C,D) Selectivity for different open pore and Nsp1 pore experiments. Also in the selectivity we don't observe a striking difference between experimental repetitions.

4.6.13. PROBE RADIUS OF BSA AND KAP95

To determine the radius of a protein (used in the void analysis and for fitting the event rates), we used the procedure as described in [54]. We started by computing the protein's moments of inertia, I_X , I_Y and I_Z , from the all-atom crystal structure. We then matched the moments of inertia of the protein with those of a constant density ellipsoid using $I_X = \frac{1}{5} m (b^2 + c^2)$, $I_Y = \frac{1}{5} m (a^2 + c^2)$ and $I_Z = \frac{1}{5} m (a^2 + b^2)$, where m is the total mass of the protein and a , b and c are the respective lengths of the three principal axes of the ellipsoid. To obtain the protein radius, we equated the volume of a sphere to the volume of the ellipsoid, i.e., $r_p = (abc)^{1/3}$. Using this method we find a probe radius of $r_p = 34\text{\AA}$ for BSA (PDB ID: 4F5S) and $r_p = 40\text{\AA}$ for Kap95 (PDB ID: 3ND2).

4.6.14. FITTING CALCULATED EVENT RATES FOR OPEN PORES

To obtain the scaling constant, k_0 , of the Arrhenius relation, we fitted the calculated event rates for open pores, obtained from the PMF barriers using the Arrhenius relation, to the (concentration-normalized) experimental open pore event rates (see Appendix 4.6.10 for fitting procedure). We note that the calculated event rates for open pores follow Equation 4.2 exactly. We therefore scaled the calculated event rates such that they align with the fits in Figure 4.4 A,B (cyan lines) and used the same constant $k_{0,BSA}$ to the Arrhenius relation for Nsp1-coated pores.

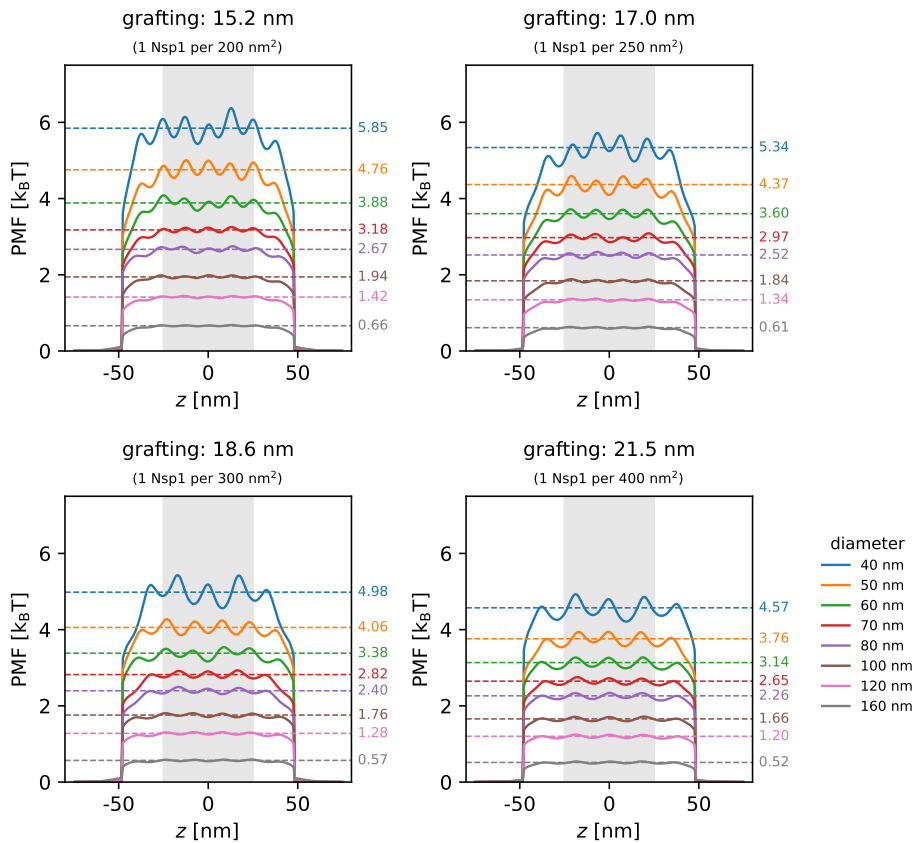


Supplementary Figure 4.18: Potentials of mean force along the pore axis of open pores with various diameters derived from void analysis using a probe radius of r_{probe} of 34\AA for BSA and 40\AA for Kap95. The numbers next to the dashed lines indicate the permeability barriers ΔE .

4.6.15. POTENTIAL OF MEAN FORCE FOR NSP1-COATED PORES

The Nsp1 proteins in our simulations were anchored to the surface in a triangular fashion to achieve a homogeneous grafting density across the entire scaffold. We note that

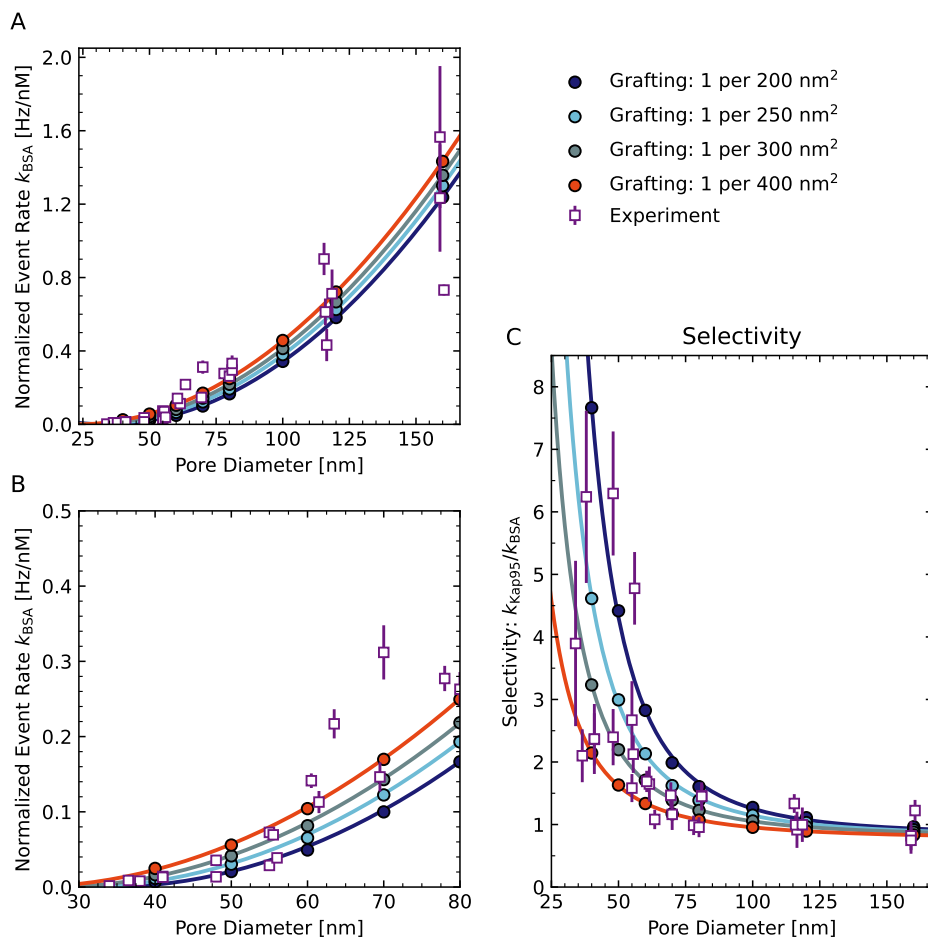
the location of the peaks in the PMF curves align with the z -coordinates of the Nsp1 anchor sites. Although the anchor sites clearly contribute to the translocation barrier, it would not be correct to use the maximum PMF as the energy barrier for translocation, as the idealized anchoring of Nsp1 on the scaffold is not a good approximation of the experiments (where Nsp1 is not anchored at discrete z -positions). Instead, to obtain a correct estimate of the energy barrier, ΔE , we used the average PMF for $-25 \text{ nm} \leq z \leq 25 \text{ nm}$.



Supplementary Figure 4.19: Potentials of mean force along the pore axis of Nsp1-coated pores with various diameters and grafting densities using a probe radius of $r_{\text{probe}} = 34 \text{ \AA}$ (BSA) derived from void analysis. The height of the PMF barrier, ΔE given on the right of the plots, is obtained by averaging the PMF between $-25 \text{ nm} \leq z \leq 25 \text{ nm}$ (gray region). The location of the peaks in the PMF curves are at the same z -coordinates as the anchoring points of the Nsp1 proteins.

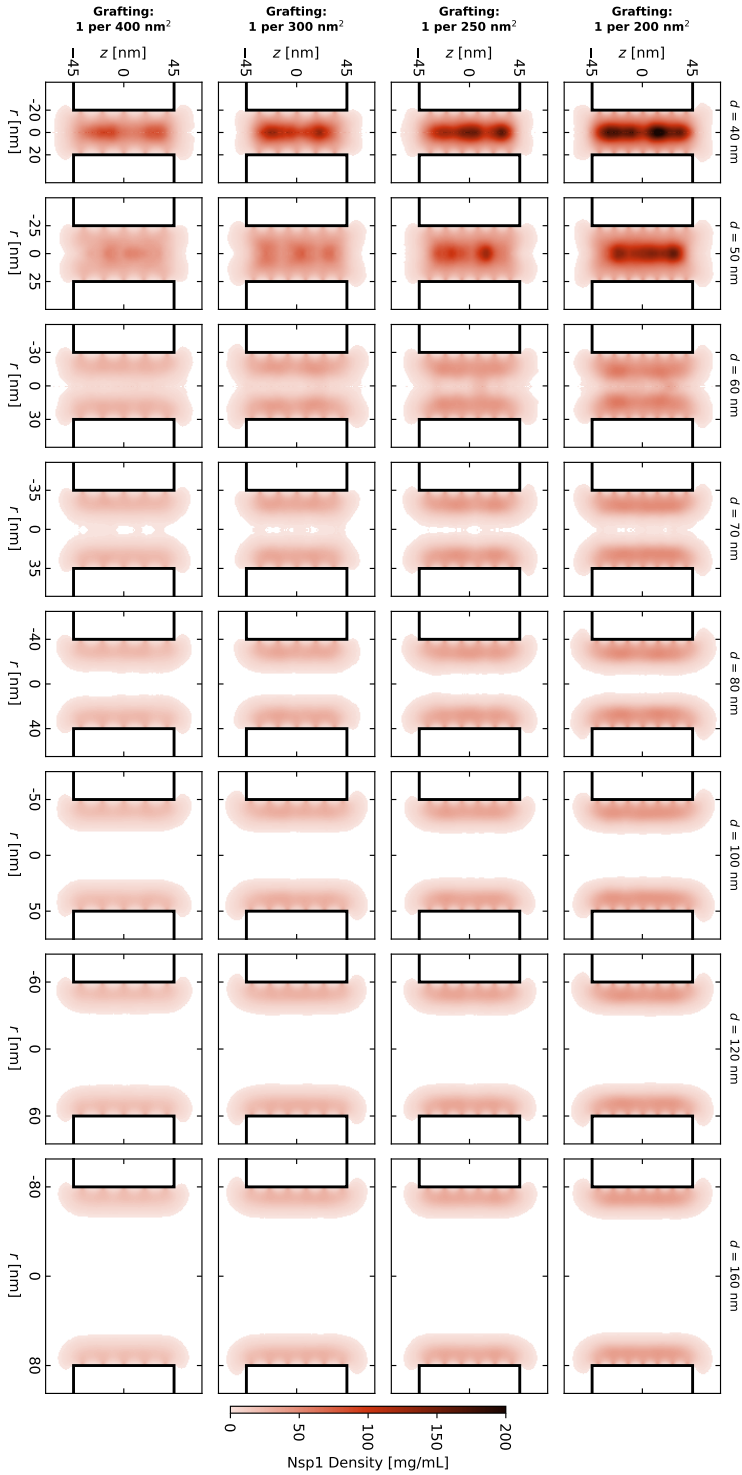
4.6.16. DEPENDENCE OF SELECTIVITY ON GRAFTING DENSITY

4



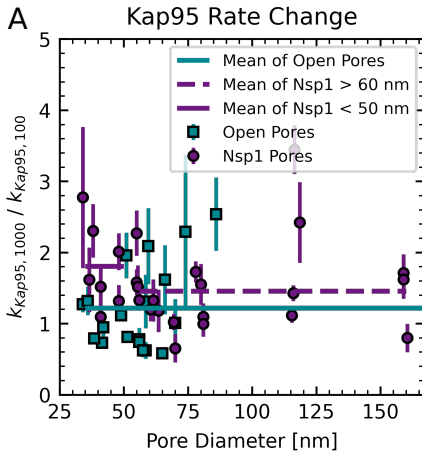
Supplementary Figure 4.20: Effect of grafting density on the selectivity of Nsp1 pores. (A) Calculated BSA event rates for Nsp1 pores for various grafting densities. (B) Zoom-in of A. (C) Apparent selectivity versus pore diameter, where the selectivity is calculated as the ratio of Kap95 to BSA event rates. For Kap95 we assumed that the event rate is the same for open pores and Nsp1 pores.

4.6.17. NSP1 DENSITY DISTRIBUTIONS



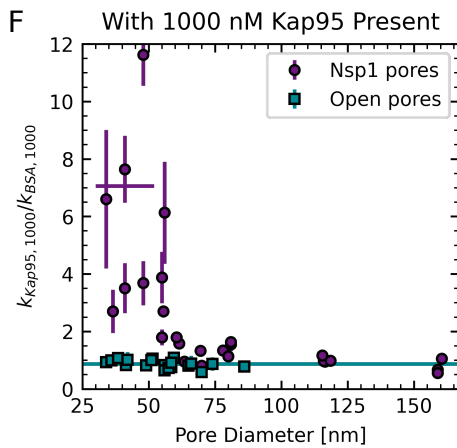
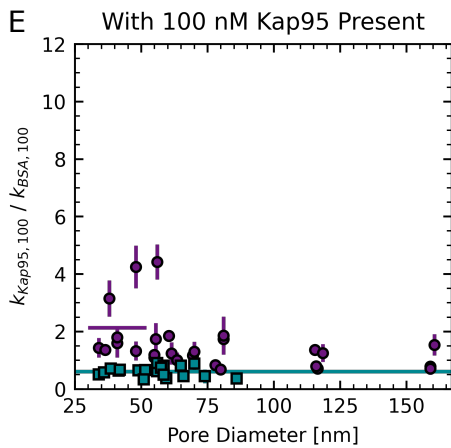
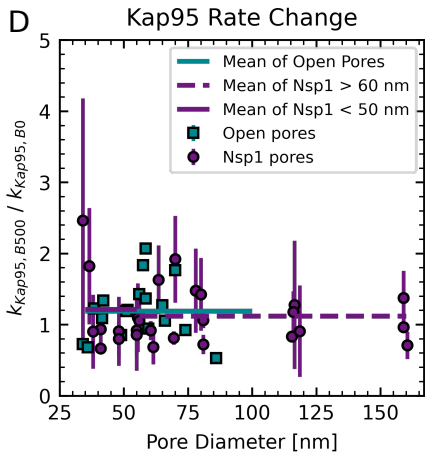
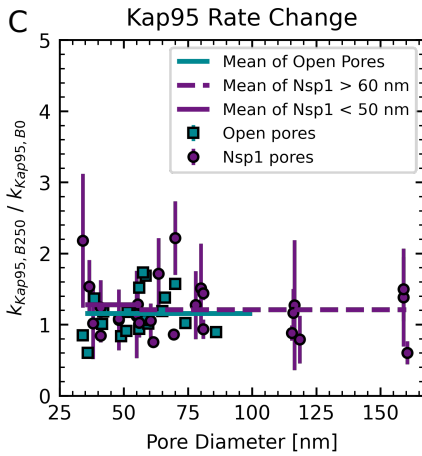
Supplementary Figure 4.21: Time-averaged r - z density distribution of Nsp1-coated nanopores for various diameters and grafting densities. Although there is a significant variation in the central channel densities for small diameter pores, the range of diameters at which the structural transition of the Nsp1 mesh takes place is largely independent of the Nsp1 grafting density in the range that was tested.

4.6.18. KAP95 RATE CHANGE



B

	Open Pores	Small Nsp1	Large Nsp1
$k_{Kap95,1000} / k_{Kap95,100}$	1.2 ± 0.1	1.8 ± 0.2	1.5 ± 0.2
$k_{Kap95,B100} / k_{Kap95,B0}$	1.2 ± 0.1	1.3 ± 0.2	1.2 ± 0.1
$k_{Kap95,B1000} / k_{Kap95,B0}$	1.2 ± 0.1	1.2 ± 0.3	1.1 ± 0.1
$k_{Kap95,100} / k_{BSA,100}$	0.61 ± 0.04	2.1 ± 0.4	
$k_{Kap95,1000} / k_{BSA,1000}$	0.87 ± 0.03	7.1 ± 1.6	



Supplementary Figure 4.22: (A) Rate change of Kap95 vs. pore diameter. Event rate of Kap95 at 1000 nM ($k_{\text{Kap95},1000}$) divided by the Kap95 event rate at 100 nM ($k_{\text{Kap95},100}$). At high Kap95 concentrations there is an increase in normalized event rate for both open and Nsp1 pores. It is largest for small Nsp1 pores. (B) The averages indicated in the plots by horizontal lines given with standard deviation estimated from fitting horizontal lines. (C,D) Influence of BSA concentration on Kap95 event rate. When dividing the Kap95 event rate with 250 nM of BSA being present $k_{\text{Kap95},\text{BSA}250}$ by the Kap95 event rate with 0 nM of BSA being present $k_{\text{Kap95},\text{BSA}0}$ (C) this shows that the Kap95 event rate is barely influenced by the presence of BSA, as expected. The same holds for the Kap95 event rate change with 500 nM of BSA to 0 nM being present. (E,F) Selectivity vs. pore diameter for different Kap95 concentrations. When switching from 100 nM of Kap95 to 1000 nM of Kap95, the selectivity of small Nsp1 pores increases by a factor of 3, whereas the selectivity of large pore decreases.

4.6.19. MODEL FOR THE RESIDUAL SELECTIVITY OF LARGE PORES

The model as presented in Figure 4.6 is based on the assumption a pore is occupied by two separate cross-sectional areas, a selective area and an unselective area, whereas no assumption over their location (such as a ring) is made. The full cross-sectional area A is thus divided as

$$A = A_{\text{open}} + A_{\text{Nsp1}}, \quad (4.18)$$

where A_{open} is the open (unselective pore area) and A_{Nsp1} is the selective (Nsp1-filled) area. Here, the selectivity S of a pore is defined as the ratio of Kap95 and BSA rates

$$S = \frac{k_{\text{Kap95}}}{k_{\text{BSA}}}, \quad (4.19)$$

which can be expressed in terms of the contributions of the two phases as

$$S = \frac{A_{\text{Nsp1}} l_{\text{Kap95}}^{\text{Nsp1}} + A_{\text{open}} l_{\text{Kap95}}^{\text{open}}}{A_{\text{Nsp1}} l_{\text{BSA}}^{\text{Nsp1}} + A_{\text{open}} l_{\text{BSA}}^{\text{open}}}, \quad (4.20)$$

where $l_{\text{protein}}^{\text{phase}}$ is the area normalized event rate constant for the respective protein in the different phases, i.e. open or Nsp1-filled.

Since we found experimentally the Kap95 event rates were unchanged by the presence of Nsp1, we approximate $l_{\text{Kap95}} \approx l_{\text{Kap95}}^{\text{open}} \approx l_{\text{Kap95}}^{\text{Nsp1}}$. The selectivity of a mixed phase pore is then given by:

$$S = \frac{l_{\text{Kap95}}}{l_{\text{BSA}}^{\text{Nsp1}} \frac{A_{\text{Nsp1}}}{A} + l_{\text{BSA}}^{\text{open}} \frac{A_{\text{open}}}{A}} = \frac{1}{\frac{l_{\text{BSA}}^{\text{Nsp1}}}{l_{\text{Kap95}}} \frac{A_{\text{Nsp1}}}{A} + \frac{l_{\text{BSA}}^{\text{open}}}{l_{\text{Kap95}}} \frac{A_{\text{open}}}{A}} = \frac{1}{\frac{1}{S_{\text{Nsp1}}} \frac{A_{\text{Nsp1}}}{A} + \frac{1}{S_{\text{open}}} \frac{A_{\text{open}}}{A}} \quad (4.21)$$

Note that this corresponds to the harmonic mean of the selectivities.

When considering the structure of the pore, the number of Nsp1 molecules in the pore is determined by the grafting density σ , the pore's radius r and length L as

$$N = 2\pi r \sigma L. \quad (4.22)$$

If we assume that each Nsp1 molecule renders a certain volume V selective, the effectively selective cross-sectional area can be calculated from the selective volume V_{Nsp1} as:

$$A_{\text{Nsp1}} = \frac{V_{\text{Nsp1}}}{L} = \frac{NV}{L} = 2\pi r \sigma V. \quad (4.23)$$

Thus, the selective area fraction depends on the pore radius as:

$$\frac{A_{\text{Nsp1}}}{A} = \frac{2\pi r}{\pi r^2} \sigma V = \frac{2}{r} \sigma V, \quad (4.24)$$

Combining both expressions for the selective area fraction, we obtain:

$$S = \frac{1}{\frac{1}{S_{\text{Nsp1}}} \frac{2}{r} \sigma V + \frac{1}{S_{\text{open}}} \left(1 - \frac{2}{r} \sigma V\right)} \quad (4.25)$$

where σV is the only fit parameter that we fit to the selectivities measured in [Figure 4.6](#).

Note that, if each Nsp1 molecule occupies the same volume V , the rim thickness would depend on the pore radius and the ring thickness h can be calculated using $A_{\text{Nsp1}} = \pi r^2 - \pi (r - h)^2$ as:

$$h = r - \sqrt{r^2 - 2r\sigma V}, \quad (4.26)$$

which requires $\sigma V < \frac{r}{2}$. For flat surfaces, where $r \rightarrow \infty$ the parameter $\sigma V \rightarrow h$ and σV can be represents the Nsp1 layer height in these cases. In the case of curved surfaces, the layer height needs to be calculated using [Equation 4.26](#). Notably, the assumption of constant volume that is applied here remains valid for situations where the Nsp1 phase is not localized in the rim, e.g. forming a central plug but is in contrast to previous models that assume a selective area (of whatever shape) similar in size to a ring of constant thickness, such as proposed by Kowalczyk *et al.* [26].

4.6.20. PROTEIN SEQUENCES

The sequence of the Nsp1 used in this study was:

MHHHHHHHHHHHGGSENLVYFQGTSMGNFNTTPQQNKTPFSFGTANNNSNTTNQNSSTG
 AGAFGTGQSTFGFNNSAPNNTNANSSITPAFGSNNTGNTAFGNSNPTSNVFGSNSTT
 NTFGSNSAGTSLFGSSSAQQTKSNGTAGGNTFGSSSLFNSTNSNTTKPAFGGLNFGGGN
 NTPPSSTGNANTSNNLFGATANANKPAFSFGATTNDDKKTEPDKPAFSFNSSVGNKTD
 QAPTTGFSFGSQLGGNKTVNEAAKPSLSFGSGSAGANPAGASQPEPTTNEPAKPALSFGTA
 TSDNKTTNTTPSFSFGAKSDENKAGATSKPAFSFGAKPEEKKDDNSSKPAFSFGAKSNEDK
 QDGTAKPAFSFGAKPAEKNNNETSKPAFSFGAKSDEKKGDDASKPAFSFGAKPDENKASA
 TSKPAFSFGAKPEEKKDDNSSKPAFSFGAKSNEDKQDGTAKPAFSFGAKPAEKNNNETSK
 PAFSFGAKSDEKKGDDASKPAFSFGAKSDEKKGDDSSKPAFSFGTGSNEKKGSSKPAFSF
 GAKPDEKKNDEVSKPAFSFGAKANEKKEDESDESASFSGSKPTGKEEGDGAKAAISFGAKP
 EEQKSSDTSKPAFTFGAQKDNKKTEC

The sequence of the GST-3C-Kap95 before removal of the GST tag and before labeling was:

MSPILGYWKIKGLVQPTRLLLEYLEEKYEEHLYERDEGDKWRNKKFELGLEFPNLPYYIDG
 DVKLTQSMARIYIADKHNMLGGCPKERAIEISMLEGAVLDIRYGVSRISYKDFETLKVDFL
 SKLPEMLKMFEDRLCHKTYLNGDHVTHPDFMLYDALDVVLYMDPMCLDAFPKLVCFKK
 RIEAIPQIDKYLKSSKYIAWPLQGWQATFGGGDHPPKSDLEVLVFGPASVSGSMSTAEFAQ
 LENSILSPDQNIIRLTSETQLKLSNDNLFQFAGLSSQVLIDENTKLEGRILAALTLKNELVSK
 DSVKTTQQAQRWITQVSPEAKNQIKTNALTALVSIEPRIANAAAQLIAAIADIELPHGAWPE
 LMKIMVDNTGAEQPENVKRASLLALGYMCESADPQSQUALVSSSNILIAIVQGAQSTETSK
 AVRLAALNALADSLIFIKNNMEREGERNYLMQVVCEATQAEDIEVQAAAFGCLCKIMSLYY

TFMKPYMEQALYALTIATMKSPNDKVASMTVEFWSTICEEEIDIA YELA QFPQSPLQSYNF
 ALSSIKDVVPNLLNLLTRQNEDEPDDDDWNVMSMSAGACLQLFAQNCGNHILEPVLEFVEQ
 NITADNWRNREAAVMAFGSIMDGPDKVQRITYYVHQALPSILNLMNDQSLQVKETTAWCI
 GRIADSVAESIDPQQHLPGVVQACLIGLQDHPKVATNCSWTIINLVEQLAEATPSPIYNFYF
 ALVDGLIGANRIDNEFNARASAFSALTTMVEYATDTVAETSASISTFVMDKLGQTMSVDE
 NQLTLEDAQSLQELQSNILTVLAAVIRKSPSSVEPVADMLMGLFFRLEKKDSAFIEDDVFY
 AISALAASLGKGFKEYLETFSPYLLKALNQVDSPPVSITAVGFIADISNSLEEDFRRYSDAMMN
 VLAQMISNPNARRELKPAVLSVFGDIASNIGADFIPYLNNDIMALCVAAQNTKPENGTLEAL
 DYQIKVLEAVLDAVVGIVAGLHDKPEALFPYVGTIFQFIAQVAEDPQLYSEDATSRAAVGLIG
 DIAAMFPDGSIKQFYGQDWVIDYIKRTRSGQLFSQATKDTARWAREQQKRQLSLLPETGG

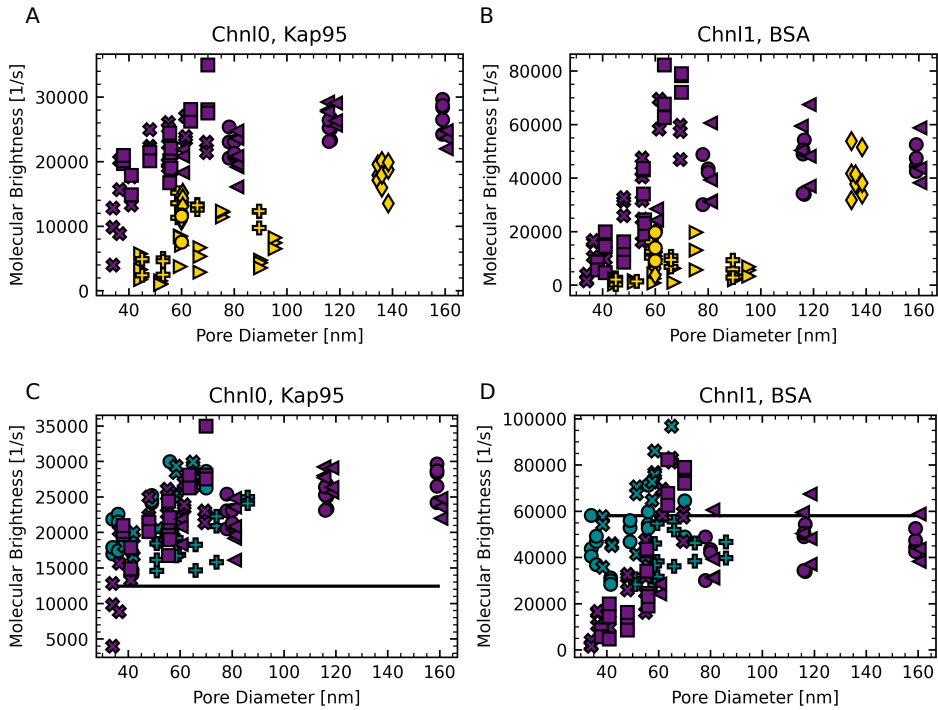
After removal of the GST tag and sortase labeling the sequence of Kap95 as used during the experiment was:

4

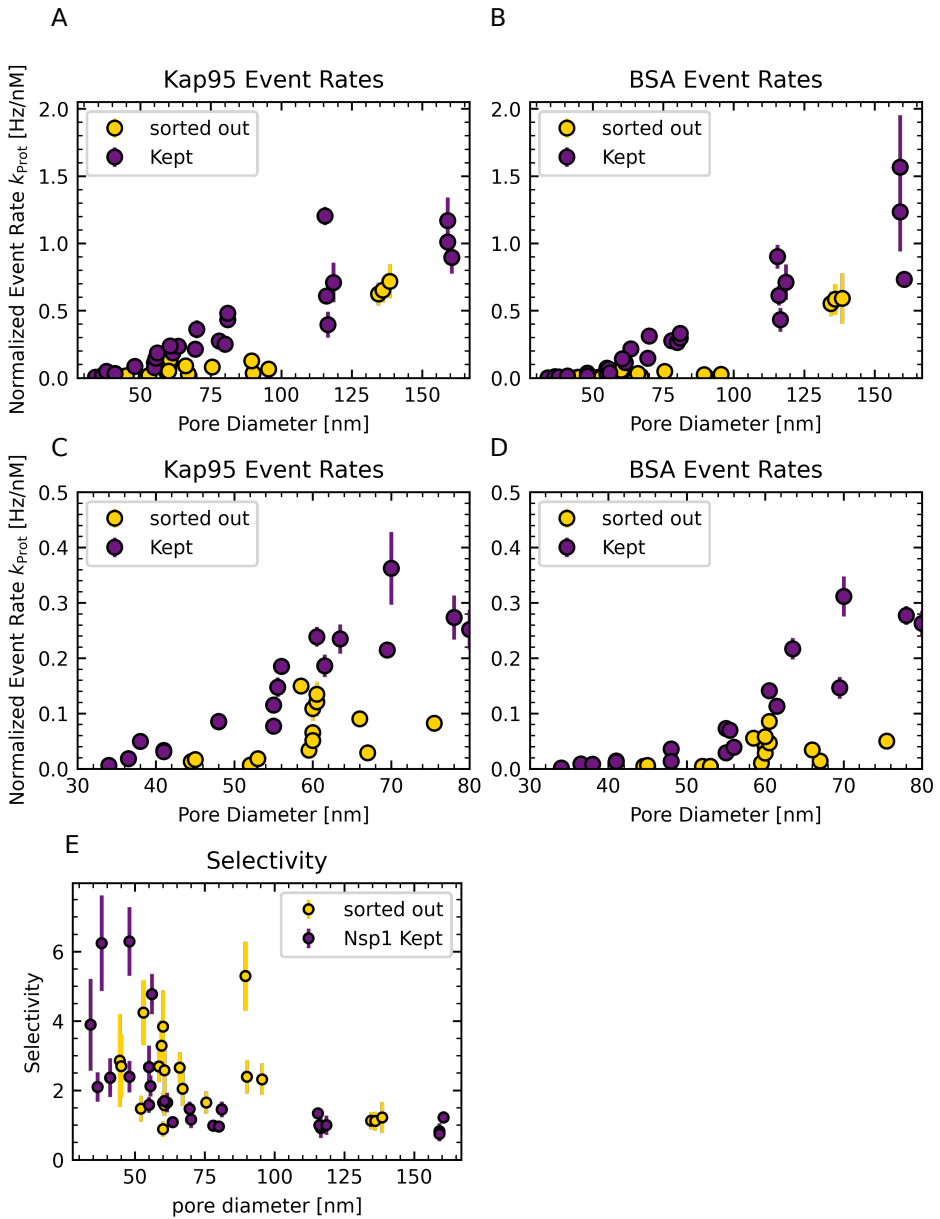
GPASVGSMTAEFAQLLENSILSPDQNI RL TSETQLK KLSNDN FLQFAGLSSQVLIDENTKL
 EGRILAAL TLKNE LVSKDSVK TQQFAQRWITQVSPEAKNQIKTNALTALVSI EPRIANAAAQ
 LIAAIADIELPHGAWPELMKIMVDNTGAEQPENVKRASLLALGYMCESADPQS QALVSSSN
 NILIAIVQGAQSTETSKAVRLAALNALADSLIFIKNNMEREGERNYLMQVVCEATQAEDIEV
 QAAAFGLCKIMSLYYTFMKPYMEQALYALTIATMKSPNDKVASMTVEFWSTICEEEIDIA
 YELA QFPQSPLQSYNFALSSIKDVVPNLLNLLTRQNEDEPDDDDWNVMSMSAGACLQLFAQN
 CGNHILEPVLEFVEQNITADNWRNREAAVMAFGSIMDGPDKVQRITYYVHQALPSILNLM
 NDQSLQVKETTAWCIGRIADSVAESIDPQQHLPGVVQACLIGLQDHPKVATNCSWTIINLV
 EQLAEATPSPIYNFYF PALVDGLIGANRIDNEFNARASAFSALTTMVEYATDTVAETSASIST
 FVMDKLGQTMSVDENQLTLEDAQSLQELQSNILTVLAAVIRKSPSSVEPVADMLMGLFFR
 LLEKKDSAFIEDDVFY AISALAASLGKGFKEYLETFSPYLLKALNQVDSPPVSITAVGFIADISN
 SLEEDFRRYSDAMMN VLAQMISNPNARRELKPAVLSVFGDIASNIGADFIPYLNNDIMALCV
 AAQNTKPENGTLEALDYQIKVLEAVLDAVVGIVAGLHDKPEALFPYVGTIFQFIAQVAEDPQ
 LYSEDATSRAAVGLIGDIAAMFPDGSIKQFYGQDWVIDYIKRTRSGQLFSQATKDTARWAR
 EQKRQLSLLPETGGG-Alexa647

4.6.21. DATA SANITATION

As described in the methods section, some data sets were discarded due to a lower molecular brightness. In a plot of the molecular brightness against the pore diameter, these datasets were clearly identified as outliers (yellow markers in panels A and B of Appendix 4.6.21- [Supplementary Figure 4.23](#)). We only used the molecular brightness of the Kap95 channel for discrimination because the low event rates for BSA at small pore diameters render the molecular brightness estimate unreliable. We additionally find a dependence of the molecular brightness on the pore diameter both for Nsp1-coated open pores, with a reduction of the molecular brightness at smaller pore diameters (panels C and D of Appendix 4.6.21 — [Supplementary Figure 4.23](#)). This effect was most evident for BSA in Nsp1-coated pores where event rates were low, where it most likely originates from a reduction of the correlation amplitude due to a larger contribution of background signal.



Supplementary Figure 4.23: (A,B) Molecular brightness per time trace versus pore diameter on Nsp1 pores. We see two populations for Kap95, labeled in purple and yellow. The yellow data sets showed a decreased molecular brightness and therefore these data sets were removed from further analysis. (C,D) Comparison of molecular brightness between open pores (cyan), Nsp1 pores (purple), and free diffusion (black horizontal line). For Kap95 we found barely any difference of the data distribution. For BSA there we observed a decrease in molecular brightness for small pores of Nsp1. This can be explained by the lower event rate in these pores. Different markers show different experiments.



Supplementary Figure 4.24: (A,B) Event rates of discarded pores of Nsp1. For completeness, we show the event rates of pores that were not further considered in the analysis (yellow) due to their lower molecular brightness, as shown in the previous figure. As expected, these pores show a much decreased normalized event rate both for Kap95 and BSA compared to the Nsp1 pores that were kept in the analysis (purple). (C,D) Zoom in of (A,B). (E) Selectivity of discarded pores. The selectivity of discarded pores (yellow) deviates from the selectivity of the kept pores (purple). This can be explained when taking into account that a changed molecular brightness influences the event detection in each channel differently.

5

INVESTIGATING THE STRUCTURE OF UNSTRUCTURED NUCLEAR PORE COMPLEX MIMICS USING CRYO ELECTRON MICROSCOPY

The nuclear pore complex (NPC) forms the gateway between the nucleus and the surrounding cytoplasm in eukaryotic cells. Structural studies have resolved the arrangement of the rigid scaffold but have been unable to address the intrinsically disordered FG-Nups filling the inner pore. These flexible and dynamic FG-Nups form a dense network that regulates the nuclear and cytoplasmic transport. Here, we are developing a method to study the structural arrangement within so-called NPC mimics that is based on solid state nanopores grafted with FG-nups. Specifically, we labelled different parts of the mimics with gold nanoparticles of which the precise location can be recorded using cryo electron microscopy and subsequent image analysis. By labelling either the nucleoporins directly or the transport protein Kap95, we show that their distributions within the nanopores can be determined at nanometer precision. We showcase the potential of this new method by investigating the arrangement of the FG-nup Nsp1 for various pore sizes and by studying the transport selectivity of Kap95 versus the inert protein BSA. The method can be extended in several directions such as different NPC transport systems and the effect of different nucleoporins on the structural arrangement of the mesh.

This chapter has not yet been published. Contributions to the work were made by Nils Klughammer, Eva Bertosin, Alessio Fragasso, Jacob Kerssemakers, and Cees Dekker. We would like to thank Tanja Kuhm, Wiel Evers, and Arjen Jakobi for image acquisition and helpful discussions.

5.1. INTRODUCTION

The nuclear pore complex (NPC) is a giant protein complex that allows for and regulates the transport between the eucaryotic cell's cytoplasm and its nucleus. These MDa-sized complexes exhibit an eightfold symmetry and are built from around 30 different nuclear pore proteins, called Nups, each appearing in copy numbers ranging from 8 to 64. When assembled correctly, they form a stable channel through the double membrane of the nuclear envelope [1]. The structure of the NPC has been studied for decades which has led to a very detailed understanding of its conformation. Briefly, the NPC consists of several principal elements: The inner pore ring that sits directly at the nuclear envelope, the cytoplasmic and nuclear rings that are anchored to the inner pore ring, the nuclear basket, and the cytoplasmic filaments. The central channel is lined with Nups that are rich in Phenylalanine-Glycine (FG) repeats, the so-called FG-Nups. These have intrinsically disordered domains, and thus can not be fully resolved in the structural studies so far. The central FG-mesh is considered to be a key player in nucleocytoplasmic transport, including cytoplasmic export, nuclear import, and the exchange of signalling molecules [2].

5

In cytoplasmic export, RNAs produced in the nucleus need to be shuttled out of the nucleus, while avoiding the nuclear DNA and premature RNA to pass through the NPC. On the other hand nuclear proteins such as histones and transcription factors that are produced in the cell's cytoplasm need to be transported into the nucleus while at the same time other proteins need to be hindered from such a translocation. These different transport mechanisms do not only need to be specific but also need to facilitate very high transport rates, a phenomenon which is referred to as the transport paradox. Looking at its central role in cells, it is not surprising that several diseases are linked to mutations and malfunctions of the NPC, emphasizing the importance to understand the different functions of the NPC [2].

Whereas small proteins of diameter less than 5 nm and 30 kDa are barely hindered by the NPC, larger molecules are effectively hindered in their translocation, unless they can specifically interact with the FG-Nups such as occurs for nuclear transport receptors (NTRs) [3]. This feature is called the NPC selectivity. By binding to NTRs, large molecules that can not translocate by themselves can be effectively transported through the NPC. One particular transport system is the Kap95-KAP60 pathway of which we will investigate a minimal set in this study. Here, Karyopherin60 from yeast, (Importin α in humans) binds to a specific amino acid sequence in target proteins, called the nuclear localization signal. KAP60 in turn binds to Kap95 (Importin β in humans), which shuttles Kap60 together with its cargo into the nucleus. There, KAP60 and its cargo get unloaded via RanGTP, which induces a conformational change in Kap95. After traveling back into the cytoplasm, the Kap95-RanGTP complex gets hydrolysed so that they unbind and Kap95 is available for import again. By making use of the RanGTPase pathway that provides energy for the process molecules can even be transported against their chemical gradient across the nuclear envelope [4].

Over the years, several models have been proposed to explain the selective properties of the nucleoporin mesh, focusing on explaining different observations and different effects [5–11]. Whereas some of them are based on structural insight, others are inferred from phase-separation experiments or from reconstituted Nup brushes on surfaces. One

particular class of models are the so-called *Kap-centric* models, in which the NTRs form an active component of the NPC to regulate its function [9–11]. These Kap-centric models became even more interesting after it was recently shown that a considerable amount of the extracted yeast NPCs with a total mass of 87 MDa comes from cargoes (10 MDa) and especially transport factors (16 MDa) such as Kap95 and Mex67 [1]. This is remarkable since these transport factors are apparently so tightly bound to the NPC that they withstand the extraction procedure.

Studying the full NPC in all its complexity is challenging especially when it comes to the properties of specific components such as individual FG-Nups. Strawn *et al.* [12] showed that a big fraction of the FG-domains can be deleted from the yeast NPC without impeding the Kap95 mediated import to a lethal extent. This makes clear that for basic functionality the NPC's complexity can be tremendously reduced. Additionally, several minimal NPC systems have shown that transport selectivity as one of the main properties of the NPC can be reconstituted from systems using only a single Nup such as Nsp1, Nup100, or even artificial Nups [7, 10, 13–17]. One specific class of systems exhibiting NPC-selectivity, are NPC mimics based on free-standing solid state membranes [13–16]. There, the Nups are directly grafted to nanopores within membranes that separate two compartments. In these bottom-up systems, all constituents can be selected at will which allows to study individual components in great detail.

Whereas the scaffold of the NPC has been resolved structurally at high resolution using cryo electron microscopy [18, 19], such information is missing for the central mesh of FG-nups. Given the importance of the FG-Nups, the lack of a structural understanding of its dynamic conformations poses a major limitation to the understanding of nuclear transport. Such insight is so far mainly gained either with indirect methods, such as surface techniques [10, 11, 20], transport studies [14, 15, 21], or simulations [15, 22–28]. Additionally, there are approaches to directly study the nucleoporin mesh with methods such as atomic force microscopy [29, 30], electron microscopy (EM) of immunostained NPCs [31, 32] and fluorescence microscopy of live cells [33, 34]. Electron microscopy of the NPC using immunostaining with gold labels has been used for localization of nucleoporins [31, 32] and studying the NPC's function [35, 36] together with the transport mechanism including the RanGTP cycle [37]. However, fluorescence microscopy suffers from a limited spatial resolution which is enhanced by the fast movement within the FG-mesh. AFM and previous EM studies based on gold labeling suffered from limited statistical sampling. To gain insight on the conformations of the FG-Nups, a high statistical sampling is necessary in order to record enough different conformations to deduct a consistent picture.

Here, we are developing a method that allows to study the structural organization within NPC mimics at high statistical sampling. The method is based on NPC mimics made from solid state nanopores which allow the imaging of thousands of identical nanopores. We developed a protocol (cf. Figure 5.1) to fabricate nanopores in free-standing Palladium or SiN membranes grafted with the FG-Nucleoporin Nsp1, making them to minimal NPC mimics. By plunge freezing the sample to cryogenic temperatures, the mimics got locked in their instantaneous conformation and could subsequently be imaged in situ in a transmission electron microscope (TEM). By labeling with gold nanoparticles, it was possible to detect the location of the transporter Kap95 within the

Nup mesh and compare this to the inert probe BSA. We could even investigate the conformation of the Nup mesh by directly labeling the Nups. For this, we established protocols to label the analytes of interest with gold particles and we determined conditions allowing the detection of the gold particles in the final EM images. Subsequently, we developed image analysis methods to record the locations of thousands of pores with the contained gold particles. Due to recent findings of variable NPC diameters [18, 19], we were especially interested in investigating a wide range of diameters which was directly possible by fabricating NPC mimics with different nanopore diameters.

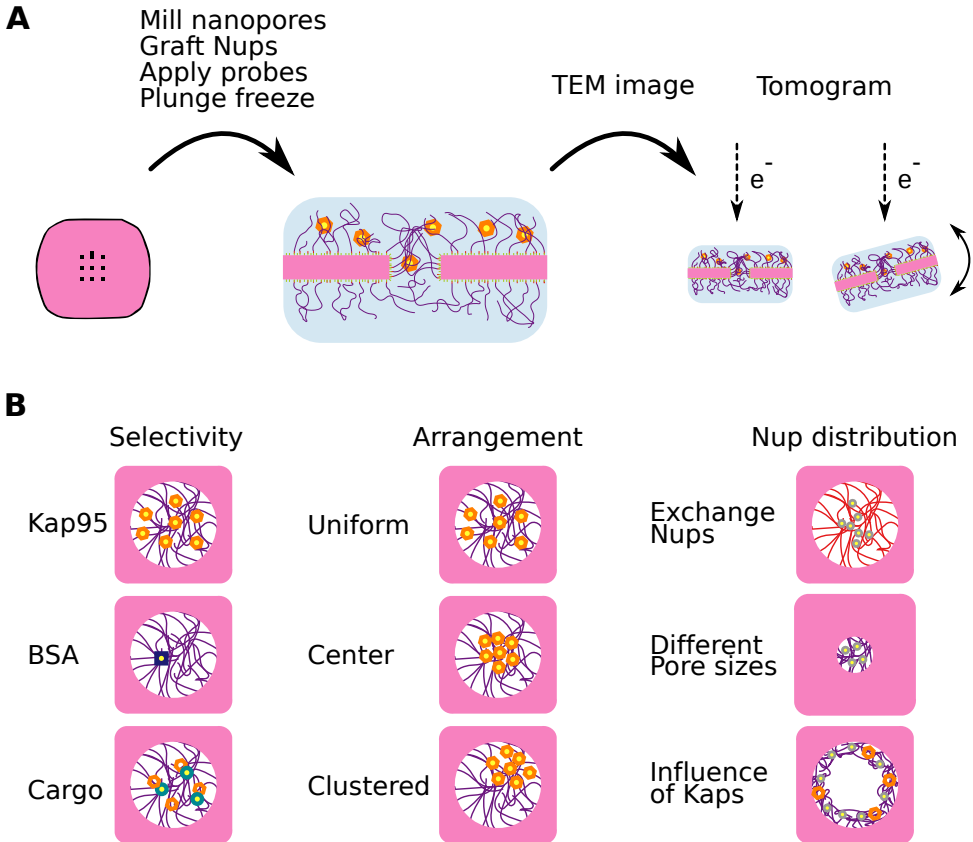


Figure 5.1: Outline of the approach A: 3 mm TEM grids with nine 20 nm thick SiN membranes are commercially available. The membrane size of $>10\,000\ \mu\text{m}^2$ allows fabrication of thousands of nanopores using Focused Ion Beam milling. The nanopores can be modified by grafting nucleoporins to the SiN surface so that the pores are filled with a brush of Nups. After grafting, gold labeled protein probes can be applied and incubated before excess liquid is removed by blotting and the grids are plunge frozen. Thousands of pores can then be imaged using electron microscopy under cryogenic conditions. Potentially, it is also possible to acquire 3D distributions of gold labeled probes through tilted acquisition and reconstruction of tomograms. B: Several interesting situations can be studied with this method. First, individual gold particles are localized using particle detection so that their distributions can be subsequently analyzed. Several parameters can be varied, such as protein concentration, pore diameter, and the type of Nup. Even the localization of the Nups can be investigated by labeling the nucleoporin.

Our proposed method allows for a variety of NPC studies and can be technically expanded in several directions. For example, it should be possible to record the location of gold particles, and thus transporters or Nups, in three dimensions by tilted image acquisition and subsequent reconstruction. Additionally, the method allows for a direct exchange of Nups and proteins of interest. More specifically, the system can be adjusted to study cargo transport by specifically labeling a cargo. With this methodology, we hope to answer questions on the arrangement of transporters such as clustering or preferential binding to specific regions of the pore. In order to answer questions about the role of transporters for the Nup mesh, it will also be possible to study the conformation of the Nup mesh in response to the presence of transporters.

5.2. MATERIALS AND METHODS

5.2.1. PROTEINS AND LABELING

Lyophilized Nsp1 protein was kindly provided by the Görlich lab (Göttingen, Germany). It was resuspended in buffer (PBS, 4 M GuHCl, 0.05 mM TCEP or 20 mM HEPES pH 7, 20 mM NaCl, 2 M Urea, 1 mM Edta, 0.05 mM TCEP) to a concentration of $\approx 10 \mu\text{M}$. Samples were snap frozen in liquid nitrogen and subsequently stored at -80°C . The sequence can be found in the appendix 5.5.1. Kap95 (sequence can be found in the Appendix 5.5.1) was purified as previously described in [16]. BSA protein was purchased from Thermo Fisher (Ultra Pure BSA (50 mg/ml), Invitrogen).

Labeling with 5 nm gold particles was performed by first reducing thiol groups of the proteins via adding 100 times excess of Tris-(2-Carboxyethyl)phosphine Hydrochloride (TCEP, Supelco, Sigma-Aldrich) and incubating for 30 min at room temperature. Subsequently, the protein was incubated for 1 h with 5 nm maleimide gold nanoparticles (MG5K-5-1, Cytodiagnosics Inc, Canada) at a ratio of 1.8:1.5 (gold:protein). Next, unreacted gold nanoparticles were removed from the solution by ion exchange purification using DEAE sepharose beads. For this, we incubated the beads with the solution for 30 min at 20°C shaking at 350 rpm. Then, the proteins bound to the beads were spun down in a centrifuge at 0.7 g for 1 min. The supernatant containing the free gold particles was discarded and the beads were resuspended in high salt buffer, which released the proteins from the beads. Gold concentration was measured by absorption spectroscopy at 515 nm and protein concentration was determined by absorbance at 280 nm, taking into account the correction factor for the gold as provided by the manufacturer, using a DS11 Spectrophotometer (DeNovix, USA). Protein labeling was verified by negative stain electron microscopy on a JEM-1400 (Jeol, Japan) transmission electron microscope.

Labeling with 1.4 nm gold particles was done by first reducing thiol groups of the proteins by adding 100 times excess of TCEP and incubating for 30 min at room temperature. Subsequently proteins were incubated for 1 h with 1.4 nm monomaleimido gold particles (2020A-5X6NMOL, Nanoprobe Inc., USA) at a ratio of 4:1 (gold:protein). The free gold was removed by gel filtration. Gold concentration was measured by absorbance spectroscopy at 420 nm and protein concentration was determined by absorbance at 280 nm, taking into account a correction factor for the gold on the same DS11 Spectrophotometer as provided by the manufacturer. Proteins were snap frozen using liquid nitrogen in aliquots and stored at -80°C until being used in the experiment.

5.2.2. NANOPORE FABRICATION AND COATING

Commercially available 20 nm thick SiN membrane chips (SN100H-A20Q33, Simpore, USA) were either coated with Pd only, the combination of Pd and SiN, or used without further treatment. For Pd coated membranes, we deposited 3 nm of titanium as an adhesion layer onto the SiN membrane at 0.05 nm/sec under a base pressure of 3×10^{-6} torr in a Temescal FC2000 e-gun evaporator, immediately followed by a 20 nm or 40 nm layer of Pd at 0.1 nm/sec to 0.2 nm/sec with a base pressure below 2×10^{-6} torr without venting the chamber in between. For Pd layers covered by SiN, another 3 nm of titanium was deposited. The samples were taken from the evaporator and transferred to an Alliance Concept 450#16 sputterer. SiN was presputtered for 120 s, followed by 160 s of sputtering SiN onto the sample at a pressure of 20 μ bar, 20 sccm Ar flow and 150 Watt power after a pressure setpoint 1 μ bar.

The samples were transferred to an FEI Helios G4 CX Focused Ion Beam/Scanning electron microscope, where we milled nanopores through the membranes. We used the same protocol to reproducibly mill circular nanopores into Pd membranes as given in [28]: First the eucentric height was adjusted on a reference sample of gold sputtered on carbon. Then the ion column for a 1.1 pA Ga beam at 30 kV acceleration voltage was aligned using the automatic procedure defined in the software. Subsequently, a test pore was milled on the SiN surface off the freestanding area. It was inspected for circularity at high magnification using the immersion mode of the SEM. The ion column alignment was repeated in case of the test pore not being circular due to astigmatism of the Ga beam. After roundness of pores was satisfactory, individual arrays of pores were milled in 2 μ m field of view one after another, using parallel milling within one array.

The Pd surface needed to be made accessible for thiol binding, and therefore we performed a cleaning procedure. It was performed as described in [28]: Chips were mounted in a custom built teflon holder, rinsed with DI water and submersed in >99 % isopropylalcohol (Riedel-de Haën, Honeywell Research Chemicals) to remove air bubbles. 30 % hydrogen peroxide (Honeywell Research Chemicals) was brought to 45 °C in a water bath. The chip was rinsed in DI water and then submersed in the hot H₂O₂ for 15 min. A note of caution: hot peroxide is extremely reactive and should be handled with the proper protective equipment.

Bare SiN grids were rinsed with ethanol, isopropanol and acetone and gently dried with a stream of nitrogen. The surface was subsequently activated in oxygen plasma (3 min 50 W pressure below 60 mtorr). The chips were mounted in a custom-built teflon holder and coated with 2 % 3-aminopropyltrimethylethoxysilane (APDMES, SIA0603.0, Gelest Inc., USA) solution in Ethanol for 60 min gently shaking at 350 rpm and subsequently washed with Ethanol for 15 min. The chip holder was dried under a stream of nitrogen and placed for 45 min at 110 °C into an oven to complete the coupling reaction of APDMES to the surface.

2 mg of sulfosuccinimidyl 4-(N-maleimidomethyl)cyclohexane-1-carboxylate (Sulfo-SMCC, A39268, Thermo-Scientific) was diluted in 200 μ L deionized water and further diluted in 1.3 mL of Ethanol. The chips were added and incubated overnight shaking at 350 rpm.

The chips were taken out of the teflon holder, washed in DI water and submersed fully in the Nsp1 solution (1 μ M Nsp1, 1 mM TCEP in phosphate buffered saline buffer)

for grafting. During the grafting, the chips were gently shaken at 450 rpm for 1 h at 20 °C. The chip was subsequently washed in PBS for at least 15 min.

For Nup localization studies, the chip was incubated in a binding buffer containing the Ni-NTA Nanogold particles, which selectively bind the His-tag at the N-terminus of the Nsp1-molecule. For this, the stock solution containing 10 μM of 1.8 nm Ni-NTA Nanogold (2080-3ML, Nanoprobes Inc., USA) in 50 mM MOPS buffer at pH 7.9 was diluted 1:30 times in TBS (20 mM Tris, 150 mM NaCl, pH 7), before incubating the grid for 30 min in the solution. Subsequently, the grid was rinsed with TBS buffer containing 10 mM imidazole to remove unspecifically bound gold particles. Subsequently, the grid is rinsed with deionized water and dried under a stream of nitrogen. A 3 μL droplet of TBS buffer was applied to the membrane side of the grid already hanging in the humidity chamber of the plunger before blotting excess liquid away.

For transporter occupancy studies, the coated chip was washed further in deionized water and dried under a stream of nitrogen. 3 μL of solution containing 3.3 μM gold labeled protein was applied to the membrane side of the chips hanging in the plunger within minutes after drying. Chips were incubated with protein solution for 1 min before blotting and plunging.

5.2.3. CRYO PLUNGING AND IMAGING

The chips were plunge frozen using a Leica EM GP vitrification robot (Leica, Germany) set to 100 % relative humidity at 20 °C. Blotting time was 4 s on the membrane side of the grid and blotting force was set to 220. Samples were immediately flash-cooled in liquid ethane. The chips were stored under liquid nitrogen until imaging in a JEM 3200FSC TEM (JEOL, Japan) operated at 300 kV at a magnification of 30 000, corresponding to a pixel size of 1.22 Å at the specimen level, at a dose between 36 $\text{e}^2/\text{Å}^2$ to 48 $\text{e}^2/\text{Å}^2$. Acquisition was performed using SerialEM [38]. Images were taken at an underfocus varying between $-2.5 \mu\text{m}$ and $-1 \mu\text{m}$. Between 40 and 100 frames were taken and exposure time was 10 s in counting mode. Images were recorded on a K2 Summit direct electron detector (Gatan).

5.3. RESULTS AND DISCUSSION

5.3.1. FREESTANDING NPC MIMICS CAN BE FABRICATED USING FIB MILLING AND SURFACE MODIFICATION

We set out to develop a method that allows to record the lateral positions of transporters and Nups within nuclear pore complex mimics at high spatial resolution. For this we built on previous work using freestanding solid state membranes as scaffold for nanopores lined with nucleoporins making them NPC mimics [13–16, 28]. These NPC mimics have shown to reproduce certain behaviour observed in the real NPC such as transport selectivity. Even though coarse-grained simulations provide some insight into the microscopic arrangement within the pore, experimentally the structural conformations of the Nup mesh so far could only be assessed indirectly, for instance from modeling the conductance change both of ions [14] and proteins [28]. Therefore, we decided to build on this system and adapt it for cryo-EM imaging.

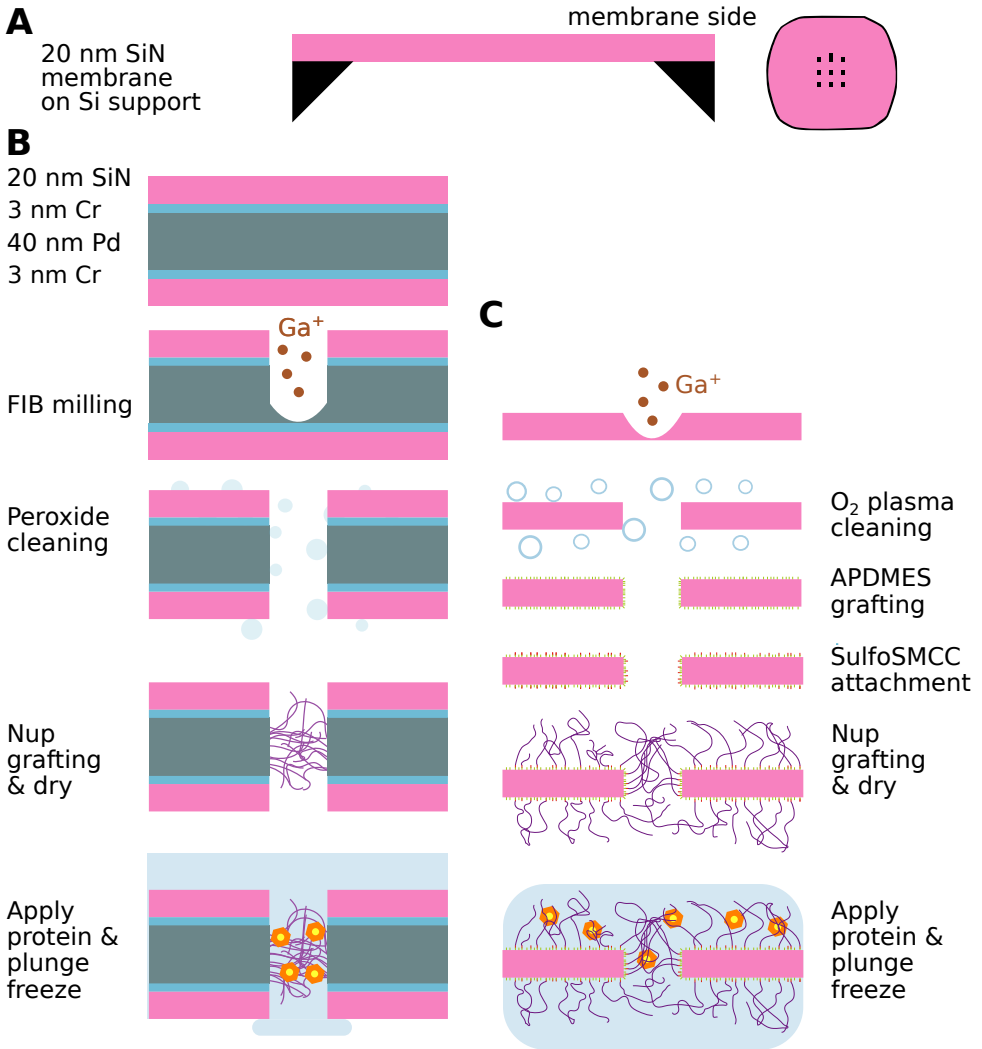


Figure 5.2: Fabrication of nanopore grids A: In this study we used two approaches to produce nanopore TEM grids, both starting with commercially available SiN membranes suspended on a Si support fitting standard TEM holders. B: To fabricate Pd grids, first an adhesion layer of Cr was evaporated onto the SiN. Subsequently, a Pd layer was added. For sandwich structures another Cr layer was added onto which a layer of SiN was sputtered. Subsequently nanopores were milled through the full stack using FIB milling. The grid was cleaned in hydrogen peroxide solution to make the Pd accessible for thiol binding of the Nups. The grafted chips were dried for transfer and immediately resuspended in a solution containing gold labeled probes only from the membrane side. Excess liquid was blotted away and the grid was plunge frozen in liquid ethane. C: For SiN membranes this process was different in the cleaning and the grafting. The SiN surface was made susceptible for Silane chemistry via oxygen plasma treatment. Next the full surface was coated with APDMES, to which Sulfo-SMCC was bound, which could react with the cysteine on the C-terminus of the Nup.

First, we set out to find a suitable scaffold that would allow the fabrication of nanopores and still allow vitrification of an ice layer thin enough for imaging with EM. We decided to use commercially available free-standing SiN membranes fabricated in a 3 mm grid (Figure 5.2 A) that can directly be used for EM imaging and that fit into standard TEM sample holders. We pursued two strategies during this study, using free-standing membranes made of either a metallic sandwich structure or bare SiN membranes. The sandwich structure (Figure 5.2 B) has the advantage that the thickness of the Nup coated layer can be set and the surface of the membrane stays unmodified irrespective of how the pore's inner surface gets grafted. Additionally, the grafting chemistry involves less steps since it is based on thiol-metal binding, and Nups are only assembled in the nanopore. The sandwich structure has the disadvantage, however, that the fabrication involved more steps. Additionally, the thicker and especially metal-rich membrane might reduce contrast within the pores during imaging. The second approach was to use the SiN membranes directly and use a three-step grafting procedure to attach the nucleoporins all over the surface (Figure 5.2 C). In both cases the pores were fabricated using focused ion beam milling, as established earlier [28, 39]. We adjusted previously developed grafting protocols (see section 5.2 for details) in order to obtain nanopores lined internally with Nups.

For TEM imaging, ice layers have to be thin enough and need to be in a vitreous state, because otherwise the electrons can not penetrate through the sample. Still, we needed the nanopores to be filled with liquid before plunge freezing, otherwise we would only have imaged a dried out sample. The SiN membrane samples were fabricated such that they have a flat membrane side that is suspended on a Silicon support (Figure 5.2 A). On the silicon support side is a large reservoir that we needed to be empty when plunge freezing. Therefore, the sample was fully dried after grafting the nucleoporins to the surface, and subsequently, we reapplied liquid only from the membrane side. This allowed the liquid to fully penetrate into the pores and thus the nucleoporins would be suspended in liquid while plunge freezing.

By FIB milling it was straightforward to define different sizes of pores in one array, so that by imaging a full array, several pore sizes would be covered at once. We reproducibly managed to produce pores larger than 25 nm in bare SiN membranes (Figure 5.3). Placing the pores on a triangular lattice allowed to fit more pores into one array which was advantageous because the locations of the arrays were determined first during the TEM imaging. After this, several images on one array were taken covering the array. Still a big enough spacing between the pores needed to be maintained, so that nearby pores would not influence each other during fabrication (which would lead to non-circular pores). In the last batches, we used a pore spacing of 200 nm which still resulted in round pores. During TEM imaging of the SiN grids, we initially had problems locating nanopore arrays, because of the little contrast the nanopores give in the SiN. Therefore, we added a big central marker to each array as shown in Figure 5.3 B even though this marker required a considerable amount of fabrication time.

Before imaging the grids in the TEM, they underwent several handling steps (Figure 5.1) where the membranes were prone to break. Especially during blow drying, the risk was high, particularly when the stream of nitrogen did hit the surface not fully parallel or was too strong. An additional risk was that the membrane was covered with too

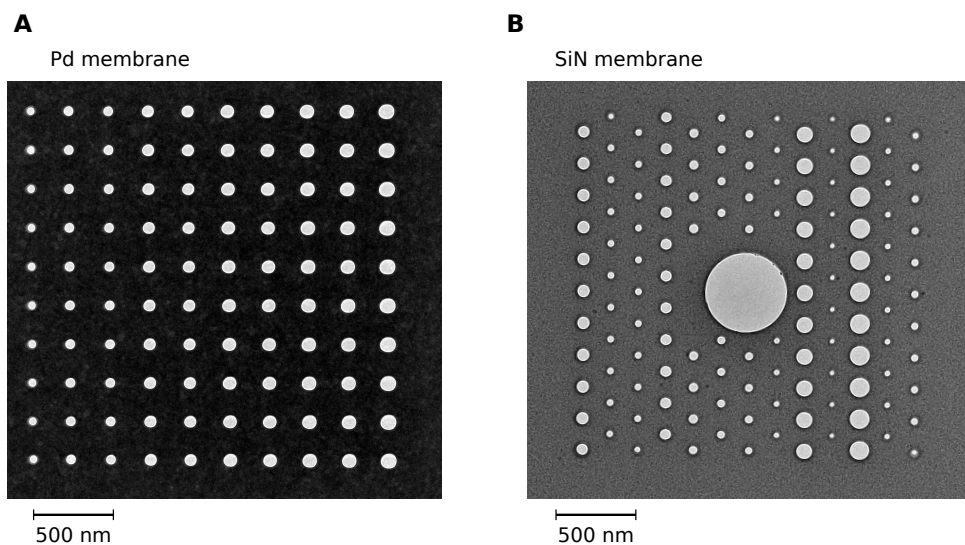


Figure 5.3: TEM images of nanopore arrays in dry conditions. A: In Pd membranes arrays of differently sized pores were milled using focused ion beam milling. The distance between rows was chosen to be big enough to avoid any influence of neighboring pores during milling. Nanopores in the Pd membranes gave a high contrast in TEM imaging and could be easily located even on a large membrane. B: Nanopores in SiN membranes gave little contrast, and therefore a big central marker was added. Pores were spaced more densely by placing them on a triangular lattice in order to make more efficient use of the space. Pore sizes varied between 25 nm and 150 nm.

thick ice or dirt, which makes them appear black in the final TEM image (Figure 5.4). Therefore, we distributed the arrays on all ten membranes available on a single grid. We typically milled around 33 000 individual pores of 11 different sizes ranging between 26 nm to 145 nm comparable to the range studied recently in [28]. This took around 2 h using the protocol described in section 5.2.

5.3.2. NPC MIMICS BASED ON PD NANOPORES CAN BE IMAGED UNDER CRYOGENIC CONDITIONS

First, we needed to verify that the full procedure we had developed for nanopore fabrication, surface coating, plunge freezing, and our imaging conditions would allow to detect individual nanopores filled with vitreous ice. For this, we prepared Pd-covered SiN membranes with a total thickness of 43 nm and grafted the nucleoporin Nsp1 to the surface (Figure 5.4 A). Nsp1 is one of the most studied nucleoporins in *in vitro* studies [6, 7, 13, 15, 21] and therefore was used also in this project. We applied Kap95 labeled with 0.8 nm gold particles to the Nsp1 mesh and plunge froze the sample after blotting away the excess liquid from the membrane side. When imaging the grid, we found that many of the membranes were either ruptured or showed up black in the TEM image (Figure 5.4 B). Nevertheless, it was possible to locate several arrays that could be imaged at high resolution, so that we could study the pores in detail. We were intrigued to find that the ice was such that imaging through the center of the pores was possible and that

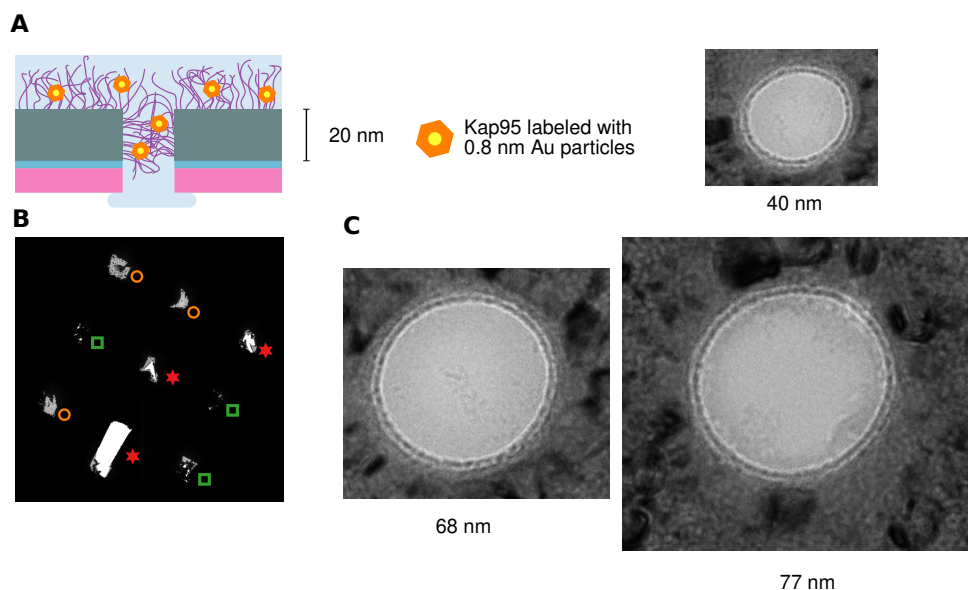


Figure 5.4: Pd nanopores in cryo conditions A: A Pd-coated SiN grid containing nanopores was grafted with Nsp1. Subsequently, Kap95 labeled with 0.8 nm gold particles was applied. B: During imaging, several membranes on the sample were broken (indicated by a star) or could not be imaged due to ice or contaminations (square). Still, we identified areas where nanopores could be imaged (circles). C: Representative nanopore images with their respective diameter. No 0.8 nm gold labels could be detected in the images. In the pores, structures could be identified that hypothetically arose from ice thickness variations.

the rim could be located at a high resolution (Figure 5.4 C-E). Even structures within the pores could be resolved, although it was unclear if these structures did originate from the nucleoporin Nsp1, the gold labeled Kap95, or variations in the ice thickness. Unfortunately, we could not detect any 0.8 nm gold labels within the nanopores. We hypothesized that these would simply not give enough contrast to be detected and we therefore tested the same system with an increased size of gold particles.

5.3.3. LABELING OF KAP95 AND BSA WITH GOLD NANOPARTICLES FOR CRYO ELECTRON MICROSCOPY

In order to study different sizes of gold particles, we established two protocols for labeling of the proteins with small 1.4 nm and large 5 nm gold particles. A major focus should be put on not to lose too much sample during the purification procedure and to maintain the integrity of the proteins after labeling which should be verified by functionality assays.

For both particle sizes, the proteins were labeled at their cysteine residues using the maleimide coupling reaction. The gold particles themselves, were functionalized with maleimide groups and reacted readily in reducing conditions. For both sizes, the unbound gold particles had to be removed from the solution. Notably, a moderate fraction of unlabeled protein would not pose a major issue, since the final occupancy data could be corrected for the labeling efficiency.

We first describe the purification strategy for the 5 nm gold beads (Figure 5.5). We separated the protein from the unreacted gold beads using ion exchange purification, where the proteins did bind electrostatically to positively charged sepharose beads and could then be separated from unreacted nanoparticles in the test tube by centrifugation. The unbound gold beads were removed by discarding the supernatant. Subsequently, the proteins were separated from the sepharose beads, by resuspension in a high salt buffer, screening the electrostatic interactions, and a subsequent centrifugation. The labeling efficiency could be estimated by comparing the light absorbance of the sample at 515 nm (for the gold beads) with the absorbance at 280 nm where the protein absorbs. From this we obtained a labeling efficiency of 10 %. Furthermore we verified the integrity of the proteins by negative stain TEM, from which we obtained a much higher labeling efficiency of 64 % from counting particles. Since we only used these samples for testing purposes, we did not investigate the reason of the discrepancy further. It shows, however that a good quantification method of the labeling efficiency is important. Additionally, functionality tests of these labeled Kap95 proteins still remain to be performed.

For the proteins labeled with 1.4 nm gold labels, the purification protocol contained less steps. We removed unreacted Au nanoparticles via gel filtration (Figure 5.5), and subsequent quantification of the labeling efficiency was done by comparing the gold absorbance at 420 nm with the protein absorbance at 280 nm wavelength. This resulted in labeling efficiencies of 80 % and 40 % respectively for Kap95 and BSA. The integrity and functionality of the proteins remain to be verified. To do this, we propose to perform binding studies to IBB peptide. IBB peptide is a short domain of the Importin- α protein, responsible for binding to Importin- β . Imp- β is homologous to Kap95 and thus the IBB domain of Imp- α binds to Kap95. Therefore, adequate binding of the IBB-peptide to Kap95 can report on the functionality of Kap95 after labeling.

A 5 nm Au particles

Reduce protein's disulfide bonds with TCEP

Add 5 nm maleimide coated Au nanoparticles incubate for 1hr

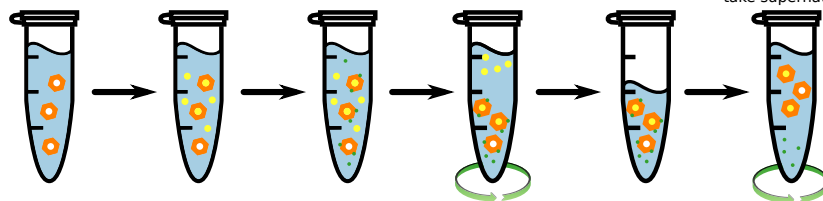
Remove unbound Au using DEAE sepharose beads ion exchange

Add beads and incubate

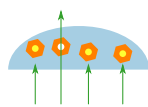
Spin down beads bound to protein

Remove supernatant containing unreacted Au

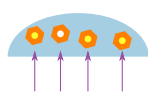
Elute protein by resuspending in high salt buffer spin down beads, take supernatant

**B**

Quantify Au via absorption at 515 nm



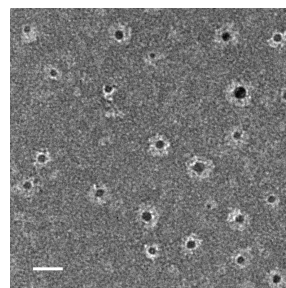
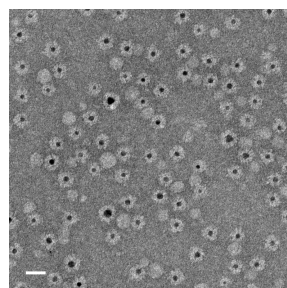
Quantify protein via absorption at 280 nm correcting for Au absorption

**C**

Validate via negative stain TEM

BSA

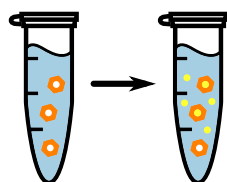
Kap95

**D 1.4 nm Au particles**

Reduce protein's disulfide bonds with TCEP

Add excess 1.4 nm monomaleimido Au nanoparticles incubate for 1hr

Remove unbound Au by gel filtration



Quantify Au via absorption at 420 nm

Quantify protein via absorption at 280 nm correcting for Au absorption

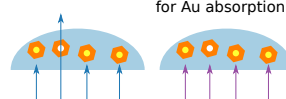


Figure 5.5: Labeling Protocol with 5 nm Au Nanoparticles. A: The proteins of interest (Kap95 and BSA) were labeled with gold nanoparticles by first reducing disulfide bonds using TCEP. Next, the proteins were incubated with an excess of maleimide coupled gold particles. For separation of the labeled proteins from unreacted 5 nm gold particles, we used ion exchange purification based on DEAE sepharose beads. In a first step the proteins bound to the beads were sedimented. The supernatant containing unreacted gold was discarded. The protein was eluted in high salt buffer and the beads were sedimented by gentle centrifugation. B: The gold and protein concentrations were quantified using absorption spectroscopy. From this, we obtained labeling efficiencies of 10% for both Kap95 and BSA. C: The protein's integrity was validated via negative stain electron microscopy which showed that the actual labeling efficiency was higher than obtained from spectroscopic measurements. Scale bars are 10 nm. D: For 1.4 nm particles, purification from unreacted gold particles was done via gel filtration and quantification of gold and protein was also done via absorption spectroscopy. Labeling efficiencies with 1.4 nm gold particles were found to be 80% and 40% respectively for Kap95 and BSA.

5.3.4. 5 NM GOLD LABELED KAP95 CAN BE IMAGED IN NSP1-COATED PD NANOPORES USING CRYO-EM

Since we could not detect any 0.8 nm sized gold particle in the nanopores in [subsection 5.3.2](#), we tested larger gold particles. We labeled Kap95 with 5 nm sized gold particles and subsequently applied them to an Nsp1-coated grid before imaging under cryogenic conditions ([Figure 5.6](#)). We were intrigued to find that in many of the pores gold particles could be detected. The number of particles per pore varied strongly from pore to pore ranging from zero to tens of particles. In several pores, the inner ice background appears to be structured and not uniform (see [Figure 5.6 E](#) for example). We hypothesized that this came from nonuniform ice that originating from melting or ice accumulation.

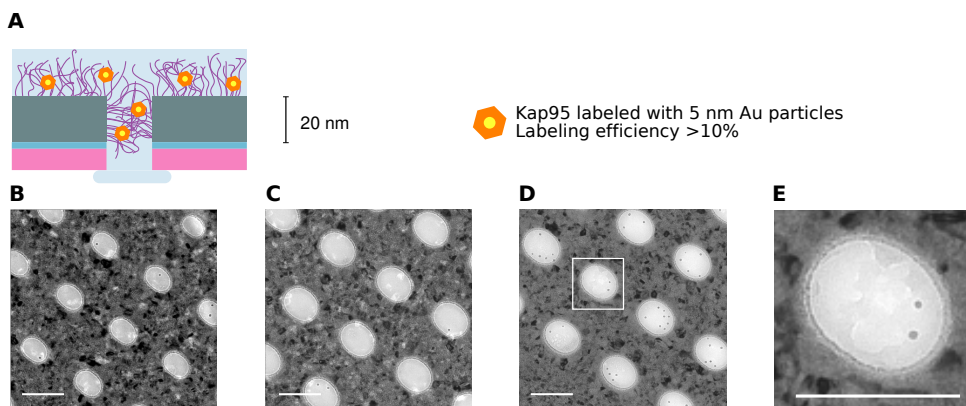


Figure 5.6: Kap95 with 5 nm Au nanoparticles in Nsp1-coated pores. A: Pd nanopores were coated with Nsp1 molecules and incubated with Kap95 proteins labeled by 5 nm Au particles. B-D: Example images of pores imaged using cryo-EM. E: Zoom-in of the box in D. The 5 nm gold particles are clearly visible in the images. Scale bar is 100 nm

To confirm that the presence of Kap95 in the pores was indeed due to the attraction by Nsp1, we performed a control experiment, where Kap95 was added on open pores. These pores had a bare Pd surface and thus should not specifically interact with Kap95. We found that the big majority of pores did not show any ice in the center. Our hypothesis is that the pores did not get properly wetted during the resuspension in buffer before plunge freezing as a consequence of the surface properties of the Pd. To avoid this in future experiments, a strategy making the pore's inner surface hydrophilic should be considered.

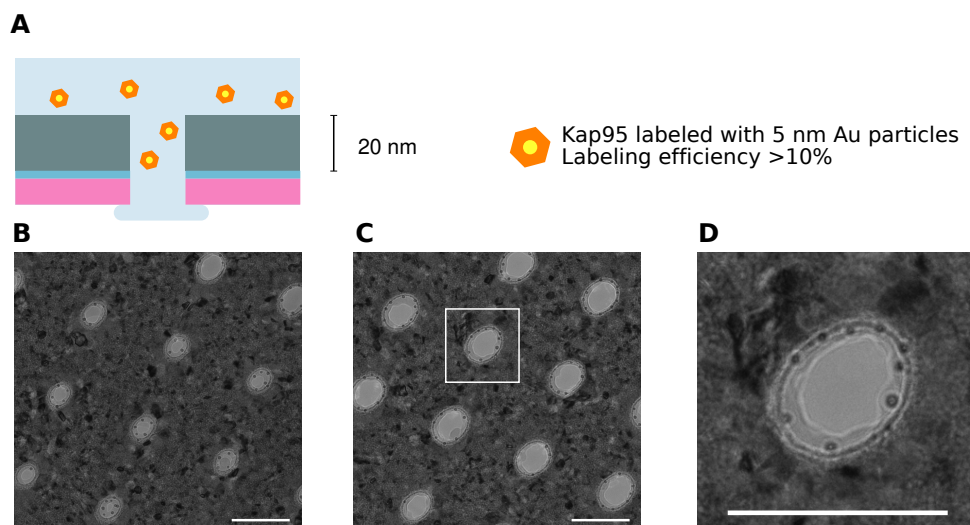


Figure 5.7: Kap95 with 5 nm Au nanoparticles in bare Pd pores. A: Untreated Pd nanopores were incubated with Kap95 proteins labeled by 5 nm Au particles. B,C: Example cryo-TEM images. D: Zoom-in of the box in C. Most of the pores were dried out, still several gold particles could be detected in the remaining ice. The scale bar is 100 nm

5.3.5. IMAGE ANALYSIS

After establishing how to observe the locations of Kap95 proteins in NPC mimics made of Nsp1, we developed an algorithm to locate particles contained inside the pores imaged using cryo-EM. Since high numbers for good statistical sampling were necessary, we chose for a fully automated image-analysis pipeline as shown in Figure 5.8. First, the locations of the pores in the image were obtained by intensity thresholding. After two sorting steps, discarding non-circular pores and discarding pores showing too much intensity heterogeneity in the ice, we ended up with a list of individual pores that were further analyzed. For each pore, the rim was detected and subsequently the locations of particles within the pore were determined. In a following step, the gold particle distributions could be analyzed with different methods such as histograms or cluster analysis (Figure 5.8 D).

Since rim detection was crucial for the subsequent localization of particles, we developed a protocol to accurately follow the pore's rim, despite image noise and low contrast (Figure 5.9). Images were first Gaussian filtered for smoothing and then Sobel filtered for gradient detection in the image. An initial rim was estimated by adjusting a closed curve to follow most accurately the maxima in the Sobel filtered image. Next this initial estimate was smoothed, so that the resulting rim would follow the overall pore shape rather than local variations in intensity emerging from noise. In a final step, an estimate of the rim's length based on the pore's area was compared to the smoothed rim. If these two deviated too much, pores were removed from further investigation.

Once the rim of a pore was accurately detected, the particles could be located within the pore (Figure 5.10). The particles, especially for small gold beads, showed only very

weak contrast. In the detection strategy, the focus was not put on the highest overall detection rate, but rather on a low false-detection rate. Since we are mostly interested in spacial distributions, it was most important to avoid the introduction of detection biases for instance that particles in the center would get detected easier than at the periphery of the pore.

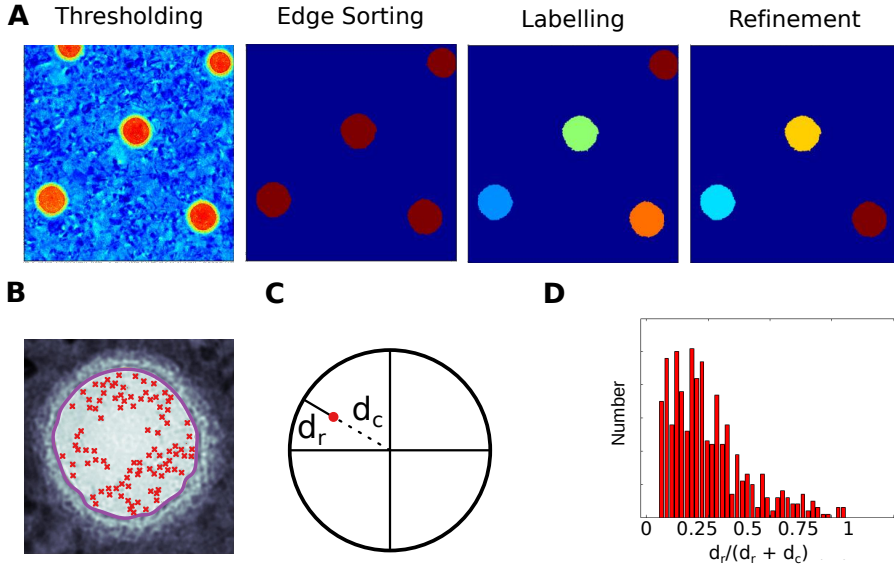


Figure 5.8: Image Analysis and Particle Detection A: First, potential pores were detected via thresholding of the image. In a next step, pores touching the edge were sorted out and individual areas containing pores were extracted (non-darkblue areas in A). In each of these pore areas, the edge was detected. Pores were discarded if their area was above or below an expected range or if their perimeters were too long for their area. Additionally, pores with large internal brightness variations were discarded. B: For each of the pores, the rim (purple) was detected and subsequently particles within the pores were located based on local peak detection (red crosses). C: The distance of the particles from the rim d_r and from the pore's center of mass d_c were calculated. D: Subsequently the particle distributions were post-processed for instance yielding histograms for investigating the particle occupancy in a certain diameter range.

To accomplish this task, we decided to use a two-step particle detection method (Figure 5.10). At first, the rim was shrunk in order to avoid false detection due to intensity inhomogeneities near the boundary of the pore. Next, the highest intensity peaks in the pore were found and a 2D-Gaussian profile of similar intensity was subtracted from the image. This procedure was repeated until only noise peaks were detected as intensity maxima. The resulting image then only contained the slowly varying background intensity, which could be subtracted from the original image. The particle detection was repeated on the background subtracted image. This resulted often in intensity peaks found within the background noise. These false detections typically showed a low intensity and therefore could be disregarded in further analysis. Summing up, only the most significant peaks in the image were kept and treated as reliable particles.

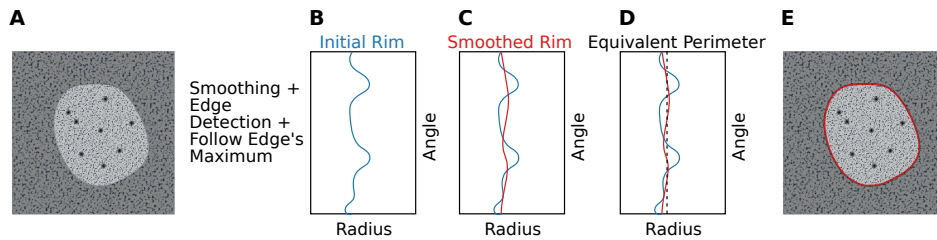


Figure 5.9: Rim Detection A: Accurate detection of the pore's rim was the first step for successful particle detection. A first estimate of the rim was obtained by applying a Gaussian smoothing filter and a Sobel filter to the area containing a pore. B: For rim detection, we started with a closed loop, which was subsequently deformed until it coincided with the pore's edge. The pore's edge was determined from the local maxima in the image's gradient. C: The initial rim was smoothed to reduce the influence of image noise. D: The length of the smoothed rim was compared with an equivalent perimeter of a circular pore with the same area. E: Only pores of which the rim's length was close to the predicted perimeter were considered for further analysis.

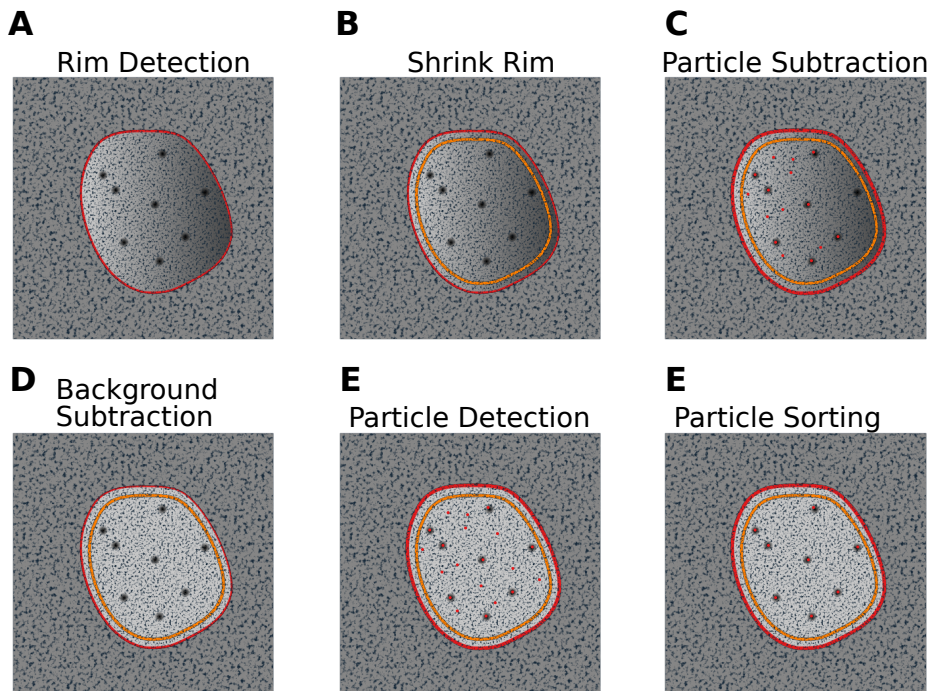


Figure 5.10: Particle Detection A: Particle detection within pores relied on identifying local intensity maxima within the pores rim. B: At first the pore's rim was shrunk by an amount equal to the particle diameter, because particle detection close to the rim would get biased by the proximity to the edge. C: Local maxima within the inner rim were subtracted from the image. The resulting image contained only slowly varying background which could be subtracted to remove any intensity gradients within the pore. (D) E: Particle detection was performed on the background subtracted image heavily oversampling the number of particles. E: Particles were distinguished from noise by considering only the most intense particles for further analysis.

5.3.6. Nsp1's N-TERMINUS FORMS A RING-LIKE STRUCTURE IN A LARGE NANOPORE

To reduce the potential influence of the big membrane area outside the nanopores, we developed a sandwich structure made of a 40 nm thick Pd layer, sandwiched by two SiN layers (Figure 5.11 A). Thus, only the central layer was available to bind nucleoporins and the surfaces on the top and bottom would remain unchanged irrespective of the grafting inside the nanopores.

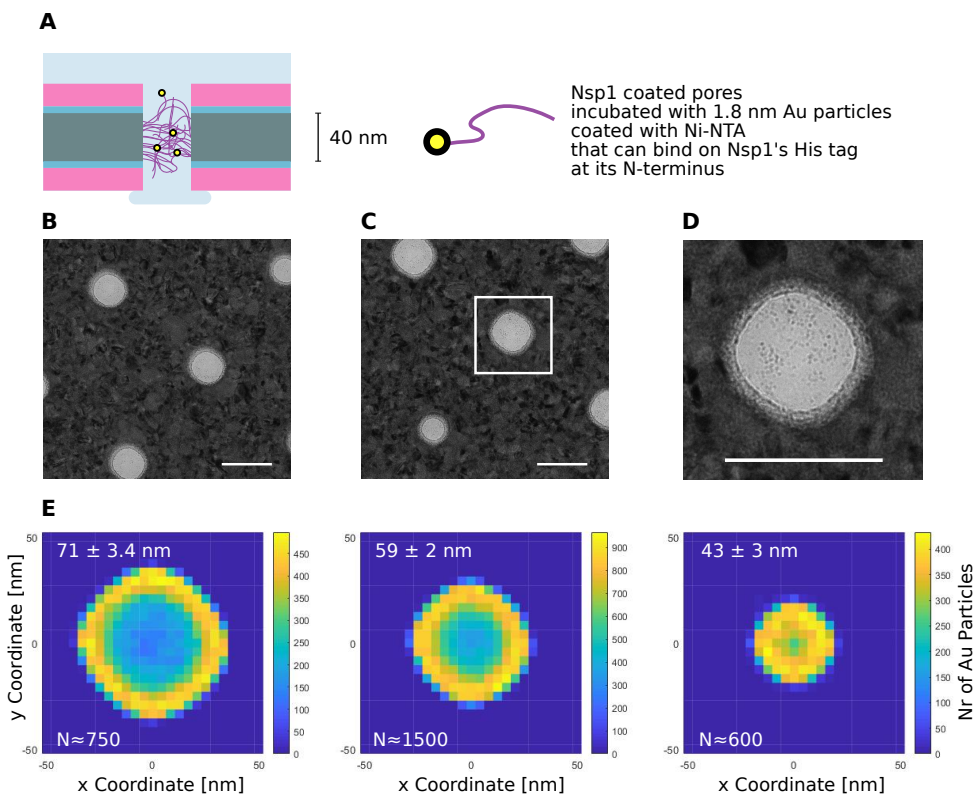


Figure 5.11: N-terminally Labeled Nsp1 in Nanopores A: Nsp1-coated Pd nanopores incubated with 1.8 nm Ni-NTA Au particles at the Nsp1's N-termini. B,C: Example cryo-TEM images. D: Zoom-in of the box in C. The gold labels are visible and were used for subsequent particle detection. Scalebar is 100 nm. E: 2D histograms of Au particle distribution obtained from analyzing N pores. The different pores were classified by their size. The amount of particles detected in a certain pore region is given by the color of the respective pixel. A ring where Nsp1 ends clustered can be identified especially in the large pores.

Since the length of the pore now became up to 80 nm, we first tested if the Nsp1 could still reach the center of the sandwich and bind to the Pd during grafting. While the arrangement of nucleoporins within artificial NPC mimics had been addressed several times with simulations, it so far was never directly tested experimentally [15, 21, 28]. We decided to make the Nsp1 residues inside the nanopore directly visible by labeling its end with a 1.8 nm gold particle. Since the Nsp1 protein had a His-tag present at the

N-terminus we could attach Ni-NTA coated gold nanoclusters to it. The stoichiometry of gold to Nsp1 is not clear, however, as one His-tag can potentially bind multiple nanoparticles and one nanoparticle can potentially bind multiple His-tags. Still, the potential presence of nanoparticles in the pores shows that grafting of the inside worked as expected. For this, the Nsp1 grafted grids were incubated with a solution containing the Ni-NTA nanoparticles. Subsequently, the unbound fraction was removed by washing with buffer containing imidazole which should facilitate the removal of unspecifically bound nanoparticles.

In [Figure 5.11 B–D](#), multiple particles can be clearly seen in the pores as dark spots. Excitingly, this showed that 1.8 nm sized gold particles produced enough contrast to be identified in our Pd nanopores. Therefore, these images were suitable for further analysis of the particle's distributions by detecting the location of the individual particles within the pores. Subsequently pores of similar size were grouped in order to obtain statistically meaningful results, as shown in [Figure 5.11](#). In total around 3500 pores were analyzed in this dataset. When looking at the 2D histograms of the particle distribution within the differently sized pores of 43 ± 3 nm, 59 ± 3 nm, and 71 ± 3 nm, we found that all showed the highest amount of nanoparticles near the rim of the pore. Whereas for the 43 ± 3 nm sized pores, a central channel was barely existent, such a lower-intensity channel was clearly visible for pores of larger size. A clear ring was observed with an approximate width of 12 nm. This suggests that the Nsp1 mesh rather formed a ring like structure than a central plug. Despite the clear formation of a ring, the center of the big pores was still populated with approximately a third of the density of gold labels, compared to the maximum found within the ring. This means that even 73 ± 3 nm sized pores did not fully open up.

As a negative control to the experiment shown in [Figure 5.11](#), we treated a second sample in the same way with Ni-NTA gold labels without previously binding Nsp1 to the surface, however. We found that the pores were still filled with ice, thus imaging in principle worked ([Figure 5.12](#)). We could not detect any gold labels inside the pores, however. We conclude that in the experiment where Nsp1 was added to the grafting solution, the gold labels were indeed showing the presence of the Nsp1 molecules on the surface.

The finding of a rim-biased organisation of Nsp1's N-termini contradicts previous simulations of Nsp1-coated 20 nm thick SiN nanopores, where a central plug was found for pore diameters up to 60 nm, with the highest density of Nsp1 residues in the center [15]. The system was a bit different, however. In the case simulated in [15], Nsp1 was only grafted to the inner part of the 20 nm thick nanopore but was not further constrained on the outside so that it could freely spill out. Additionally, we recently found that in confinement a lower grafting density needs to be assumed compared to unconfined pores, in order get to a physiological protein density within the nanopore [28]. When assuming such a lower grafting density, it was shown that pores of diameters above 60 nm start opening up in the center, first transiently and permanently for pores above 80 nm [28]. In both studies, the distribution of Nsp1 could not be studied directly but only simulated or indirectly from the ion or protein conductance, which shows the importance of direct visualizations of the Nup mesh within NPC mimics.

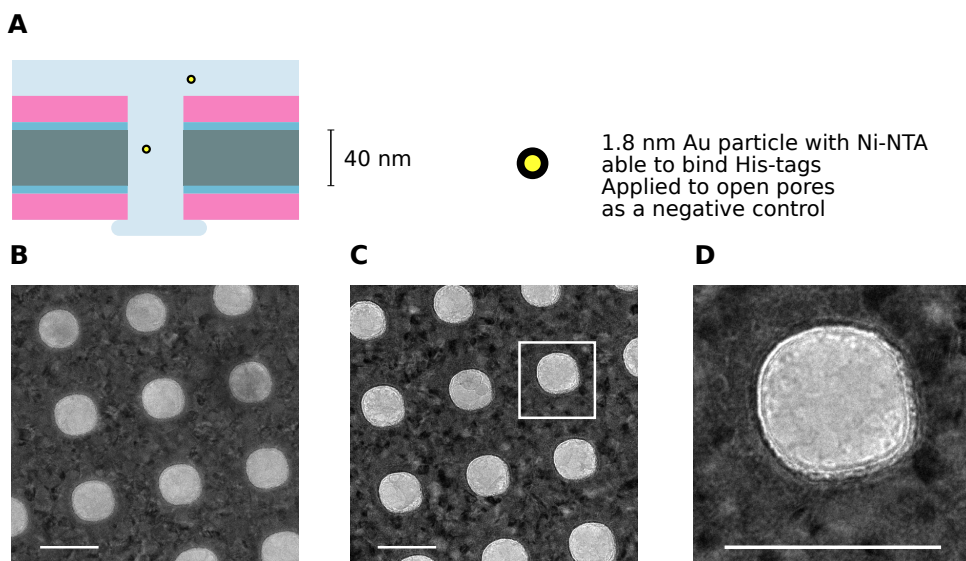


Figure 5.12: Ni-NTA Au nanoparticles in uncoated nanopores A: Bare Pd nanopores incubated with 1.8 nm Ni-NTA Au particles as a negative control to the experiment shown in [Figure 5.11](#) B,C: Example cryo-TEM images. D: Zoom-in of the box in C. No significant amount of Au particles can be detected, which shows that in [Figure 5.11](#) indeed Nsp1 was labeled by the nanoparticles. Scale bar is 100 nm

5.3.7. PROTEINS LABELED WITH 1.4 NM AU NANOPARTICLES CAN BE DETECTED IN NSP1-COATED SiN NANOPORES

Stimulated by the successfully imaging 1.8 nm Au nanoparticles in the sandwich structures, we attempted to use 1.4 nm gold particles for protein labeling, as described in [subsection 5.3.3](#). This was to reduce any potential influence of the gold particle on the function of the proteins.

We applied Kap95 labeled with 1.4 nm Au nanoclusters to Nsp1-coated nanopores comparable to the experiment described in [subsection 5.3.4](#) using the same sandwich structures as in [Figures 5.11](#) and [5.12](#). Unfortunately, we could not detect any gold particles within the pore, in contrast to the previous experiment with 5 nm sized gold labels. We hypothesize that this was mainly due to limited contrast within the pores and distortions introduced by the metal layer. The exact cause of the absence of the Au particles in the TEM images still needs further investigation.

Since the metal layer in the freestanding membrane potentially reduced the contrast within the pores and was mainly needed for the binding chemistry, we decided to remove it and to work with bare 20 nm thick freestanding SiN membranes. One disadvantage of this system was that the whole surface is modified by the grafting and that the surface modification required more steps as shown in [Figure 5.2](#). Additionally, the thin SiN membranes were more fragile and prone to break during handling. On two separate samples of Nsp1-coated pores, we applied Kap95 and BSA, both labeled with 1.4 nm particles.

For the BSA with a labeling efficiency of 40 %, multiple particles could be detected in

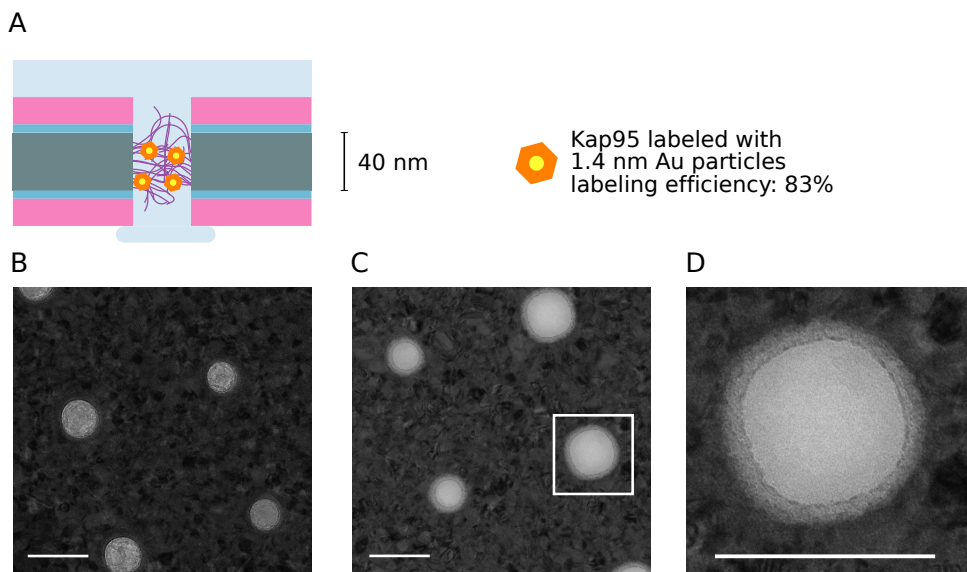


Figure 5.13: Kap95 with 1.4 nm Au Nanoparticles in Nsp1-Coated Pd Pores. A: Nsp1-coated Pd nanopores were incubated with Kap95 labeled with 1.4 nm Au particles. B,C: Example cryo-TEM images. D: Zoom-in of the box in C. No Au particles could be detected, supposedly because the 1.4 nm particles were too small to be visible in Pd nanopores. Scalebar is 100 nm

the pores (Figure 5.14). This finding further strengthened our hypothesis that probably the Pd layer in the experiment from Figure 5.13 reduced image contrast within the pores and rendered the detection of 1.4 nm Au particles impossible. In addition to the particles within the pores, gold particles could also be detected on the SiN surface. This was not surprising since the thin SiN membrane produced much less contrast compared to the Pd membranes. Advantageously, this adds an internal control to the experiment since now the distributions of particles within the pores can be compared with areas on the membrane where the particles in principle should be uniformly distributed.

Whereas for BSA both the pores and the membrane surface was only weakly populated with gold particles, in the case of Kap95, many particles could be detected at a high density, both within the pore and on the membrane (Figure 5.15). Even though the labeling efficiency of Kap95 (83 %) was roughly double of the one for BSA, the amount of particles in the pores seemed to be much more than double. This preliminary finding suggests that the NPC mimics based on SiN grids imaged with cryo-TEM showed selectivity of the transporter Kap95 versus the inert probe BSA. Further quantitative analysis is needed to avoid any perception biases and to verify the statistical significance of this finding. Subsequently, also differences in the particles distributions could be further investigated. For this task the particle detection algorithms presented earlier need to be adjusted for the particle size and the contrast between the SiN membrane and the pores of these experiments. Yet, this is a very promising first result that shows the capability of our approach to precisely localize both transporters and Nups in NPC mimics.

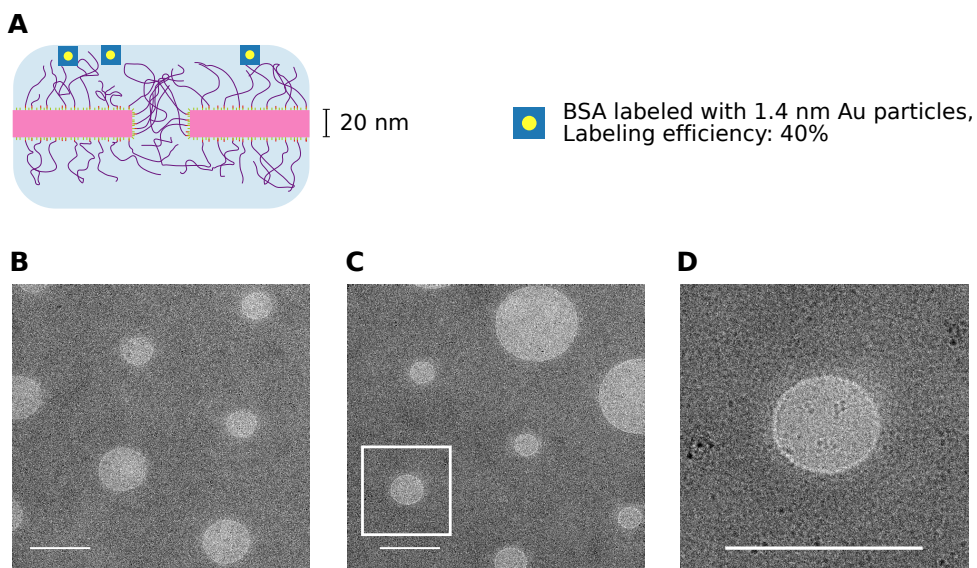


Figure 5.14: BSA with 1.4 nm Au Nanoparticles in Nsp1-coated SiN pores. A: Nsp1-coated SiN nanopores were incubated with BSA labeled with 1.4 nm Au particles. B,C: Example cryo-TEM images. D: Zoom-in of the box in C. A few individual Au particles could be detected per pore. Scalebar is 100 nm.

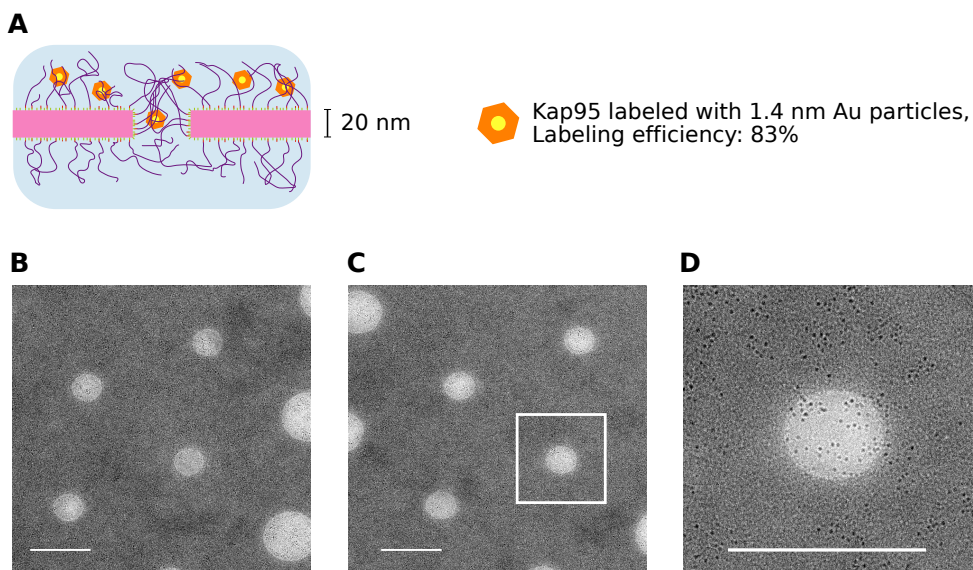


Figure 5.15: Kap95 with 1.4 nm Au Nanoparticles in Nsp1-Coated SiN pores. A: Nsp1-coated SiN nanopores incubated with Kap95 labeled with 1.4 nm Au particles. B,C: Example cryo-TEM images. D: Zoom-in of the box in C. Several Au particles can be detected in the pores. Scalebar is 100 nm

5.4. CONCLUSIONS AND OUTLOOK

In this chapter, we showed that we can use cryo electron microscopy to determine the precise location of both transporters and nucleoporins within NPC mimics. We used two different systems, both being based on freestanding solid state membranes containing nanopores lined with Nups. Whereas nanopores in Pd films allowed to use a surface modification procedure of fewer steps, SiN pores allowed the localization of smaller 1.4 nm particles within the pores. We can not exclude that the protein carrying the particle was simply not present in the Pd pore experiment shown in [Figure 5.13](#) and therefore no particles could be detected. We find this very unlikely, however, since in three other experiments using comparable conditions ([Figures 5.6, 5.14, and 5.15](#)) proteins could be found within the pores. Therefore, for future experiments, we would propose to NPC mimics based on nanopores within SiN membranes.

One major advantage of our proposed method is that it allows for good statistical sampling with thousands of pores similar in shape involved. Due to the reliable fabrication process in solid-state membranes, the shape of the pores varied by less than 10% and thus allowed averaging over thousands of pores. We showed the potential of this by analyzing more than 2500 pores lined with Nsp1 being labeled at its N-terminus with gold nanoparticles. When reconstructing the distribution of the nanoparticles in our TEM images, we could see that they were forming a ring-like structure close to the rim, which was especially prominent in the larger pores. In order to average out pore-to-pore variations and obtain smooth distributions such as shown in [Figure 5.11](#) a large amount of similar pores is needed. This comes, however, at the price for the requirement of an automated image analysis procedure. We proposed a potential workflow for this in [subsection 5.3.5](#). Unfortunately, our procedure requires fine-tuning for different data sets that differ slightly in image contrast from one another. Therefore, the data presented in [Figures 5.14 and 5.15](#) still lack a full analysis.

A drawback of the method is that it requires access very specific equipment both for the sample fabrication but also for the final imaging. Additionally, the throughput is relatively low as it is limited by the data acquisition, since for instance already imaging a single grid takes a full day on the TEM.

After having showed the potential of this approach, we can envision multiple interesting applications and extensions of the method. It would be, for instance, straightforward to study the reaction of the Nsp1 mesh to specific concentrations of transporters as is proposed by the Kap-centric models [9–11]. This would be done by end labeling of Nsp1 residues as shown in [Figure 5.11](#) and additionally adding Kap95 proteins without a gold label after the washing step. Kap95 would thus appear invisible in the micrograph its effect on the Nup mesh should still be visible in the distribution of the Nup labels. It would even be possible to collect the locations of the Kap95 proteins by labeling them with a large (5 nm for instance) gold particle that can be clearly distinguished from the 1.4 nm particles.

Furthermore, an extension of the method to threedimensional reconstruction would be possible by acquiring the TEM images at different angles and reconstructing tomograms. At first this would be interesting as a control that the NTRs actually manage to sit *within* the nanopores and not only top. Additionally, both the actual Nup and NTR distributions in three dimensions could be particularly interesting when coupled back

to coarse-grained simulations. It is however a priori not clear if the contrast produced by 1.4 nm gold particles would be large enough under tilted image acquisition for such experiments.

Another interesting application would be to look for both the Nup and transporter distribution in plunge-frozen fully assembled NPCs, comparable to what was done in previous studies [31, 32, 35–37]. With an in vitro reconstitution of full NPCs [1] together with gold labelled constituents, a much higher statistical sampling could be achieved than previously possible with NPCs in the nuclear envelope. In that case, nanoporous freestanding membranes would not be required so standard cryo-EM sample preparation could be employed for these studies.

Summing up, we think that using the method we propose has great potential in studying the structure of the unstructured NPC mimics at excellent spatial resolution together with great statistical coverage.

REFERENCES

- [1] S. J. Kim, J. Fernandez-Martinez, I. Nudelman, Y. Shi, W. Zhang, B. Raveh, T. Hericks, B. D. Slaughter, J. A. Hogan, P. Upla, I. E. Chemmama, R. Pellarin, I. Echeverria, M. Shivaraju, A. S. Chaudhury, J. Wang, R. Williams, J. R. Unruh, C. H. Greenberg, E. Y. Jacobs, Z. Yu, M. J. de la Cruz, R. Mironska, D. L. Stokes, J. D. Aitchison, M. F. Jarrold, J. L. Gerton, S. J. Ludtke, C. W. Akey, B. T. Chait, A. Sali, and M. P. Rout, *Integrative structure and functional anatomy of a nuclear pore complex*, *Nature* **555**, 475 (2018), doi:[10.1038/nature26003](https://doi.org/10.1038/nature26003).
- [2] M. Beck and E. Hurt, *The nuclear pore complex: understanding its function through structural insight*, *Nature Reviews Molecular Cell Biology* **18**, 73 (2017), doi:[10.1038/nrm.2016.147](https://doi.org/10.1038/nrm.2016.147).
- [3] H. B. Schmidt and D. Görlich, *Transport selectivity of nuclear pores, phase separation, and membraneless organelles*, *Trends in Biochemical Sciences* **41**, 46 (2016), doi:<https://doi.org/10.1016/j.tibs.2015.11.001>.
- [4] D. Görlich and U. Kutay, *Transport between the cell nucleus and the cytoplasm*, *Annual Review of Cell and Developmental Biology* **15**, 607 (1999), doi:[10.1146/annurev.cellbio.15.1.607](https://doi.org/10.1146/annurev.cellbio.15.1.607).
- [5] M. P. Rout, J. D. Aitchison, M. O. Magnasco, and B. T. Chait, *Virtual gating and nuclear transport: the hole picture*, *Trends in Cell Biology* **13**, 622 (2003), doi:<https://doi.org/10.1016/j.tcb.2003.10.007>.
- [6] S. Frey, R. P. Richter, and D. Görlich, *Fg-rich repeats of nuclear pore proteins form a three-dimensional meshwork with hydrogel-like properties*, *Science* **314**, 815 (2006), doi:[10.1126/science.1132516](https://doi.org/10.1126/science.1132516).
- [7] S. Frey and D. Görlich, *A saturated fg-repeat hydrogel can reproduce the permeability properties of nuclear pore complexes*, *Cell* **130**, 512 (2007), doi:<https://doi.org/10.1016/j.cell.2007.06.024>.

- [8] J. Yamada, J. L. Phillips, S. Patel, G. Goldfien, A. Calestagne-Morelli, H. Huang, R. Reza, J. Acheson, V. V. Krishnan, S. Newsam, A. Gopinathan, E. Y. Lau, M. E. Colvin, V. N. Uversky, and M. F. Rexach, *A bimodal distribution of two distinct categories of intrinsically disordered structures with separate functions in fg nucleoporins*, *Molecular & Cellular Proteomics* **9**, 2205 (2010), doi:[10.1074/mcp.M000035-MCP201](https://doi.org/10.1074/mcp.M000035-MCP201).
- [9] K. D. Schleicher, S. L. Dettmer, L. E. Kapinos, S. Pagliara, U. F. Keyser, S. Jeney, and R. Y. H. Lim, *Selective transport control on molecular velcro made from intrinsically disordered proteins*, *Nature Nanotechnology* **9**, 525 (2014), doi:[10.1038/nnano.2014.103](https://doi.org/10.1038/nnano.2014.103).
- [10] L. Kapinos, R. Schoch, R. Wagner, K. Schleicher, and R. Lim, *Karyopherin-centric control of nuclear pores based on molecular occupancy and kinetic analysis of multivalent binding with fg nucleoporins*, *Biophysical Journal* **106**, 1751 (2014), doi:<https://doi.org/10.1016/j.bpj.2014.02.021>.
- [11] L. E. Kapinos, B. Huang, C. Rencurel, and R. Y. Lim, *Karyopherins regulate nuclear pore complex barrier and transport function*, *Journal of Cell Biology* **216**, 3609 (2017), doi:[10.1083/jcb.201702092](https://doi.org/10.1083/jcb.201702092).
- [12] L. A. Strawn, T. Shen, N. Shulga, D. S. Goldfarb, and S. R. Wenthe, *Minimal nuclear pore complexes define fg repeat domains essential for transport*, *Nature Cell Biology* **6**, 197 (2004), doi:[10.1038/ncb1097](https://doi.org/10.1038/ncb1097).
- [13] T. Jovanovic-Taliman, J. Tetenbaum-Novatt, A. S. McKenney, A. Zilman, R. Peters, M. P. Rout, and B. T. Chait, *Artificial nanopores that mimic the transport selectivity of the nuclear pore complex*, *Nature* **457**, 1023 (2009), doi:[10.1038/nature07600](https://doi.org/10.1038/nature07600).
- [14] S. W. Kowalczyk, L. Kapinos, T. R. Blosser, T. Magalhães, P. van Nies, R. Y. H. Lim, and C. Dekker, *Single-molecule transport across an individual biomimetic nuclear pore complex*, *Nature Nanotechnology* **6**, 433 (2011).
- [15] A. N. Ananth, A. Mishra, S. Frey, A. Dwarkasing, R. Versloot, E. van der Giessen, D. Görlich, P. Onck, and C. Dekker, *Spatial structure of disordered proteins dictates conductance and selectivity in nuclear pore complex mimics*, *eLife* **7**, e31510 (2018), doi:[10.7554/eLife.31510](https://doi.org/10.7554/eLife.31510).
- [16] A. Fragasso, H. W. de Vries, J. Andersson, E. O. van der Sluis, E. van der Giessen, A. Dahlin, P. R. Onck, and C. Dekker, *A designer fg-nup that reconstitutes the selective transport barrier of the nuclear pore complex*, *Nature Communications* **12**, 2010 (2021), doi:[10.1038/s41467-021-22293-y](https://doi.org/10.1038/s41467-021-22293-y).
- [17] S. C. Ng, T. Güttler, and D. Görlich, *Recapitulation of selective nuclear import and export with a perfectly repeated 12mer glfg peptide*, *Nature Communications* **12**, 4047 (2021), doi:[10.1038/s41467-021-24292-5](https://doi.org/10.1038/s41467-021-24292-5).
- [18] C. E. Zimmerli, M. Allegretti, V. Rantos, S. K. Goetz, A. Obarska-Kosinska, I. Zagoriy, A. Halavatyi, G. Hummer, J. Mahamid, J. Kosinski, and M. Beck,

- Nuclear pores dilate and constrict in cellulose*, *Science* **374**, eabd9776 (2021), doi:[10.1126/science.abd9776](https://doi.org/10.1126/science.abd9776).
- [19] C. W. Akey, D. Singh, C. Ouch, I. Echeverria, I. Nudelman, J. M. Varberg, Z. Yu, F. Fang, Y. Shi, J. Wang, D. Salzberg, K. Song, C. Xu, J. C. Gumbart, S. Suslov, J. Unruh, S. L. Jaspersen, B. T. Chait, A. Sali, J. Fernandez-Martinez, S. J. Ludtke, E. Villa, and M. P. Rout, *Comprehensive structure and functional adaptations of the yeast nuclear pore complex*, *Cell* **185**, 361 (2022), doi:<https://doi.org/10.1016/j.cell.2021.12.015>.
- [20] R. Wagner, L. Kapinos, N. Marshall, M. Stewart, and R. Lim, *Promiscuous binding of karyopherin β 1 modulates fg nucleoporin barrier function and expedites ntf2 transport kinetics*, *Biophysical Journal* **108**, 918 (2015), doi:<https://doi.org/10.1016/j.bpj.2014.12.041>.
- [21] A. Fragasso, H. W. de Vries, J. Andersson, E. O. van der Sluis, E. van der Giessen, P. R. Onck, and C. Dekker, *Transport receptor occupancy in nuclear pore complex mimics*, *Nano Research* (2022), [10.1007/s12274-022-4647-1](https://doi.org/10.1007/s12274-022-4647-1), doi:[10.1007/s12274-022-4647-1](https://doi.org/10.1007/s12274-022-4647-1).
- [22] A. Ghavami, E. van der Giessen, and P. R. Onck, *Coarse-grained potentials for local interactions in unfolded proteins*, *Journal of Chemical Theory and Computation* **9**, 432 (2013), doi:[10.1021/ct300684j](https://doi.org/10.1021/ct300684j).
- [23] A. Ghavami, L. Veenhoff, E. van der Giessen, and P. Onck, *Probing the disordered domain of the nuclear pore complex through coarse-grained molecular dynamics simulations*, *Biophysical Journal* **107**, 1393 (2014), doi:[10.1016/j.bpj.2014.07.060](https://doi.org/10.1016/j.bpj.2014.07.060).
- [24] H. Jafarinaia, E. Van der Giessen, and P. R. Onck, *Phase separation of toxic dipeptide repeat proteins related to c9orf72 als/ftd*, *Biophysical Journal* **119**, 843 (2020), doi:[10.1016/j.bpj.2020.07.005](https://doi.org/10.1016/j.bpj.2020.07.005).
- [25] D. Winogradoff, H.-Y. Chou, C. Maffeo, and A. Aksimentiev, *Percolation transition prescribes protein size-specific barrier to passive transport through the nuclear pore complex*, *Nature Communications* **13**, 5138 (2022), doi:[10.1038/s41467-022-32857-1](https://doi.org/10.1038/s41467-022-32857-1).
- [26] H. Jafarinaia, E. Van der Giessen, and P. R. Onck, *Molecular basis of c9orf72 poly-pr interference with the β -karyopherin family of nuclear transport receptors*, *Scientific Reports* **12**, 21324 (2022), doi:[10.1038/s41598-022-25732-y](https://doi.org/10.1038/s41598-022-25732-y).
- [27] M. Dekker, E. Van der Giessen, and P. R. Onck, *Phase separation of intrinsically disordered fg-nups is driven by highly dynamic fg motifs*, *Proceedings of the National Academy of Sciences* **120**, e2221804120 (2023), doi:[10.1073/pnas.2221804120](https://doi.org/10.1073/pnas.2221804120).
- [28] N. Klughammer, A. Barth, M. Dekker, A. Fragasso, P. Onck, and C. Dekker, *Diameter dependence of transport through nuclear pore complex mimics studied using optical nanopores*, *eLife* **12** (2023), [10.7554/eLife.87174](https://doi.org/10.7554/eLife.87174), doi:[10.7554/eLife.87174](https://doi.org/10.7554/eLife.87174).

- [29] D. Stoffer, K. N. Goldie, B. Feja, and U. Aebi, *Calcium-mediated structural changes of native nuclear pore complexes monitored by time-lapse atomic force microscopy* Edited by W. Baumeister, *Journal of Molecular Biology* **287**, 741 (1999), doi:[10.1006/jmbi.1999.2637](https://doi.org/10.1006/jmbi.1999.2637).
- [30] Y. Sakiyama, A. Mazur, L. E. Kapinos, and R. Y. H. Lim, *Spatiotemporal dynamics of the nuclear pore complex transport barrier resolved by high-speed atomic force microscopy*, *Nature Nanotechnology* **11**, 719 (2016), doi:[10.1038/nnano.2016.62](https://doi.org/10.1038/nnano.2016.62).
- [31] N. Panté, F. Thomas, U. Aebi, B. Burke, and R. Bastos, *Recombinant Nup153 Incorporates in Vivo into Xenopus Oocyte Nuclear Pore Complexes*, *Journal of Structural Biology* **129**, 306 (2000), doi:[10.1006/jsbi.2000.4232](https://doi.org/10.1006/jsbi.2000.4232).
- [32] B. Fahrenkrog, B. Maco, A. M. Fager, J. Köser, U. Sauder, K. S. Ullman, and U. Aebi, *Domain-specific antibodies reveal multiple-site topology of Nup153 within the nuclear pore complex*, *Journal of Structural Biology* **140**, 254 (2002), doi:[10.1016/S1047-8477\(02\)00524-5](https://doi.org/10.1016/S1047-8477(02)00524-5).
- [33] F. Cardarelli, L. Lanzano, and E. Gratton, *Capturing directed molecular motion in the nuclear pore complex of live cells*, *Proceedings of the National Academy of Sciences* **109**, 9863 (2012), doi:[10.1073/pnas.1200486109](https://doi.org/10.1073/pnas.1200486109).
- [34] M. Yu, M. Heidari, S. Mikhaleva, P. Tan, S. Mingu, H. Ruan, C. Reinkermeier, A. Obarska-Kosinska, M. Siggel, M. Beck, G. Hummer, and E. Lemke, *Deciphering the conformations and dynamics of fg-nucleoporins in situ*, *bioRxiv* (2022), [10.1101/2022.07.07.499201](https://doi.org/10.1101/2022.07.07.499201), doi:[10.1101/2022.07.07.499201](https://doi.org/10.1101/2022.07.07.499201).
- [35] S. I. Dworetzky, R. E. Lanford, and C. M. Feldherr, *The effects of variations in the number and sequence of targeting signals on nuclear uptake*. *Journal of Cell Biology* **107**, 1279 (1988), doi:[10.1083/jcb.107.4.1279](https://doi.org/10.1083/jcb.107.4.1279).
- [36] N. Panté and M. Kann, *Nuclear Pore Complex Is Able to Transport Macromolecules with Diameters of ~ 39 nm*, *Molecular Biology of the Cell* **13**, 425 (2002), doi:[10.1091/mbc.01-06-0308](https://doi.org/10.1091/mbc.01-06-0308).
- [37] D. Görlich, N. Panté, U. Kutay, U. Aebi, and F. R. Bischoff, *Identification of different roles for RanGDP and RanGTP in nuclear protein import*. *The EMBO Journal* **15**, 5584 (1996), doi:[10.1002/j.1460-2075.1996.tb00943.x](https://doi.org/10.1002/j.1460-2075.1996.tb00943.x).
- [38] D. N. Mastronarde, *Automated electron microscope tomography using robust prediction of specimen movements*, *Journal of Structural Biology* **152**, 36 (2005), doi:<https://doi.org/10.1016/j.jsb.2005.07.007>.
- [39] N. Klughammer and C. Dekker, *Palladium zero-mode waveguides for optical single-molecule detection with nanopores*, *Nanotechnology* **32**, 18LT01 (2021), doi:[10.1088/1361-6528/abd976](https://doi.org/10.1088/1361-6528/abd976).

5.5. APPENDIX

5.5.1. SEQUENCES OF KAP95 AND NSP1

The sequence of the Nsp1 used here was:

MHHHHHHHHHHGSGENLYFQGTSMGNFNTQQNKTPFSFGTANNNSNTTNQNSSTG
 AGAFGTGQSTFGFNNSAPNNTNNANSSITPAFGSNNTGNTAFGNSNPTSINVFGSNNSTT
 NTFGSNSAGTSLFGSSSAQQTKSNGTAGGNTFGSSSLFNNSTNSNTTKPAFGGLNFGGGN
 NTPSSTGNANTSNNLFGATANANKPAFSFGATTNDDKKTEPKPAFSFNSSVGNKTD
 QAPTTGFSFGSQLGGNKTVNEAAKPSLSFGSGSAGANPAGASQPEPTTNEPAKPAFSFGTA
 TSDNKTTNTTPSFSFGAKSDENKAGATSKPAFSFGAKPEEKKDDNSSKPAFSFGAKSNEDK
 QDGTAKPAFSFGAKPAEKNNNETSKPAFSFGAKSDEKKDGDASKPAFSFGAKPDENKASA
 TSKPAFSFGAKPEEKKDDNSSKPAFSFGAKSNEDKQDGTAKPAFSFGAKPAEKNNNETSK
 PAFSFGAKSDEKKDGDASKPAFSFGAKSDEKKDSDSSKPAFSFGTKSNEKKDSSKPAFSF
 GAKPDEKKNDEVSKPAFSFGAKANEKKESEKSAFSGSKPTGKEEGDGAKAAISFGAKP
 EEQSSDTSKPAFTFGAQKDNEKKTEC

And the sequence of Kap95 used here was: MSTAEFAQLLENSILSPDQNIRLTSETQLKK
 LSNDNFLQFAGLSSQVLIDENTKLEGRILAALTLKNELVSKDSVKTQQFAQRWITQVSPEAK
 NQIKTNALTALVSIEPRIANAAAQLIAAIADIELPHGAWPELMKIMVDNTGAEQPENVKRAS
 LLALGYMCESADPQSQUALVSSSNNILIAIVQGAQSTETSKAVRLAALNALADSLIFIKNNME
 REGERNYLMQVVCEATQAEDIEVQAAAFGLCKIMSLYTFMKPYMEQALYALTIATMKS
 PNDKVASMTVEFWSTICEEEIDIAVELAQFPQSPLQSYNFALSSIKDVVPNLLNLLTRQNE
 PEDDDWNVMSAGACLQLFAQNCGNHILEPVLEFVEQNITADNWRNREAAVMAFGSIM
 DGPDKVQRTYVHVALPSILNLMNDQSLQVKETTAWCIGRIADSVAESIDPQQHLPGVVQ
 ACLIGLQDHPKVATNCSWTIINLVEQLAEATPSPIYNFYALVDGLIGANRIDNEFNARAS
 AFSALTTMVEYATDTVAETSASISTFVMDKLGQTMVDENQLTLEDAQSLQELQSNILTVL
 AAVIRKSPSSVEPVADMLMGLFFRLEKKDSAFIEDDVFYAISALAASLGKGFKEYLETFSPY
 LLKALNQVDSPVSITAVGFIADISNSLEEDFRYSDDAMMNVLQAMISPNARRELKPAVLSV
 FGDIASNIGADFIPYLNIDIMALCVAQNTKPENGTLEALDYQIKVLEAVLDAYVGVAVGLHD
 KPEALFPYVGTIFQFIAQVAEDPQLYSEDATSRAAVGLIGDIAAMFPDGSIKQFYGGQDWVID
 YIKRTRSGQLFSQATKDTARWAREQQKRQLSL

6

ZERO-MODE WAVEGUIDE NANOWELLS FOR SINGLE-MOLECULE DETECTION IN LIVING CELLS

Single-molecule fluorescence imaging experiments generally require sub-nanomolar protein concentrations to isolate single protein molecules, which makes such experiments challenging in live cells due to high intracellular protein concentrations. Here, we show that single-molecule observations can be achieved in live cells through a drastic reduction in the observation volume using overmilled zero-mode waveguides (ZMWs - subwavelength-size holes in a metal film). Overmilling of the ZMW in a palladium film creates a nanowell of tunable size in the glass layer below the aperture, which cells can penetrate. We present a thorough theoretical and experimental characterization of the optical properties of these nanowells over a wide range of ZMW diameters and overmilling depths, showing an excellent signal confinement and a five-fold fluorescence enhancement of fluorescent molecules inside nanowells. ZMW nanowells facilitate live-cell imaging, as cells form stable protrusions into the nanowells. Importantly, the nanowells greatly reduce cytoplasmic background fluorescence, enabling detection of individual membrane-bound fluorophores in the presence of high cytoplasmic expression levels, which could not be achieved with TIRF microscopy. Zero-mode waveguide nanowells thus provide great potential to study individual proteins in living cells.

This chapter has been published at *ACS Nano* as Sora Yang*, Nils Klughammer*, Anders Barth*, Marvin E. Tanenbaum*, and Cees Dekker*, Zero-mode waveguide nanowells for single-molecule detection in living cells. doi:[10.1021/acsnano.3c05959](https://doi.org/10.1021/acsnano.3c05959)

6.1. INTRODUCTION

Single-molecule techniques are widely applied to study the behavior of biomolecules or biomolecular complexes, providing mechanistic insights into individual steps of biological processes that would otherwise be averaged out in bulk experiments [1]. Imaging-based approaches have been especially powerful in studying single nucleic acid and protein molecules, as they allow tracking of individual biomolecules in space and time. Central to all single-molecule fluorescence imaging techniques is the ability to detect and distinguish a single molecule of interest over the background of fluorescent molecules that are freely diffusing through the solution. The ability to isolate a single molecule by imaging therefore depends on the concentrations of fluorescent molecules and the observation volume; if multiple freely diffusing molecules are present within the observation volume, the isolation of one specific molecule of interest becomes very challenging. [2]

In *in vitro* experiments, single-molecule observation can easily be achieved by using low concentrations of fluorescent molecules, which limits the number of molecules in the observation volume. However, weak biomolecular interactions ($K_d > 1 \mu\text{M}$) that require high concentrations cannot be studied at the nano- to picomolar concentrations that are typically employed in *in vitro* single-molecule experiments. Moreover, studying biomolecules in their natural habitat, the crowded environment of live cells, is also very challenging, as protein concentrations in cells are often in the high nanomolar to micromolar range [3], which is incompatible with single-molecule observations [2]. Fundamentally, the concentration limit for single-molecule observation is bounded by the size of the observation volume, which can be minimized using used common optical sectioning methods such as confocal microscopy, total internal reflection microscopy (TIRF), or light-sheet microscopy [4]. Despite such improvements, the volumes remain on the order of femtoliters, which puts the concentration limit for isolating single molecules at $\approx 1 \text{ nM}$ [2, 5].

A much more drastic confinement of the observation volume can be achieved using zero-mode waveguides (ZMW), which are subwavelength apertures in a metal film. Owing to their small size ($\sim 100 \text{ nm}$), ZMWs effectively block the propagation of incident light of wavelengths above a characteristic cutoff wavelength λ_c , $\lambda > \lambda_c = 1.7d$, where d is the diameter of the aperture. Within the ZMW, an evanescent field forms which to first order follows an exponential decay as $I(z) = I_0 \exp\left(-2z\sqrt{\frac{1}{\lambda_c^2} - \frac{1}{\lambda^2}}\right)$ [6]. Typical decay lengths are on the scale of several tens to hundred of nanometers, depending on the ZMW diameter, the wavelength of incident light in the surrounding medium, and the ZMW material. Thus, by providing observation volumes in the zeptoliter range, ZMWs enable single-molecule studies at even micromolar concentrations [7]. ZMWs made from gold or aluminum have been extensively studied [7–14] and used for a variety of *in vitro* single-molecule applications [15–21], and notably for DNA sequencing [22]. Recently, we have introduced the use of palladium for free-standing ZMWs [23], which were applied to the *in vitro* study of nuclear transport [24]. Palladium offers excellent mechanical and chemical stability, can easily be modified *via* thiol chemistry [24–26], and provides reduced photoluminescence in the blue spectral region compared to gold [23, 27, 28]. Importantly, Pd is compatible with live cell experiments due to its low cytotoxicity [29].

While the vast majority of studies applying ZMWs to single-molecule measurements have been performed *in vitro*, a few studies have shown that ZMWs made of aluminum can be applied to single-molecule imaging of cellular (membrane) proteins as well, as cells can form protrusions that penetrate into ZMWs [30–32], which has enabled single-molecule observation of membrane composition [30] and membrane channels [32]. Inspired by this work, we hypothesized that the creation of nanowells in the glass coverslip below the ZMWs (see Figure 6.1 A) provide a means of fine-tuning the size of the observation volume and result in excellent optical properties, while allowing cellular protrusions to enter the nanowells. [33, 34]. Moving the observation volume slightly away from the ZMW cavity can potentially lead to an increase of the single-molecule fluorescence signal due to enhancement of the excitation field or modulation of the radiative and non-radiative rates by the metal, as has previously been shown for aluminum [35–37] and gold [12]. Overmilling could also allow cells to penetrate more deeply through the ZMWs and allow facile imaging not only of membrane bound proteins, but of proteins in the cytoplasm too, greatly expanding the potential applications of ZMW imaging of living cells.

Here, we establish palladium ZMWs nanowells as a tool for single-molecule studies in live cells (Figure 6.1 A). We fabricated ZMW arrays using focused ion beam (FIB) milling, which allowed us to survey a wide range of diameters and overmilling depths to optimize the design for both optical performance and cell compatibility. Finite-difference time-domain (FDTD) simulations of the excitation intensity and fluorescence emission showed an effective reduction of the observation volume to the nanowell below the ZMW and suggested a potential fluorescence enhancement due to the focusing of the excitation intensity within the well, facilitated by the formation of a standing wave below the metal layer. The theoretical results are corroborated by single-molecule experiments on freely diffusing fluorophores which confirmed the signal confinement and showed an up to five fold fluorescence enhancement. Using live-cell imaging, we show that human osteosarcoma U2OS cells readily protruded into the nanowells, protruding more efficiently when ZMWs were overmilled. Cell protrusions remained stable over the timescale of minutes, enabling single-molecule observation of individual membrane-bound fluorophores even in the presence of high cytoplasmic concentrations of the same fluorophores. This was only possible due to the efficient suppression of cytoplasmic background signal by the ZMW, whereas conventional TIRF microscopy did not allow single molecules to be followed in this setting. Oblique illumination of the nanowells lead to a further reduction of the background levels. Due to their excellent cell compatibility, overmilled Pd ZMWs can be readily applied for single-molecule studies of biological processes in living cells at physiological concentrations.

6.2. RESULTS

6.2.1. FABRICATION OF Pd ZMWs ON GLASS

To fabricate nanowells, we first applied a thin (100 nm or 150 nm) palladium layer to standard glass coverslips covered with a 5 nm Ti adhesion layer by physical vapor deposition (Figure 6.1 B). In contrast to previous studies that used aluminum [30–32], we chose palladium due to its suitability for nanostructuring, good chemical stability, low

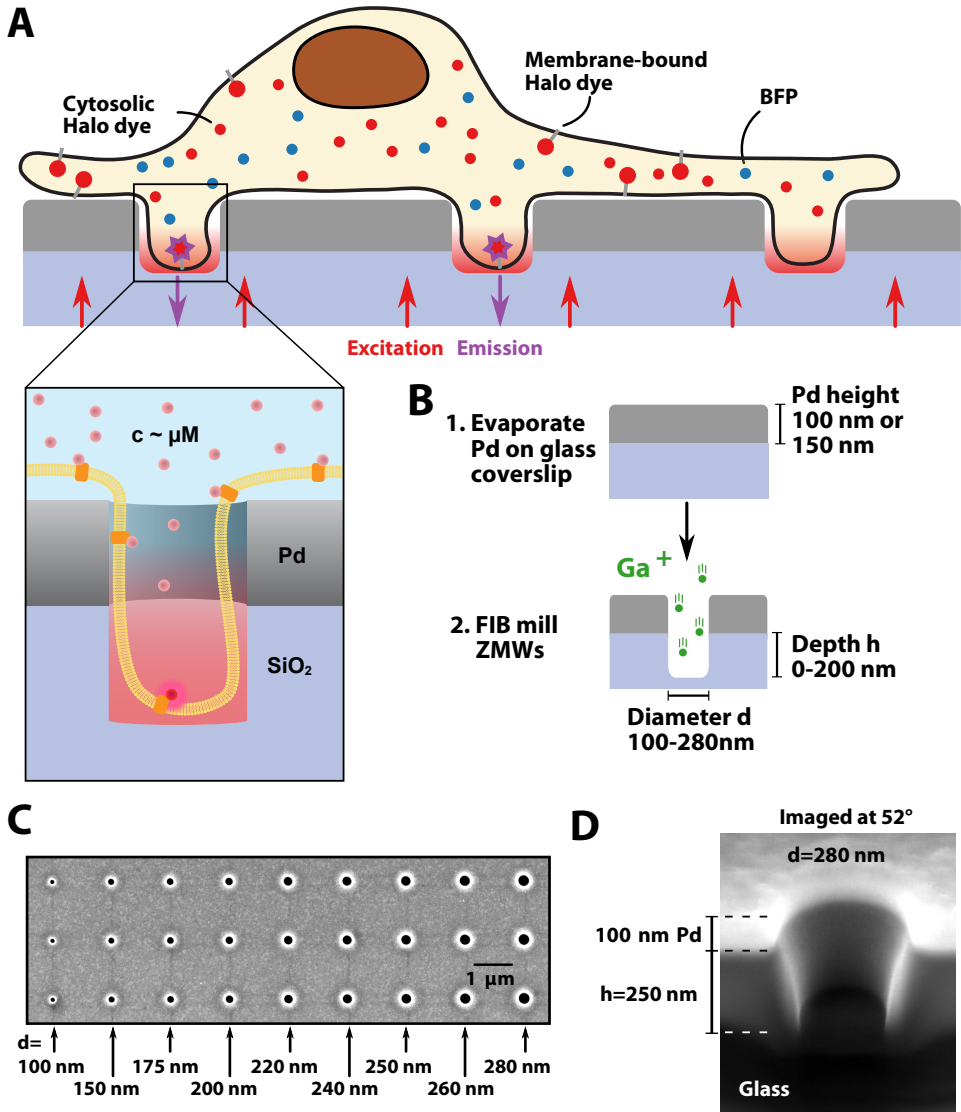


Figure 6.1: Schematic of the experiment and fabrication of overmilled ZMWs. **A:** Schematic of a cell on top of an array of overmilled ZMWs. Nanowells below Pd ZMWs allow for the observation of single membrane bound fluorophores despite a high abundance of cytoplasmic fluorophores. **B:** Pd is evaporated onto a glass coverslip and ZMWs are created by local focused ion beam milling. Pore diameters used in the study ranged between 100 nm to 280 nm and overmilling depths ranged between 0 nm to 200 nm. **C:** SEM image showing ZMWs with different pore diameters. **D:** The depth of milling was measured by cutting through the pores with a focused ion beam, and measuring the height when imaging under an angle of 52°.

photoluminescence in the visible spectrum, and low cytotoxicity [23, 26, 29]. Palladium surfaces can also easily be functionalized using thiols, which provides a strategy for the specific immobilization of molecules and thus can be used for surface passivation *via* self-assembled monolayers or may be useful for promoting cell adhesion for certain cell types [25]. As in our previous studies [23, 24], we used focused ion beam (FIB) milling to create pores in the metal layer, which allows the precise tuning of pore diameters and pore depths within a single array (Figure 6.1 B). We manufactured arrays containing pores of different sizes and depths, including larger marker holes for identification of the different areas within the arrays (Figure 6.1 — Supplementary Figure 6.1). Typically, 16 arrays were placed on a single glass coverslip, each containing ≈ 3000 nanowells of varying diameter and depth (Figure 6.1 C, Figure 6.1 — Supplementary Figure 6.1). Pore diameters were chosen to range between 100 nm to 280 nm based on a previous study that showed cell protrusion into ZMWs [32]. The depth of the nanowells was varied by overmilling into the glass surface below the palladium layer up to 200 nm. An example cross-section is shown in Figure 6.1 D.

6.2.2. SIMULATING THE OPTICAL PROPERTIES OF PALLADIUM ZMW NANOWELLS

To guide the selection of the optimal width and depth of the well below the ZMW, we performed finite-difference time-domain (FDTD) simulations of the excitation electromagnetic field and dipole emission within overmilled ZMWs (Figure 6.2 A). These simulations allow us to assess the spatial distribution of the excitation intensity, the modulation of the fluorescence quantum yield of the fluorophore, and the fraction of signal directed towards the detection side, which together define the detectable signal from within the nanowell as the product of these quantities.

To cover the different excitation modes applied in this study, we probed the excitation field distribution at wavelengths of 488 nm and 640 nm upon excitation by a plane wave (widefield), under an angled illumination as used in TIRF microscopy (Figure 6.2 B, C, F, H, and Figure 6.2 — Supplementary Figure 6.2 – 6.5), as well as upon excitation by a focused beam (Figure 6.2 — Supplementary Figure 6.6 – 6.7). As expected, the zero-mode waveguide effectively blocks the propagation of the excitation light under all conditions for small pore diameters of 100 nm or below, as evident from the profiles of the excitation intensity along the pore axis (Figure 6.2 F, H). At large pore diameters of 200 nm and above, a finite amount of excitation light propagates beyond the ZMW. Due to the reflective surface of the metal, a standing wave is formed on the detection side which leads to an undulation of the excitation field intensity within the overmilled volume (Figure 6.2 B) [12, 36, 37]. Under TIRF illumination at an angle of 70° , the first maximum of the standing wave pattern is shifted to longer distances from the metal surface compared to widefield excitation because the magnitude of the wave vector orthogonal to the metal surface is reduced (Figure 6.2 C). This results in a reduced excitation intensity within the well, but also provides a more even intensity distribution with an intensity maximum at the bottom of the well. Additionally, the propagation of light through the ZMW is reduced under TIRF illumination compared to widefield excitation, which may limit background cytoplasmic fluorescence in imaging experiments (Figure 6.2 H).

In addition to modulating the excitation field, the metal nanostructure affects the

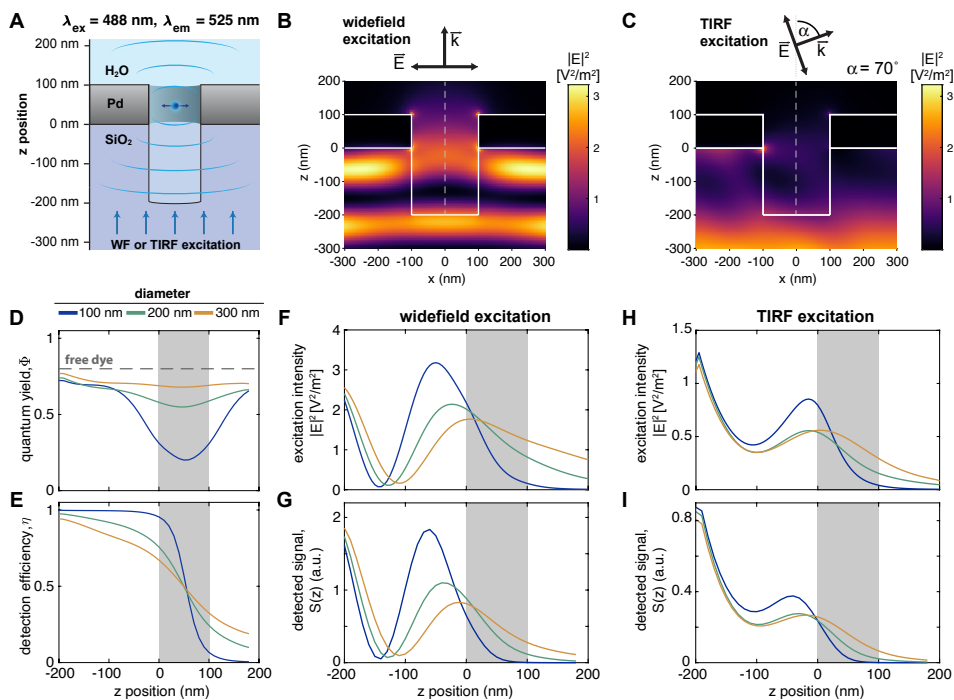


Figure 6.2: FDTD simulations of the excitation field and fluorescence emission within a nanowell underneath a ZMW. **A:** Schematic of the simulation setup. A dipole was placed at varying depths within the aperture and excited by a plane wave incident from the bottom (widefield, WF) or under an angle of 70° resembling conditions used in TIRF microscopy. **B,C:** Resulting distributions of the excitation field intensity for widefield (B) or TIRF (C) excitation for a ZMW diameter of 200 nm and an overmilling depth of 200 nm. The electric field is polarized along the x-axis. **D,E:** Computed quantum yield and detection efficiency of the dye Alexa488 as a function of the z-position along the central pore axis (dashed line in B,C). **F-I:** Z-profiles of the excitation intensity along the central pore axis (F,H) and the detected signal $S(z)$ (G,I) under widefield (F,G) and TIRF (H,I) excitation. The position of the metal membrane is indicated as a gray shaded area.

quantum yield of the fluorophore by modulating radiative and non-radiative decay rates, which we assess by simulating dipole emission at varying depths along the central axis of the nanowell (Figure 6.2 A,D and Figure 6.2 — Supplementary Figure 6.8 – 6.9). Within the ZMW, the radiative rate is reduced while the non-radiative rate is strongly increased due to coupling to the metal nanostructure (grey area in Figure 6.2 — Supplementary Figure 6.10). As the distance to the metal increases, the non-radiative losses decrease, while the radiative rate remains relatively constant within the volume beneath the ZMW. Overall, within the proximity of the ZMW, these effects lead to a strong predicted reduction of the quantum yield (Figure 6.2 D) and hence the fluorescence lifetime (Figure 6.2 — Supplementary Figure 6.8 D, Supplementary Figure 6.9 D), as will be assessed experimentally below. Within the nanowell below the ZMW, the modulation of the decay rates was only weakly dependent on the lateral position (Figure 6.2 — Supplementary Figure 6.11). Finally, we consider the fraction of the fluorescence emission that can be detected in the experiment, *i.e.*, the signal emitted towards lower side of the ZMW facing

the objective lens. Part of the dipole emission from within the ZMW is lost as it propagates towards the upper side of the ZMW that faces away from the objective lens, leading to a sharp decay of the detection efficiency within the ZMW (Figure 6.2 E). Below the ZMW, the effective detection efficiency of the dipole emission is increased approximately two-fold compared to the absence of a metal nanostructure because the metal layer acts as a mirror and propagation of radiation through the ZMW is blocked (Figure 6.2 E and Figure 6.2 — Supplementary Figure 6.8,6.9). Overall, these processes lead to a more effective restriction of the detected signal to the well below the ZMW compared to what is expected from the excitation intensity alone.

The end result is a near-complete suppression of background signals originating from the top side of the ZMW. Under widefield excitation, the simulations predict a background level of 3 % at a pore diameter of 100 nm in a 100 nm thin Pd film, which increases to 10% at 300 nm diameter (numbers are given for overmilling depth of 200 nm, Figure 6.2 — Supplementary Figure 6.12 A,D). Under TIRF excitation, the background level decreases further by approximately a factor of two compared to widefield excitation because the excitation intensity is more effectively confined to the nanowell, reaching an excellent signal-to-background ratio of ~25 even for a large pore diameter of 300 nm at an overmilling depth of 200 nm (Supplementary Figure 6.12 E).

In summary, the FDTD simulations show that the observed signal remains effectively confined to the overmilled volume and the ZMW even for pore diameters of up to 300 nm (Figure 6.2 G,I and Figure 6.2 — Supplementary Figure 6.8 – 6.12). Notably, no enhancement of the fluorescence emission is expected as the presence of the metal waveguide is found to significantly reduce the fluorescence quantum yield (Figure 6.2 D). On the other hand, the excitation field is enhanced in the proximity of the metal surface due to the formation of the standing wave, reaching peak intensities that are up to three-times higher compared to the absence of waveguide (Figure 6.2 B,C,F,H), and the detection efficiency is increased two-fold because the dipole emission is directed towards the detection side (Figure 6.2 E). Together, these effects lead to a significant enhancement of the detected signal from the nanowells.

6.2.3. NANOWELLS PROVIDE SIGNAL CONFINEMENT AND ENHANCEMENT

To corroborate the theoretical results, we performed measurements on freely diffusing dyes in water in the nanowells using confocal excitation, see Figure 6.3 A. As expected, the detected fluorescence signal of the dyes Alexa488 and JFX650 in the nanowells increased with both the pore diameter and milling depth (Figure 6.3 B and Figure 6.3 — Supplementary Figure 6.13 and C,H,M of Figure 6.3 — Supplementary Figure 6.14 and 6.15). Time traces of the signal within the wells showed fluctuations originating from the diffusion of fluorophores (Figure 6.3 C). Using fluorescence correlation spectroscopy (FCS), we estimated the number of particles within the nanowells which ranged between 0 and 20 (Figure 6.3 D and Figure 6.3 — Supplementary Figure 6.14 – 6.15). We observed a linear scaling of the particle number with the milling depth and quadratic scaling with the pore diameter as expected for the cylindrical wells (Figure 6.3 — Supplementary Figure 6.16 A,B). While the corresponding volumes scaled well with predictions, absolute volumes estimated by FCS exceeded the volume of the nanowells including the ZMW volume by a factor of 2-6 (Figure 6.3 — Supplementary Figure 6.16 C,D). Comparable

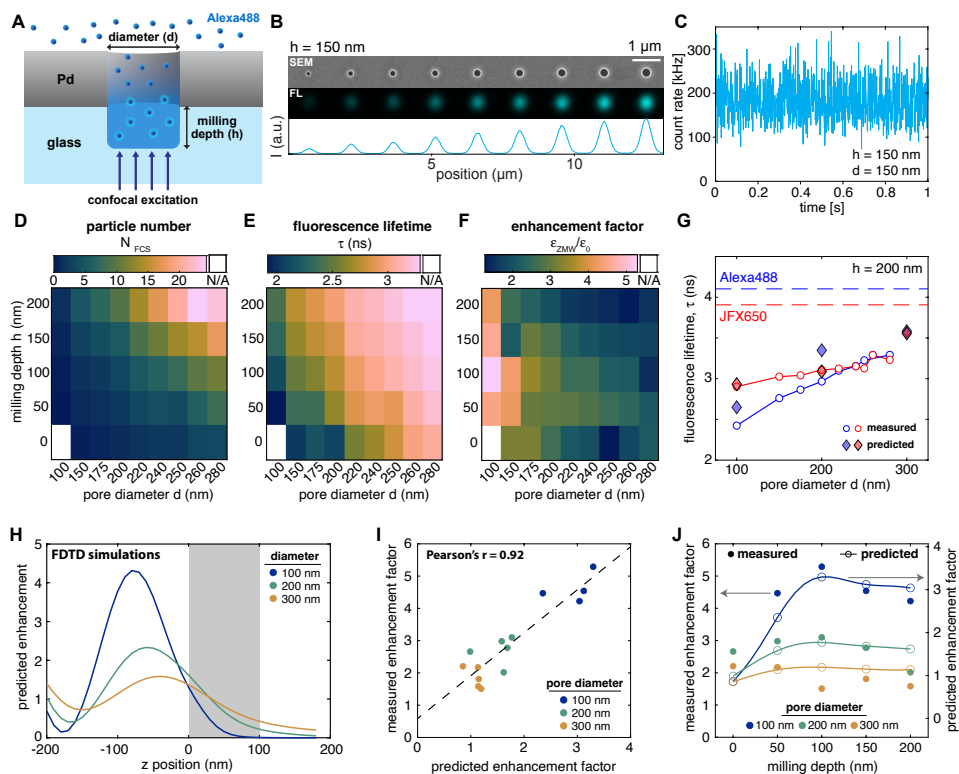


Figure 6.3: Experimental characterization of fluorescence properties in ZMWs. **A:** Schematic of a ZMW with freely diffusing Alexa488 dye. **B:** SEM (top) and confocal fluorescence (middle) image of a pore array with a milling depth of 150 nm. The fluorescence image was acquired at a $1 \mu\text{M}$ concentration of Alexa488. The intensity profile of the fluorescence image is shown below. The scalebar corresponds to $1 \mu\text{m}$. **C:** Example fluorescence time trace (binning: 1 ms) acquired at a concentration of 500 nM Alexa488 for a ZMW with a diameter of 280 nm and no overmilling ($h = 0 \text{ nm}$). **D–F:** Heatmaps of the average number of particles in the observation volume N_{FCS} , fluorescence lifetime τ , and signal enhancement factor defined as the ratio of the counts per molecule in the ZMW compared to free diffusion, $\epsilon_{\text{ZMW}}/\epsilon_0$ acquired for 500 nM of Alexa488. Data marked as N/A could not be quantified due to insufficient signal. **G:** Comparison of measured and predicted fluorescence lifetimes from FDTD simulations for an overmilling depth of 200 nm. The lifetimes of the free dyes are shown as dashed lines. **H:** Predicted signal enhancement compared to a free-diffusion experiment as a function of the z position obtained from FDTD simulations (see [Supplementary Figure 6.19](#) for details). **I:** Linear regression of the measured versus the predicted signal enhancement. **J:** Comparison of measured and predicted enhancement factors as a function of the overmilling depth.

deviations had also been observed in previous studies [7, 8, 12, 38], and were attributed to the signal contribution of many dim fluorophores from the highly concentrated solution that leaks through the ZMW from the other side [7]. This explanation is further supported by the fact that the volume mismatch is largest at high volumes (Figure 6.3 — [Supplementary Figure 6.16 C,D](#)), since large ZMW diameters showed a higher background signal also in FDTD simulations (Figure 6.2 G–I, Figure 6.2 — [Supplementary Figure 6.12](#)). The residence time of the dyes within the nanowell, as seen from the decay

of the FCS curves, likewise increased with the size of the well (Figure 6.3 — Supplementary Figure 6.13 – 6.14).

To gauge the amount of radiative and non-radiative rate enhancement experienced by the dyes, we quantified the excited state fluorescence lifetime (Figure 6.3 E), where a reduced lifetime indicates a stronger enhancement of either radiative or non-radiative relaxation. Fluorescence decays were well described by a mono-exponential model function (Figure 6.3 — Supplementary Figure 6.13). We observed the strongest modulation of the fluorescence lifetime for small pore diameters and shallow wells where the dye is restricted within the proximity of the metal aperture. The predicted signal-averaged fluorescence lifetimes from the FDTD simulations showed excellent quantitative agreement with the experimental values (Figure 6.3 G).

To test for a potential enhancement of the signal emanating from the nanowells, we define a signal enhancement factor by comparing the molecular brightness of the fluorophore (as measured from the FCS analysis) within the nanowell to the free-diffusion value. For both dyes, a signal enhancement of 2-5 was observed across the entire parameter space (Figure 6.3 F, Figure 6.3 — Supplementary Figure 6.17). The largest enhancement was observed at small pore diameters, reaching a maximum value of 4-5 at a pore diameter of 100 nm and a milling depth of 100 nm for Alexa488. Higher molecular brightness correlated with a reduced fluorescence lifetime (Figure 6.3 — Supplementary Figure 6.18). Notably, the highest signal enhancement was not obtained at zero over-milling where the dyes are confined to the ZMW, but rather increased as the nanowell extended into the glass up to a depth of 100 nm, after which the signal enhancement was reduced.

To understand the observed enhancement, we computed the theoretical enhancement factor from the FDTD simulations (Figure 6.3 H, Figure 6.3 – Supplementary Figure 6.19). This enhancement originates predominantly from a focusing of the excitation light due to the formation of the standing wave, as no quantum yield enhancement was found to be present due to losses to the metal nanostructure (Figure 6.2 – Supplementary Figure 6.10). Accordingly, the z-profile of the enhancement factor is dominated by the profile of the excitation field. Experimental and predicted enhancement factors showed excellent correlation, although the experimental enhancement factors slightly exceeded the predicted values (Figure 6.3 I). The predicted enhancement factors reproduced well the experimental trends obtained for different pore diameters and milling depths, confirming the maximum of the enhancement at a depth of approximately 100 nm (Figure 6.3 J).

In summary, overmilled palladium ZMWs provide an excellent confinement of the detected signal to the volume in a nanowell below the metal aperture for pore diameters up to 300 nm, while simultaneously offering up to a five-fold signal enhancement by focusing the excitation power within the nanowell.

6.2.4. MEMBRANE PROTRUSIONS OF LIVE CELLS CAN BE IMAGED THROUGH PD ZMWs

To investigate the extent of cell membrane protrusion into ZMWs, cell membranes were fluorescently labeled using a blue fluorescent protein (BFP) fused to the transmembrane domain of the transmembrane protein CD40 (CD40TM-BFP). Cells expressing CD40TM-

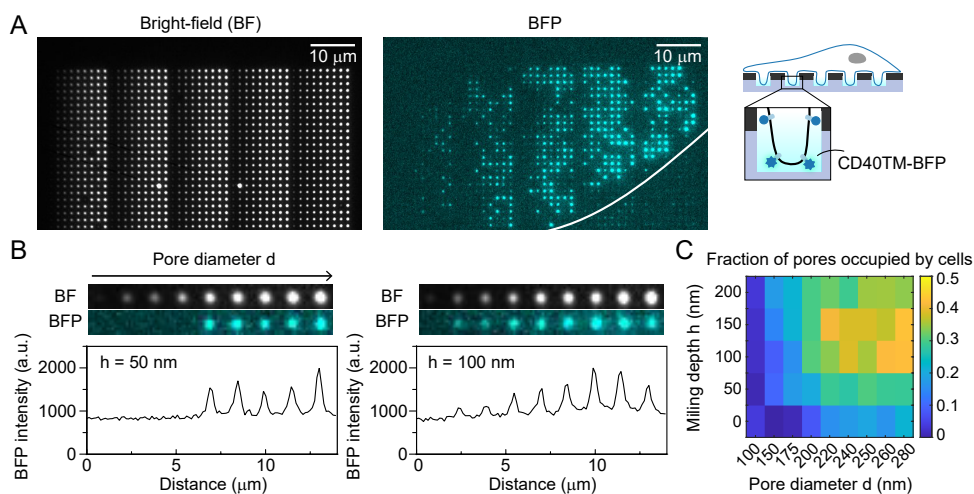


Figure 6.4: The cell membrane protrudes into nanowells. **A:** U2OS cells expressing CD40TM-BFP on a ZMW array of version 1. Bright-field (left) and BFP fluorescence (right) images are shown. White outline represents an estimated outline of a cell on the surface. **B:** Intensity profiles of BFP fluorescence along different pore diameters (100 nm to 280 nm) for a milling depth of 50 nm (left) and 100 nm (right). **C:** Fraction of pores with detectable BFP signal for each pore size, as determined from 7367 pores potentially covered by cells.

6

BFP were grown on a Pd film containing arrays of ZMWs with different diameters and depths (Figure 6.1 — Supplementary Figure 6.1). Based on their morphology, cells appeared healthy on Pd surfaces for at least two days. When imaged through the ZMWs, we observed BFP signal in many nanowells (Figure 6.4 A). To verify the presence of cells on the ZMW arrays, coverslips were flipped upside-down to image the entire cells using widefield fluorescence microscopy (Figure 6.4 — Supplementary Figure 6.22). The location of BFP-positive nanopores corresponded well to the position of cells on the nanopore array, indicating that the observed fluorescence in nanopores originated from cells that had membrane protrusions in the pores. To examine the relationship between pore size and cell membrane protrusion into pores, the BFP fluorescence intensities inside nanowells were analyzed for different pore sizes (Figure 6.4 B and Figure 6.4 — Supplementary Figure 6.22 C). The amount of protrusions into nanowells, as assessed from the BFP signal, decreased both with the decreased pore diameter and milling depth, with the smallest pore diameter ($d = 100 \text{ nm}$) only showing a very small amount (few percent) of occupied pores (Figure 6.4 C). Efficient cell protrusions into nanowells with an occupancy of up to 50% occurred for pore diameter above 200 nm and milling depths above 50 nm. Importantly, the low occupancy for pores with no overmilling confirmed that the creation of nanowells with overmilling is key to observation of the cell protrusions. Increased area of the glass surface in overmilled nanowells may facilitate the cell adhesion within the nanowells, leading to improved protrusion in nanowells compared to ZMWs without overmilling.

Having established that cells protrude into the nanowells, we assessed the stability and dynamics of the signals from the cell protrusions. For this, we generated a monoclonal cell line that expressed cytoplasmic BFP to assess whether cytoplasmic pro-

teins could be imaged on experimentally relevant timescales within the nanowells (Figure 6.5 A). Based on the efficiency of cell protrusion into nanopores of different sizes (Figure 6.4 C), we narrowed the range of pore diameters down to a range of 170 nm to 250 nm (Figure 6.1 — Supplementary Figure 6.1). We observed BFP cytoplasmic fluorescence of varying intensity in a large proportion of the pores (Figure 6.5 A and Figure 6.5 — Supplementary Figure 6.23). To assess the stability of the cell protrusions in nanowells, we monitored the BFP signal within individual pores over time (Figure 6.5 C,D). For approximately 50 % of pores with BFP signal, the intensity remained largely constant over the acquisition time of 5 minutes, during which no significant photobleaching of the BFP signal occurred (Figure 6.5 — Supplementary Figure 6.21). However for a subset of pores, large fluctuations of the BFP intensity were observed, suggesting movement of cell protrusions in and out of the observation volume (Figure 6.5 — Supplementary Figure 6.24). The occurrence of pores with switching signal did not depend on the pore diameter (Figure 6.5 — Supplementary Figure 6.24 D,E). When analyzing BFP intensities among different pores, we found a clear bimodal distribution for all pore sizes, with BFP-positive pores either having a high or low BFP signal (with <10 % of the signal obtained for pores with high intensity, Figure 6.5 B,E). Shallow pores ($h = 50$ nm) exhibited such a stable high signal more frequently compared to deeper pores (Figure 6.5 — Supplementary Figure 6.24 C), suggesting that pore depth influenced the stability of cell protrusions in the nanowell. We hypothesized that the high BFP intensities originated from pores containing well-defined cell protrusions, while low intensities reflected pores that were covered by a cell, but in which cells did not insert a protrusion (see cartoons in Figure 6.5 B). The signal from pores with low BFP intensities then would reflect the fluorescence signal originating from above the ZMW. In our simulations, we found that oblique angle illumination (*i.e.*, TIRF) reduced light penetration through the ZMWs and could thus, in theory, reduce this cytoplasmic signal leaking through the ZMWs (Figure 6.2 F-I and Figure 6.2 — Supplementary Figure 6.12). To test this, we measured BFP intensities under both widefield and TIRF illumination. The BFP intensity for pores with low signal was indeed markedly reduced when pores were imaged under TIRF illumination compared to widefield illumination (Figure 6.5 H and Figure 6.5 — Supplementary Figure 6.25). The average BFP intensity of pores showing a stable high-BFP signal positively correlated with pore size (Figure 6.5 F), again indicating that the BFP intensity represents the cytoplasmic volume inside the pore. The results support the hypothesis that pores with low BFP signal were covered by cells but their membrane did not penetrate into the pores, while the nanowell was occupied by a cell protrusion in the case of a high BFP signal.

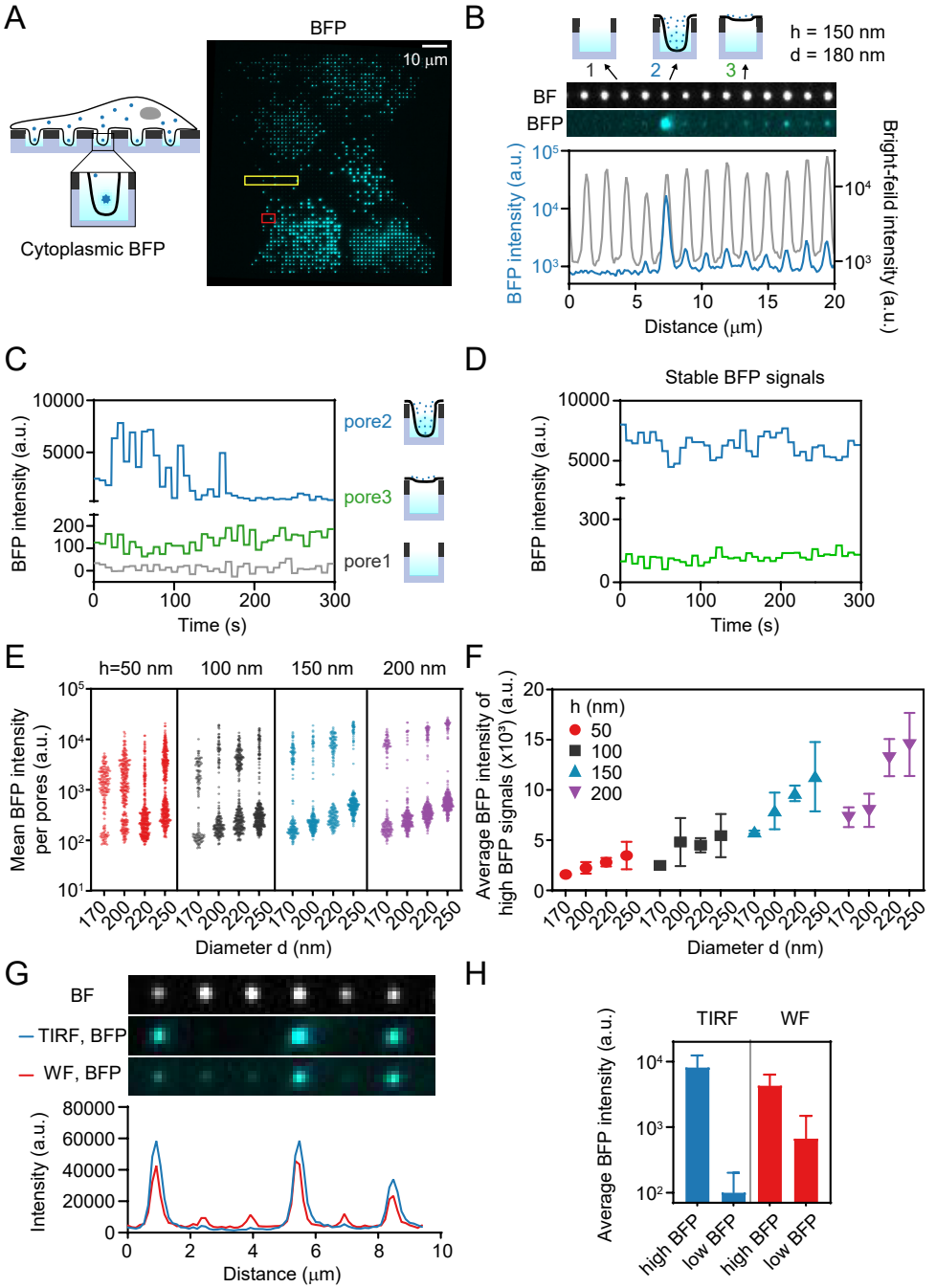
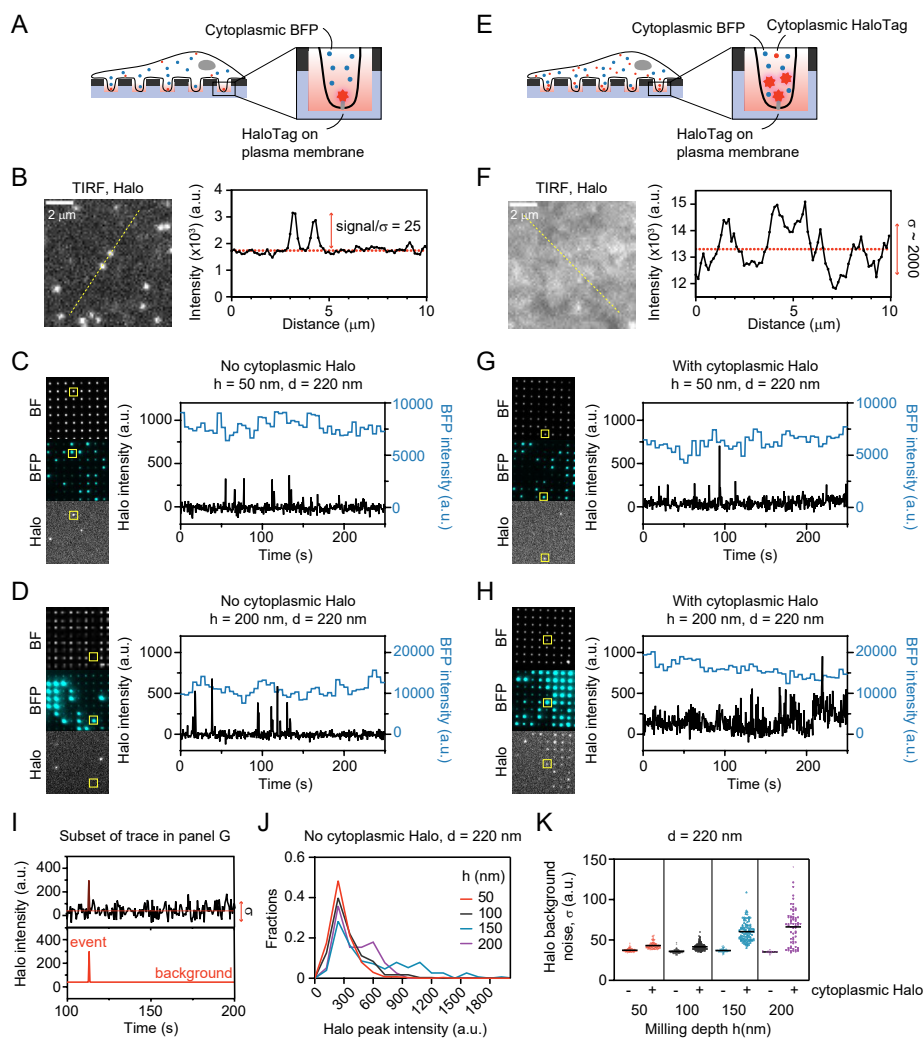


Figure 6.5: Imaging of single fluorophores in live cells that protrude into nanowells. **A:** U2OS cells expressing cytoplasmic BFP were grown on the ZMW arrays of version 2 and imaged using transmission light (left) or BFP fluorescence (right). Scale bar: 10 μm . **B:** Intensity profiles of BFP and transmission light for pores in the yellow box in (A). **C:** BFP fluorescence time traces of the pores indicated in B. **D:** Representative time traces of BFP intensity for pores with stable high (blue line) or stable low (green line) BFP signal intensity. The pores correspond to the pores denoted by the red box in (A). Images were acquired every 7.5 s. **E:** Each dot represents the average BFP intensity of a time trace for an individual pore showing stable signal. There are two distinct populations for each pore size. The number of measurements per pore size ranges from 113 to 413. **F:** Average BFP intensity (Mean \pm sd from 3 independent experiments) of the high BFP signals in (E). **G:** BFP intensity profiles under widefield and TIRF illumination. Under TIRF illumination, peak intensities are increased while background levels are reduced. **H:** Average BFP intensities of high and low intensity pores under TIRF or WF illumination. Error bars represent the standard deviation.

6.2.5. CYTOPLASMIC BACKGROUND CAN BE EFFICIENTLY SUPPRESSED USING PD ZMWs

Having confirmed that cell protrusions remained stable within nanopores over a timescale of minutes, we next tested whether single protein molecules could be visualized within the ZMWs. As a model, we used the transferrin receptor (TfR), a transmembrane protein involved in iron delivery into the cells. To achieve specific labeling TfR, we fused it to the HaloTag, a small protein tag that can be covalently labeled with fluorescent dyes [39]. We generated a cell line, stably expressing HaloTag-TfR as well as cytoplasmic BFP. BFP was used as a marker to identify which pores were occupied by cell protrusions (Figure 6.6 A). For single-molecule imaging, we chose the JFX650 dye as the fluorophore for labeling HaloTag-TfR (JFX650-HaloTag ligand) due to its high brightness and photostability [40]. Conventional TIRF microscopy on glass coverslips confirmed the correct localization of the HaloTag-TfR in the plasma membrane and identified the optimal dye concentration to visualize single-HaloTag-TfR molecules (Figure 6.6 B). Cells were then cultured on ZMWs and imaged using TIRF illumination. HaloTag-TfR signal was monitored from pores with stable cell protrusion as evidenced by constant high cytoplasmic BFP signal over the duration of the experiment (Figure 6.6 C,D). Only pores with high BFP signal intensities exhibited HaloTag-TfR signal (Figure 6.6 — Supplementary Figure 6.26), further supporting that pores with low BFP signal originated from cells lying on top of the pore without protruding into the pore.

Next, we probed whether the reduction of the observation volume provided by the ZMWs would allow the detection of single membrane-bound molecules in the presence of a high cytoplasmic background in the same detection channel. To this end, we generated a cell line that expresses high levels of freely-diffusing cytoplasmic HaloTag in addition to membrane-localized HaloTag-TfR (Figure 6.6 E). TIRF microscopy is the gold standard for reduction of fluorescence background from high levels of cytoplasmic proteins. However, at high cytoplasmic Halo expression, TIRF microscopy no longer yielded sufficient background fluorescence reduction to observe single HaloTag-TfR proteins on the membrane, as can be seen in Figure 6.6 F. In contrast, when cells were cultured on ZMWs with a 50 nm milling depth, single HaloTag-TfR molecules could readily be observed, with a signal-to-noise comparable to when no cytoplasmic HaloTag was present (Figure 6.6 C,G). This shows that the ZMWs effectively suppressed the background signal from the cytoplasmic HaloTag and allowed observation of membrane-localized HaloTag-



TfR molecules. In contrast, ZMWs with a 200 nm milling depth, which yield larger optical volumes due to increased nanowell sizes, resulted in significantly higher HaloTag fluorescence background, rendering it impossible to distinguish single HaloTag-TfR molecules from cytoplasmic background signal (Figure 6.3 H).

To quantify the signal-to-noise ratio of single HaloTag-TfR proteins, we applied a hidden Markov model (HMM) analysis to detect the signal spikes representing single HaloTag-TfR molecules diffusing in and out of nanowells (Figure 6.6 I). In the cell line without cytoplasmic HaloTag, no significant differences in the Halo peak intensity and background noise were observed across different milling depths (Figure 6.6 J,K). However, in the cell line expressing high cytoplasmic HaloTag, the background signal significantly increased for deeper pores, due to the larger cytoplasmic volume present within

Figure 6.6: Suppression of cytoplasmic background signal using Pd ZMWs . **A:** Schematic of U2OS cells expressing cytoplasmic BFP and HaloTag-TfR localized in the plasma membrane. **B:** Representative TIRF image of JFX650-labeled HaloTag-TfR. Graph on the right represents an intensity profile along the yellow line. **C,D:** Representative images of bright-field (BF), BFP, and JFX650-HaloTag acquired through nanopores. Fluorescence time trace of a single pore, representing the yellow boxed area in the images. Pore diameter $d = 220$ nm, milling depth $d = 50$ nm (C) and $d = 200$ nm (D). Time interval, 5 s for BFP, 500 ms for JFX650-Halo. **E:** Expression of cytoplasmic HaloTag in the same cell line as in (A). **F:** Representative TIRF image of JFX650-labeled HaloTag-TfR. Graph on the right represents an intensity profile through the yellow line. Scale bar $2 \mu\text{m}$. **G,H:** Representative images of BF, BFP, and JFX650-HaloTag acquired under the same imaging condition as C,D, but from the cell line additionally expressing cytoplasmic HaloTag. Fluorescence time trace of a single pore representing the yellow boxed area in the images. Pore diameter $d = 220$ nm, milling depth $h = 50$ nm (G) and $h = 200$ nm (H). Time interval, 5 s for BFP, 500 ms for JFX650-Halo. **I:** Analysis of the Halo intensity time trace using a hidden Markov model to determine the Halo peak intensity and background noise of each trace. The background noise is defined as the standard deviation (σ) of the background intensity. **J:** Distribution of Halo peak intensities for pores with different milling depths and a constant pore diameter of 220 nm, obtained from the cell line without cytoplasmic HaloTag described in (A). **K:** Background noise σ in the red HaloTag channel from individual pores. Each dot represents a single pore. The mean is indicated by black bars. Number of pores: $n = 86, 133, 116, 177, 72, 113, 14, 69$ (in the same order as the graph).

the observation volume (Figure 6.3 K). These results show that the milling depth plays a crucial role for background suppression. Taken together, this work reveals that imaging cells on overmilled ZMWs allows for the visualization of single fluorescent molecules even in the presence of high fluorescent background in the cytoplasm.

6.3. DISCUSSION

Here, we have introduced overmilled palladium ZMWs combined with TIRF illumination as a platform for single-molecule studies in live cells. By creating an attoliter-volume size-tunable nanowell below the ZMW, we achieved a highly confined observation volume that is efficiently penetrated by cell protrusions. The resulting reduction of the cytoplasmic volume combined with favorable optical properties of the nanowell enabled the observation of single fluorescently-labeled cellular membrane proteins even in the presence of high cytoplasmic concentrations of the same fluorophore.

We demonstrated an effective confinement of the observation volume to the nanowell, a strong rejection of background fluorescence originating from the other side of the ZMW and an up to 5-fold signal enhancement, both theoretically using FDTD simulations and by *in vitro* experiments of freely diffusing fluorophores (Figure 6.2 and Figure 6.3). Significant non-radiative losses to the metal occurred for shallow milling depths and small pore diameters where the dyes are confined to the proximity of the metal, as evidenced by a strong decrease of the excited state lifetime of the fluorophore, reaching up to a 2.3-fold reduction. Similar changes of the fluorescence lifetime were reported for aluminum [8, 37] and aluminum/gold alloy ZMWs [13], with a 2 to 6-fold reduction of the fluorescence lifetime for various fluorophores and ZMW diameters. Due to a lack of radiative enhancement, this results in a strong quantum yield reduction of up to 4-fold within ZMWs with small pore diameters, which however approaches the free dye value quickly with increasing distance from the metal (Figure 6.2 B).

Despite a $\approx 10\%$ reduction of the quantum yield throughout the observation volume, the signal from within the nanowells is enhanced by a factor of 2 to 5 due to the

combination of two effects. First, the excitation intensity is focused within the nanowell due to the formation of a standing wave below the metal layer that leads to a 3-fold increase of the excitation intensity at its maximum (Figure 6.2 F, [36, 37]). Second, an approximate 2-fold increase of the detection efficiency arises because the emission is guided towards the detection side due to the reflective metal surface (Figure 6.2 E). The conclusions reached here for the green detection channel using the dye Alexa488 ($\lambda_{\text{ex}} = 488 \text{ nm}$, $\lambda_{\text{em}} = 525 \text{ nm}$) apply also to the far-red detection channel using the dye JFX650 ($\lambda_{\text{ex}} = 640 \text{ nm}$, $\lambda_{\text{em}} = 670 \text{ nm}$), both from the theoretical (Figure 6.2 — Supplementary Figure 6.8,6.9) and experimental side (Figure 6.3 — Supplementary Figure 6.17), and are thus expected to remain valid over the whole visible spectrum. While similar results are expected also for other metals such as gold and aluminum [8–10, 12, 13, 35–38], palladium offers a simpler fabrication process compared to aluminum by eliminating the need for a SiO_2 passivation layer, and a reduced photoluminescence in the green spectral range compared to gold [23] which overlaps with the emission of the widely-used GFP tag.

Our insights into the optical properties of the nanowells have a number of consequences for *in vitro* and in cellulo applications of ZMWs. For standard ZMWs without overmilling, the zeptoliter-size observation volume results in very short dwell times of freely diffusing molecules in the observation volume, necessitating immobilization of the molecules of interest. Using overmilled ZMWs, we achieve dwell times for freely diffusing molecules that are comparable to residence times in a diffraction-limited confocal volume, enabling potential applications of overmilled ZMWs in single-molecule spectroscopy and single-molecule FRET experiments [41, 42]. The larger volume of the overmilled ZMWs also provides the possibility to study large and flexible molecules, such as extended DNA/RNA molecules, that are otherwise difficult to confine to the small volume. Furthermore, the distance-dependent quenching by the metal can lead to a significant signal reduction in standard ZMWs [33], which is avoided in overmilled ZMWs where molecules are at sufficient distance from the metal. The excitation intensity within standard ZMWs also generally remains limited when molecules are not directly immobilized on the glass surface due to the exponentially decaying evanescent field. This situation is resolved in overmilled ZMWs where the excitation power is effectively focused to the nanowell due to the formation of a standing wave, an effect that cannot be exploited in standard ZMWs. While an increase of the excitation intensity can also be achieved by increasing laser powers, the distinctive intensity distribution within the nanowell further improves the background suppression by preferential excitation of molecules below the ZMW. Lastly, the metal layer acts a mirror surface that leads to a more efficient collection of the fluorescence emission from within the nanowell. This provides a more efficient use of the limited signal in single-molecule experiments, which is especially crucial in live cell applications where photostabilization by oxygen scavenging and use of reducing-oxidizing agents is difficult. A drawback of nanowells compared to standard ZMWs is that that larger observation volume in nanowells limits single-molecule detection sensitivity when very high protein concentrations are used (micromolar-millimolar). Therefore, standard ZMWs and nanowells will each have their specific applications, with nanowells performing especially well in cell-based imaging.

Pd-based ZMW nanowells showed excellent compatibility with live-cell imaging. Cells

grew readily on palladium-coated glass coverslips, adhered to the untreated metal surface, and showed healthy morphologies. Efficient protrusion into the nanowells was observed for most pore sizes, except for the smallest diameter of 100 nm, with the frequency of membrane protrusions increasing both with milling depth and pore diameter, in agreement with previous results on Al ZMWs [31]. Time-dependent fluctuations of the fluorescence signals of cytoplasmic BFP confirmed that cells dynamically explored the nanowells over a timescale of minutes (Figure 6.5 C,D). Approximately 10 % of pores exhibited significant cytoplasmic signal that remained stable over a timescale of 5 min, showing that cells formed stable protrusions into the nanowells on relevant timescales for many biological processes. While the cytoplasmic background signal increased both with pore size (Figure 6.5 E, in agreement with [31]), it was markedly reduced under TIRF illumination due to a reduced propagation of the excitation light through the ZMW and a more even excitation intensity within the nanowell (Figure 6.5 H, Figure 6.2 F-I, Figure 6.2 — Supplementary Figure 6.12).

We showed the applicability of the nanowells for single-molecule fluorescence experiments in live cells and its superiority compared to TIRF microscopy with respect to single-molecule observations. By following the fluorescence of single membrane-bound fluorophores, we found that signal spikes originating from single molecules were only observed for pores with stable protrusions. Most importantly, single-molecule signals could still be observed under conditions of high cytoplasmic expression, which did not allow for single-molecule experiments using conventional TIRF excitation (Figure 6.6 F-H). Despite the high concentration of fluorophores in the cytoplasm, we could achieve a signal-to-noise ratio of ≈ 7 for shallow pores up to a depth of 100 nm, with noise levels equivalent to when no cytoplasmic signal was present (Figure 6.6 J,K). The results confirm the excellent suppression of the cytoplasmic signal provided by the ZMWs nanowells, allowing monitoring of single fluorophores despite a high cytoplasmic background of the same fluorophore.

We envision that overmilled ZMWs will allow live-cell single-molecule fluorescence experiments in a wider range of cases. More specifically, it provides a benefit in cases where expression levels cannot be controlled, for example when studying endogenously expressed proteins of interest, or when weak interactions are studied requiring high concentrations of the interaction partners. While we have only tested the human osteosarcoma U2OS cell line in this study, live-cell ZMW imaging has been applied successfully in other cell lines, including COS-7 cells [30], Rat basophilic leukemia (RBL) mast cells [31], and mouse neuroblastoma N2a cells [32], suggesting its potential for broad applications. To facilitate cell protrusion into the nanopores, surface coatings or functionalization with specific molecules or peptides can be employed as effective strategies [29, 43, 44], which may extend the application further to a variety of cell types. Since the total cellular membrane fraction that protrudes into the nanowells is small ($\leq 1\%$), efficient approaches for membrane recruitment and immobilization of low-concentration complexes will be required. A potential strategy could be through introduction of a designed transmembrane protein with an intracellular docking platform and extracellular binding to the glass wells below the Pd layer using silane chemistry [45] or electrostatic interactions with the glass surface using poly-lysine [44, 46]. Alternatively, higher throughput could be achieved by employing fabrication methods based on electron-

beam lithography [47] with subsequent wet etching [48]. We envision many applications of our method for the study of protein-protein and protein-RNA interactions in the cytoplasm, enzymatic activities of single proteins or complexes such as ribosomes [49] or proteasomes [50], and protein conformational dynamics by combination with single-molecule FRET [41]. In this study, we focused on membrane-associated proteins, which have a longer residence time within the nanowells compared to cytoplasmic fluorophores. Nonetheless, it is likely that ZMW nanowells can similarly be adopted to study freely diffusing molecules which would increase the applicability of overmilled ZMWs even further.

6.4. CONCLUSIONS

We introduced the use of overmilled zero-mode waveguides made of palladium combined with TIRF illumination for live-cell imaging. We performed a thorough theoretical and experimental characterization of the optical properties of the nanowells using FDTD simulations and fluorescence experiments of freely diffusing organic dyes, which together delineated the signal confinement and fluorescence enhancement within the overmilled nanowell volume. Live-cell experiments showed that cells readily protrude into the nanowells, enabling single-molecule fluorescence experiments with excellent signal-to-noise ratio, despite a high cytosolic concentration of the fluorophore. By scanning a wide range of pore diameters and milling depths, we provided comprehensive guidelines for future *in vitro* or in cellulo single-molecule studies where a compromise must be found between the required background suppression, the desired fluorescence enhancement, and the efficiency of cell protrusions.

6.5. METHODS AND MATERIALS

6.5.1. FABRICATION OF PALLADIUM ZERO-MODE WAVEGUIDES

Standard borosilicate coverslips (#1.5H, Marienfeld, Germany) were cleaned by consecutive sonication in deionized water, isopropyl alcohol, acetone, and 1 M potassium hydroxide solution, washed with deionized water, and spin dried. A thin adhesion layer of 3 nm titanium was deposited at a rate of 0.05 nm/s under a base pressure of 3×10^{-6} torr in a Temescal FC2000 e-gun evaporator. In the same vacuum, a layer of Pd was immediately added on top of the Ti. Two versions of Pd ZMWs were used in this study, which differed by the thickness of the Pd layer. Either 100 nm of Pd was deposited at a rate of 0.1 nm/s (Version 1) or 150 nm at a rate of 0.2 nm/s (Version 2), both under a base pressure below 2×10^{-6} torr.

Nanopores were milled through the layers *via* focused ion beam (FIB) milling on a FEI Helios G4 CX FIB/SEM. To improve consistency, the focus and stigmatism of the ion beam was optimized on a graphite standard sample before milling. For the pore arrays of version 1, a 33 pA beam with an acceleration voltage of 30 kV was used. For the pores of version 2, the beam current was set to 430 pA at the same voltage. Due to the higher beam current used for version 2, milling time was reduced to around 4 min per array coming at the cost of less well defined pore diameters (Figure 6.1 — Supplementary Figure 6.1). The diameters of the resulting pores were measured using the immersion mode of the scanning electron microscope on the same machine. The depth and opening angle of

the pores, resulting from overmilling into the glass surface, was measured by cutting through the pores with the ion beam and imaging under 52° incident angle. The diameters, depths and taper angles of the pores can be found in [Figure 6.1 C,D](#) and [Figure 6.1 — Supplementary Figure 6.1 C-E](#).

Prior to experiments, ZMWs were thoroughly cleaned by consecutive sonication in deionized water, ethanol, isopropyl alcohol, acetone, and 1 M potassium hydroxide solution for about 10 min each and exposed to oxygen plasma at a power of 90 W for 1 min. The coverslips could be reused about 10 times, after which the Pd film started to show signs of degradation.

6.5.2. SINGLE-MOLECULE MEASUREMENTS OF FREE FLUOROPHORES

Measurements of freely diffusing fluorophores inside Pd ZMWs were performed on coverslips of version 1 on a Picoquant Microtime 200 microscope operated using the Symphotime software in a temperature controlled room at $21.5 \pm 1.0^\circ\text{C}$. Lasers were focused by an 60x Olympus UPLAPO 60XW water immersion objective with a working distance of $280\mu\text{m}$ and a numerical aperture of 1.2. Excitation at wavelengths of 640 nm and 485 nm was performed at powers of $10\mu\text{W}$ as measured at the sample plane. Pulsed lasers were operated in pulsed interleaved excitation at a repetition frequency of 40 MHz [51]. The molecular brightness of a solution of Alexa488 fluorophores was optimized by adjusting the correction collar of the objective prior to the experiment. The emission light was passed through a $50\mu\text{m}$ pinhole, split by a dichroic mirror and was filtered by 525/50 or 600/75 optical band pass filters for the blue and red detection channels, respectively (Chroma, Bellow Falls). Fluorescence emission was detected on single-photon avalanche-diode detectors (PD5CTC and PD1CTC, Micro Photon Devices, Bolzano). Fluorophore solutions of 500 nM of Alexa488 and JFX650-HaloTag were supplemented by 0.1 % Tween20 (Fischer Scientific) to minimize surface adhesion of the fluorophores. Transmission light images of the pore arrays were used to locate the pores prior to fine tuning of the position of the laser focus to maximize the signal.

6.5.3. FDTD SIMULATIONS OF LIGHT FIELDS INSIDE Pd ZMWs

Three-dimensional FDTD simulations were performed using Lumerical FDTD (ANSYS Inc., USA) as described previously for the characterization of free-standing ZMWs [24] and reiterated here for convenience of the reader. The surrounding medium was modeled as water with a refractive index of 1.33 and the refractive indices of the 100 nm thick palladium membrane and the SiO_2 layer were modelled according to [52]. For the simulation of the excitation field, the ZMW was illuminated by a total-field scattered-field source which was polarized in the x-direction. The source was set as a plane wave for widefield excitation and TIRF excitation under an incidence angle of 70° , and a Gaussian source with a numerical aperture of 1.2 for focused excitation. The simulation box size was $1 \times 1 \times 0.8\mu\text{m}^3$ for widefield and TIRF excitation with a grid resolution of 5 nm. To correctly model the focused beam, a larger box of $4 \times 4 \times 0.8\mu\text{m}^3$ was required for the Gaussian source, in which case a larger grid resolution of 50 nm was used to model the field further away from the nanowell keeping the 5 nm grid resolution close to the nanowell. The electromagnetic field intensity distributions, computed as the absolute value of the complex electric field, $|E|^2$, in the xz- and yz-planes at the center of the nanow-

ell and in the xy-plane at the ZMW entry are shown in [Figure 6.2 — Supplementary Figure 6.2 - Supplementary Figure 6.7](#). To model the fluorescence emission, a dipole emitter was placed at varying z-positions along the central axis of the nanowell. The radiated power was monitored on all sides of the simulation box (see below). To compute the detection efficiency, the radiated power was integrated only over the detection side below the palladium layer. For dipole emission, all reported quantities were averaged over horizontal and vertical orientations of the dipole to model isotropic emission. The power was only weakly affected by the lateral position of the emitter with respect to the center of the nanowell ([Figure 6.2 — Supplementary Figure 6.11, \[7\]](#)).

ESTIMATION OF QUANTUM YIELD AND FLUORESCENCE LIFETIMES

Quantum yields and fluorescence were computed as described previously [24]. For convenience of the reader, we here repeat this description. In the absence of the nanostructure, the decay rate of the excited molecule is given by $\gamma^0 = \gamma_r^0 + \gamma_{nr}^0$, where γ_r^0 and γ_{nr}^0 are the radiative and non-radiative decay rates. Here, γ_{nr}^0 represents the rate of non-radiative relaxation to the ground state due to internal processes, which is assumed to be unaffected by the nanostructure. The intrinsic quantum yield of the fluorophore is defined as $\Phi_0 = \gamma_r^0 / (\gamma_r^0 + \gamma_{nr}^0)$ and was obtained from literature as $\Phi_0 = 0.8$ and 0.53 for Alexa488 and JFX650 [40, 53].

Within the nanowell, the radiative decay rate γ_r is modified. Additionally, a non-radiative loss rate γ_{loss} arises due to absorption by the metal nanostructure [54]. The quantum yield Φ in the presence of the ZMW is given by [55]:

$$\Phi = \frac{\gamma_r / \gamma_r^0}{\gamma_r / \gamma_r^0 + \gamma_{\text{loss}} / \gamma_r^0 + (1 - \Phi_0) / \Phi_0}, \quad (6.1)$$

where γ_r^0 and γ_r are the radiative rates in the absence and the presence of the ZMW respectively. While absolute decay rates γ_r , γ_{loss} , and γ_r^0 are inaccessible from FDTD simulations, relative rates normalized to the radiative rate in the absence of the ZMW, γ_r^0 , can be obtained from the power P radiated by the dipole [56] as:

$$\frac{\gamma_r}{\gamma_r^0} = \frac{P_{\text{ff}}}{P_r^0} \quad \text{and} \quad \frac{\gamma_{\text{loss}}}{\gamma_r^0} = \frac{P_r}{P_r^0} - \frac{P_{\text{ff}}}{P_r^0}, \quad (6.2)$$

where P_r and P_r^0 are the powers radiated by the dipole in the presence and absence of the ZMW, and P_{ff} is the power that is radiated into the far-field in the presence of the ZMW. See [Figure 6.2 — Supplementary Figure 6.10](#) for the obtained z-profiles of the normalized radiative and non-radiative rates.

To obtain the fluorescence lifetime τ , which is given by the inverse of the sum of all de-excitation rates, we use the relation $\tau = \Phi / \gamma_r$ in combination with eq. 6.1 :

$$\tau = \frac{1}{\gamma_r + \gamma_{\text{loss}} + \gamma_{nr}^0} = \frac{1 / \gamma_r^0}{\gamma_r / \gamma_r^0 + \gamma_{\text{loss}} / \gamma_r^0 + (1 - \Phi_0) / \Phi_0}, \quad (6.3)$$

where the intrinsic radiative rate γ_r^0 was estimated as $\gamma_r^0 = \Phi_0 / \tau_0$, with the experimentally measured fluorescence lifetimes τ_0 for Alexa488 and JFX650 of 4.0 ns and 3.9 ns. The

detection efficiency η was estimated as the fraction of the power radiated towards the lower (detection) side of the ZMW, P_{ff}^{z-} , with respect to the total radiated power:

$$\eta = \frac{P_{\text{ff}}^{z-}}{P_{\text{ff}}}. \quad (6.4)$$

Finally, the total detected signal as a function of the z -position of the emitter within the nanowell was computed as the product of the excitation intensity $I_{\text{ex}}(z)$, detection efficiency $\eta(z)$, and quantum yield $\Phi(z)$ as:

$$S(z) = I_{\text{ex}}(z)\eta(z)\Phi(z). \quad (6.5)$$

The computed detection efficiency η , quantum yield Φ , detected signal $S(z)$ and lifetime τ as a function of the z -position within the ZMW are shown in [Figure 6.2 — Supplementary Figure 6.8,6.9](#).

ESTIMATION OF SIGNAL ENHANCEMENT FACTORS

To estimate the theoretical signal enhancement factor, we performed simulations in the absence of the palladium layer and glass nanowell to mimic the free diffusion experiment ([Figure 6.3 — Supplementary Figure 6.19](#)). A 50 nm thin glass layer was added at the edge of the simulated volume (at $z \approx -4 \mu\text{m}$) to account for the glass-water interface. The signal enhancement factor at each z -position was computed as the ratio of the detected signal in the nanowell and the free diffusion value:

$$\frac{\varepsilon_{\text{ZMW}}}{\varepsilon_0}(z) = \frac{I_{\text{ex,ZMW}}(z)\eta(z)\Phi(z)}{I_{\text{ex},0}(z)\eta_0\Phi_0}, \quad (6.6)$$

where Φ_0 is the reference quantum yield. Here, we assume that 50% of the signal is detected in the free diffusion case ($\eta_0 = 0.5$) and neglect detection losses due to the limited numerical aperture of the objective lens which are assumed to be identical for the compared conditions. The predicted average enhancement factors were then computed as the signal-weighted average along the central pore axis ($x = 0, y = 0$) from the bottom of the well of depth h towards the end of the simulation box at height 200 nm:

$$\left\langle \frac{\varepsilon_{\text{ZMW}}}{\varepsilon_0} \right\rangle_h = \frac{\int_{-h}^{200\text{nm}} S(z) \frac{\varepsilon_{\text{ZMW}}}{\varepsilon_0}(z) dz}{\int_{-h}^{200\text{nm}} S(z) dz}, \quad (6.7)$$

where $S(z)$ is the detected signal as defined in eq. 6.5. See [Figure 6.3 — Supplementary Figure 6.19](#) for details.

6.5.4. LIVE CELL IMAGING ON PD ZMWs

CELL LINES

Human U2OS (ATCC, HTB-96) and HEK 293T (ATCC, CRL-3216) cells were used for imaging and lentivirus production, respectively. They were grown in DMEM (4.5 g/L glucose, Gibco) with 5% fetal bovine serum (Sigma-Aldrich) and 1% penicillin / streptomycin (Gibco) and maintained at 37 °C with 5% CO₂. The cell lines were confirmed to be mycoplasma-free. Cell lines stably expressing transgenes were generated *via* lentiviral

transduction. Lentivirus was produced by transfecting HEK 293T cells with polyethylenimine (Polysciences Inc.) and packaging vectors (psPAX2, pMD2.g) and the lentiviral plasmid of interest. The viral supernatant was collected 72 h after transfection. Cells were seeded for infection at $\approx 35\%$ confluency 24 h prior to lentivirus addition. The cells were spin-infected with the viral supernatant and Polybrene ($10\ \mu\text{g}/\text{ml}$) for 90 min at 2000 rpm at 32°C , then cultured for 48 h. Monoclonal cell lines expressing the transgene were isolated by single cell sorting into 96-well plates *via* FACS. The TfR coding sequence was amplified from Addgene plasmid # 133451.

CELL CULTURE FOR IMAGING

Cells were seeded on ZMW coverslips in a 6-well plate at 40% to 45% confluency 1 day before the imaging experiment. The cell culture medium was replaced with imaging medium (pre-warmed CO_2 -independent Leibovitz's-15 medium (Gibco) with 5% fetal bovine serum and 1% penicillin / streptomycin) 30 min prior to imaging. All live-cell imaging experiments were performed at 37°C . For experiments with HaloTag expressing cell lines, the cell culture medium was replaced with the imaging medium (pre-warmed Leibovitz's-15 medium with 5% fetal bovine serum and 1% penicillin / streptomycin) containing 5 nM JFX650-Halo ligands. After 10 min incubation with the Halo ligands, the cells were washed three times with fresh imaging medium.

MICROSCOPE AND IMAGE ACQUISITION

Live-cell imaging experiments were performed using a Nikon TI inverted microscope equipped with a TIRF illuminator, perfect focus system and NIS Element Software. A Nikon CFI Apochromat TIRF 100X 1.49 NA oil-immersion objective was used. The microscope was equipped with a temperature-controlled incubator. Bright-field and fluorescence images at each ZMW array position were recorded using an Andor iXon Ultra 888 EMCCD camera.

6.5.5. DATA ANALYSIS

SINGLE-MOLECULE FLUORESCENCE EXPERIMENTS

Fluorescence correlation spectroscopy (FCS) and lifetime analysis was performed using the PAM software package [57]. Autocorrelation functions $G(t_c)$ were fit to a standard model function for 3D diffusion:

$$G(t_c) = \frac{1}{N} \left(1 + \frac{t_c}{\tau_D}\right)^{-1} \left(1 + \frac{t_c}{p^2\tau_D}\right)^{-1/2}, \quad (6.8)$$

where t_c is the correlation time, N is the average number of particles in the observation volume, τ_D is the diffusion time, and p is a geometric factor that accounts for the axial elongation of the confocal volume ($p = 3.4$). While, strictly speaking, the 3D diffusion model is not applicable for the complex geometries in this study, we apply it here as a simple means to extract the amplitude and average decay time of the curves. The molecular brightness ε was calculated from the average signal $\langle I \rangle$ as $\varepsilon = \langle I \rangle / N$. The effective volume was computed using the known concentration c of the fluorophore as $V_{\text{FCS}} = N / (N_A c)$, where N_A is Avogadro's number. Fluorescence decays of Alexa488 were fitted to a single-exponential decay that was convoluted with the instrument response

function. Decays for JFX650 generally required two lifetimes to achieve a good fit, of which we report the average. The second component most likely originates from a fraction of dyes that were sticking to the surface.

CELL IMAGING

The images were analysed using custom-written software for MATLAB. The program automatically determined the positions of pores from bright-field images and calculated the fluorescence intensity of each pore from the fluorescence images. The BFP and JFX650-Halo fluorescence signals were obtained by calculating the mean intensity over a 7x7 pixel area around the pore and subtracting the background intensity determined from the outer edge pixels of the pore. To analyze the fraction of pores occupied by cells for each pore size (Figure 6.4 C), we estimated the area occupied by cells by manually determining an outline containing connected areas of occupied wells from 6 images. We analyzed the BFP intensity of each well in this area, with a total of 7367 wells analyzed. As a negative control, we measured the BFP intensity of the pores where no cells were present and set a threshold to determine positive BFP intensity pores. The total number of pores with a positive BFP signal above the threshold was 1890 (Figure 6.4 — Supplementary Figure 6.22 C). This panel illustrates the fraction of pores with positive BFP intensity among the analyzed pores for each pore size. For the analysis of the JFX650-Halo time traces, a hidden Markov model (vbFRET algorithm, [58]) with the default setting of the algorithm was used to assign on and off states of the Halo signal.

6.6. DATA AVAILABILITY

All data underlying this study is made available in an open repository [59]

REFERENCES

- [1] P. Hinterdorfer and A. Oijen, eds., *Handbook of Single-Molecule Biophysics*, 1st ed. (Springer New York, New York, 2009) p. 626, doi:10.1007/978-0-387-76497-9.
- [2] D. S. White, M. A. Smith, B. Chanda, and R. H. Goldsmith, *Strategies for Overcoming the Single-Molecule Concentration Barrier*, *ACS Measurement Science Au* **3**, 239 (2023), doi:10.1021/acsmesuresciau.3c00002.
- [3] R. Milo and R. Phillips, *Cell Biology by the Numbers* (Garland Science, Taylor & Francis Group, 2015) doi:10.1201/9780429258770.
- [4] Z. Liu, L. Lavis, and E. Betzig, *Imaging live-cell dynamics and structure at the single-molecule level*, *Mol Cell* **58**, 644 (2015), doi:10.1016/j.molcel.2015.02.033.
- [5] U. Kubitschek, *Fluorescence Microscopy: From Principles to Biological Applications*, 2nd ed. (John Wiley & Sons, Incorporated, 2017).
- [6] J. D. Jackson, *Classical electrodynamics* (Wiley, New York, 1962) pp. XVII, 641.
- [7] M. J. Levene, J. Korlach, S. W. Turner, M. Foquet, H. G. Craighead, and W. W. Webb, *Zero-mode waveguides for single-molecule analysis at high concentrations*, *science* **299**, 682 (2003), doi:10.1126/science.1079700.

- [8] H. Rigneault, J. Capoulade, J. Dintinger, J. Wenger, N. Bonod, E. Popov, T. W. Ebbesen, and P.-E. Lenne, *Enhancement of single-molecule fluorescence detection in subwavelength apertures*, *Phys. Rev. Lett.* **95**, 117401 (2005), doi:[10.1103/PhysRevLett.95.117401](https://doi.org/10.1103/PhysRevLett.95.117401).
- [9] D. Gérard, J. Wenger, N. Bonod, E. Popov, H. Rigneault, F. Mahdavi, S. Blair, J. Dintinger, and T. W. Ebbesen, *Nanoaperture-enhanced fluorescence: Towards higher detection rates with plasmonic metals*, *Physical Review B* **77**, 045413 (2008), doi:[10.1103/PhysRevB.77.045413](https://doi.org/10.1103/PhysRevB.77.045413).
- [10] H. Aouani, J. Wenger, D. Gérard, H. Rigneault, E. Devaux, T. W. Ebbesen, F. Mahdavi, T. Xu, and S. Blair, *Crucial role of the adhesion layer on the plasmonic fluorescence enhancement*, *ACS Nano* **3**, 2043 (2009), doi:[10.1021/nn900460t](https://doi.org/10.1021/nn900460t).
- [11] W. E. Martin, B. R. Srijanto, C. P. Collier, T. Vosch, and C. I. Richards, *A comparison of single-molecule emission in aluminum and gold zero-mode waveguides*, *The Journal of Physical Chemistry A* **120**, 6719 (2016), doi:[10.1021/acs.jpca.6b03309](https://doi.org/10.1021/acs.jpca.6b03309).
- [12] M. Wu, W. Liu, J. Hu, Z. Zhong, T. Rujiralai, L. Zhou, X. Cai, and J. Ma, *Fluorescence enhancement in an over-etched gold zero-mode waveguide*. *Optics express* **27** **13**, 19002 (2019), doi:<https://doi.org/10.1364/OE.27.019002>.
- [13] A. Al Masud, W. E. Martin, F. H. Moonschi, S. M. Park, B. R. Srijanto, K. R. Graham, C. P. Collier, and C. I. Richards, *Mixed metal zero-mode guides (zms) for tunable fluorescence enhancement*, *Nanoscale Adv.* **2**, 1894 (2020), doi:[10.1039/C9NA00641A](https://doi.org/10.1039/C9NA00641A).
- [14] S. Patra, J.-B. Claude, and J. Wenger, *Fluorescence Brightness, Photostability, and Energy Transfer Enhancement of Immobilized Single Molecules in Zero-Mode Waveguide Nanoapertures*, *ACS Photonics* **9**, 2109 (2022), doi:[10.1021/acsp Photonics.2c00349](https://doi.org/10.1021/acsp Photonics.2c00349).
- [15] K. T. Samiee, M. Foquet, L. Guo, E. C. Cox, and H. G. Craighead, *λ -repressor oligomerization kinetics at high concentrations using fluorescence correlation spectroscopy in zero-mode waveguides*, *Biophysical Journal* **88**, 2145 (2005), doi:[10.1529/biophysj.104.052795](https://doi.org/10.1529/biophysj.104.052795).
- [16] K. Samiee, J. Moran-Mirabal, Y. Cheung, and H. Craighead, *Zero Mode Waveguides for Single-Molecule Spectroscopy on Lipid Membranes*, *Biophysical Journal* **90**, 3288 (2006), doi:[10.1529/biophysj.105.072819](https://doi.org/10.1529/biophysj.105.072819).
- [17] T. Auger, J. Mathé, V. Viasnoff, G. Charron, J.-M. Di Meglio, L. Auvray, and F. Montel, *Zero-mode waveguide detection of flow-driven dna translocation through nanopores*, *Phys. Rev. Lett.* **113**, 028302 (2014), doi:[10.1103/PhysRevLett.113.028302](https://doi.org/10.1103/PhysRevLett.113.028302).
- [18] O. N. Assad, T. Gilboa, J. Spitzberg, M. Juhasz, E. Weinhold, and A. Meller, *Light-enhancing plasmonic-nanopore biosensor for superior single-molecule detection*, *Advanced Materials* **29**, 1605442 (2016), doi:[10.1002/adma.201605442](https://doi.org/10.1002/adma.201605442).

- [19] J. Larkin, R. Y. Henley, V. Jadhav, J. Koriach, and M. Wanunu, *Length-independent dna packing into nanopore zero-mode waveguides for low-input dna sequencing*, *Nature nanotechnology* **12**, 1169 (2017), doi:[10.1038/nnano.2017.176](https://doi.org/10.1038/nnano.2017.176).
- [20] M. Baibakov, S. Patra, J.-B. Claude, A. Moreau, J. Lumeau, and J. Wenger, *Extending single molecule Förster resonance energy transfer (fret) range beyond 10 nanometers in zero-mode waveguides*, *ACS Nano* **13**, 8469–8480 (2019), doi:[10.1021/acsnano.9b04378](https://doi.org/10.1021/acsnano.9b04378).
- [21] M. Hoyer, A. H. Crevenna, J. R. C. Correia, A. G. Quezada, and D. C. Lamb, *Zero-mode waveguides visualize the first steps during gelsolin-mediated actin filament formation*. *Biophys J* **121**, 327–335 (2022), doi:[10.1016/j.bpj.2021.12.011](https://doi.org/10.1016/j.bpj.2021.12.011).
- [22] A. Rhoads and K. F. Au, *PacBio Sequencing and Its Applications*, *Genomics, Proteomics & Bioinformatics SI: Metagenomics of Marine Environments*, **13**, 278 (2015), doi:[10.1016/j.gpb.2015.08.002](https://doi.org/10.1016/j.gpb.2015.08.002).
- [23] N. Klughammer and C. Dekker, *Palladium zero-mode waveguides for optical single-molecule detection with nanopores*, *Nanotechnology* **32**, 18LT01 (2021), doi:[10.1088/1361-6528/abd976](https://doi.org/10.1088/1361-6528/abd976).
- [24] N. Klughammer, A. Barth, M. Dekker, A. Fragasso, P. Onck, and C. Dekker, *Diameter dependence of transport through nuclear pore complex mimics studied using optical nanopores*, *eLife* **12** (2023), [10.7554/eLife.87174](https://doi.org/10.7554/eLife.87174), doi:[10.7554/eLife.87174](https://doi.org/10.7554/eLife.87174).
- [25] J. C. Love, D. B. Wolfe, R. Haasch, M. L. Chabinyc, K. E. Paul, G. M. Whitesides, and R. G. Nuzzo, *Formation and structure of self-assembled monolayers of alkanethiolates on palladium*, *Journal of the American Chemical Society* **125**, 2597 (2003), doi:[10.1021/ja028692+](https://doi.org/10.1021/ja028692+).
- [26] J. C. Love, L. A. Estroff, J. K. Kriebel, R. G. Nuzzo, and G. M. Whitesides, *Self-assembled monolayers of thiolates on metals as a form of nanotechnology*, *Chemical Reviews* **105**, 1103 (2005), doi:[10.1021/cr0300789](https://doi.org/10.1021/cr0300789).
- [27] A. Mooradian, *Photoluminescence of Metals*, *Physical Review Letters* **22**, 185 (1969), doi:[10.1103/PhysRevLett.22.185](https://doi.org/10.1103/PhysRevLett.22.185).
- [28] G. T. Boyd, Z. H. Yu, and Y. R. Shen, *Photoinduced luminescence from the noble metals and its enhancement on roughened surfaces*, *Phys. Rev. B* **33**, 7923 (1986), doi:[10.1103/PhysRevB.33.7923](https://doi.org/10.1103/PhysRevB.33.7923).
- [29] X. Jiang, D. A. Bruzewicz, M. M. Thant, and G. M. Whitesides, *Palladium as a substrate for self-assembled monolayers used in biotechnology*, *Analytical Chemistry* **76**, 6116 (2004), doi:[10.1021/ac049152t](https://doi.org/10.1021/ac049152t).
- [30] J. Wenger, F. Conchonaud, J. Dintinger, L. Wawrezynieck, T. W. Ebbesen, H. Rigneault, D. Marguet, and P.-F. Lenne, *Diffusion Analysis within Single Nanometric Apertures Reveals the Ultrafine Cell Membrane Organization*, *Biophysical Journal* **92**, 913 (2007-02), doi:[10.1529/biophysj.106.096586](https://doi.org/10.1529/biophysj.106.096586).

- [31] J. M. Moran-Mirabal, A. J. Torres, K. T. Samiee, B. A. Baird, and H. G. Craighead, *Cell investigation of nanostructures: zero-mode waveguides for plasma membrane studies with single molecule resolution*, *Nanotechnology* **18**, 195101 (2007), doi:10.1088/0957-4484/18/19/195101.
- [32] C. I. Richards, K. Luong, R. Srinivasan, S. W. Turner, D. A. Dougherty, J. Korlach, and H. A. Lester, *Live-cell imaging of single receptor composition using zero-mode waveguide nanostructures*, *Nano Letters* **12**, 3690 (2012), doi:10.1021/nl301480h.
- [33] P. Holzmeister, E. Pibiri, J. J. Schmied, T. Sen, G. P. Acuna, and P. Tinnefeld, *Quantum yield and excitation rate of single molecules close to metallic nanostructures*, *Nature Communications* **5**, 5356 (2014), doi:10.1038/ncomms6356.
- [34] I. Gregor, A. Chizhik, N. Karedla, and J. Enderlein, *Metal-induced energy transfer*, *Nanophotonics* **8**, 1689 (2019), doi:10.1515/nanoph-2019-0201.
- [35] T. Miyake, T. Tanii, H. Sonobe, R. Akahori, N. Shimamoto, T. Ueno, T. Funatsu, and I. Ohdomari, *Real-time imaging of single-molecule fluorescence with a zero-mode waveguide for the analysis of protein-protein interaction*, *Analytical Chemistry* **80**, 6018 (2008), doi:10.1021/ac800726g.
- [36] T. Tanii, R. Akahori, S. Higano, K. Okubo, H. Yamamoto, T. Ueno, and T. Funatsu, *Improving zero-mode waveguide structure for enhancing signal-to-noise ratio of real-time single-molecule fluorescence imaging: A computational study*, *Phys Rev E Stat Nonlin Soft Matter Phys* **88**, 012727 (2013), doi:10.1103/physreve.88.012727.
- [37] X. Jiao, E. M. Peterson, J. M. Harris, and S. Blair, *Uv fluorescence lifetime modification by aluminum nanoapertures*, *ACS Photonics* **1**, 1270 (2014), doi:10.1021/ph500267n.
- [38] P.-F. Lenne, H. Rigneault, D. Marguet, and J. Wenger, *Fluorescence fluctuations analysis in nanoapertures: physical concepts and biological applications*, *Histochemistry and Cell Biology* **130**, 795 (2008), doi:10.1007/s00418-008-0507-7.
- [39] G. V. Los, L. P. Encell, M. G. McDougall, D. D. Hartzell, N. Karassina, C. Zimprich, M. G. Wood, R. Learish, R. F. Ohana, M. Urh, D. Simpson, J. Mendez, K. Zimmerman, P. Otto, G. Vidugiris, J. Zhu, A. Darzins, D. H. Klaubert, R. F. Bulleit, and K. V. Wood, *HaloTag: A Novel Protein Labeling Technology for Cell Imaging and Protein Analysis*, *ACS Chemical Biology* **3**, 373 (2008), doi:10.1021/cb800025k.
- [40] J. B. Grimm, L. Xie, J. C. Casler, R. Patel, A. N. Tkachuk, N. Falco, H. Choi, J. Lippincott-Schwartz, T. A. Brown, B. S. Glick, Z. Liu, and L. D. Lavis, *A General Method to Improve Fluorophores Using Deuterated Auxochromes*, *JACS Au* **1**, 690 (2021), doi:10.1021/jacsau.1c00006.
- [41] G. Agam, C. Gebhardt, M. Popara, R. Mächtel, J. Folz, B. Ambrose, N. Chamachi, S. Chung, T. Craggs, M. de Boer, D. Grohmann, T. Ha, A. Hartmann, J. Hendrix, V. Hirschfeld, C. Hübner, T. Hugel, D. Kammerer, H. Kang, A. Kapanidis, G. Krainer, K. Kramm, E. Lemke, E. Lerner, E. Margeat, K. Martens, J. Michaelis, J. Mitra,

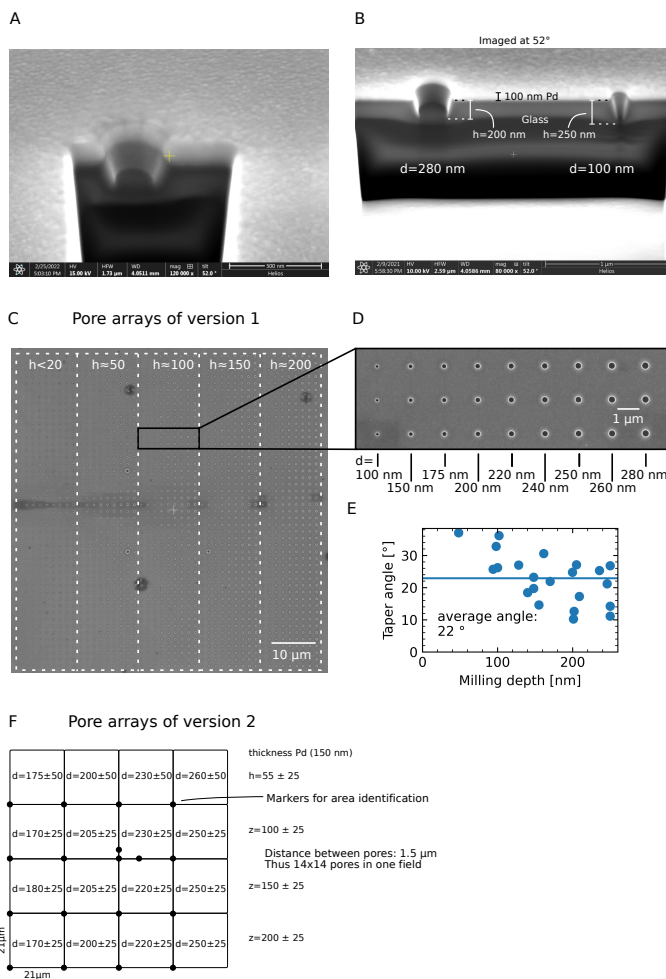
- G. Moya Muñoz, R. Quast, N. Robb, M. Sattler, M. Schlierf, J. Schneider, T. Schröder, A. Sefer, P. Tan, J. Thurn, P. Tinnefeld, J. van Noort, S. Weiss, N. Wendler, N. Zijlstra, A. Barth, C. Seidel, D. Lamb, and T. Cordes, *Reliability and accuracy of single-molecule fret studies for characterization of structural dynamics and distances in proteins*. *Nat Methods* (2023).
- [42] E. Lerner, A. Barth, J. Hendrix, B. Ambrose, V. Birkedal, S. Blanchard, R. Börner, H. Sung Chung, T. Cordes, T. Craggs, A. Deniz, J. Diao, J. Fei, R. Gonzalez, I. Gopich, T. Ha, C. Hanke, G. Haran, N. Hatzakis, S. Hohng, S. Hong, T. Hugel, A. Ingargiola, C. Joo, A. Kapanidis, H. Kim, T. Laurence, N. Lee, T. Lee, E. Lemke, E. Margeat, J. Michaelis, X. Michalet, S. Myong, D. Nettels, T. Peulen, E. Ploetz, Y. Razvag, N. Robb, B. Schuler, H. Soleimaninejad, C. Tang, R. Vafabakhsh, D. Lamb, C. Seidel, and S. Weiss, *Fret-based dynamic structural biology: Challenges, perspectives and an appeal for open-science practices*. *eLife* **10**, e60416 (2021).
- [43] A. J. García and D. Boettiger, *Integrin–fibronectin interactions at the cell-material interface: initial integrin binding and signaling*, *Biomaterials* **20**, 2427 (1992), doi:[10.1016/S0142-9612\(99\)00170-2](https://doi.org/10.1016/S0142-9612(99)00170-2).
- [44] S. VandeVondele, J. Vörös, and J. A. Hubbell, *RGD-grafted poly-l-lysine-graft-(polyethylene glycol) copolymers block non-specific protein adsorption while promoting cell adhesion*, *Biotechnology and Bioengineering* **82**, 784 (2003), doi:[10.1002/bit.10625](https://doi.org/10.1002/bit.10625).
- [45] B. Malekian, R. L. Schoch, T. Robson, G. Ferrand Drake del Castillo, K. Xiong, G. Emilsson, L. E. Kapinos, R. Y. H. Lim, and A. Dahlin, *Detecting selective protein binding inside plasmonic nanopores: Toward a mimic of the nuclear pore complex*, *Frontiers in Chemistry* **6**, 637 (2018), doi:[10.3389/fchem.2018.00637](https://doi.org/10.3389/fchem.2018.00637).
- [46] Y.-J. Liu, M. Le Berre, F. Lautenschlaeger, P. Maiuri, A. Callan-Jones, M. Heuzé, T. Takaki, R. Voituriez, and M. Piel, *Confinement and Low Adhesion Induce Fast Amoeboid Migration of Slow Mesenchymal Cells*, *Cell* **160**, 659 (2015), doi:[10.1016/j.cell.2015.01.007](https://doi.org/10.1016/j.cell.2015.01.007).
- [47] M. Foquet, K. T. Samiee, X. Kong, B. P. Chauduri, P. M. Lundquist, S. W. Turner, J. Freudenthal, and D. B. Roitman, *Improved fabrication of zero-mode waveguides for single-molecule detection*, *Journal of Applied Physics* **103**, 034301 (2008), doi:[10.1063/1.2831366](https://doi.org/10.1063/1.2831366).
- [48] B. Malekian, K. Xiong, G. Emilsson, J. Andersson, C. Fager, E. Olsson, E. M. Larsson-Langhammer, and A. B. Dahlin, *Fabrication and Characterization of Plasmonic Nanopores with Cavities in the Solid Support*, *Sensors* **17**, 1444 (2017), doi:[10.3390/s17061444](https://doi.org/10.3390/s17061444).
- [49] X. Yan, T. A. Hoek, R. D. Vale, and M. E. Tanenbaum, *Dynamics of Translation of Single mRNA Molecules In Vivo*, *Cell* **165**, 976 (2016), doi:[10.1016/j.cell.2016.04.034](https://doi.org/10.1016/j.cell.2016.04.034).
- [50] J. A. Bard, E. A. Goodall, E. R. Greene, E. Jonsson, K. C. Dong, and A. Martin, *Structure and function of the 26s proteasome*, *Annual Review of Biochemistry* **87**, 697 (2018), doi:[10.1146/annurev-biochem-062917-011931](https://doi.org/10.1146/annurev-biochem-062917-011931).

- [51] B. K. Müller, E. Zaychikov, C. Bräuchle, and D. C. Lamb, *Pulsed interleaved excitation*, *Biophys J* **89**, 3508 (2005), doi:[10.1529/biophysj.105.064766](https://doi.org/10.1529/biophysj.105.064766).
- [52] S. A. Alterovitz, P. M. Amirtharaj, P. Apell, E. T. Arakawa, J. Ashok, J. Barth, D. F. Bezuidenhout, J. R. Birch, H.-G. Birken, C. Blessing, I. Bloomer, A. Borghesi, T. A. Callcott, M. Cardona, Y.-c. Chang, T. M. Cotter, D. F. Edwards, J. E. Eldridge, J. Fink, A. R. Forouhi, F. Gervais, O. J. Glembocki, G. Guizzetti, R. T. Holm, D. R. Huffman, J. Humlíček, O. Hunderi, W. R. Hunter, T. Inagaki, B. Jensen, R. Johnson, C. Kunz, F. Lukeš, D. W. Lynch, K. Navrátil, L. Ohlídal, E. D. Palik, E. Pelletier, J. Pflüger, A. Piaggi, H. Piller, M. R. Querry, C. G. Ribbing, D. M. Roessler, A. Roos, N. Savvides, E. Schmidt, M. L. Scott, D. J. Segelstein, F. W. Smith, G. J. Sprokel, J. D. Swalen, K. Takarabe, R. Tatchyn, Y. Y. Teng, M. E. Thomas, W. J. Tropf, P. L. H. Varaprasad, L. Ward, R. H. White, D. M. Wieliczka, J. A. Woollam, and C. Wong, *Handbook of Optical Constants of Solids*, edited by E. D. Palik, Vol. 3 (Academic Press, Boston, 1998) p. 1096, doi:[10.1016/B978-0-08-055630-7.50003-1](https://doi.org/10.1016/B978-0-08-055630-7.50003-1).
- [53] B. Hellenkamp, S. Schmid, O. Doroshenko, O. Opanasyuk, R. Kühnemuth, S. Rezaei Adariani, B. Ambrose, M. Aznauryan, A. Barth, V. Birkedal, M. E. Bowen, H. Chen, T. Cordes, T. Eilert, C. Fijen, C. Gebhardt, M. Götz, G. Gouridis, E. Gratton, T. Ha, P. Hao, C. A. Hanke, A. Hartmann, J. Hendrix, L. L. Hildebrandt, V. Hirschfeld, J. Hohlbein, B. Hua, C. G. Hübner, E. Kallis, A. N. Kapanidis, J.-Y. Kim, G. Krainer, D. C. Lamb, N. K. Lee, E. A. Lemke, B. Levesque, M. Levitus, J. J. McCann, N. Naredi-Rainer, D. Nettels, T. Ngo, R. Qiu, N. C. Robb, C. Röcker, H. Sanabria, M. Schlierf, T. Schröder, B. Schuler, H. Seidel, L. Streit, J. Thurn, P. Tinnefeld, S. Tyagi, N. Vandenberk, A. M. Vera, K. R. Weninger, B. Wünsch, I. S. Yanez-Orozco, J. Michaelis, C. A. M. Seidel, T. D. Craggs, and T. Hugel, *Precision and accuracy of single-molecule FRET measurements—a multi-laboratory benchmark study*, *Nature Methods* **15**, 669 (2018-09), doi:[10.1038/s41592-018-0085-0](https://doi.org/10.1038/s41592-018-0085-0).
- [54] L. Novotny and B. Hecht, *Principles of Nano-Optics* (Cambridge University Press, Cambridge, 2006) doi:[10.1017/CBO9780511813535](https://doi.org/10.1017/CBO9780511813535).
- [55] P. Bharadwaj and L. Novotny, *Spectral dependence of single molecule fluorescence enhancement*, *Optics Express* **15**, 14266–14274 (2007), doi:[10.1364/oe.15.014266](https://doi.org/10.1364/oe.15.014266).
- [56] F. Kaminski, V. Sandoghdar, and M. Agio, *Finite-difference time-domain modeling of decay rates in the near field of metal nanostructures*, *Journal of Computational and Theoretical Nanoscience* **4**, 635–643 (2007).
- [57] W. Schrimpf, A. Barth, J. Hendrix, and D. C. Lamb, *Pam: A framework for integrated analysis of imaging, single-molecule, and ensemble fluorescence data*, *Biophysical Journal* **114**, 1518 (2018), doi:<https://doi.org/10.1016/j.bpj.2018.02.035>.
- [58] J. E. Bronson, J. Fei, J. M. Hofman, R. L. Gonzalez, and C. H. Wiggins, *Learning Rates and States from Biophysical Time Series: A Bayesian Approach to Model Selection and Single-Molecule FRET Data*, *Biophysical Journal* **97**, 3196 (2009), doi:[10.1016/j.bpj.2009.09.031](https://doi.org/10.1016/j.bpj.2009.09.031).

- [59] S. Yang, N. Klughammer, and A. Barth, *Datasets underlying the paper zero-mode waveguide nanowells for single-molecule detection in living cells*, Online (Zenodo, 2023) doi:[10.5281/zenodo.8060099](https://doi.org/10.5281/zenodo.8060099).
- [60] C. Xu and W. W. Webb, *Multiphoton excitation of molecular fluorophores and non-linear laser microscopy*, in *Topics in Fluorescence Spectroscopy: Volume 5: Nonlinear and Two-Photon-Induced Fluorescence*, edited by J. R. Lakowicz (Springer US, Boston, MA, 2002) Chap. 11, pp. 471–540, doi:[10.1007/0-306-47070-5_11](https://doi.org/10.1007/0-306-47070-5_11).
- [61] E. M. Purcell, *Spontaneous emission probabilities at radio frequencies*, *Phys. Rev. Lett.* **69**, 839 (1946), doi:[10.1007/978-1-4615-1963-8_40](https://doi.org/10.1007/978-1-4615-1963-8_40).

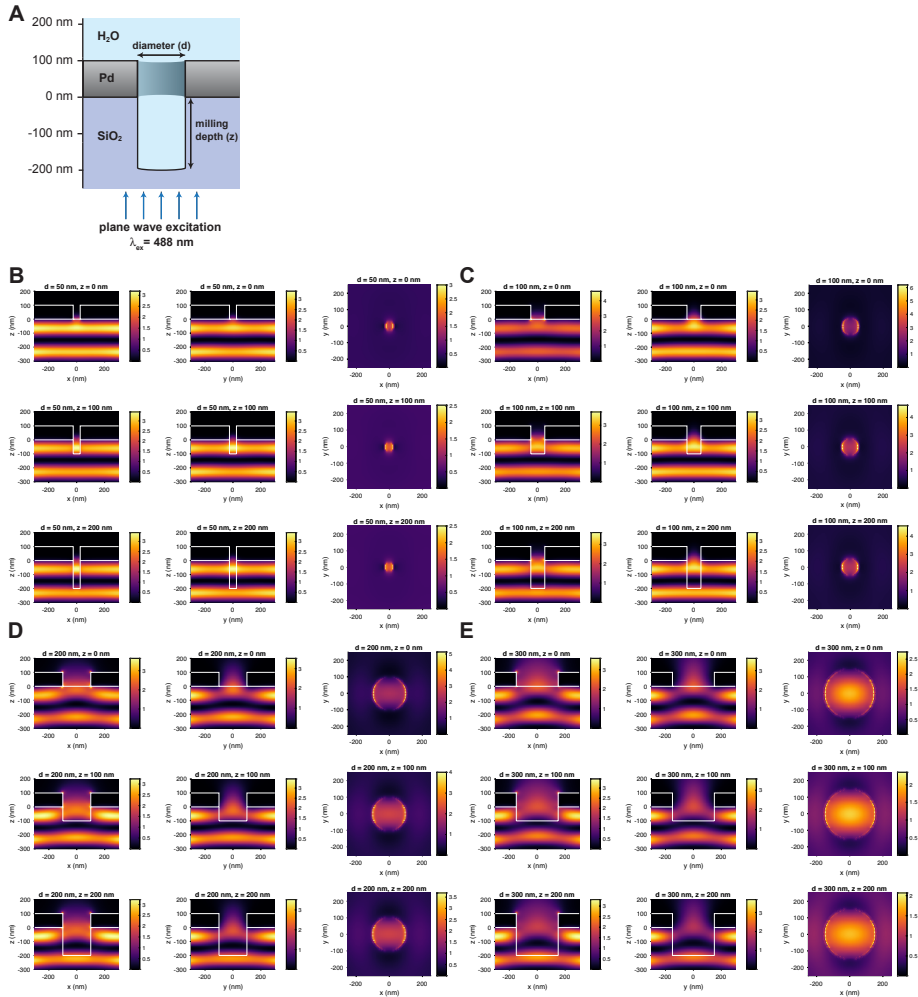
6.7. APPENDIX

6.7.1. SUPPLEMENTARY FIGURE TO FIGURE 1

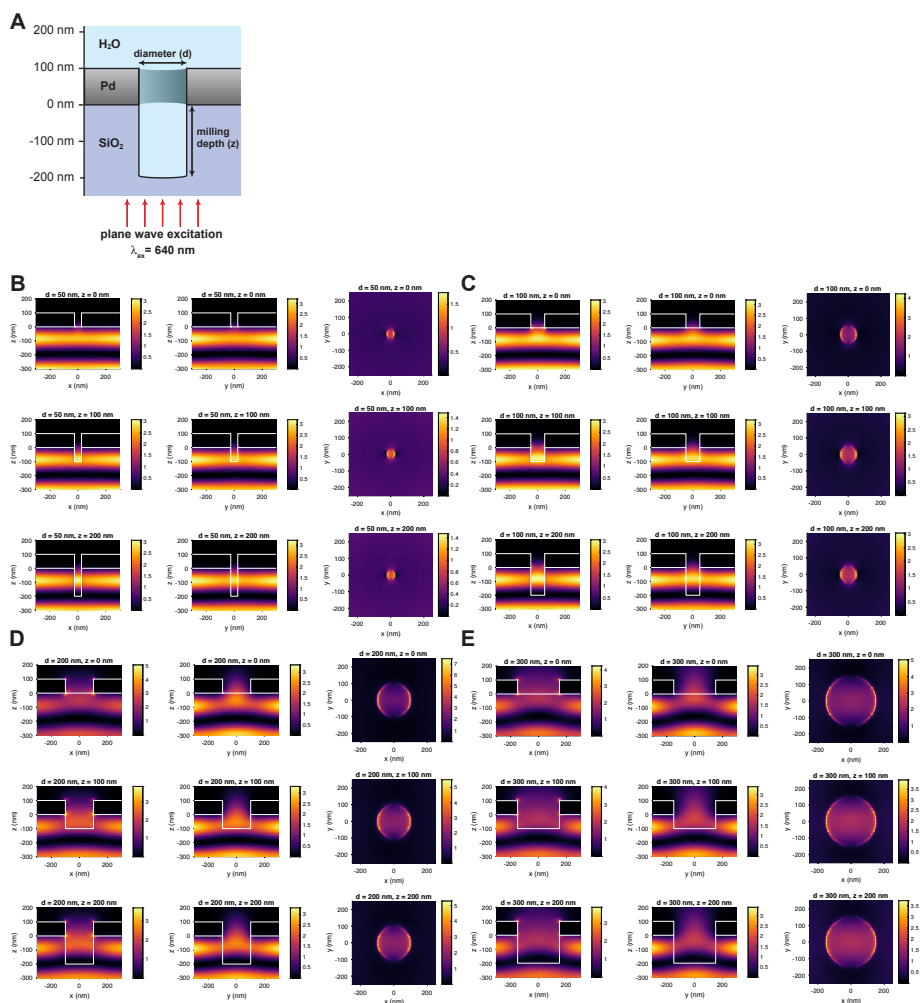


Supplementary Figure 6.1: Additional SEM images and layouts of version 1 and 2 arrays. **A,B:** SEM images of overmilled Pd ZMWs, imaged under 52°. Pd shows up as a bright layer and glass as a dark layer. **C:** An SEM image of a Pd ZMW array of version 1 containing five regions of different milling depths (h), each made from nine rows of pores with varying diameter. **D:** Zoom in of C. **E:** Taper angle vs. milling depth. For deeper pores, the edges were more perpendicular with an average of 22° (horizontal line). **F:** Diameters (d) and depths (h) in nm of ZMW arrays for arrays of version 2 together with their uncertainty (estimated from measuring several pores).

6.7.2. SUPPLEMENTARY FIGURES TO FIGURE 2

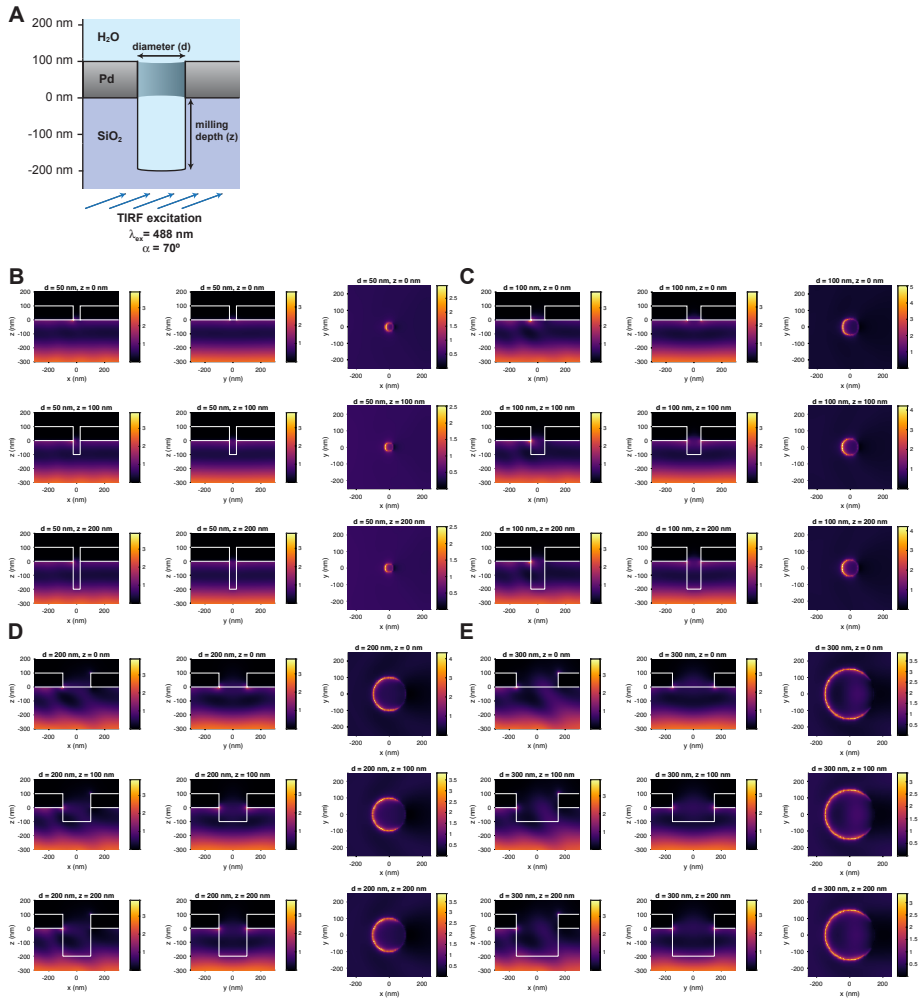


Supplementary Figure 6.2: Excitation field intensity distributions from FDTD simulations under widefield excitation at $\lambda_{\text{ex}} = 488 \text{ nm}$. **A:** Schematic of the simulation setup. **B-E:** Excitation field intensity distributions $|E|^2$ in V^2/m^2 in the x-z (left), y-z (middle) and x-y plane at the entrance to the ZMW (right) at pore diameters d of 50 nm (B), 100 nm (C), 200 nm (D), and 300 nm (E) and milling depths h of 0 nm (top), 100 nm (middle), and 200 nm (bottom). The electric field is polarized along the x-axis.

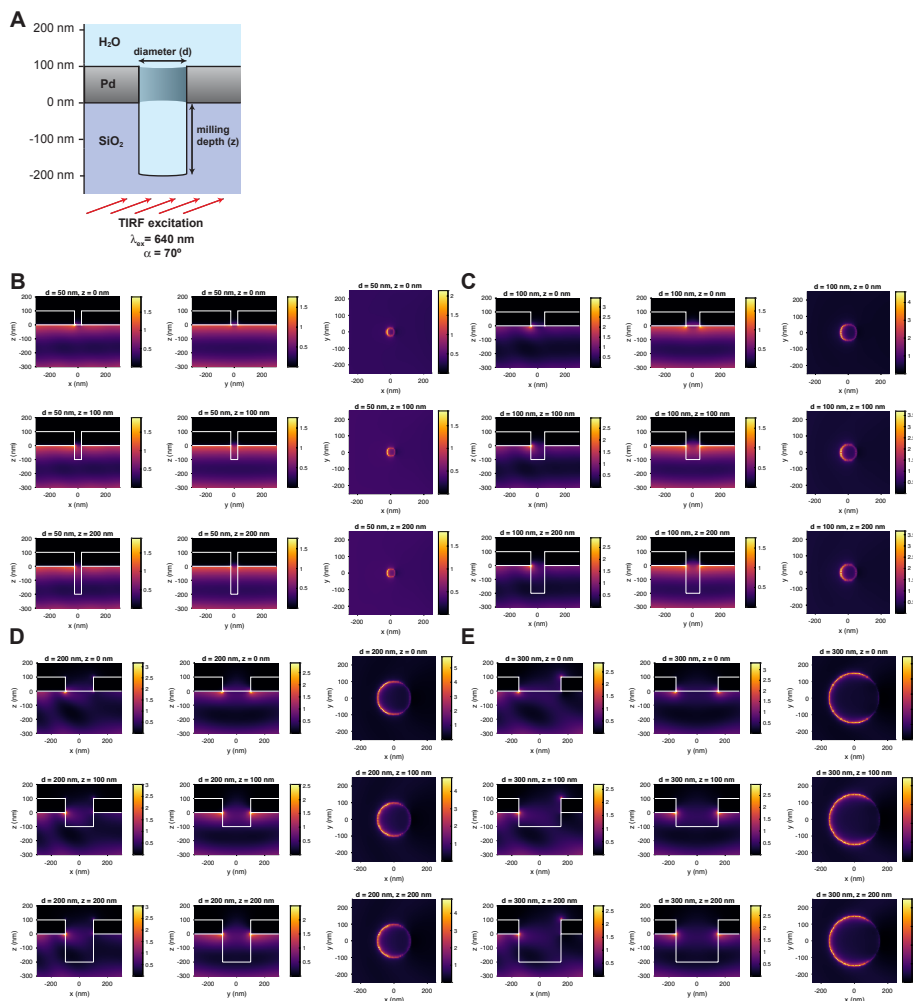


6

Supplementary Figure 6.3: Excitation field intensity distributions from FDTD simulations under widefield excitation at $\lambda_{ex} = 640 \text{ nm}$. **A:** Schematic of the simulation setup. **B-E:** Excitation field intensity distributions $|E|^2$ in V^2/m^2 in the x-z (left), y-z (middle) and x-y plane at the entrance to the ZMW (right) at pore diameters d of 50 nm (B), 100 nm (C), 200 nm (D), and 300 nm (E) and milling depths h of 0 nm (top), 100 nm (middle), and 200 nm (bottom). The electric field is polarized along the x-axis.

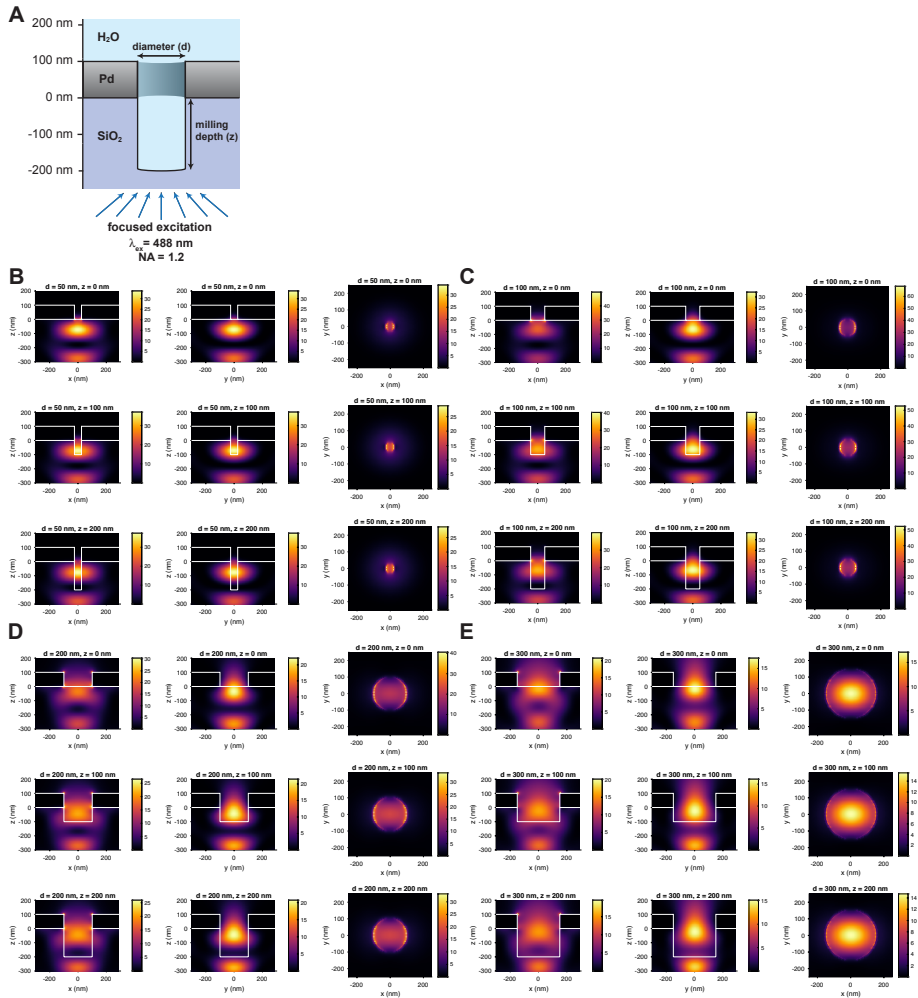


Supplementary Figure 6.4: Excitation field intensity distributions from FDTD simulations under TIRF illumination at an angle of 70° at $\lambda_{\text{ex}} = 488 \text{ nm}$. **A:** Schematic of the simulation setup. **B-E:** Excitation field intensity distributions $|E|^2$ in V^2/m^2 in the x - z (left), y - z (middle) and x - y plane (right) at pore diameters d of 50 nm (**B**), 100 nm (**C**), 200 nm (**D**), and 300 nm (**E**) and milling depths h of 0 nm (top), 100 nm (middle), and 200 nm (bottom). The electric field is polarized along the x -axis.

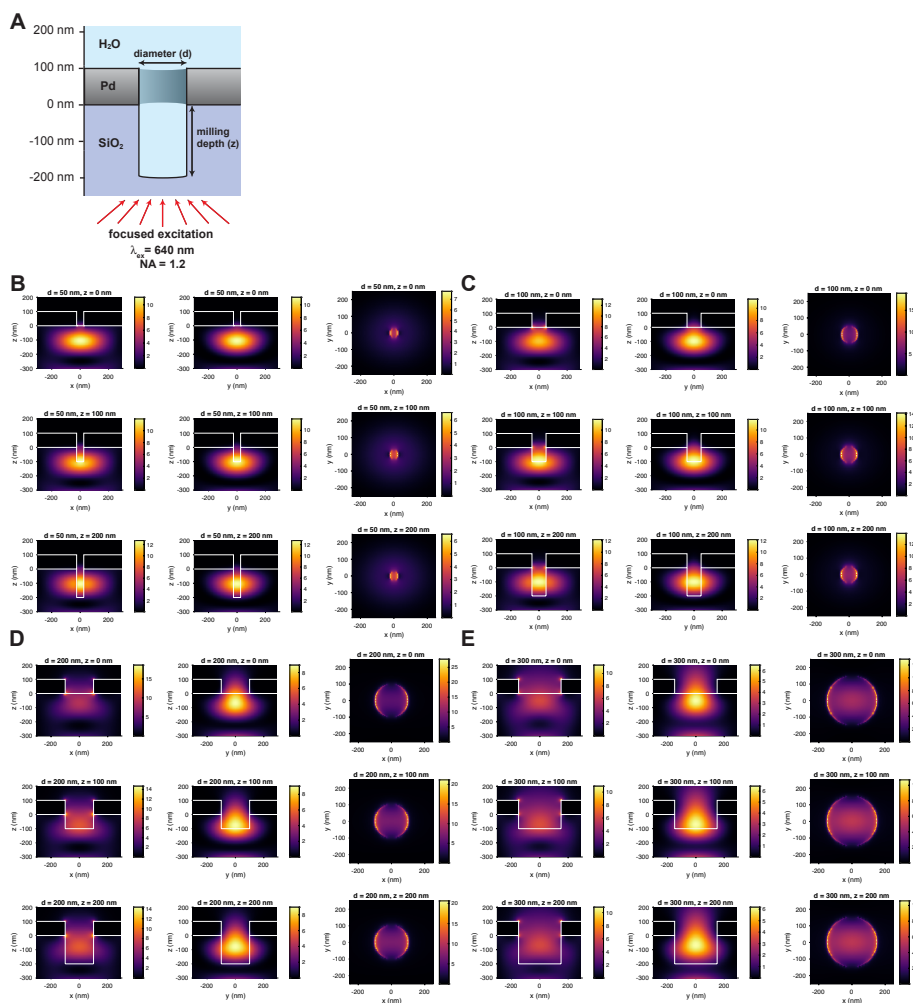


6

Supplementary Figure 6.5: Excitation field intensity distributions from FDTD simulations under TIRF illumination at an angle of 70° at $\lambda_{\text{ex}} = 640 \text{ nm}$. **A:** Schematic of the simulation setup. **B-E:** Excitation field intensity distributions $|E|^2$ in V^2/m^2 in the x - z (left), y - z (middle) and x - y plane at the entrance to the ZMW (right) at pore diameters d of 50 nm (**B**), 100 nm (**C**), 200 nm (**D**), and 300 nm (**E**) and milling depths h of 0 nm (top), 100 nm (middle), and 200 nm (bottom). The electric field is polarized along the x -axis.

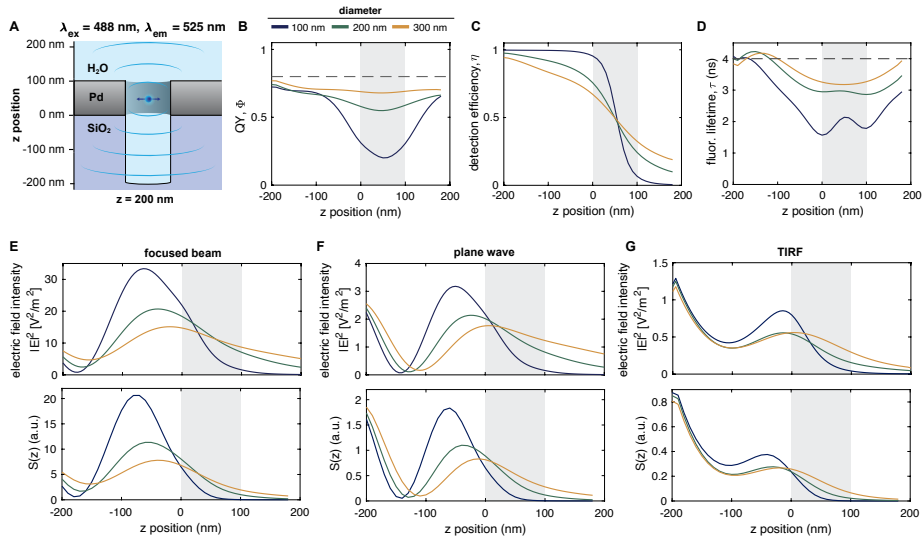


Supplementary Figure 6.6: Excitation field intensity distributions from FDTD simulations under excitation by a focused Gaussian beam at NA = 1.2 and a wavelength of $\lambda_{\text{ex}} = 488 \text{ nm}$. **A:** Schematic of the simulation setup. **B-E:** Excitation field intensity distributions $|E|^2$ in V^2/m^2 in the x-z (left), y-z (middle) and x-y plane at the entrance to the ZMW (right) at pore diameters d of 50 nm (B), 100 nm (C), 200 nm (D), and 300 nm (E) and milling depths h of 0 nm (top), 100 nm (middle), and 200 nm (bottom). The electric field is polarized along the x-axis.

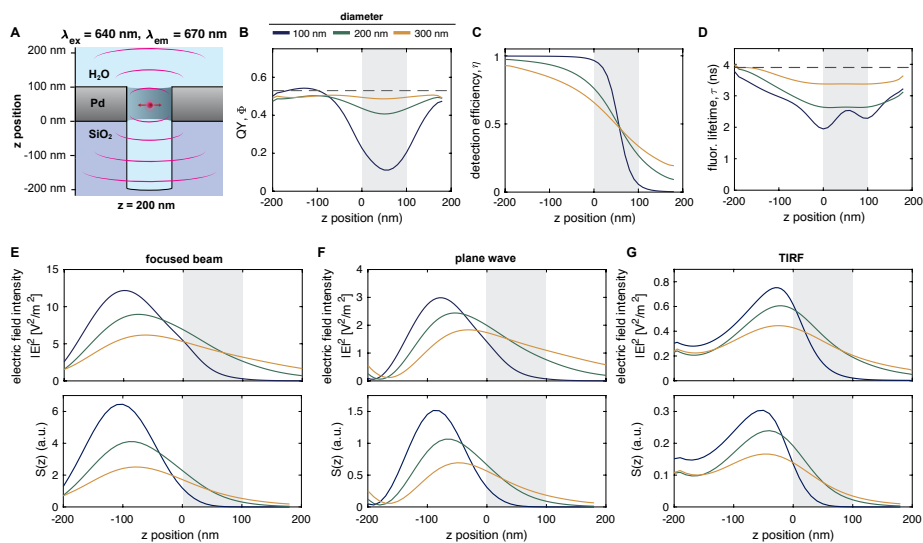


6

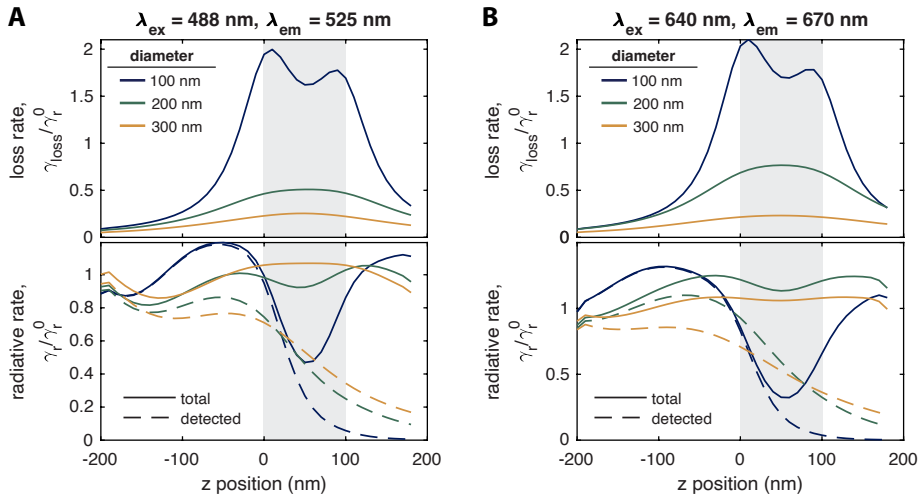
Supplementary Figure 6.7: Excitation field intensity distributions obtained from FDTD simulations under excitation by a focused Gaussian beam at $NA = 1.2$ and $\lambda_{ex} = 640$ nm. **A:** Schematic of the simulation setup. **B-E:** Excitation field intensity distributions $|E|^2$ in V^2/m^2 in the x-z (left), y-z (middle) and x-y plane at the entrance to the ZMW (right) at pore diameters d of 50 nm (B), 100 nm (C), 200 nm (D), and 300 nm (E) and milling depths h of 0 nm (top), 100 nm (middle), and 200 nm (bottom). The electric field is polarized along the x-axis.



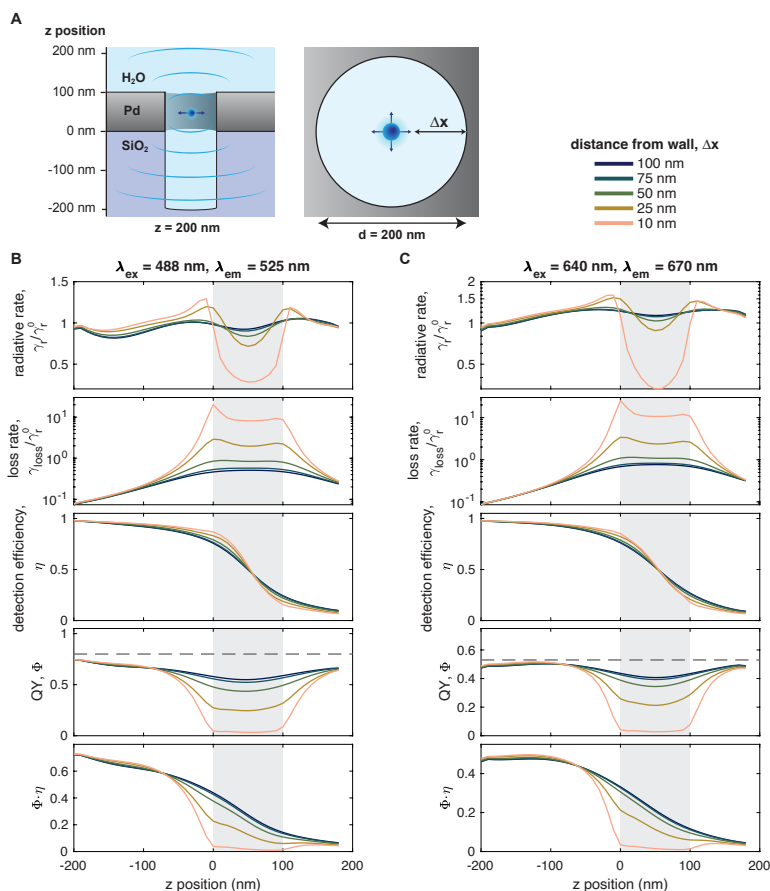
Supplementary Figure 6.8: FDTD simulations of fluorescence emission and detected signal from overmilled ZMWs for Alexa488. **A:** Schematic of the simulation setup. **B-D:** Computed quantum yield Φ , detection efficiency η , and fluorescence lifetime τ profiles of the dye Alexa488 as a function of the z position. Dashed lines indicate the values in the absence of a ZMW. **E-G:** Z-profiles of the excitation intensity profiles along the central pore axis (top) and the total detected signal $S(z)$ (bottom) under excitation by a focused Gaussian beam (E), plane wave (*i.e.*, widefield) (F) or excitation under TIRF angle (G). The position of the metal membrane is indicated as a gray shaded area.



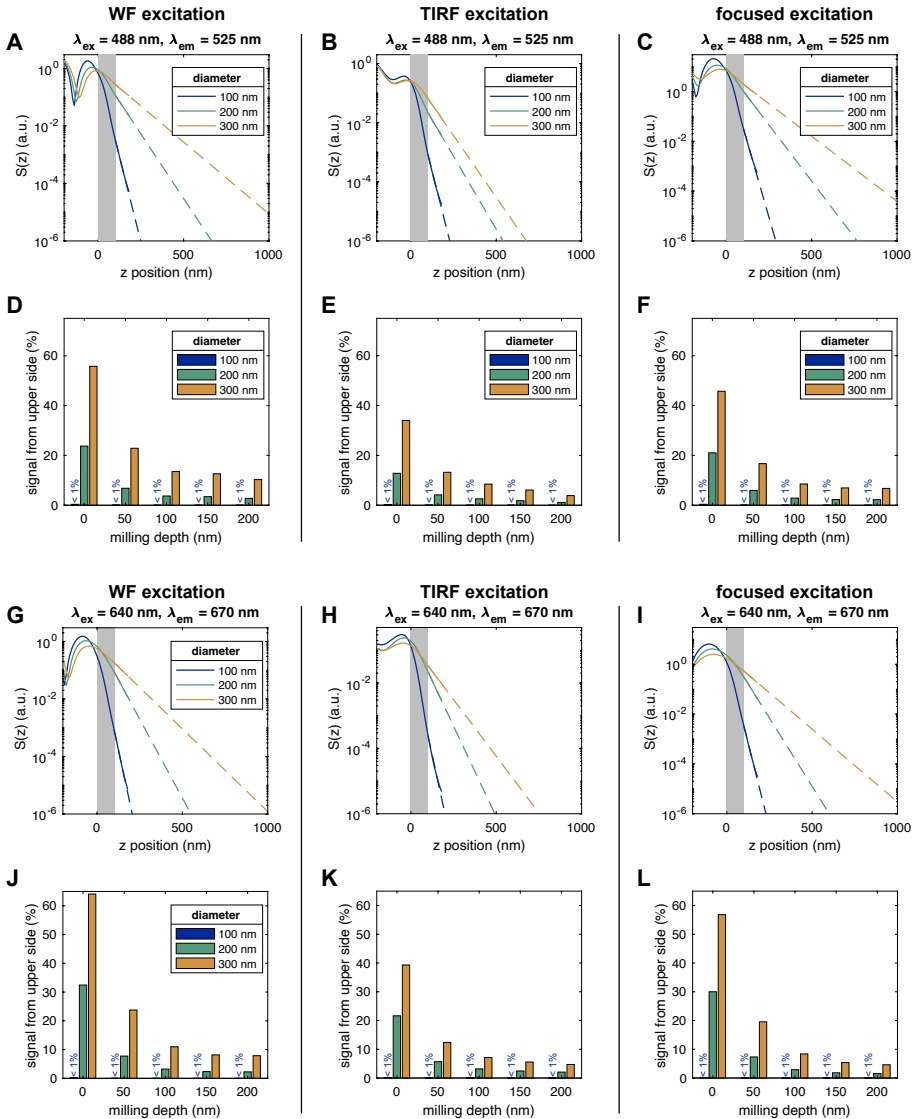
Supplementary Figure 6.9: FDTD simulations of fluorescence emission and detected signal from overmilled ZMWs for JFX650. **A:** Schematic of the simulation setup. **B-D:** Computed quantum yield Φ , detection efficiency η , and fluorescence lifetime τ profiles of the dye JFX650 as a function of the z position. Dashed lines indicate the values in the absence of a ZMW. **E-G:** Z -profiles of the excitation intensity profiles along the central pore axis (top) and the total detected signal $S(z)$ (bottom) under excitation by a focused Gaussian beam (E), plane wave (*i.e.*, widefield) (F) or excitation under TIRF angle (G). The position of the metal membrane is indicated as a gray shaded area.



Supplementary Figure 6.10: Overview of radiative and non-radiative rates obtained from FDTD simulations of fluorescence emission within overmilled ZMWs. Shown are the non-radiative loss rate (top) and radiative rate (bottom) in the presence of the metal nanostructure for the dyes Alexa488 (A) and JFX650 (B). The radiative rate towards the detection side is given as a dashed line, from which the detection efficiency is computed. Note that the given rates are normalized to the rates in the absence of the ZMW as described in the methods.

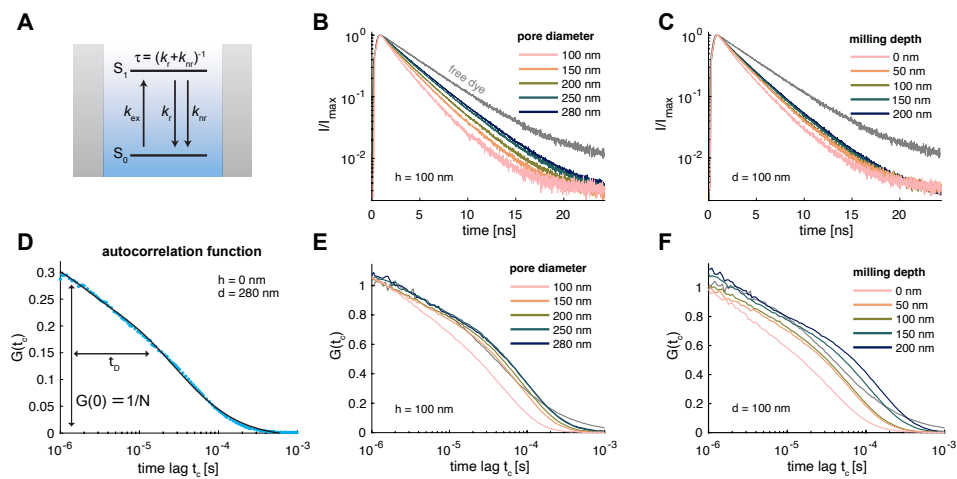


Supplementary Figure 6.11: FDTD simulations of dipole emission as a function of the distance to the pore walls. **A:** Schematic of the simulation setup. The dipole was placed at varying distances Δx from the pore walls and the emission was monitored as a function of the z-position. **B,C:** Z-profiles of the normalized radiative and loss rates, the detection efficiency η , the quantum yield Φ , and the product of the detection efficiency and quantum yield, $\Phi \cdot \eta$ for Alexa488 (B) and JFX650 (C) at the indicated excitation and emission wavelengths. The quantum yield of the free dye is shown as a dashed line. The dipole emission within the overmilled volume in the glass was found to be approximately independent of the lateral displacement within the pore at distance of $\approx 25 \text{ nm}$ away from the ZMW. Within the ZMW, the non-radiative rate is strongly increased as the dipole approaches the pore wall, with significant non-radiative losses occurring at distances below 25 nm that result in a reduction of the quantum yield. Note that the loss rate is given on a log scale. The position of the palladium layer is indicated as a gray shaded area.

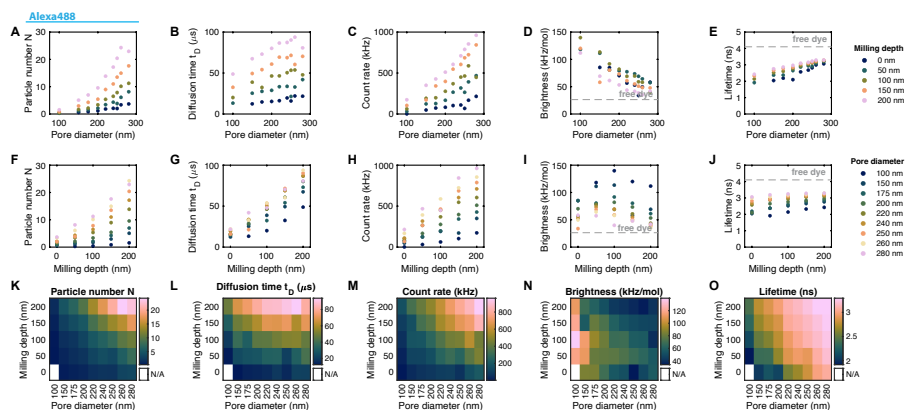


Supplementary Figure 6.12: Estimation of background signal from FDTD simulations for the dyes Alexa488 (A-F) and JFX650 (G-L) under the different excitation modes. A-C, G-I: The detected signal $S(z)$ obtained for widefield (WF), TIRF, and focused excitation (solid lines) is extrapolated by fitting the signal profile in the z -range from 100 nm to 200 nm to an exponential decay (dashed lines). **D-F, J-L:** From the extrapolated signal profiles, the amount of signal detected from the upper side (above a z position of 100 nm) is estimated for different pore diameters and milling depths. The bars for 100 nm are barely visible due to their small height.

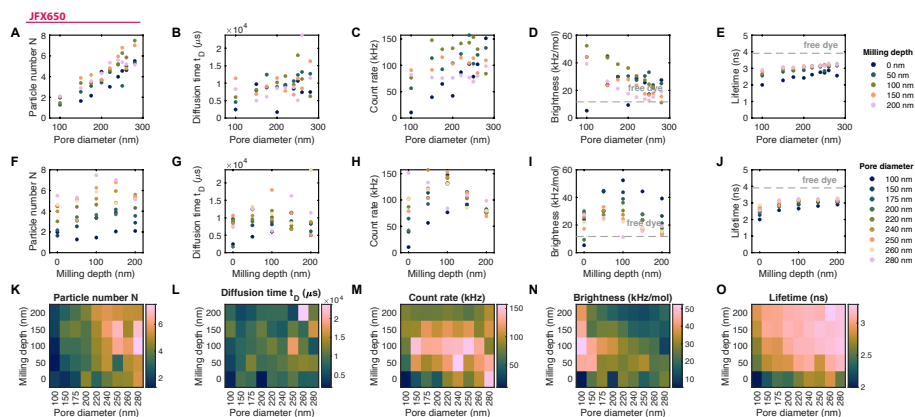
6.7.3. SUPPLEMENTARY FIGURES TO FIGURE 3



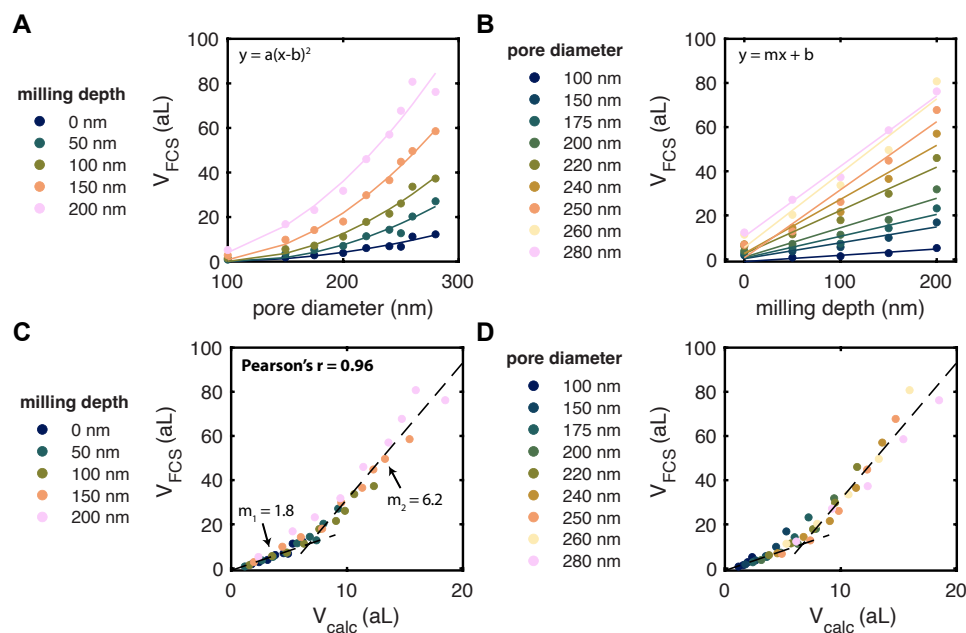
Supplementary Figure 6.13: Experimental characterization of photophysics and diffusion within ZMWs. A: Jablonski scheme of the photophysics in the ZMW. Dyes are radiatively excited from the electronic ground state S_0 to the first excited state S_1 with rate k_{ex} , from where relaxation can occur radiatively (k_r) or non-radiatively (k_{nr}). In the waveguide, all displayed rates change due to excitation field enhancement, plasmonic coupling, and metal-induced quenching. The excited state lifetime reports on the sum of the radiative and non-radiative rates. **B,C:** Fluorescence decays acquired at different pore diameters for a constant milling depth of 100 nm (B) and at different milling depths for a constant pore diameter of 100 nm (C). **D:** Autocorrelation function of the fluorescence time trace shown in Figure 3 C. The FCS analysis informs on the average number of particles (N) and the residence time of molecules within the ZMW (t_D). **E,F:** FCS curves of the data shown in Figure 3 D-E. In B,C,E, and F the curves for the free dye obtained from a free diffusion experiment are shown in gray.



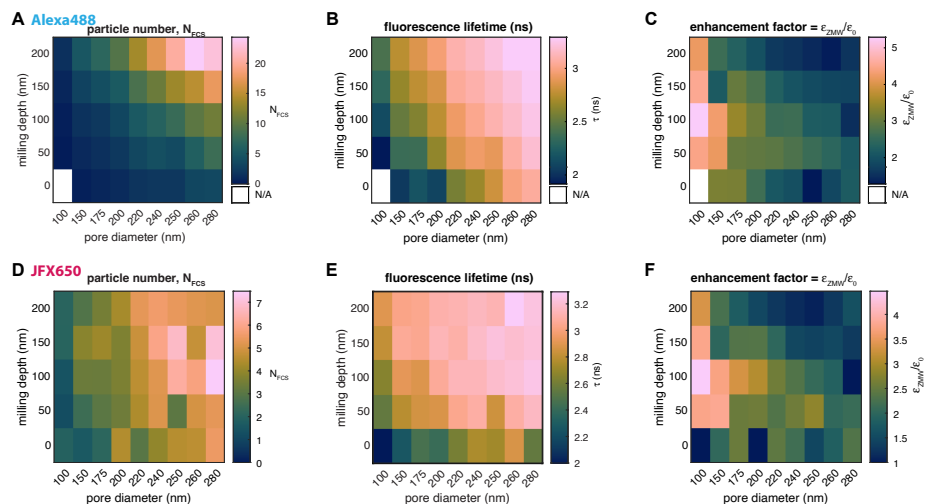
Supplementary Figure 6.14: Extracted parameters for the dye Alexa488 in overmilled Pd ZMWs. Shown are the estimated particle number N , diffusion time t_D , count rate, molecular brightness ϵ_{ZMW} , and fluorescence lifetime τ as a function of the pore diameter at constant milling depth (A-E), as a function of the milling depth at constant pore diameter (F-J), and as heatmap plots (K-O). The molecular brightness and fluorescence lifetime of the free dye are indicated by gray dashed lines.



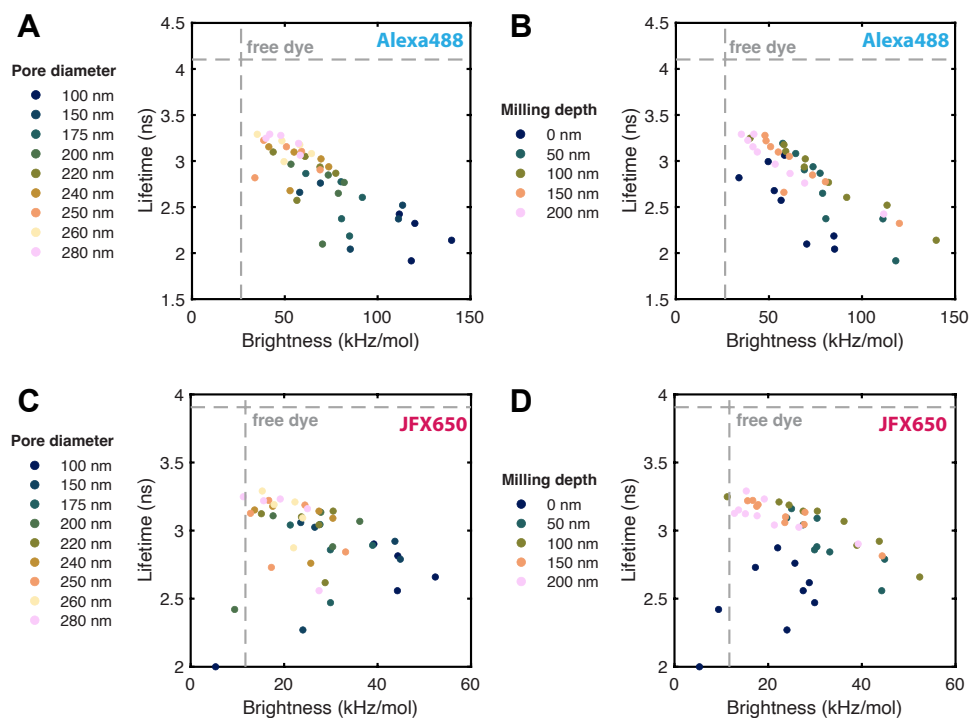
Supplementary Figure 6.15: Extracted parameters for the dye JFX650 in overmilled Pd ZMWs. Shown are the estimated particle number N , diffusion time t_D , count rate, molecular brightness ϵ_{ZMW} , and fluorescence lifetime τ as a function of the pore diameter at constant milling depth (A-E), as a function of the milling depth at constant pore diameter (F-J), and as heatmap plots (K-O). The molecular brightness and fluorescence lifetime of the free dye are indicated by gray dashed lines. The robustness of the FCS analysis is markedly reduced compared to the Alexa488 dye due to significant sticking of the JFX650 dye to the glass and metal surfaces, as evident from the drastically prolonged diffusion times (B,G,L).



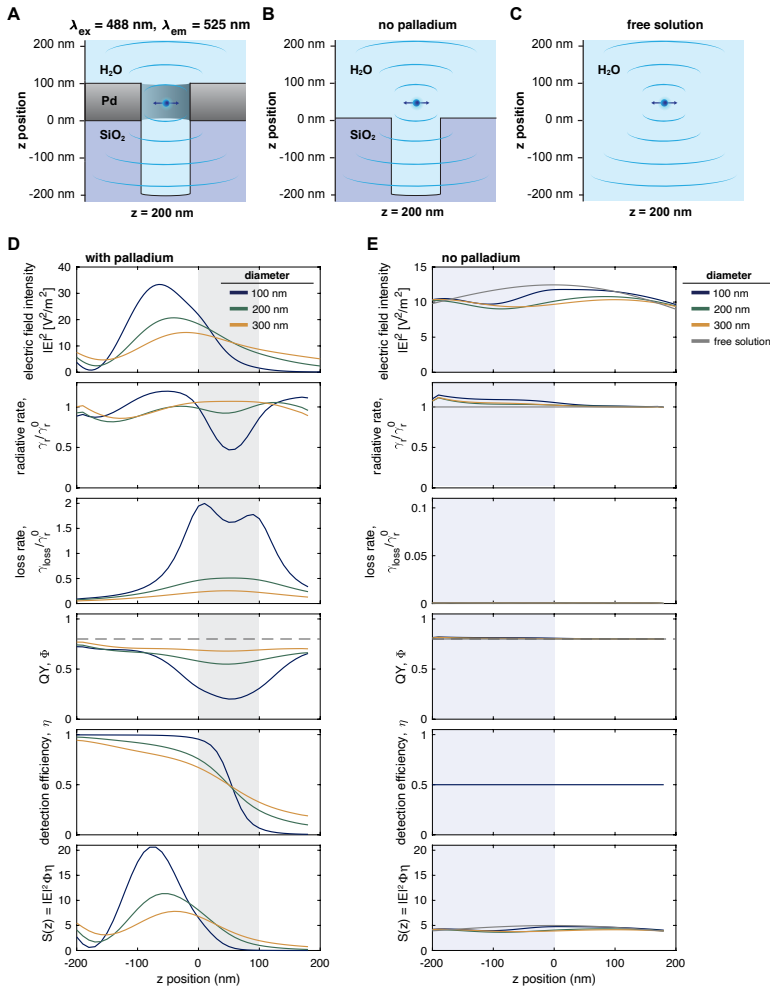
Supplementary Figure 6.16: Quantification of the observation volume in overmilled ZMWs. **A,B:** Estimated effective volumes V_{FCS} as a function of the pore diameter (A) and milling depth (B). The effective volume V_{FCS} was estimated from the particle number N determined from FCS as $V_{\text{FCS}} = N/c$, where c is the concentration of the dye ($c = 500$ nM). Note that the effective volume in FCS corresponds to a hypothetical volume with constant signal that contains N particles [7, 60]. The effective volume shows a quadratic scaling with the pore diameter and linear scaling with the milling depth, as expected for the approximately cylindrical volume of the overmilled ZMWs. **C,D:** Comparison of the calculated volume of the overmilled aperture in the glass, V_{calc} , and the experimentally determined effective volume, V_{FCS} , color coded by milling depth (C) and pore diameter (D). V_{calc} is given by $V_{\text{calc}} = (\pi/4)d^2(z+l)$, where d is the diameter, z the overmilling depth, and l is the thickness of the Pd layer ($l = 100$ nm). An excellent correlation is observed between the two quantities (Pearson's correlation coefficient $r = 0.96$), however the measured volumes V_{FCS} are consistently overestimated by a factor of ≈ 2 for small pores ($V_{\text{calc}} \leq 5$ aL) and ≈ 6 for large pores ($V_{\text{calc}} \geq 10$ aL). Note that this overestimation is also present at small pore diameters where only little signal is detected from within the ZMW. Similar overestimation of the particle numbers within ZMW by FCS have previously been reported and attributed to a contribution of constant signal from many dim particles outside of the ZMW [7, 8, 12, 38].



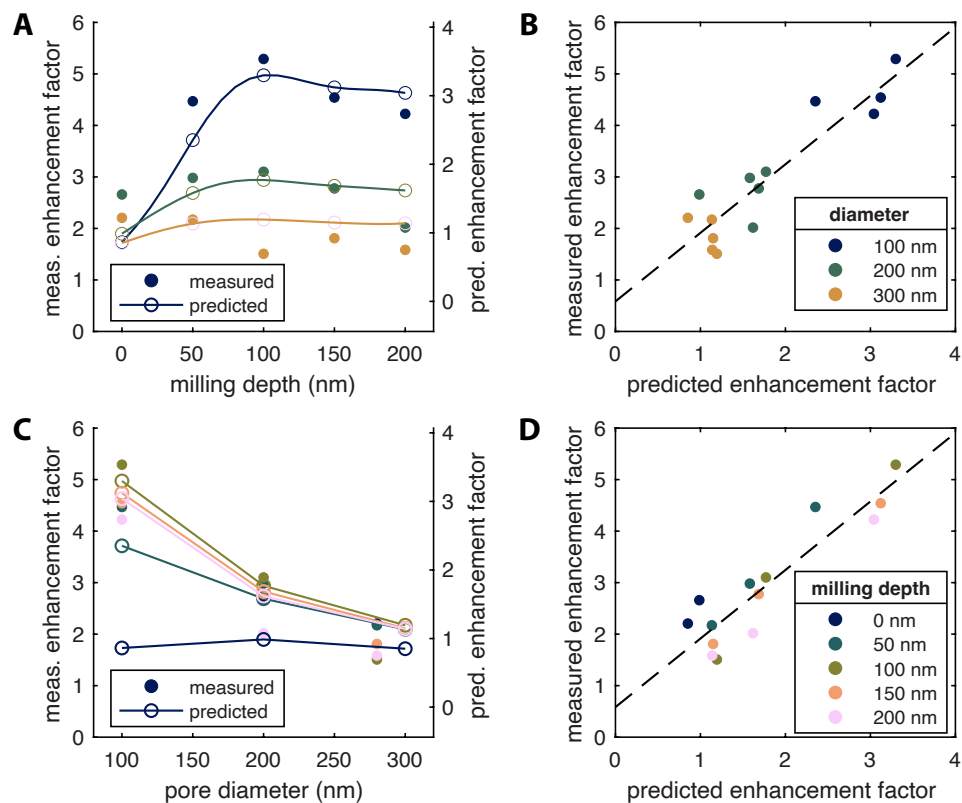
Supplementary Figure 6.17: Comparison of extracted parameters for the dyes Alexa488 and JFX650 in ZMW. The heatmap plots show the average number of particles in the observation volume N , fluorescence lifetime τ , and signal enhancement factor for the dyes Alexa488 (A-C) and JFX650 (D-F). The enhancement factor is defined as the ratio of the counts per molecule in the ZMW compared to free diffusion, $\epsilon_{ZMW}/\epsilon_0$. Data marked as N/A could not be quantified due to insufficient signal. The trends visible for Alexa488 are not as clear with JFX650 due to non-specific sticking interactions of the fluorophore with the surface, as evidenced by the increased diffusion time (see Figure 3—[Supplementary Figure 6.15](#)).



Supplementary Figure 6.18: Correlation between fluorescence lifetime and molecular brightness in ZMW for Alexa488 (A,B) and JFX650 (C,D). The data is color coded either by pore diameter (A,C) or milling depth (B,D). The fluorescence lifetime is given by the inverse of the excited state decay rate. A reduction of the lifetime thus indicates the enhancement of the radiative and/or non-radiative relaxation rates due to the ZMW. A negative correlation is observed, where a lower lifetime corresponds with an increased molecular brightness.

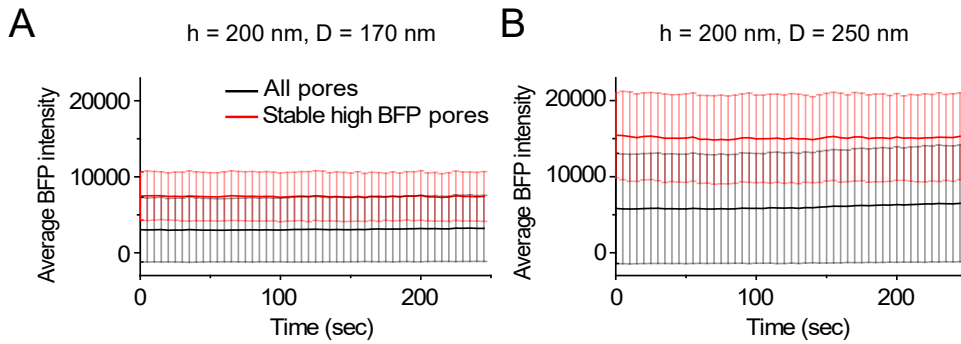


Supplementary Figure 6.19: FDTD simulations of excitation field and fluorescence emission in the absence of a Pd layer. **A,B:** Schematic of the simulation setup with (A), without (B) the Pd layer and for the free solution case (C). **D,E:** Computed excitation field intensity $|E|^2$, normalized radiative rate γ_r/γ_r^0 , normalized loss rate $\gamma_{\text{loss}}/\gamma_r^0$ quantum yield Φ , detection efficiency η , and total fluorescence signal $S(z)$ as a function of the z position in the presence (D) and absence (E) of the Pd layer. In D, the position of the metal membrane is indicated as a gray shaded area. In E, the position of the SiO_2 layer is indicated as a blue shaded area (except for the free diffusion case). The detection efficiency was set to 0.5 in the absence of the Pd layer. A small radiative rate enhancement arises even in the absence of the Pd layer when the dipole is placed in the SiO_2 nanocavity due to the Purcell effect [61].

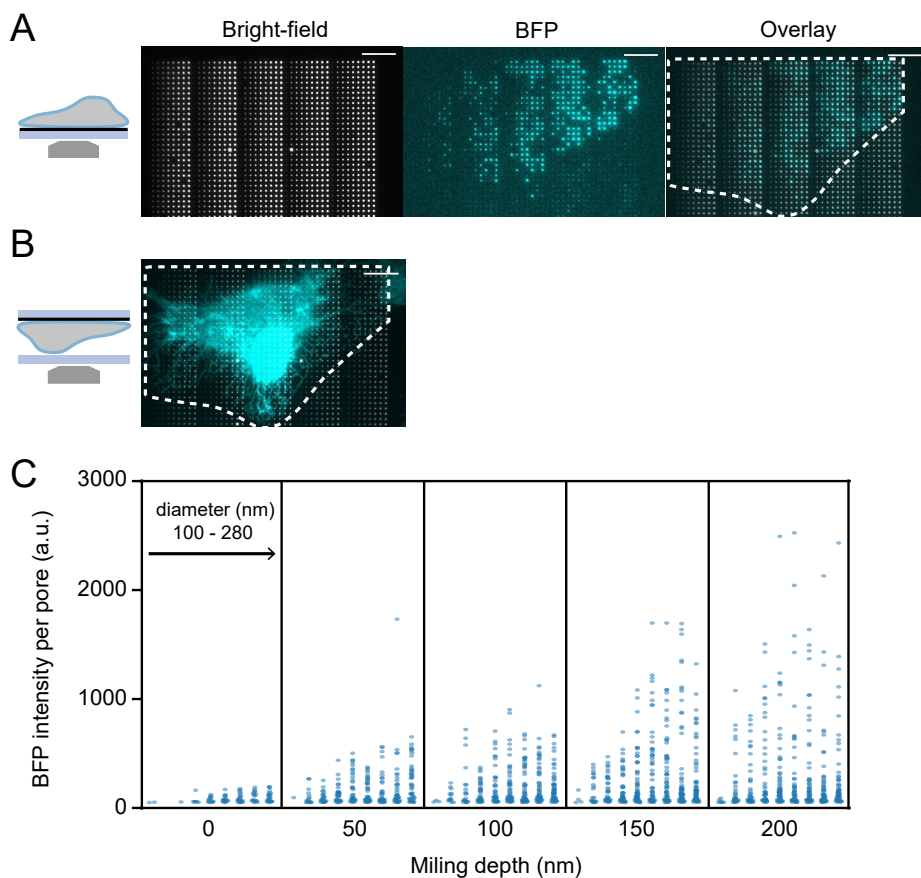


Supplementary Figure 6.20: Comparison of experimental and predicted enhancement factors in overmilled Pd ZMWs. **A,C:** Measured and predicted enhancement factors as a function of the milling depths (A) or pore diameter (C). The scaling of the two y-axes was adjusted according to the results of the linear regression between measured and predicted enhancement factors. **B,D:** Plots of the measured versus the predicted enhancement factors, color coded by milling depth (B) or pore diameter (D). The solid line is a linear fit given by $y = 1.33x + 0.58$. The Pearson correlation coefficient is $r = 0.92$.

6.7.4. SUPPLEMENTARY FIGURES TO FIGURE 4

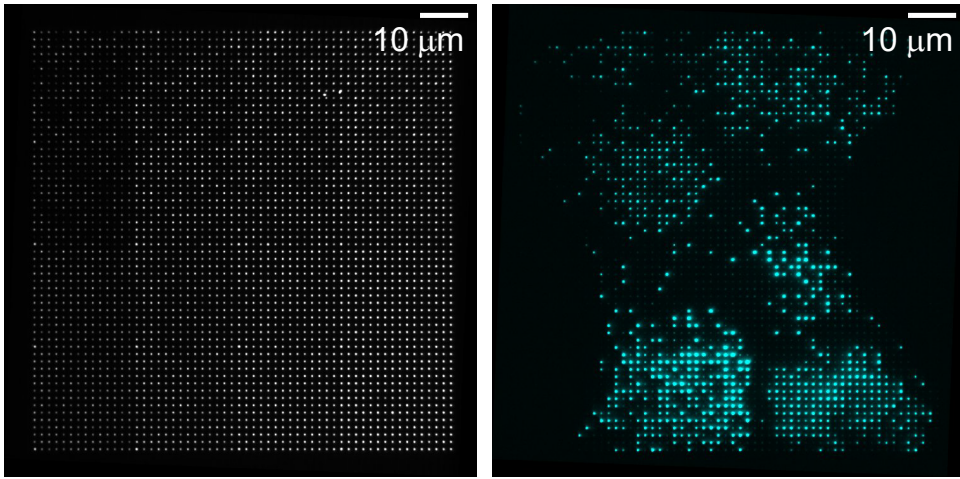


Supplementary Figure 6.21: Stability of the BFP signal during the experiments. (A) Time dependence of the average BFP intensity across for all pores (black) and for pores showing high BFP signal (red). The milling depth was 200 nm and the diameter was 170 nm. (B) Same as panel A for a pore diameter of 250 nm. Error bars represent the standard deviation of the signal. No photobleaching was observed over the course of the experiment.

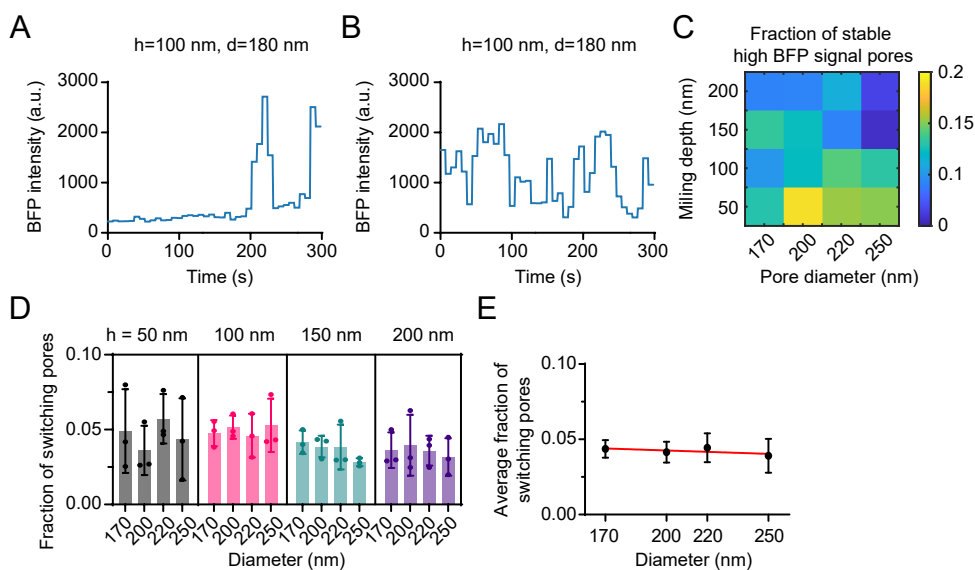


Supplementary Figure 6.22: Correlated imaging of flipped coverslips confirms the colocalization of pores with BFP signal with the presence of cells on the ZMW array. A: From left to right, bright-field, BFP fluorescence, and composite images of the experiment shown in Figure 4 A, depicting cells attached to the coverslip. B: Overlay of bright-field and BFP fluorescence images obtained from the same field of view as in (A) after flipping the orientation of the coverslip, where cells attached to the Pd surface are not imaged through the ZMWs but from the top side. Note that the image is mirrored to visualize cells in the same orientation as in (A). Scale bars: 10 μm . C: BFP fluorescence intensities of individual pores with varying sizes. Each dot represents a single pore. The total number of analyzed pores was 1890.

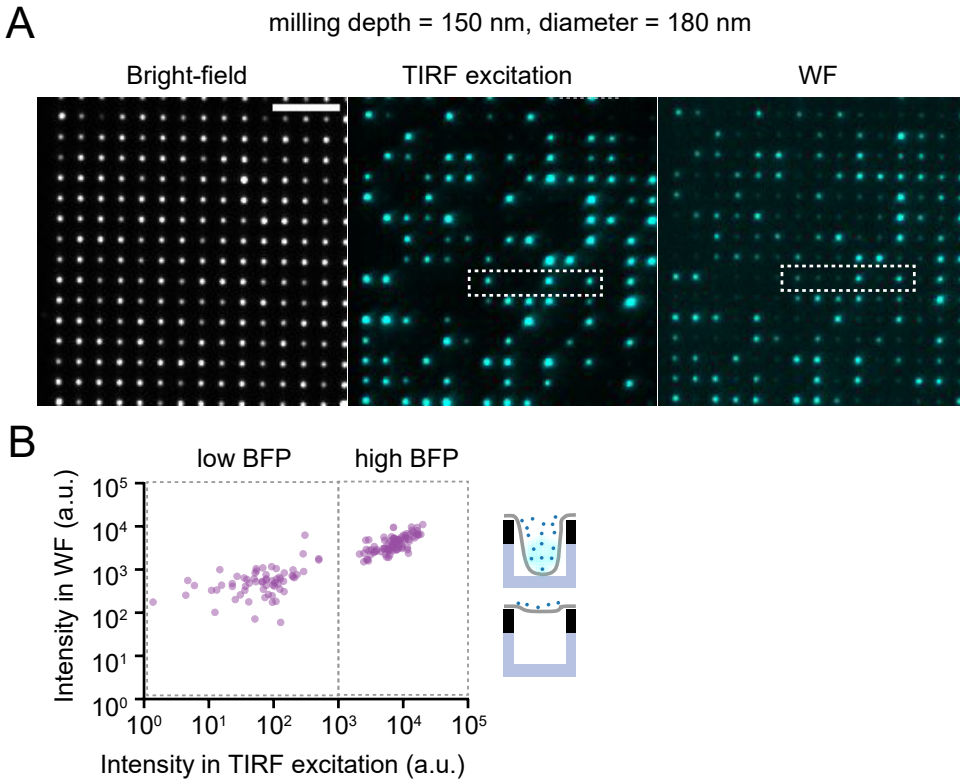
6.7.5. SUPPLEMENTARY FIGURES TO FIGURE 5



Supplementary Figure 6.23: Brightfield and BFP-fluorescence images of array version 2 Orientation is the same as in Figure 1—[Supplementary Figure 6.1 F](#). The brightfield image (left) shows the location of pores and the BFP-fluorescence image (right) shows their occupation.

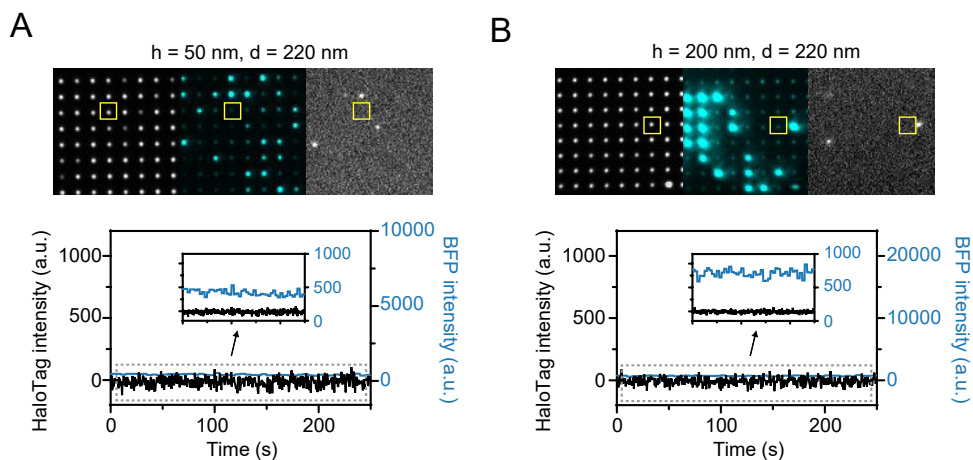


Supplementary Figure 6.24: BFP fluorescence intensity switching between high and low signal levels. A,B: Representative examples of BFP fluorescence intensity time traces for individual pores where the intensity switched between the high and low intensity levels. **C:** Percentage of pores with high stable BFP signal for the duration of the movie (300 s). The total number of pores analyzed is 30907, with approximately 1900 pores for each pore size. **D:** Fraction of pores exhibiting switching between different BFP intensity levels as a function of pore size. Given are the mean and standard deviation from three independent experiments. Each dot represents an individual experiment. **E:** Average fraction of pores showing switching behavior versus diameter. No significant dependence of switching on diameter and milling depth is evident.



Supplementary Figure 6.25: TIRF illumination vs. widefield illumination. **A:** Bright-field image (left), and BFP fluorescence images acquired with either TIRF illumination (center) or WF illumination (right) of nanopores with milling depth $h = 150$ nm and diameter $d = 180$ nm. Scale bar, $5 \mu\text{m}$. The boxes indicate the location of the zoom-in shown in Figure 5 G. **B:** Scatter plot of BFP intensities in individual pores for TIRF and widefield illumination, with each dot representing a single pore. Note that the two populations can be distinguished much more readily when using TIRF excitation compared to widefield illumination. The number of pores analyzed is 150.

6.7.6. SUPPLEMENTARY FIGURES TO FIGURE 6



Supplementary Figure 6.26: BFP and JFX650-HaloTag signal of pores showing low BFP signal. Bright-field, BFP, and JFX650-HaloTag signal from representative pores showing only low BFP signal with milling depths of 50 nm (left) or 200 nm (right). A fluorescence time trace of a single pore is shown for each condition. Insets provide a zoom-in on the grey box. While a low signal from BFP is observed, no single molecule events of the red fluorophore could be detected. Time interval, 5 s for BFP; 500 ms for JFX650-Halo

7

FUTURE DIRECTIONS

In this thesis, we have introduced palladium zero-mode waveguides as a valuable tool for biophysics research and have showcased several applications thereof. In this final chapter, we discuss research areas building upon the work presented in earlier chapters that would be interesting to follow. We cover both improvements in method development of Pd ZMWs and deepening the understanding of the nuclear pore complex.

In this thesis, we worked both on the method development, such as palladium zero-mode waveguides as a tool for single-molecule biophysics studies, and fundamental questions, such as how does the nuclear pore complex facilitate transport. Concretely, we studied diffusio-phoretic transport of DNA through palladium nanopores before moving towards nuclear pore complex mimics that use Pd ZMWs as a platform for single-molecule detection. We further studied the structure of NPC mimics using cryo electron microscopy by highlighting individual parts of them using gold labels. In a last step, we used glass supported ZMWs for background suppression during live-cell imaging, which shows the wide applicability of Pd ZMWs across different fields of research. For both the method development and the question driven research, we see a number of potential follow-up projects that we describe in this chapter. We first start by formulating a number of steps that would improve the applicability of freestanding and glass supported Pd ZMWs, before looking into new applications that would benefit from using Pd ZMWs. In the second part, we discuss future directions for studying the nuclear pore complex both regarding the structure of the FG mesh and towards a better understanding of nucleocytoplasmic transport.

7.1. Pd ZMWs

At several points in this thesis, we witnessed that the surface chemistry of Pd nanopores is of prime importance for successful single-molecule experiments. Both the desired surface modification and the undesired non-specific interaction are governed by the effects on the Pd surface. Additionally, also for live-cell applications the right surface treatment of Pd has been shown to influence the adhesion properties of cells on the surface [1]. In this thesis, we mainly developed protocols for specific applications such as thiol attachment after nanofabrication [2]. We think that future applications would benefit from a deeper understanding of the processes governing the chemical reactions happening on the nanoscale at the Pd surface. Especially interesting would be the development of surface modification strategies that allow to selectively graft a molecule for instance to the Pd surface while grafting a different molecule to a glass surface. A potential candidate would be thiol-based attachment to the Pd surface (as performed in [chapter 4](#)) together with silane-based attachment to the glass surface as performed in [chapter 5](#). One major issue we foresee here is to keep the surfaces clean and susceptible for binding while not damaging already attached organic molecules. Such a system would for instance allow to produce sandwich structures for translocation studies, that allow fine tuning of the NPC mimic height while maintaining a good passivation (comparable to [3]).

In [chapter 6](#), where we studied single-molecule fluorescence in live cells, we encountered that only about 1 % of the total membrane area is present in the ZMWs due to the small size of the apertures [4]. This poses a serious problem for analytes that are only present in low densities on the membrane. Therefore, it would be attractive to increase the amount of area that could be simultaneously observed through the ZMWs while not sacrificing the good light-blocking properties. We envision two different approaches to tackle this issue. At first one could try to simply increase the density of pores in an array by reducing the pore-to-pore distance and arranging them on a hexagonal lattice. Two points should be considered here: First, at too close distances individual ZMWs might not be resolved any more during imaging. While this might not pose a big problem for

single-molecule observation where the pores are populated only for a short amount of time, the second point might create more problems. For densely spaced arrays of pores in metal films, it has been shown that extraordinary transmission from plasmonic effects increases the amount of light transmitted through the pores above what would be expected from the same number of individual pores [5]. This extraordinary transmission would thus counteract the light-blocking capabilities of the ZMWs. We believe, however, that by fine-tuning the pore spacing to the laser wavelengths these issues could be circumvented. A different way of increasing accessible membrane area, without sacrificing the background suppression, could be fabricating nanoslits, instead of nanopores, together with polarized illumination. When illuminated by light with a polarization parallel to the nanoslit, it has been shown that the amount of transmitted light can be significantly reduced [6]. The light-blocking capabilities of this setup would need to be tested for the specific case of single-molecule fluorescence in live-cells, however.

Apart from technical challenges as described above, we see several future applications for Pd ZMWs. Firstly, one could benefit from the possibility to observe nanopore translocations in the absence of strong driving forces and build on the insight we gained from [chapter 3](#), where we studied the fundamental forces that influence nanopore transport. We were, however, not able to explain the observed variation between experiments which shows a lack of understanding of the underlying effects and the interplay of different driving forces. Therefore, we think it would be important to study the forces acting within the Pd ZMWs in order to get a better understanding of nanopore transport. Especially the effect of surface interaction, so far, has only been studied with very minimalistic models [7] and would benefit from a more detailed view.

Freestanding ZMWs, additionally, offer the great possibility to act as a gate that reduces the amount of particles in the observation volume. In protein-binding studies and fluorescence correlation spectroscopy it is required to operate at concentrations that lead to individual molecules in the observation volume. This requirement is hard to achieve when analytes with weak interactions should be studied. This issue has been circumvented by reducing the observation volume using ZMWs fabricated on a glass surface. This volume reduction, however, comes at the cost of low observation times since the analyte quickly diffuses out of the observation volume. Freestanding ZMWs, however, can act as a sort of gate, leading to a certain translocation rate that can be calculated from a modified Fick's law [8]. After translocation, the molecules subsequently get released to a big observation volume that allows for a long observation time of individual molecules. This allows to add a high concentration of analytes to the reservoir side which is required for weakly interacting analytes. We envision this method to be attractive both for Förster resonance energy transfer and fluorescence correlation spectroscopy studies.

Apart from fluorescence in the visible spectrum, fluorescence in the UV spectrum became a field of active research for single-molecule fluorescence [9–11]. Since the three aromatic amino acids, tyrosine, tryptophan, and phenylalanine, exhibit autofluorescence in the ultraviolet spectral range, UV fluorescence allows to detect the presence of these amino acids and any molecule containing them. Thus, molecules can be specifically detected without the requirement of labelling them with fluorescent proteins or organic dyes. Another promising application for this would be protein fingerprinting, where the

sequence and distance of specific markers in the amino acid sequence is recorded for protein identification [12, 13]. So far, we have not investigated the possibility to use palladium for this purpose but we find it a promising candidate for these applications due to its good chemical and nanofabrication properties.

7.2. NPCs

After the structure of the NPC scaffold was solved to atomistic precision [14–16], the focus of attention shifted more and more to the central mesh filled with the unstructured regions of the FG-Nups [17, 18]. It is especially interesting to assess the mesh in native NPCs, guided by several questions: Are there openings (volumes not occupied by Nups) present in the mesh, does the mesh change in the presence of transport receptors, and are the Nups well dissolved or do they form a phase condensate. Based on the success we had using gold labeling in chapter 5, we would propose a comparable approach, where specifically labelled Nups or transport receptors would be added to full NPCs in vitro before plunge freezing. By electron microscopic imaging, the locations of the gold particles can be recorded with respect to the NPCs. This allows to draw conclusions about the distribution of the Nup mesh and the arrangement of transport receptors in it. Adding specific gold labels is of course not only restricted to full NPCs, but can also be applied to DNA origami-based NPC mimics that in principle allow for full control over the number and attachment-point location of individual FG Nups. In addition to perpendicular imaging, tilted image acquisition could be performed together with tomogram reconstruction which would allow to investigate the 3D organisation within the NPC and NPC mimics.

In the end, investigating the organisation of the FG Nup mesh serves to understand how NPC transport works. Here, one question is of prime importance: how can the NPC maintain very high transport rates while simultaneously and efficiently separating molecules that get blocked from the ones that translocate. One interesting model attributes the NPC selectivity mainly to an entropic exclusion of large molecules together with an energetic barrier reduction for transport molecules. This energetic interaction effectively leads to a flat free energy landscape for transporters [19]. The model has been put to the test using weakly interacting polymers that fill solid-state nanopores [20, 21] but is not generally accepted in the NPC field. It does not fully incorporate effects such as the FG nup cohesivity and accumulation of transport receptors in the mesh. We envision to put this model to the test using NPC mimics based on ZMWs. For this, we propose to recreate a system that forms an entropic barrier but of which the interaction with a certain particle can be tuned. We would expect three regimes: For low interaction strengths, all particles would be blocked from translocating, for intermediate interaction strengths, the interacting particles should be able to translocate while inert particles would still be blocked, and for high interaction strengths, all particles would be blocked again, since the interacting particles would accumulate in the mesh and thus reduce the available space even more. A potential candidate would be a single-strand DNA functionalized poly-ethylene glycol that is grafted to a nanopore surface and thus entropically blocks inert particles. The hypothesis would be that a nanoparticle covered with the complementary DNA strand would be able to translocate. The interaction strength could then be adjusted by tuning base pair mismatches between the DNA strands on the polymer

and the particles.

In addition to looking at transport through NPC mimics made from fully artificial components, it will be interesting and straightforward to test different nups and transport systems at our freestanding ZMW platform. This would allow to study the influence of, for instance, the charge-to-hydrophobicity ratio and the effect of the abundance of FG repeats separately [22]. Moreover, so far we did barely benefit from the possibility to follow single-molecule transport through the Pd ZMW based NPC mimics. This will totally change in studies of cargo transport and release, where an individual transporter together with a cargo can be followed. Interesting questions that could be investigated would for example be: How many transporters cover a single cargo? Does the cargo travel through the NPC with the same transporter molecule or does it get handed over? Does the presence of a cargo-releasing proteins such as RanGTP enhance the transport? All of these questions can be directly targeted with only minimal modifications to the platform we described in [chapter 4](#).

Summing up, we see plenty of directions building upon the work presented in this thesis, both towards a better understanding of nanopores that are based on palladium, but also novel experiments targeted at understanding transport through the nuclear pore complex.

REFERENCES

- [1] X. Jiang, D. A. Bruzewicz, M. M. Thant, and G. M. Whitesides, *Palladium as a substrate for self-assembled monolayers used in biotechnology*, *Analytical Chemistry* **76**, 6116 (2004), doi:[10.1021/ac049152t](https://doi.org/10.1021/ac049152t).
- [2] N. Klughammer, A. Barth, M. Dekker, A. Fragasso, P. Onck, and C. Dekker, *Diameter dependence of transport through nuclear pore complex mimics studied using optical nanopores*, *eLife* **12** (2023), [10.7554/eLife.87174](https://doi.org/10.7554/eLife.87174), doi:[10.7554/eLife.87174](https://doi.org/10.7554/eLife.87174).
- [3] B. Malekian, R. L. Schoch, T. Robson, G. Ferrand Drake del Castillo, K. Xiong, G. Emilsson, L. E. Kapinos, R. Y. H. Lim, and A. Dahlin, *Detecting selective protein binding inside plasmonic nanopores: Toward a mimic of the nuclear pore complex*, *Frontiers in Chemistry* **6**, 637 (2018), doi:[10.3389/fchem.2018.00637](https://doi.org/10.3389/fchem.2018.00637).
- [4] S. Yang, N. Klughammer, A. Barth, M. E. Tanenbaum, and C. Dekker, *Zero-mode waveguide nanowells for single-molecule detection in living cells*, *ACSNano* (2023), [10.1021/acsnano.3c05959](https://doi.org/10.1021/acsnano.3c05959), doi:[10.1021/acsnano.3c05959](https://doi.org/10.1021/acsnano.3c05959).
- [5] T. W. Ebbesen, H. J. Lezec, H. Ghaemi, T. Thio, and P. Wolff, *Extraordinary optical transmission through sub-wavelength hole arrays*, *Nature* **391**, 667 (1998), doi:[10.1038/35570](https://doi.org/10.1038/35570).
- [6] J. Wenger, P-F. Lenne, E. Popov, H. Rigneault, J. Dintinger, and T. W. Ebbesen, *Single molecule fluorescence in rectangular nano-apertures*, *Opt. Express* **13**, 7035 (2005), doi:[10.1364/OPEX.13.007035](https://doi.org/10.1364/OPEX.13.007035).
- [7] M. Muthukumar, *Communication: Charge, diffusion, and mobility of proteins through nanopores*, *The Journal of Chemical Physics* **141**, 081104 (2014), doi:[10.1063/1.4894401](https://doi.org/10.1063/1.4894401).

- [8] P. Dechadilok and W. M. Deen, *Hindrance factors for diffusion and convection in pores*, *Industrial & Engineering Chemistry Research* **45**, 6953 (2006), doi:[10.1021/ie051387n](https://doi.org/10.1021/ie051387n).
- [9] Y. Gutiérrez, R. Alcaraz de la Osa, D. Ortiz, J. M. Saiz, F. González, and F. Moreno, *Plasmonics in the ultraviolet with aluminum, gallium, magnesium and rhodium*, *Applied Sciences* **8**, 64 (2018), doi:[10.3390/app8010064](https://doi.org/10.3390/app8010064).
- [10] A. Barulin, J.-B. Claude, S. Patra, N. Bonod, and J. Wenger, *Deep ultraviolet plasmonic enhancement of single protein autofluorescence in zero-mode waveguides*, *Nano Letters* **19**, 7434 (2019), doi:[10.1021/acs.nanolett.9b03137](https://doi.org/10.1021/acs.nanolett.9b03137).
- [11] A. Barulin, P. Roy, J.-B. Claude, and J. Wenger, *Ultraviolet optical horn antennas for label-free detection of single proteins*, *Nature Communications* **13**, 1842 (2022), doi:[10.1038/s41467-022-29546-4](https://doi.org/10.1038/s41467-022-29546-4).
- [12] L. Restrepo-Pérez, C. Joo, and C. Dekker, *Paving the way to single-molecule protein sequencing*, *Nature Nanotechnology* **13**, 786 (2018), doi:[10.1038/s41565-018-0236-6](https://doi.org/10.1038/s41565-018-0236-6).
- [13] J. A. Alfaro, P. Bohländer, M. Dai, M. Filius, C. J. Howard, X. F. van Kooten, S. Ohayon, A. Pomorski, S. Schmid, A. Aksimentiev, E. V. Anslyn, G. Bedran, C. Cao, M. Chinnappi, E. Coyaud, C. Dekker, G. Dittmar, N. Drachman, R. Eelkema, D. Goodlett, S. Hentz, U. Kalathiya, N. L. Kelleher, R. T. Kelly, Z. Kelman, S. H. Kim, B. Kuster, D. Rodriguez-Larrea, S. Lindsay, G. Maglia, E. M. Marcotte, J. P. Marino, C. Masselon, M. Mayer, P. Samaras, K. Sarthak, L. Sepiashvili, D. Stein, M. Wanunu, M. Wilhelm, P. Yin, A. Meller, and C. Joo, *The emerging landscape of single-molecule protein sequencing technologies*, *Nature Methods* **18**, 604 (2021), doi:[10.1038/s41592-021-01143-1](https://doi.org/10.1038/s41592-021-01143-1).
- [14] S. J. Kim, J. Fernandez-Martinez, I. Nudelman, Y. Shi, W. Zhang, B. Raveh, T. Hericks, B. D. Slaughter, J. A. Hogan, P. Upla, I. E. Chemmama, R. Pellarin, I. Echeverria, M. Shivaraju, A. S. Chaudhury, J. Wang, R. Williams, J. R. Unruh, C. H. Greenberg, E. Y. Jacobs, Z. Yu, M. J. de la Cruz, R. Mironska, D. L. Stokes, J. D. Aitchison, M. F. Jarrold, J. L. Gerton, S. J. Ludtke, C. W. Akey, B. T. Chait, A. Sali, and M. P. Rout, *Integrative structure and functional anatomy of a nuclear pore complex*, *Nature* **555**, 475 (2018), doi:[10.1038/nature26003](https://doi.org/10.1038/nature26003).
- [15] C. E. Zimmerli, M. Allegretti, V. Rantos, S. K. Goetz, A. Obarska-Kosinska, I. Zagoriy, A. Halavatyi, G. Hummer, J. Mahamid, J. Kosinski, and M. Beck, *Nuclear pores dilate and constrict in cellulose*, *Science* **374**, eabd9776 (2021), doi:[10.1126/science.abd9776](https://doi.org/10.1126/science.abd9776).
- [16] C. W. Akey, D. Singh, C. Ouch, I. Echeverria, I. Nudelman, J. M. Varberg, Z. Yu, F. Fang, Y. Shi, J. Wang, D. Salzberg, K. Song, C. Xu, J. C. Gumbart, S. Suslov, J. Unruh, S. L. Jaspersen, B. T. Chait, A. Sali, J. Fernandez-Martinez, S. J. Ludtke, E. Villa, and M. P. Rout, *Comprehensive structure and functional adaptations of the yeast nuclear pore complex*, *Cell* **185**, 361 (2022), doi:<https://doi.org/10.1016/j.cell.2021.12.015>.

- [17] M. Yu, M. Heidari, S. Mikhaleva, P. S. Tan, S. Mingu, H. Ruan, C. D. Reinkemeier, A. Obarska-Kosinska, M. Siggel, M. Beck, G. Hummer, and E. A. Lemke, *Visualizing the disordered nuclear transport machinery in situ*, *Nature* **617**, 162 (2023), doi:[10.1038/s41586-023-05990-0](https://doi.org/10.1038/s41586-023-05990-0).
- [18] D. Cowburn and M. Rout, *Improving the Hole Picture: Towards a Consensus on the Mechanism of Nuclear Transport*, *ArXiv* (2023).
- [19] A. Matsuda and M. R. K. Mofrad, *Free energy calculations shed light on the nuclear pore complex's selective barrier nature*, *Biophysical Journal* **120**, 3628 (2021), doi:[10.1016/j.bpj.2021.07.025](https://doi.org/10.1016/j.bpj.2021.07.025).
- [20] T. Jovanovic-Talisman, J. Tetenbaum-Novatt, A. S. McKenney, A. Zilman, R. Peters, M. P. Rout, and B. T. Chait, *Artificial nanopores that mimic the transport selectivity of the nuclear pore complex*, *Nature* **457**, 1023 (2009), doi:[10.1038/nature07600](https://doi.org/10.1038/nature07600).
- [21] G. Emilsson, Y. Sakiyama, B. Malekian, K. Xiong, Z. Adali-Kaya, R. Y. H. Lim, and A. B. Dahlin, *Gating protein transport in solid state nanopores by single molecule recognition*, *ACS Central Science* **4**, 1007 (2018), doi:[10.1021/acscentsci.8b00268](https://doi.org/10.1021/acscentsci.8b00268).
- [22] A. Fragasso, *Towards a bottom-up reconstitution of the nuclear pore complex*, *Ph.D. thesis*, TU Delft (2021), doi:[10.4233/uuid:c717460d-eb79-495a-b239-4d030d0412c6](https://doi.org/10.4233/uuid:c717460d-eb79-495a-b239-4d030d0412c6).

SUMMARY

The nanoworld is full of effects for which our everyday intuition fails. One such effect which is studied extensively in this thesis is the light-blocking behavior of zero-mode waveguides (ZMWs): light that refuses to propagate through a hole in a metal film. Nanopores are fascinating due to their conceptual simplicity. In the end, they are *just very tiny holes*. And one can translocate single molecules through them, just as one would pull a string through a macroscopic hole. Bridging the gap between conceptual simplicity and inherent complexity is a reoccurring theme in this thesis, when establishing new ways to look through nanopores. These new ways are aimed towards a variety of applications ranging from studying single-molecule translocations, to understanding the nuclear pore complex, and even to monitoring the local fluorescence of proteins in living cells. Here, we briefly summarize the key concepts and results of this thesis.

In **chapter 1**, we first introduce the general concepts underlying this thesis and give an introduction to nanopores. We start by looking at different classes of nanopores and key concepts, such as nanopore transport and nanopores as single-molecule sensors. We then focus on zero-mode waveguides that are intriguing due to their optical properties. Finally, we describe the nuclear pore complex, a giant nanopore in the nuclear envelope that regulates nucleo-cytoplasmic transport. In the second section of this chapter, we cover the relevant techniques that were used throughout the thesis, introducing basic concepts for nanofabrication, optical microscopy, electron microscopy, and computer simulations. We conclude this chapter with an outline of the thesis.

In **chapter 2**, we aimed to observe single-molecule translocations through nanopores with a 50 nm diameter that were immersed in low salinity buffers. Additionally, we aimed to distinguish different kinds of analytes driven through the pores without being disturbed by external fields (and thus only translocating due to free diffusion). These goals are very hard to achieve using conductance based nanopores. Using freestanding zero-mode waveguides, we could fulfill all these requirements at the same time, however. In the previous literature, ZMWs were either made from aluminum or gold. After initial tests using these metals, we found that aluminum nanopores were unstable in the salt solutions we used, and gold nanopores produced a high photoluminescent background in the green detection channel. Therefore, we fabricated ZMWs from palladium (Pd) and showed that it offers advantages compared to gold, aluminum, titanium, and platinum with respect to chemical stability, optical background, and fabrication. By optically following single-molecule translocations through the Pd nanopores, we showed that freestanding Pd ZMWs are suitable to detect the diffusion-driven translocations of a variety of biomolecules. By driving DNA electrically, we further showed that Pd nanopores are compatible with common methods that are usually applied to nanopores as single-molecule sensors.

Chapter 3 presents a study of DNA translocations originating from asymmetric salt concentrations, which was enabled by the properties of Pd nanopores established in the

previous chapter, since the translocation process was not perturbed by external electric fields. Electrodes, which would complicate the data interpretation, could be fully avoided in these ZMW studies. The effect underlying DNA translocations due to salt gradients, is called diffusiophoresis and this has barely been discussed in the context of nanopores. We showed that a particle carrying negative charges can translocate through a nanopore due to the presence of a salt gradient across the nanopore. We compared the effect of different salts and different gradients in order to identify trends in the translocation rate that were previously predicted theoretically. In the regimes covered by our experiments, we found that DNA travels up the gradient and gets driven stronger by a steeper gradient. By comparing different salts, we verified that the same concentration gradient of NaCl leads to a higher translocation rate than KCl. In the end of the chapter, we extensively discuss a number of shortcomings of the experiments which led to a high experiment-to-experiment variability hindering us from a thorough quantitative analysis of the observed effects.

Chapter 4 presents the main results of this thesis, where we applied freestanding Pd ZMWs to study the transport selectivity of nuclear pore complex mimics by comparing the translocation rates of the nuclear transport receptor Kap95 to BSA. Of both proteins, the single-molecule translocation events due to free diffusion could be followed, which is an advantage compared to previously used methods to study the transport selectivity. Kap95 is known to interact with FG nucleoporins whereas BSA does not and thus served as an inert control probe. The use of ZMWs allowed to investigate how the selectivity is influenced by the pore size. NPC mimics were made by attaching the nucleoporin Nsp1 to the inner surface of the nanopores. Thus, the pores were filled with a mesh of nucleoporins which allowed to study the properties of this minimal system. By comparing the translocation rates through Nsp1-filled pores with open pores, we could establish that NPC mimics based on Pd ZMWs indeed exhibit transport selectivity. We found that the translocation rate of Kap95 was barely influenced by the presence of the Nups whereas BSA showed almost no translocations through small Nsp1 pores. Larger Nsp1 pores, however, decreased gradually in their capability to block BSA, which we could explain using coarse-grained molecular-dynamics simulations that showed that BSA translocations mostly happen via transient openings in the Nup mesh. These openings became more abundant for larger pores until they formed a stable central channel. By analyzing the BSA translocation rate for various Kap95 concentrations, we could test the influence of Kap95 on the Nsp1 mesh, which is one of the central predictions from the Kap-centric models of nucleo-cytoplasmic transport. Being able to investigate this prediction on a single-molecule basis is one of the big advantages of NPC mimics based on Pd ZMWs. We could identify an increased BSA leakage for big Nsp1 pores in the presence of Kap95 while we only observed a minor effect of Kap95 on small Nsp1 pores. Thus we were able to add another piece to the puzzle how Kap95 influences the NPC.

In **chapter 5**, we moved from studying the transport properties of the Nup mesh to studying the structural arrangement of it. We developed a new method using cryo EM to investigate the locations of proteins in NPC mimics based on solid-state nanopores. To achieve high enough contrast during imaging, we labeled the proteins of interest with small gold particles that would show up as dark spots in the EM images. The locations of the labeled analytes could be recorded with respect to the pore boundary.

Since the pores were prepared by nanofabrication, thousands of similar pores could be imaged and compared in one experiment. This allowed to make statistically relevant statements about the distributions of Nsp1 and Kap95, allowing to study the structure of the unstructured NPC mimics. After discussing the development of the technique, we showed the application of it to two different questions: The distribution of Nsp1 within the pores with varying sizes and selectivity of Kap95 vs. BSA, together with their distributions. These initial tests show the potential of the method, and we can envision plenty of possible applications thereof in the future, which are discussed in the end of the chapter.

In [chapter 6](#), we moved towards in cellulo studies using Pd ZMWs. It was previously shown that cells can penetrate into the tiny volumes of the ZMWs with their cell membrane. We applied this feature for cytoplasmic background suppression to image single fluorescently labelled proteins attached to the cell membrane. Due to high fluorescence background emerging from cytosolic fluorophores, this was impossible using conventional TIRF microscopy. To achieve an optimal background suppression, we developed overmilled Pd ZMWs together with non-perpendicular illumination which allowed the cells to position their cell membrane below the metal layer. Thus, the membrane bound fluorophores were specifically excited by the incoming laser light, while most of the cytoplasm was excluded from the excitation volume. To understand the physical basis of this background suppression, we performed in vitro single-molecule fluorescence experiments together with detailed simulations of the expected light fields which explained the observed fluorescence lifetime reduction and fluorescence enhancement both qualitatively and quantitatively very well. Taken together, we believe that overmilled Pd ZMWs together with oblique angle illumination offers great potential for single-molecule studies in live cells.

To conclude the thesis, in [chapter 7](#), we discussed a few possible future directions based on the work presented in this thesis. These cover both suggestions to further improve the methods presented in this thesis as well as new approaches to study NPC functionality.

SAMENVATTING

De nanowereld staat bol van de wonderlijke effecten die ons alledaagse voorstellingsvermogen te boven gaan. In dit proefschrift bestuderen we één van die effecten uitvoerig, de zogenaamde *zero-mode waveguides* (ZMWs¹): het plotselinge uitdoven van een lichtstraal wanneer deze gericht wordt op een heel klein gaatje, oftewel een *nanopore*, in een dunne laag metaal. In al hun eenvoud zijn deze *nanopores* eigenlijk fascinerende objecten, die beschouwd kunnen worden als een moleculair „oog van de naald” waar je van alles doorheen kunt trekken. Een terugkerend thema in dit proefschrift is het overbruggen van de kloof tussen de conceptuele eenvoud van *nanopores* aan de ene kant, en de inherente complexiteit aan de andere kant, bij het ontwikkelen van „nieuwe manieren om door *nanopores* te kijken”. Deze nieuwe manieren zijn op verschillende toepassingen gericht, beginnend met het studeren van transportprocessen op moleculaire schaal, tot de bestudering van kernporiën (*nuclear pore complex*, NPC), en zelfs lokale fluorescentie in levende cellen. Wat nu volgt is een beknopt overzicht van de belangrijkste bevindingen van dit proefschrift.

In **Hoofdstuk 1** introduceren we eerst de basisprincipes die ten grondslag liggen aan dit onderzoek, en geven we een inleiding over *nanopores*. Zo beschrijven we de verschillende categorieën van *nanopores* en belangrijke concepten, zoals moleculair transport door *nanopores* en het gebruik van *nanopores* als moleculaire sensoren. Vervolgens zoomen we in op de intrigerende optische eigenschappen van ZMWs. En tenslotte beschrijven we de biologische NPC, een gigantisch grote *nanopore* die zich bevindt in de kernmembraan van de meeste cellen en die aldaar de communicatie verzorgt tussen het cytoplasma en de celkern. In het tweede deel van dit hoofdstuk behandelen we de relevante technieken die in dit proefschrift aan bod komen, zoals nano-fabricatie, optische microscopie, elektronen microscopie, en computersimulaties. We sluiten dit hoofdstuk af met een overzicht van het proefschrift.

In **Hoofdstuk 2** beschrijven we onze pogingen om moleculaire transportprocessen waar te nemen in *nanopores* met een diameter van slechts 50 nanometer en in buffers met een laag zoutgehalte. Tevens hebben we gepoogd om verschillende biologische moleculen te onderscheiden die gedreven door diffusie (en dus niet door een extern krachtveld) door de *nanopores* stroomden. Door gebruik te maken van vrijstaande ZMWs konden we deze doelen bereiken. Hoewel ZMWs in eerder onderzoek gemaakt werden van aluminium of goud, ontdekten wij dat aluminium *nanopores* niet stabiel waren in onze buffers, en dat gouden *nanopores* een hoog achtergrondsignaal van fotoluminescentie genereerden in het groen-licht regime. ZMWs die gemaakt werden van palladium (Pd) daarentegen vertoonden deze nadelen niet, en deze gedroegen zich ook beter dan ZMWs van titanium of platina. Aldus konden we aantonen dat vrijstaande Pd-ZMWs geschikt

Dank aan Eli van der Sluis voor het vertalen van deze samenvatting.

¹Bij gebrek aan een geschikte Nederlands equivalenten zullen we in deze samenvatting (de afkorting van) Engelse termen gebruiken

zijn om diffusie-gedreven transport van verschillende biologische moleculen waar te nemen met optische technieken. Door DNA moleculen aan een elektrisch veld bloot te stellen konden we ook aantonen dat Pd-*nanopores* compatibel zijn met gangbare methoden die *nanopores* gebruiken als moleculaire sensoren.

In **Hoofdstuk 3** bouwen we voort op de *nanopores* uit het vorige hoofdstuk, en bestuderen we DNA-transport dat gedreven wordt door asymmetrische zoutconcentraties aan weerskanten van de Pd-ZMW. Dit fenomeen wordt *diffusioforese* genoemd, en werd tot nu toe nauwelijks beschreven in de context van *nanopores*. De interpretatie van dergelijke meetgegevens is eenvoudiger, doordat mogelijk storende electrodes en externe elektrische velden vermeden worden door het gebruik van Pd ZMWs. We konden aantonen dat negatief geladen moleculen inderdaad door *diffusiophorese* door de *nanopore* getransporteerd kunnen worden, en we hebben het effect van zout-types en -concentraties vergeleken met voorspellingen op basis van theoretische modellen. In onze experimenten bleek dat DNA van een laag naar een hoog zoutgehalte stroomt, en dat een groter concentratieverschil leidt tot een sterkere DNA-stroming. Ook blijkt dat een gradiënt van natriumchloride (NaCl) een sterkere DNA-stroming veroorzaakt dan een even hoge gradiënt van kaliumchloride (KCl). Aan het eind van dit hoofdstuk bespreken we een aantal experimentele tekortkomingen die hebben geleid tot een hoge variatie tussen afzonderlijke metingen, waardoor we geen uitgebreide kwantitatieve analyse van de waargenomen effecten hebben kunnen uitvoeren.

Hoofdstuk 4 omvat de kern van dit proefschrift: de toepassing van vrijstaande Pd-ZMWs om het selectieve transport van biologische moleculen (zoals transport-eiwitten) door een nagebootste NPC te bestuderen. Hiervoor vergeleken we de transportsnelheid van het kern transport-eiwit (*karyopherin*) Kap95 met die van een willekeurig bloed-eiwit BSA (*bovine serum albumin*). Van Kap95 is bekend dat het bindt aan de zogenaamde FG-nucleoporins die de binnenkant van de NPC bekleeden; BSA daarentegen fungeerde als een inert controleëiwit. Om zo goed mogelijk een echte NPC na te bootsen was de binnenkant van onze *nanopore* bekleed met de FG-nucleoporin Nsp1, dat een voor de NPC karakteristiek gaaswerk vormt in de porie. Met behulp van de Pd-ZMWs konden we onder andere onderzoeken hoe de diameter van de *nanopore* diens selectiviteit beïnvloedt. In tegenstelling tot open *nanopores* bleken Pd-ZMWs die voorzien waren van een Nsp1 gaaswerk inderdaad selectief te zijn voor Kap95: Het Nsp1 gaaswerk had geen invloed op het transport van Kap95 door kleine poriën, maar BSA werd hier nauwelijks doorgelaten. Naarmate de diameter van de poriën groter werd verloren ze echter hun selectiviteit, dat wil zeggen dat ze niet meer in staat waren om BSA te blokkeren. Dit fenomeen konden we verklaren met zogenaamde *coarse-grained molecular dynamics* simulaties: BSA doorkruist het Nsp1 gaaswerk voornamelijk via tijdelijke openingen. Bij grotere nanopores vormen zich meer van die openingen, totdat uiteindelijk in het midden een stabiel open kanaal ontstaat in het gaaswerk. Een belangrijke voorspelling die volgt uit het theoretische *Kap-centric* model, is dat Kap95 de eigenschappen van het Nsp1 gaaswerk beïnvloedt. Met onze unieke single-molecule Pd-ZMW experimenten konden we dit effect bestuderen door de transport frequentie van BSA te meten bij verschillende Kap95 concentraties. Bij grote poriën bleek de aanwezigheid van Kap95 inderdaad te leiden tot meer lekkage van BSA, terwijl dat bij kleine poriën nauwelijks het geval was. Al met al hebben we dus hiermee kunnen bijdragen aan het begrip van het

mechanisme van Kap95-gedreven transport door de kernporie.

In **Hoofdstuk 5** maken we de overstap van transport-metingen naar de interne structuur van het Nsp1 gaaswerk. Hiervoor hebben we een nieuwe *cryo*-electronen microscopie methode ontwikkeld om de locatie van transport-eiwitten te bepalen in *solid-state nanopores* waarmee we NPCs nabootsen. Om genoeg contrast te genereren werden de betreffende transport-eiwitten voorzien van een klein goud-deeltje, waardoor ze als donkere vlekken zichtbaar werden in de doorgaans grijzige microscopische opnames. Hierdoor konden we precies bepalen waar ze zich in de porie bevonden ten opzichte van de rand. En aangezien de poriën werden gemaakt met een nanofabricatie proces konden we er in één experiment duizenden tegelijk bekijken, om vervolgens statistisch significante uitspraken te kunnen doen over de locatie van zowel Kap95 als Nsp1. Deze methode kan toegepast worden om (op zijn minst) twee vragen te beantwoorden: Hoe is Nsp1 precies gedistribueerd over poriën met verschillende diameters? En hoe verhoudt zich de Nsp1-distributie tot de selectiviteit (en distributie) van Kap95 *versus* BSA? Onze initiële experimenten lijken veelbelovend, en aan het eind van dit hoofdstuk bespreken we een aantal andere mogelijke toepassingen voor deze nieuwe methode.

In **Hoofdstuk 6** hebben we Pd-ZMWs gebruikt om levende cellen te bestuderen. Eerdere studies hadden al aangetoond dat humane cellen de kleine holtes van de ZMWs kunnen binnendringen met een soort tentakels; wij hebben deze cellulaire lenigheid uitgebuit om individuele fluorescent gelabelde membraan-eiwitten te kunnen bestuderen. Met conventionele microscopische methoden zoals *TIRF* was dit niet mogelijk door de sterke achtergrond-fluorescentie vanuit het cytoplasma. Optimale onderdrukking van de achtergrond werd bereikt door de ZMWs dwars door de laag palladium heen te boren tot in de onderliggende laag glas (*overmilling*), waardoor de cellulaire tentakels tot onder het metaal reikten. Door schuin in plaats van loodrecht van onderen te belichten sloeg de laser specifiek de membraan eiwitten in de tentakels aan, en niet (of nauwelijks) de cytoplasmatische achtergrond. Om de natuurkundige basis van deze achtergrond onderdrukking beter te begrijpen hebben we *single-molecule* fluorescentie experimenten gecombineerd met simulaties van het laser lichtveld. Zowel kwalitatief als kwantitatief konden we hiermee verklaren waardoor de waargenomen fluorescentie een relatief hoge intensiteit had en een relatief korte levensduur. Kort samengevat denken we dat schuine belichting van *overmilled* Pd-ZMWs een veelbelovende methode is voor *single-molecule* experimenten in levende cellen.

In **Hoofdstuk 7** tenslotte bespreken we een aantal mogelijke onderzoeksrichtingen die voortvloeien uit het werk dat gepresenteerd is in de voorgaande hoofdstukken. Hier komen zowel potentiële verbeteringen van de huidige methodes aan bod, als nieuwe benaderingen om de functie van de NPC in meer detail te onderzoeken.

ZUSAMMENFASSUNG

Die Nanowelt ist voller Effekte, die sich unserer alltäglichen Intuition entziehen. Einer dieser Effekte, der in dieser Arbeit ausführlich studiert wird, ist die Fähigkeit von Nullmodenwellenleitern (Zero-Mode Waveguides - ZMWs), einfallendes Licht zu blockieren: Genügend kleine Poren in Metallfilmen verhindern das Durchscheinen von einfallendem Licht. Andererseits sind solche Nanoporen wegen ihrer konzeptionellen Einfachheit faszinierend. Im Endeffekt sind sie nur *sehr kleine Löcher*. Man kann selbst Moleküle durch sie hindurchbefördern ähnlich wie man einen Faden durch ein makroskopisches Loch ziehen würde. Die Brücke zu schlagen zwischen dieser konzeptionellen Einfachheit und der inhärenten Komplexität ist ein wiederkehrendes Motiv in dieser Arbeit, in der wir *Neue Wege beschreiten um durch Nanoporen zu schauen*. Diese neuen Wege haben eine Vielzahl an Anwendungen welche von Einzelmolekültranslokationen durch Nanoporen über Untersuchungen der Funktion des Kernporenkomplexes bis zu Einzelmolekülfluoreszenz in lebenden Zellen reichen.

In **Kapitel 1** führen wir kurz die wesentlichen Konzepte ein, die für das Verständnis dieser Arbeit notwendig sind. Des weiteren gehen wir eingängig auf Nanoporen ein und erklären wesentliche Eigenschaften. Wir benennen verschiedene Klassen von Nanoporen und beschreiben verschiedene Konzepte die zur Untersuchung von Nanoporen wichtig sind, wie zum Beispiel molekularer Transport durch Nanoporen und die Anwendung von Nanoporen als Einzelmolekülsensoren. Metallische Nanoporen, eine spezielle Klasse von Nanoporen, können dabei als sogenannte Nullmodenwellenleiter fungieren, welche durch ihre optischen Eigenschaften besonders interessant sind und deren Eigenschaften danach genauer besprochen werden. Abschließend besprechen wir die Eigenschaften des Kernporenkomplexes, welcher eine riesige Nanopore ist, die in der Kernmembran den Transport zwischen dem Zellkern und dem Zytoplasma reguliert. Im zweiten Teil dieses Kapitels gehen wir näher auf die experimentellen Methoden ein, die in dieser Arbeit verwendet wurden. Dabei erklären wir die grundlegenden Konzepte der Nanofabrikation, der Optischen- und Elektronenmikroskopie und der Computersimulationen, welche in dieser Arbeit verwendet wurden. Wir beenden das Kapitel mit einem Ausblick auf den Rest der Arbeit.

In **Kapitel 2** haben wir eine Methode gesucht, mit der man Einzelmolekültranslokationen durch Nanoporen beobachten kann, die eine Größe von ungefähr 50 nm besitzen und welche mit Puffern mit einer niedrigen Molarität an gelösten Salzen umspült werden. Des weiteren wollten wir verschiedene Arten von Proben (z.B. verschiedene Proteine) bei ihrer Translokation unterscheiden können. Diese Translokation sollte rein durch freie Diffusion getrieben sein und nicht durch externe elektrische Felder beeinflusst werden. Dabei ist es extrem schwierig all diese Voraussetzungen mit klassischen Nanoporen zu erfüllen bei denen eine Änderung in der elektrischen Leitfähigkeit, ausgelöst durch die räumliche Blockade während einer Translokation, detektiert wird. Mittels freistehenden Nullmodenwellenleitern konnten wir all diese Voraussetzungen jedoch

gleichzeitig erfüllen. Typischerweise werden für diese Anwendungen Nullmodenwellenleiter aus Gold oder Aluminium verwendet, welche sich allerdings in unseren Experimenten als ungeeignet herausstellten, da Aluminiumnanoporen in den von uns verwendeten salzhaltigen Puffern nicht stabil waren und Goldnanoporen starke Photolumineszenz im grünen Spektralbereich zeigten, wenn sie mit blauem Licht beschienen werden. Darum stellten wir Nanoporen in einem Palladiumfilm her. Danach zeigten wir, dass dieses Edelmetall vorteilhaft gegenüber anderen Metallen wie Gold, Aluminium, Titan und Platin ist für die Anwendung bei Nullmodenwellenleitern ist. Dies kommt durch seine chemische Stabilität, Handhabbarkeit und optischen Eigenschaften. Indem wir optisch die Translokation von Einzelmolekülen durch Palladiumnanoporen verfolgten, konnten wir zeigen, dass freistehende Palladium-Nullmodenwellenleiter geeignet sind um die diffusionsgetriebene Translokation von verschiedensten Biomolekülen zu studieren. Darüberhinaus untersuchten wir elektrisch getriebene Translokationen von DNS Molekülen und zeigten damit, dass Pd-Nanoporen für typische Nanoporenanwendungen geeignet sind.

In **Kapitel 3** untersuchen wir DNS Translokationen, die durch unterschiedliche Salzkonzentrationen auf beiden Seiten der Nanopore angetrieben werden. Dies war erst mittels der Methoden, die wir im vorangegangenen Kapitel entwickelt hatten, möglich geworden, da Palladium-Nullmodenwellenleiter es erlauben DNS Translokationen auch ohne ein extern angelegtes elektrisches Feld zu untersuchen. Des weiteren konnte auf die Verwendung von Elektroden vollständig verzichtet werden, welche durch potentiell stattfindende elektrochemische Reaktionen in den unterschiedlichen Salzlösungen die Interpretation der Daten erheblich erschwert hätten. Der Effekt der zu salzgradientgetriebenen DNS Translokationen führt nennt sich Diffusiophorese und ihr Einfluss auf die Physik in Nanoporen wurde bisher nur wenig untersucht. In diesem Kapitel konnten wir zeigen, dass ein negativ geladenes Molekül, wie es die DNS ist, mittels Diffusiophorese durch Nanoporen transportiert werden kann, welche durch einen Gradienten in der Salzkonzentration über die Nanopore hinweg ausgelöst wird. Daraufhin verglichen wir den Einfluss verschiedener Salze und verschieden starker Gradienten auf diesen Transportmechanismus, um verschiedene Einflussfaktoren zu untersuchen, welche bereits zuvor theoretisch vorhergesagt worden waren. In den durch uns untersuchten Parameterbereichen stellten wir fest, dass DNS durch Nanoporen in Richtung höherer Salzkonzentrationen getrieben wird, wobei ein größerer Gradient zu einer stärkeren treibenden Kraft führte. Des weiteren konnten wir feststellen, dass ein NaCl Gradient zu mehr Translokationen führte als wenn der selbe Gradient mit KCl erzeugt wurde. Am Ende des Kapitels diskutieren wir einige Probleme mit dem experimentellen Aufbau ausführlich, welche zu großen Diskrepanzen zwischen verschiedenen Experimenten geführt haben könnten und welche im Endeffekt eine tiefgehende quantitative Analyse verhinderten.

Die Hauptergebnisse dieser Arbeit stellen wir in **Kapitel 4** dar. Dort verwendeten wir freistehende Palladium-Nullmodenwellenleiter, um die Transportselektivität von Kernporenkomplexnachbauten zu untersuchen, indem wir die Translokationsraten des Kerntransportproteins Karyopherin 95 (Kap95) mit derer von einem Vergleichsprotein namens Bovinem Serum Albumin (BSA) durch diese Kernporenkomplexnachbauten verglichen. Bei beiden Proteinen konnten die Translokationen von einzelnen Molekülen mittels freier Diffusion verfolgt werden, was einen Vorteil gegenüber bestehenden Me-

thoden bedeutet. Von Kap95 ist bekannt, dass es an die sogenannten FG-Nucleoporine binden kann, wobei BSA keine solche Interaktion zeigt und daher als Kontrollmolekül verwendet wurde. Die Verwendung von Nullmodenwellenleitern ermöglichte dabei die Selektivität der Kernporenkomplexnachbauten in Abhängigkeit von der Porengröße zu untersuchen. Wir verglichen dafür die Translokationsraten beider Proteine, welche wir bei offenen Poren maßen, mit denen, welche wir durch Poren maßen, die mit dem Nucleoporin Nsp1 gefüllt waren und damit einen simplistischen Nachbau des echten Kernporenkomplexes bildeten. Solche Kernporenkomplexnachbauten erzeugten wir, indem wir das Nucleoporin Nsp1 an die Palladiumoberfläche hängten, woraufhin die Palladiumnanoporen von einem Geflecht dieser unstrukturierten und filamentösen Proteine gefüllt waren. Wir konnten zeigen, dass solche Kernporenkomplexnachbauten basierend auf Palladium-Nullmodenwellenleitern tatsächlich die erwartete Transportselektivität zeigten. Dabei fanden wir, dass das Transportprotein Kap95 beinahe ungehindert durch das dichte Geflecht von Nsp1 diffundieren konnte, wobei das Kontrollprotein BSA kaum noch durch kleine Nsp1-gefüllte Poren translokieren konnte. Größere Nsp1-gefüllte Poren verloren die Fähigkeit BSA zu blockieren graduell mit steigender Größe, was wir mittels vereinfachter molekulardynamischer Simulationen erklären konnten. Diese zeigten, dass BSA Translokationen hauptsächlich durch spontane und kurzfristige Öffnungen im Nsp1-Geflecht stattfanden. Die Simulationen zeigten auch, dass diese Löcher im Nsp1-Geflecht mit zunehmendem Porendurchmesser häufiger und größer wurden. Des Weiteren konnten wir den Einfluss des Transporters Kap95 auf die Selektivität des Nsp1 Geflechts messen. Ein solcher Einfluss ist eine der zentralen Aussagen des kapzentristischen Modells zur Beschreibung des Transports durch den Kernporenkomplex. Auch dies war mit bisherigen Einzelmolekülmethoden kaum möglich. Wir stellten fest, dass bei großen Nanoporen BSA leichter durch die ohnehin geöffneten Nsp1-Poren diffundieren konnte, wenn eine hohe Konzentration von Kap95 anwesend war. Im Gegensatz dazu, hatten die von uns getesteten Kap95-Konzentrationen kaum einen Effekt auf die Selektivität von kleinen Nsp1-Poren. Somit konnten wir ein kleines weiteres Puzzlestück dazu beitragen, wie Kap95 den Kernporenkomplex beeinflusst.

In **Kapitel 5** gingen wir darüber hinaus den Transport durch das Nucleoporingeflecht zu messen und untersuchten direkt die strukturellen Eigenschaften dieses Geflechts. Wir entwickelten eine Methode basierend auf der Cryo-Elektronenmikroskopie, mit der wir den Aufenthaltsort einzelner Proteine innerhalb von Kernporenkomplexnachbauten basierend auf Festkörpernanoporen sichtbar machen konnten. Um genügend Bildkontrast in den extrem verrauschten elektronenmikroskopischen Bildern zu erzeugen, markierten wir spezifische Proteine, indem wir nanometergroße Gold Partikel an sie anhängten, welche dann als dunkle Punkte in den elektronenmikroskopischen Bildern sichtbar wurden. Der Aufenthaltsort der Goldpartikel relativ zur umgebenden Pore konnten dann mittels Bildverarbeitung registriert werden, was Rückschlüsse über die räumliche Verteilung der markierten Proteine zuließ. Dabei konnten Bilder tausender gleichartiger Poren aufgenommen werden, da die Poren mit nanotechnologischen Methoden hergestellt worden waren und sich daher in ihrer Form nur geringfügig voneinander unterschieden. Durch die große Menge an Bildern, konnten statistisch signifikante Aussagen über die Verteilung von beispielsweise Kap95 und Nsp1 in der Pore getroffen werden, was uns ermöglichte die Struktur der unstrukturierten Kernporenkomplexnachbauten

zu untersuchen. Nachdem wir in dem Kapitel die einzelnen Schritte zur Entwicklung der Methode gezeigt haben, gehen wir auf ihre Anwendung bezüglich zweier Fragestellungen ein: Wie ist das Nucleoporin Nsp1 innerhalb der Pore in Abhängigkeit vom Porendurchmesser verteilt? Und können wir Selektivität zwischen Kap95 und BSA zusammen mit der Verteilung der einzelnen Proteine sehen? Diese beiden Untersuchungen sollten dabei hauptsächlich die prinzipielle Machbarkeit der Methode nachweisen, für welche wir eine Vielzahl von Anwendungen in der Zukunft erwarten. Auf diese wird am Ende des Kapitels näher eingegangen.

In **Kapitel 6** entwickelten wir eine Methode, die es mithilfe von Palladium-Nullmodenwellenleitern erlaubt, Untersuchungen in lebenden Zellen durchzuführen, welche anders nicht möglich wären. In früheren Studien war schon gezeigt worden, dass Zellen ihre äußere Membran in kleinste Volumina, wie man sie bei Nullmodenwellenleitern findet, hineinstülpen können. Diese Eigenschaft nutzten wir, um den Fluoreszenzhintergrund zu unterdrücken, welcher die Mikroskopie von einzelnen fluoreszenten Molekülen an der Zellmembran in manchen Anwendungen unmöglich macht. Diese Unmöglichkeit kommt durch einen zu hohen Fluoreszenzhintergrund welcher von fluoreszenten Molekülen aus dem Zellplasma entstammt und selbst mit in diesen Fällen normalerweise verwendeter TIRF Mikroskopie nicht unterdrückt werden kann. Um den Hintergrund optimal zu unterdrücken haben wir Palladium-Nullmodenwellenleiter auf Glas entwickelt, die ein kleines offenes Volumen im Glas unter der Palladiumnanopore besitzen. Zusammen mit schief einfallendem Anregungslicht, war es so möglich, dass die Fluorophore auf der Zellmembran so unter der Metallschicht positioniert wurden, dass sie vom Anregungslicht angeregt wurden, die Fluorophore im Zellinneren allerdings nicht. Um die physikalischen Prozesse besser zu verstehen, die in diesen Nanolöchern stattfinden, haben wir Experimente mit freien Fluorophoren in Lösung durchgeführt deren Ergebnisse wir mittels detaillierten Computersimulationen des Lichtfeldes innerhalb der Poren erklären konnten. Diese Simulationen konnten die beobachtete Verkürzung der Fluoreszenzabregungszeit und der Fluoreszenzverstärkung sowohl qualitativ als auch quantitativ gut erklären. Alles in allem glauben wir, dass Palladium-Nullmodenwellenleiter mit darunterliegenden Volumina zusammen mit schräg einfallendem Anregungslicht ein großes Anwendungspotenzial bei Einzelmoleküluntersuchungen in lebenden Zellen hat.

Zum Abschluss diskutieren wir in **Kapitel 7** einige zukünftige Möglichkeiten, in die man ausgehend von dieser Arbeit weitere Untersuchungen anstellen kann. Diese behandeln sowohl Verbesserungsvorschläge der dargestellten Methoden als auch neue Ansätze um die Funktion des Kernporenkomplexes besser zu verstehen.

ACKNOWLEDGEMENTS

These acknowledgements have been removed from the public online version due to privacy. If you are interested in them, please contact Nils Klughammer for the full version of this thesis.

CURRICULUM VITÆ

Nils KLUGHAMMER

- 2011–2015 **Bachelor in Physics**
Heidelberg University, Heidelberg, Germany
*Thesis: Application of multiparticle collision dynamics (MPCD)
to channel flow and reaction fronts*
with Prof. Dr. Ulrich Schwarz
at Institute for Theoretical Physics, Heidelberg.
Studying the basic properties of the MPCD algorithm.
- 2013–2014 **iGEM competition**
Project: Ring of Fire
with Prof. Dr. Roland Eils and Dr. Barbara DiVentura,
at BioQuant, Heidelberg
Building a toolbox for protein circularization via inteins
and exploring methylation maintaining PCR.
- 2015–2018 **Master in Physics**
Heidelberg University, Heidelberg, Germany
*Thesis: Forces And Flow During
Starfish Oocyte Surface Contraction Waves*
with Prof. Dr. Ulrich Schwarz
at Institute for Theoretical Physics, Heidelberg.
Establishing an analytical model for the hydrodynamic flows
inside starfish oocytes originating from surface contraction waves.
- 2018–2023 **PhD in Bionanoscience**
Delft University of Technology, Delft, The Netherlands
Thesis: New Ways to Look through Nanopores
with Prof. dr. C. Dekker
at Bionanoscience department, Kavli Institute for Nanoscience

LIST OF PUBLICATIONS

PUBLICATIONS

- 2015 Max C. Waldhauer*, Silvan N. Schmitz*, Constantin Ahlmann-Eltze, Jan G. Gleixner, Carolin C. Schmelas, Anna G. Huhn, Charlotte Bunne, Magdalena Büscher, Max Horn, Nils Klughammer, Jakob Kreft, Elisabeth Schäfer, Philipp A. Bayer, Stephen G. Krämer, Julia Neugebauer, Pierre Wehler, Matthias P. Mayer, Roland Eils, and Barbara Di Ventura.
Backbone circularization of bacillus subtilis family 11 xylanase increases its thermostability and its resistance against aggregation.
Mol. BioSyst., 11:3231–3243, 2015.
<http://dx.doi.org/10.1039/C5MB00341E>,
Citations on Semantic Scholar: 15.
- 2018 Klughammer, Nils, Johanna Bischof, Nikolas D. Schnellbacher, Andrea Callegari, Péter Lénárt, and Ulrich S. Schwarz.
Cytoplasmic flows in starfish oocytes are fully determined by cortical contractions.
PLOS Computational Biology, 14(11):1–29, 11 2018.
<https://doi.org/10.1371/journal.pcbi.1006588>,
Citations on Semantic Scholar: 26.
- 2021 Nils Klughammer and Cees Dekker.
Palladium zero-mode waveguides for optical single-molecule detection with nanopores.
Nanotechnology, 32(18):18LT01, feb 2021.
<https://doi.org/10.1088/1361-6528/abd976>,
<https://arxiv.org/abs/2010.00276>,
Citations on Semantic Scholar: 15.
- 2023 Nils Klughammer*, Anders Barth*, Maurice Dekker, Alessio Fragasso, Patrick Onck, and Cees Dekker. Diameter dependence of transport through nuclear pore complex mimics studied using optical nanopores. *eLife*, 2023.
<https://doi.org/10.7554/eLife.87174>,
Citations on Semantic Scholar: 1.
- 2023 Sora Yang*, Nils Klughammer*, Anders Barth*, Marvin E. Tanenbaum°, and Cees Dekker°. Zero-mode waveguide nanowells for single-molecule detection in living cells. *ACS Nano*, 2023.
<https://doi.org/10.1101/2023.06.26.546504>,
Citations on Semantic Scholar: 1.

OTHER PUBLISHED WORK

SOFTWARE

- 2020 Klughammer, Nils.
Code from paper palladium zero-mode waveguides for optical single molecule detection with nanopores.
<https://doi.org/10.4121/12888551>.
- 2023 Nils Klughammer*, Anders Barth*, and Maurice Dekker. Code for paper diameter dependence of transport through nuclear pore complex mimics studied using optical nanopores, Feb 2023. <https://doi.org/10.4121/21027850>.

DATA

- 2020 Klughammer, Nils.
Data from paper palladium zero-mode waveguides for optical single molecule detection with nanopores.
<https://doi.org/10.4121/12888455>.
- 2023 Nils Klughammer*, Anders Barth*, and Maurice Dekker. Data from paper diameter dependence of transport through nuclear pore complex mimics studied using optical nanopores, Feb 2023. <https://doi.org/10.4121/22059227>.
- 2023 Sora Yang*, Nils Klughammer*, Anders Barth*. Datasets underlying the paper Zero-mode waveguide nanowells for single-molecule detection in living cells Zenodo, 2023. <https://doi.org/10.5281/zenodo.8060099>.

* denotes equal contribution, ° denotes equal contribution by senior authors



Casimir PhD series 2023-30
ISBN 978-90-8593-577-3